

Diss. ETH No. 20683

**Observation of Diffractive
W and Z Boson Production
and
Standard Model Higgs Boson Search
in the $H \rightarrow WW \rightarrow l\nu l\nu$ Channel
in $\sqrt{s} = 7$ TeV pp Collisions at CMS**

A dissertation submitted to
ETH ZÜRICH

for the degree of
Dr. Sc. ETH Zürich

presented by
Jürg Eugster

Dipl.-Phys. ETH Zürich
born October 21th 1981
citizen of Obereregg, AI - Switzerland

accepted on the recommendation of
Prof. G. Dissertori, examiner
Prof. Ch. Anastasiou, co-examiner

Abstract

In this thesis, two analyses using proton-proton (pp) collision data at a center of mass energy of $\sqrt{s} = 7$ TeV, recorded with the Compact Muon Solenoid (CMS) experiment at the Large Hadron Collider (LHC), are presented:

The first analysis, using an integrated luminosity of 36 pb^{-1} of low pile-up data recorded in 2010, uses the forward energy flow and the central charged particle multiplicity in events with leptonically decaying W and Z bosons to study the effects of the underlying event model. None of the studied Monte Carlo simulations describes the observed distributions from data sufficiently. Weak boson events with no significant energy deposits in one of the forward calorimeters are observed. This corresponds to a large pseudorapidity gap (LRG) of at least 1.9 units. The fraction of W(Z) events having a LRG is found to be $1.46 \pm 0.09(\text{stat.}) \pm 0.38(\text{syst.})\%$ ($1.57 \pm 0.25(\text{stat.}) \pm 0.42(\text{syst.})\%$). The majority of the charged leptons from these W/Z decays are found in the hemisphere opposite to the gap. This gives a strong indication of a diffractive component in the weak boson production, and the fraction of diffractively produced W bosons is found to be $0.73 \pm 0.34\%$ which is in agreement with observations from the Tevatron.

The second analysis presents the search for the SM Higgs boson decaying to a pair of W bosons in the fully leptonic final state. The pp collision data corresponding to a luminosity of 4.9 fb^{-1} recorded in 2011 are used. The W^+W^- event candidates are selected by requiring exactly two oppositely charged leptons and large missing transverse momentum from the escaping neutrinos. The shapes of the distributions of a multivariate discriminator are used to calculate upper limits on the SM Higgs production cross section. Different systematic uncertainties are studied in detail and included in the limit setting procedure using the 2011 dataset. The SM Higgs boson is excluded in the mass range of 134–211 GeV at the 95% confidence level. This is a slightly smaller range than the expected exclusion range of 125–230 GeV. An excess of about 2σ significance is observed in the low mass region below 140 GeV, consistent with a SM Higgs boson with a mass around 125 GeV.

Zusammenfassung

In dieser Dissertation werden zwei Analysen vorgestellt, welche Daten von Proton-Proton (pp) Kollisionen mit einer Schwerpunktsenergie von $\sqrt{s} = 7$ TeV verwenden, die mit dem Compact Muon Solenoid (CMS) Experiment am Large Hadron Collider (LHC) aufgezeichnet wurden.

Die erste Analyse verwendet Daten aus 2010 mit einer integrierten Luminosität von ungefähr 36 pb^{-1} . Sie benützt den vorwärts gerichteten Energiefluss und die zentrale Multiplizität der geladenen Teilchen in W und Z Ereignissen mit leptonischem Endzustand, um die unterliegende Struktur (*underlying event*) von pp Kollisionen zu untersuchen. Keines der untersuchten Simulations-Modelle beschreibt diese Verteilungen vollständig. Zusätzlich werden W und Z Ereignisse beobachtet, welche keine signifikante vorwärts gerichtete Energie aufweisen. Dies entspricht einem Unterbruch im Energiefluss (*Large Rapidity Gap*, LRG) von mindestens 1.9 Einheiten der Pseudorapidität. Der relative Anteil von W (Z) Ereignissen welche einen solchen LRG aufweisen wird als $1.46 \pm 0.09(\text{stat.}) \pm 0.38(\text{syst.})\%$ ($1.57 \pm 0.25(\text{stat.}) \pm 0.42(\text{syst.})\%$) bestimmt.

Die Mehrzahl der geladenen Leptonen vom W/Z Boson Zerfall werden in der dem LRG gegenüberliegenden Hemisphäre gefunden. Das ist ein starkes Indiz für eine diffraktive Komponente in der Produktion von W und Z Bosonen. Der Anteil der so erzeugten W Bosonen beträgt $0.73 \pm 0.34\%$, was kompatibel ist mit der Messung welche am Tevatron durchgeführt wurde.

Die zweite Analyse befasst sich mit der Suche nach dem vom Standard Modell der Teilchenphysik vorhergesagten Higgs Boson, welches unter anderem in zwei W Bosonen zerfällt. Diese W^+W^- -Kandidaten sind charakterisiert durch genau zwei entgegengesetzt geladene Leptonen sowie durch grossen fehlenden transversalen Impuls von den, einer Detektion entgehenden, Neutrinos. Die pp Kollisionen wurden 2011 aufgezeichnet und entsprechen einer integrierten Luminosität von 4.9 fb^{-1} .

Die Formen der Verteilungen einer multivariaten Diskriminierenden werden für die Berechnung eines oberen Limits für den Wirkungsquerschnitt der Higgs Produktion benützt. Verschiedene systematische Unsicherheiten werden im Detail studiert und fliessen in die Limit-Berechnung mit ein. Der beobachtete Bereich in dem das SM Higgs Boson mit 95% Aussagewahrscheinlichkeit ausgeschlossen werden kann ist 134–211 GeV. Dieser ist etwas kleiner als der erwartete Bereich von 125–230 GeV. Unterhalb von etwa 140 GeV kann ein Überschuss an Daten mit einer Signifikanz von ca. 2σ beobachtet werden.

Because it is there.
GEORGE MALLORY [1]

Contents

I	Introduction	5
1	The Standard Model of Particle Physics	7
1.1	Introduction	7
1.2	Quantum Electrodynamics	8
1.3	The Glashow-Salam-Weinberg Model	10
1.4	Quantum Chromo Dynamics	16
1.5	Limitations of the Standard Model	20
2	The Large Hadron Collider	21
2.1	Experimental Needs - Energy and Luminosity	22
2.2	LHC Design and Injection Chain	23
2.3	Physics at the LHC	23
3	The Compact Muon Solenoid Experiment	27
3.1	Overall Design of the CMS Detector	27
3.2	Tracker System	28
3.3	Calorimetry	30
3.4	Superconducting Solenoid	33
3.5	Muon System	34
3.6	Data Taking	35
3.7	Event Reconstruction	37
II	Observation of Diffractive W and Z Boson Production	41
4	Diffractive Production of W and Z Bosons	45
4.1	Diffraction - A General Introduction	45
4.2	Detour: “Why is Diffraction Called Diffraction?”	47
4.3	Diffractive Parton Distribution Functions	47
4.4	Underlying Event and Gap Survival Probability	48

4.5	Diffractive production of W and Z Bosons	49
4.6	Analysis Strategy	50
4.7	Datasets	51
4.8	Event Reconstruction	51
4.9	W and Z Event Selection	56
5	Forward Energy Flow and Central Track Multiplicity in W and Z Events	59
5.1	Forward Energy Flow	59
5.2	Central Charged Particle Multiplicity	65
5.3	Correlations between Forward Energy Flow and Central Charged Particle Multiplicity	65
5.4	Selection of W Events with a LRG	67
6	Observation of Diffractive Weak Boson Production	71
6.1	LRG Events and Invisible Pile-up Correction	71
6.2	Forward Energy Flow and Charged Particle Multiplicity in LRG Events . .	74
6.3	Size of the LRG	75
6.4	Hemisphere Correlations in LRG Events	77
6.5	Diffractive W Boson Production	79
III	Standard Model Higgs Boson Search	81
7	Higgs Production and the $H \rightarrow WW \rightarrow \ell\nu\ell\nu$ Signature	85
7.1	The Standard Model Higgs Boson at the LHC	85
7.2	The $H \rightarrow WW \rightarrow \ell\nu\ell\nu$ Signature	89
8	Monte Carlo Simulation of the Gluon-Fusion Higgs Production	93
8.1	Event Generators	93
8.2	Comparison of Different Event Generators	95
9	$H \rightarrow WW \rightarrow \ell\nu\ell\nu$ Analysis	107
9.1	Analysis Strategy	107
9.2	Datasets	109
9.3	Event Reconstruction and Pre-Selection	109
9.4	Background Estimates	116
9.5	Signal Extraction	122

10	Systematic Uncertainties for the $H \rightarrow WW \rightarrow l\nu l\nu$ Analysis	129
10.1	Sources of Systematic Uncertainties	129
10.2	Theoretical Uncertainties	130
10.3	Experimental Effects	132
10.4	Statistical Uncertainties	139
11	Cross Section Limits and Statistical Significance	141
11.1	Statistical Method	141
11.2	Results for the SM Higgs Boson Search	143
12	Higgs Boson Production with a Jet Veto	151
12.1	Simulation of the Jet Veto Efficiency in Parton Shower Monte Carlo	151
12.2	Ratios of Jet Veto Efficiencies	155
12.3	Jet Veto Efficiency in Data	156
IV	Summary and Appendices	159
13	Summary and Discussion	161
13.1	Summary and Discussion of Part II	161
13.2	Summary and Discussion of Part III	163
A	Lepton Definitions	167
A.1	2010 Electron Reconstruction	167
A.2	2010 Muon Reconstruction	167
A.3	2011 Muon Reconstruction	168
B	2010 and 2011 Datasets	171
B.1	2010 Datasets	171
B.2	2011 Datasets	171
C	2010 and 2011 Lepton Triggers	175
C.1	2010 Lepton Triggers	175
C.2	2011 Lepton Triggers	176
D	Higgs Analysis — Detailed Results	179
D.1	Detailed Event Yields at BDT-Level	179
D.2	Pre- and Post-Fit Normalization	179
D.3	Channel Compatibility for Signal Injection	180

E	Event Display of a Diffractive W Event	185
E.1	Non-Diffractive W Event	185
E.2	Diffractive W Event	185

Introduction

The pursuit to understand and explain the world around us is an enduring one — already two and a half millennia ago the first cornerstones of the modern understanding of nature were set: Democritus *atomic hypothesis* shaped the idea of basic indivisible building blocks out of which everything is made of. More than thousand years later, Roger Bacon introduced the need of empirical methods in order to study nature. Another thousand years later, such *experiments* led to the discovery of the electron (J. J. Thomson, 1897) and the nucleus (E. Rutherford, 1911), rendering the atom a composite entity with electrons orbiting the nucleus. The *atomic structure* (Niels Bohr, 1913) led to the rapid development of *quantum mechanics* (M. Planck, W. Heisenberg, W. Pauli, E. Schrödinger, P. A. M. Dirac among others) which together with special relativity (A. Einstein, 1905) and classical electro-magnetism (J. C. Maxwell, 1873) gave rise to the very successful theory of *quantum electrodynamics* (QED) (R. Feynman, J. Schwinger, S. Tomonaga).

During the same period, more particles have been discovered, e.g. the proton (E. Rutherford, 1913) and the neutron (J. Chadwick, 1931), both constituents of nuclei, but also the positron and the muon (C. D. Anderson, 1932, 1936) or the pion (C. Powell, 1947). With the use of particle accelerators in the following decades a proper *zoo of particles* (hadrons) was discovered and their systematic characterization led to the *quark model* (M. Gell-Mann, 1961) and the quarks as fundamental particles and constituents of hadrons.

Based on the success of QED, attempts were made to find an analogous formulation of the weak interaction, which is responsible for nuclear decays, and the strong force, which describes the formation of hadrons. The electromagnetic and weak interactions, which is mediated by the weak bosons (S. Glashow, 1961), could be combined into the *electroweak theory* (A. Salam, S. Weinberg, 1967) predicting massless photons, and W^\pm and Z bosons. In addition the *Higgs mechanism* was able to describe the acquisition of mass of the W and Z bosons through *spontaneous symmetry breaking* (R. Brout, F. Englert, P. Higgs, G. Guralnik, C. R. Hagen, T. Kibble, 1964), with the prediction of the famous *Higgs boson* as a consequence. The strong interaction was found to be described by *quantum chromodynamics* (QCD) and with the discovery of *asymptotic freedom* (D. Gross, F. Wilczek, D. Politzer, 1973), quantum field theoretical predictions became possible.

The discovery of the W and Z bosons at CERN in 1983 was a great confirmation of the *Standard Model of particle physics*. But no evidence for the existence of the Higgs boson was found, also not at the subsequent collider experiments at CERN or Fermilab and it took until 2011 when a first sign of a new boson, compatible with the Standard Model Higgs boson, was observed at the Large Hadron Collider.

This thesis is divided in four parts.

The first Chapter in Part I gives a short introduction to the Standard Model of particle physics. It summarizes the theoretical formalism and explains the physics consequences as e.g. the prediction of the Standard Model Higgs boson. In the subsequent two Chapters the experimental setup of the Large Hadron Collider and of the Compact Muon Solenoid experiment at CERN is presented and includes a description of the data taking procedure and gives an overview of the processing of the recorded data.¹

Part II presents, after a short introduction to diffractive processes, an analysis of the forward energy flow and the charged particle multiplicity in the central range of the detector in W and Z events, which then leads to the observation of diffractively produced weak bosons. The study of the forward energy flow, the charged particle multiplicity and their correlation allows a comparison of different simulation models describing the underlying event structure of proton-proton collisions in W and Z events. The last Chapter of Part II presents a measurement of the fraction of diffractively produced weak bosons.

The third Part covers the search for a Standard Model Higgs boson in the fully leptonic final state of the $H \rightarrow WW \rightarrow \ell\nu\ell\nu$ channel using the information of the shape of a multivariate discriminating variable. The first two Chapters of Part III give an introduction to the possible Higgs production modes and decay channels, and present a study of the simulation of the gluon-fusion Higgs production. Differential weights, in order to re-weight the Higgs transverse momentum spectrum in simulated events to the most up-to-date theoretical prediction, are derived.

In the following chapters (Chapters 9-11), the Higgs boson search strategies and the results using 2011 data are presented. After an overview of the different methods used in the analysis and the event selection, the different sources of systematic uncertainties, which enter the upper limit calculation on the Higgs production cross section, are discussed in detail, as well as the results. The last Chapter of Part III presents a study of the SM Higgs boson production in the gluon-fusion process with the application of a jet veto.

The fourth and last Part contains a summary and a brief discussion of the presented thesis, as well as a short discussion of the observation of a new boson in summer 2012 by the CMS experiment. It also contains a few Appendices and the Bibliography.

Due to the vast complexity of a modern high energy physics experiment any analysis result is the product of a large number of physicists involved. My contributions concentrate mainly on the experimental analysis presented in Part II and the studies presented in Chapters 8, 10 and 12. The overall analysis strategies etc. are the products of working groups of collaborating physicists in the CMS collaboration.

Conventions: Charged leptons are denoted with the symbol ℓ which stands for an electron (e) or a muon (μ) which are the experimentally detectable “stable” leptons. Similarly for neutrinos: ν stands for ν_e or ν_μ . Tau leptons (τ , ν_τ) are always mentioned separately, except in Part I where the word lepton includes all three families of leptons. Signs, indicating the charge of a particle, as in ℓ^\pm are omitted most of the time and are only used where it is of contextual importance. The same is valid for the bar indicating anti-particles. For example $H \rightarrow WW \rightarrow \ell\nu\ell\nu$ stands for $H \rightarrow W^+W^- \rightarrow \ell^+\bar{\nu}_\ell\ell^-\nu_\ell$. One of the Ws can be off-shell, usually denoted as W^* ; the asterisk will also be ignored. Natural units are used,

¹CERN is the European Organization for Nuclear Research.

i.e. $\hbar = c = 1$ and thus masses are given in GeV instead of GeV/c^2 .

Part I

Introduction

Chapter 1

The Standard Model of Particle Physics

The goal of particle physics is to identify the basic building blocks of matter and to understand the fundamental forces which are acting between them. This idea is based on the concept of fundamental “atomic” units of matter from which any complex system is made of. The fundamental forces are expected to be simple and predictable. Countless experiments, carried out during the past centuries, helped to consolidate the actual theoretical description of matter and forces: the *Standard Model (SM) of particle physics*. Practically all experimental data which so far have been recorded by the different high energy physics experiments can be described by this SM of particle physics.

This Chapter summarizes the basic concepts of the SM and its theoretical description. First the quantum field theories are discussed and later in the Chapter, the Higgs mechanism is described, which leads to the prediction of the SM Higgs boson. At the very end of the Chapter, some limitations are summarized, indicating why there is “new” physics beyond the SM to expect.

1.1 Introduction

In the SM, all matter is built from fundamental spin $\frac{1}{2}$ particles, called *fermions*, which are further divided into *leptons* and *quarks* (and their corresponding anti-particles). Table 1.1 lists these fermions and summarizes some of their properties. Leptons can further be divided into massive, integer charged leptons (e, μ, τ) and neutral almost massless neutrinos (ν_e, ν_μ, ν_τ). The quarks have fractional charges and do not exist as free particles — they can only be observed in compound states as hadrons. From observations, it is known that fermions exist in three *families* of analogous sets of particles which practically only differ in mass. The stable, observable matter around us is made of fermions of the first family: protons and neutrons, composites of up- and down-quarks, and electrons with which they form atoms and molecules.

These fermions and the basic known interactions between them, which are the *electromagnetic* interaction (which for example bounds the electrons into orbitals around the nuclei in order to form atoms), the *weak* interaction (which is responsible for nuclear de-

Fermions	$Q/ e $	1 st family	2 nd family	3 rd family
Leptons	0 -1	$\begin{pmatrix} \nu_e \\ e \end{pmatrix}$ $< 2 \text{ eV}$ $\sim 0.5 \text{ MeV}$	$\begin{pmatrix} \nu_\mu \\ \mu \end{pmatrix}$ $< 0.2 \text{ MeV}$ $\sim 106 \text{ MeV}$	$\begin{pmatrix} \nu_\tau \\ \tau \end{pmatrix}$ $< 18.2 \text{ MeV}$ $\sim 1.78 \text{ GeV}$
Quarks	+2/3 -1/3	$\begin{pmatrix} u \\ d \end{pmatrix}$ $\sim 2.5 \text{ MeV}$ $\sim 5 \text{ MeV}$	$\begin{pmatrix} c \\ s \end{pmatrix}$ $\sim 1.28 \text{ GeV}$ $\sim 95 \text{ MeV}$	$\begin{pmatrix} t \\ b \end{pmatrix}$ $\sim 173.5 \text{ GeV}$ $\sim 4.2 \text{ GeV}$

Table 1.1: The fermions of the SM of particle physics. The charge in multiples of the unit charge $|e|$ and the approximate masses [2] are also given.

cays) and the *strong* interaction (which is responsible for the formation of hadrons), are described in the form of *quantum field theories*. These field theories belong to the so called *gauge theories*, where the matter fields are described by the representations of a *symmetry group*, and the interactions between these fields are mediated by the *gauge bosons*, which arise from the requirement of the invariance of the *Lagrangian* under *local transformations* of the fields under these symmetry groups.

Quantum electrodynamics (QED), which describes the interaction of electromagnetically charged particles and is mediated by the *photon*, arises from $U(1)$ gauge symmetry. The weak interaction can be derived from the $SU(2)$ symmetry group, giving rise to the *weak vector bosons*, the W^\pm and the Z bosons. The strong interaction, described by *quantum chromodynamics* (QCD), has an underlying $SU(3)$ symmetry and is mediated by *gluons*. These bosons all have spin 1 and are summarized in Table 1.2. There is no deep understanding yet of why the gauge group of the SM is $SU_C(3) \times SU_L(2) \times U_Y(1)$, but its particle content is an experimental fact.¹ The electromagnetic and weak interactions can be generalized into one single theory: the *electroweak* theory.

In the following Sections, the different ingredients to a quantum field theoretical description of the SM are briefly summarized. More details can be found in many corresponding textbooks [3–6].

1.2 Quantum Electrodynamics

Quantum field theories are based on Feynman's path integral formulation, a quantum mechanical generalization of the classical *principle of least action*, using the *Lagrangian density* \mathcal{L} (or just Lagrangian), which is containing the dynamics of a system, to calculate the amplitudes of a certain process.

For example, the Dirac Lagrangian \mathcal{L} for fermions is

$$\mathcal{L}_{\text{Dirac}} = \bar{\psi}(i\gamma^\mu \partial_\mu - m)\psi, \quad (1.1)$$

where γ^μ are the so called γ -matrices and ψ is a complex valued Dirac spinor.

A symmetry is a transformation which keeps the equations of motion, and thus also the Lagrangian, invariant. Using *Noether's theorem*, which connects symmetries to conservation laws, one can find the conserved quantities of a given theory.

¹The index C stands for color, L for weak isospin and Y for hypercharge. The meaning of these quantum numbers will become clearer at a later point.

The first example is a transformation of the form

$$U(\alpha(x)) = e^{i\alpha(x)} \quad (1.2)$$

which forms the $U(1)$ group. If $\alpha(x)$ is a real phase which is constant in x , the transformation is called *global*. The Dirac Lagrangian from Equation (1.1) for example, is invariant under such a transformation of the form

$$\psi(x) \rightarrow e^{i\alpha}\psi(x). \quad (1.3)$$

The conserved quantity, following Noether's theorem, of such a $U(1)$ gauge symmetry is the *electric charge*. But if $\alpha(x)$ is not constant in x anymore, the transformation is called *local* and Equation (1.1) is no longer invariant under the transformation $\psi(x) \rightarrow e^{i\alpha(x)}\psi(x)$, because of the derivative $\partial_\mu\psi$ in Equation (1.1), i.e. it transforms like

$$\partial_\mu\psi \rightarrow e^{i\alpha(x)}\partial_\mu\psi + ie^{i\alpha(x)}\psi\partial_\mu\alpha(x). \quad (1.4)$$

By introducing the *covariant derivative*

$$D_\mu = \partial_\mu - ieA_\mu, \quad (1.5)$$

with an arbitrary constant e and $A_\mu(x, t)$ an arbitrary *vector field* which transforms as

$$A_\mu \rightarrow A_\mu + \frac{1}{e}\partial_\mu\alpha(x), \quad (1.6)$$

one can make the Dirac Lagrangian of Equation (1.1) again invariant under local gauge transformations by replacing ∂_μ with D_μ . Thus one can re-write the Lagrangian as

$$\mathcal{L} = \bar{\psi}(i\gamma^\mu D_\mu - m)\psi \quad (1.7)$$

$$= \underbrace{\bar{\psi}(i\gamma^\mu\partial_\mu - m)\psi}_{=\mathcal{L}_{\text{Dirac}}} + e\bar{\psi}\gamma^\mu\psi A_\mu. \quad (1.8)$$

The first term, $\mathcal{L}_{\text{Dirac}}$, is again the free Lagrangian for fermions and the second term is the coupling of the fermion to the *gauge field* A_μ .

In order to get to the final QED Lagrangian, a kinetic term for the field A_μ itself has to be added. The *electromagnetic field strength tensor* is defined as

$$F_{\mu\nu} = \partial_\mu A_\nu - \partial_\nu A_\mu, \quad (1.9)$$

which is also locally gauge invariant. The QED Lagrangian is

$$\mathcal{L}_{\text{QED}} = \bar{\psi}(i\mathcal{D} - m)\psi - \frac{1}{4}(F_{\mu\nu})^2, \quad (1.10)$$

with $\mathcal{D} = D_\mu\gamma^\mu$.

In a physical picture, this Lagrangian describes the coupling of e.g. a lepton of charge e which couples to a photon field A_μ . For a fermion of charge q , one has to replace $e \rightarrow q$.

Two remarks are worth to be stressed:

- i)* The requirement of local invariance (e.g. for QED the transformation is given by Equation (1.2)) of the Lagrangian implies the introduction of a new field — here the photon field A_μ .
- ii)* Local gauge invariance forbids the direct introduction of mass terms for the gauge fields in the Lagrangian, i.e. the bosons are massless.

1.3 The Glashow-Salam-Weinberg Model

The previously described method to find the Lagrangian can be applied to any symmetry group. Thus, attempts were made to formulate an analogous theory for the weak force. In the next Section, the $SU(2)$ symmetry of the weak interaction is discussed.

1.3.1 $SU(2)$: A non-Abelian Gauge Theory

The procedure to find the Lagrangian for the weak interaction, with its symmetry group $SU(2)$, is similar to the one presented in Section 1.2. Again, one has to introduce a covariant derivative D_μ in order to obtain a local invariance under a transformation of the $SU(2)$ group

$$\psi(x) \rightarrow e^{i\alpha(x)\frac{\sigma^i}{2}}\psi(x), \quad (1.11)$$

where $\psi(x) = \begin{pmatrix} \psi_1 \\ \psi_2 \end{pmatrix}$ is a doublet of Dirac fields and σ^i are the Pauli matrices.² This is done by introducing additional gauge fields A_μ^i , one per generator of the group.

For the $SU(2)$ group, the covariant derivative is

$$D_\mu = \partial_\mu - igA_\mu^i \frac{\sigma^i}{2}, \quad (1.12)$$

with g the coupling constant (and summing over repeated indices). With this covariant derivative, one can write the general Lagrangian. In order to get the final Lagrangian, one needs again the gauge invariant kinetic terms of the fields (which depend only on A_μ^i). The field strength tensors, equivalent to the electromagnetic field strength tensor from Section 1.2, are defined via the commutators of the covariant derivatives

$$[D_\mu, D_\nu] = -igF_{\mu\nu}^i \frac{\sigma^i}{2}, \quad (1.13)$$

which results in

$$F_{\mu\nu}^i = \partial_\mu A_\nu^i - \partial_\nu A_\mu^i - g\epsilon^{ijk}A_\mu^j A_\nu^k, \quad (1.14)$$

with ϵ^{ijk} the total antisymmetric tensor. In contrast to Section 1.2, the last term of Equation (1.14) does not vanish, because $SU(2)$ is a *non-Abelian* group, in which the elements do not commute. Thus the field theory based on non-Abelian groups are called *non-Abelian gauge theories*. This term introduces interactions between the gauge fields and thus between the gauge bosons themselves.

The final *Yang-Mills* Lagrangian looks similar to the QED Lagrangian

$$\mathcal{L} = \psi(i\not{D}\psi) - \frac{1}{4}(F_{\mu\nu}^i)^2 - m\bar{\psi}\psi, \quad (1.15)$$

and depends again on the coupling g and the mass m of the fermion.

²The $i\sigma^i$ are the generators of the $SU(2)$ Lie algebra.

1.3.2 The Higgs Mechanism and the Electroweak Theory

As already mentioned, mass terms (like e.g. $m_A^2 A_\mu A^\mu$) for the gauge-fields are forbidden in the Lagrangian because they do not preserve local gauge invariance. Thus another mechanism was proposed in the mid 1960s to get massive bosons: the *Higgs mechanism* [7–9] which gives masses to the gauge bosons via spontaneous symmetry breaking.

Glashow, Salam and Weinberg introduced a way to unify the electromagnetic and the weak interactions, into the electroweak theory, predicting the W and Z bosons [10–12]. In 1973, the first evidence for neutral currents, as predicted by the electroweak theory, was observed by the Gargamelle bubble chamber at CERN [13]. The actual discoveries of the weak bosons at the CERN SPS p \bar{p} collider in 1983 can be considered a huge success of the electroweak theory [14–17].

From experiments we know of three massive weak bosons (W $^\pm$, Z) and one massless electromagnetic boson (photon). Together with the Higgs mechanism a way was found that one obtains one massless photon, corresponding to a combination of symmetry generators that remain unbroken, and three massive vector bosons.

In order to achieve this, a doublet of scalar fields has to be introduced

$$\phi = \begin{pmatrix} \phi_+ \\ \phi_0 \end{pmatrix}, \quad (1.16)$$

which transforms under $SU(2)$ and under $U(1)$ transformations like

$$\phi(x) \rightarrow \underbrace{e^{i\alpha^i(x)\frac{\sigma^i}{2}}}_{SU(2)} \underbrace{e^{i\beta(x)\frac{1}{2}}}_{U(1)} \phi(x), \quad (1.17)$$

with a $U(1)_Y$ charge of $Y = +1/2$ assigned to ϕ . σ^i are the generators of $SU(2)$, i.e. Pauli matrices. One can assume that the *vacuum expectation value* v of the field ϕ is of the form

$$v = \langle \phi \rangle = \frac{1}{\sqrt{2}} \begin{pmatrix} 0 \\ v \end{pmatrix} \quad (1.18)$$

and thus non-zero.

The covariant derivative (see Equations (1.5) and (1.12)) for a field ϕ is

$$D_\mu \phi = \left(\partial_\mu - igA_\mu^i \sigma^i - i\frac{1}{2}g'B_\mu \right) \phi, \quad (1.19)$$

where A_μ^i and B_μ are the $SU(2)$ and $U(1)$ gauge bosons respectively and g and g' two different couplings. The gauge boson mass terms are obtained from $(D_\mu \phi)^2$, evaluated at the vacuum expectation value, as

$$\mathcal{L}_{\text{mass}} = \frac{v^2}{8} \left(g^2 (A_\mu^1)^2 + g^2 (A_\mu^2)^2 + (-gA_\mu^3 + \frac{1}{2}g'B_\mu)^2 \right). \quad (1.20)$$

The gauge fields can be re-written as linear combinations of the interaction eigenstates A_μ^i

and B_μ as

$$W_\mu^\pm = \frac{1}{\sqrt{2}}(A_\mu^1 \mp iA_\mu^2) \quad \text{with mass} \quad m_W = g\frac{v}{2}, \quad (1.21)$$

$$Z_\mu = \frac{1}{\sqrt{g^2 + g'^2}}(gA_\mu^3 - g'B_\mu) \quad \text{with mass} \quad m_Z = \sqrt{g^2 + g'^2}\frac{v}{2}, \quad (1.22)$$

$$A_\mu = \frac{1}{\sqrt{g^2 + g'^2}}(g'A_\mu^3 + gB_\mu) \quad \text{with mass} \quad m_A = 0, \quad (1.23)$$

where W_μ^\pm , Z_μ (i.e. three massive vector bosons with mass $m_{W/Z}$) and A_μ (i.e. one massless photon) are the physical gauge bosons or mass eigenstates. So, the final mass term in the Lagrangian becomes

$$\mathcal{L}_{\text{mass}} = \frac{v^2}{8} (g^2(W_\mu^+)^2 + g^2(W_\mu^-)^2 + (g^2 + g'^2)Z_\mu^2). \quad (1.24)$$

Consider now a fermion field in a representation of $SU(2)$, with generators T^i and electroweak *hypercharge* Y in $U(1)$. In the basis of the physical gauge fields, the covariant derivative is

$$D_\mu = \partial_\mu - i\frac{g}{\sqrt{2}}(W_\mu^+T^+ + W_\mu^-T^-) - i\frac{1}{\sqrt{g^2 + g'^2}}Z_\mu(g^2T^3 - g'^2Y) - i\frac{gg'}{\sqrt{g^2 + g'^2}}A_\mu(T^3 + Y), \quad (1.25)$$

with $T^\pm = T^1 \pm iT^2$ and the T^i 's are the generators of the $SU(2)$ algebra. T^3 is the z -projection of the *weak isospin*. The last term of Equation (1.25) shows that the photon couples to the gauge generator $(T^3 + Y)$. A_μ can now be identified to be the electromagnetic potential and thus the electron charge is

$$e = \frac{gg'}{\sqrt{g^2 + g'^2}} \quad (1.26)$$

and the electromagnetic charge Q is

$$Q = T^3 + Y. \quad (1.27)$$

This means that the $SU(2)_L \times U(1)_Y$ symmetry is broken and thus gives the three massive bosons, but at the same time a $U(1)_Q$ symmetry is retained, resulting in a massless boson.

It follows that one can define θ_w , which is called the *weak mixing angle*, given by the rotation of (A^3, B) into (Z, A)

$$\begin{pmatrix} Z \\ A \end{pmatrix} = \begin{pmatrix} \cos(\theta_w) & -\sin(\theta_w) \\ \sin(\theta_w) & \cos(\theta_w) \end{pmatrix} \begin{pmatrix} A^3 \\ B \end{pmatrix}, \quad (1.28)$$

as

$$\cos(\theta_w) = \frac{g}{\sqrt{g^2 + g'^2}} \quad \text{and} \quad \sin(\theta_w) = \frac{g'}{\sqrt{g^2 + g'^2}}. \quad (1.29)$$

In this basis, the covariant derivative can be re-written in terms of the physical bosons as

$$D_\mu = \partial_\mu - \frac{ig}{\sqrt{2}}(W_\mu^+T^+ + W_\mu^-T^-) - i\frac{g}{\cos(\theta_w)}Z_\mu(T^3 - \sin^2(\theta_w)Q) - ieA_\mu Q, \quad (1.30)$$

Boson	Mass [GeV]	$Q/ e $	Color	Interaction
γ	0	0	no	Electromagnetic
W^\pm	80.419	± 1	no	Weak
Z	91.188	0	no	Weak
8 gluons	0	0	yes	Strong

Table 1.2: Summary of the SM bosons.

and the coupling g of the weak bosons is described by two parameters: the electric charge e and the mixing angle θ_w via

$$g = \frac{e}{\sin(\theta_w)}. \quad (1.31)$$

The weak boson masses are not independent of each other but are related by

$$m_W = m_Z \cos(\theta_w). \quad (1.32)$$

Table 1.2 summarizes some properties of the SM bosons.

1.3.3 Fermions in the Electroweak Theory

The spin component in the direction of motion of a particle is called *helicity*. The massive W^\pm and Z bosons may have three different helicity states, i.e. ± 1 or 0, whereas massless particles cannot have helicity state 0 and only exist in one state; their helicity is relativistically invariant. For example, the massless neutrinos only exist with a negative, i.e. $-\frac{1}{2}$, helicity state, which is called *left-handed* (anti-neutrinos are *right-handed*), and the massive fermions exist in both states with a left- and a right-handed component.

In order to describe the experimental fact that the weak bosons only couple to left-handed fermions, the fermion fields can be written in the form of a doublet and a singlet representation of the $SU(2)$ group: for example for the electron field

$$e_L = \begin{pmatrix} \nu_e \\ e \end{pmatrix}_L \quad \text{and} \quad e_R, \quad (1.33)$$

and analogously for all other leptons. The hypercharge Y is defined by Equation (1.27). The photon couples to the left- and right-handed component.

This allows to introduce kinetic terms for these fermion fields in the Lagrangian and allows the calculation of the fermion couplings. Also the fermion mass terms, and thus the fermion masses, can be calculated where the neutrino mass turns out to be zero as there is no coupling to the right-handed neutrino.

1.3.4 The SM Higgs Boson

The scalar field of Equation 1.16 can be parametrized as

$$\phi(x) = \frac{1}{\sqrt{2}} \begin{pmatrix} 0 \\ v + h(x) \end{pmatrix}, \quad (1.34)$$

with v the vacuum expectation value and $h(x)$ a scalar real-valued field, describing fluctuations around v . The Lagrangian containing the Higgs field is

$$\mathcal{L}_H = |D_\mu\phi|^2 - V, \quad (1.35)$$

with the potential

$$V = -\mu^2\phi^\dagger\phi + \lambda(\phi^\dagger\phi)^2, \quad (1.36)$$

which has its minimum at

$$v = \left(\frac{\mu^2}{\lambda}\right) \quad (1.37)$$

and leads to a Higgs mass term in Equation (1.35) of

$$m_H = \sqrt{2}\mu = \sqrt{2\lambda}v. \quad (1.38)$$

The Higgs boson is a scalar (i.e. spin = 0), neutral particle with mass m_H which is not predictable by theory as it depends on the vacuum expectation value v and on the coupling constant λ , which is a free parameter. Via the fermion and gauge boson mass terms, the couplings of the Higgs boson to these particles can be calculated. In general the Higgs boson coupling is proportional to the mass (mass squared) of the fermions (bosons)

$$g_{Hff} = i\frac{m_f}{v} \quad \text{and} \quad g_{HVV} = -2i\frac{M_V^2}{v}. \quad (1.39)$$

1.3.5 Theoretical and Experimental Constraints on the Higgs Mass

The mass of the SM Higgs boson can be constrained in three ways:

- i)* theoretically,
- ii)* via a SM fit to the electroweak precision data, and
- iii)* via direct searches.

Theoretical Constraints

The Higgs boson mass m_H can not be predicted by the theory, but upper and lower bounds can be given. One upper limit is given by $W_L W_L \rightarrow W_L W_L$ scattering of longitudinally polarized W bosons. For this process, the cross section has two terms: one $\propto -\frac{s}{32\pi v^2}$ and the other $\propto -\frac{m_H^2}{8\pi v^2}$, which cancel and thus limit the indefinite growth of the cross section. In order to conserve unitarity, the Higgs boson mass has to have an upper bound of approximately $m_H < 900$ GeV [18].

The so called vacuum stability gives a lower bound for the Higgs mass [19], by requiring that $\lambda(\Lambda_C)$ is positive for all energy scales Λ_C (cut-off scale). Otherwise the potential V from Equation (1.36) becomes unstable and the SM breaks down. Thus the lower bounds on m_H depends on the scale Λ_C ; e.g. for $\Lambda_C \sim 10^4$ GeV $\Rightarrow m_H \geq 70$ GeV.

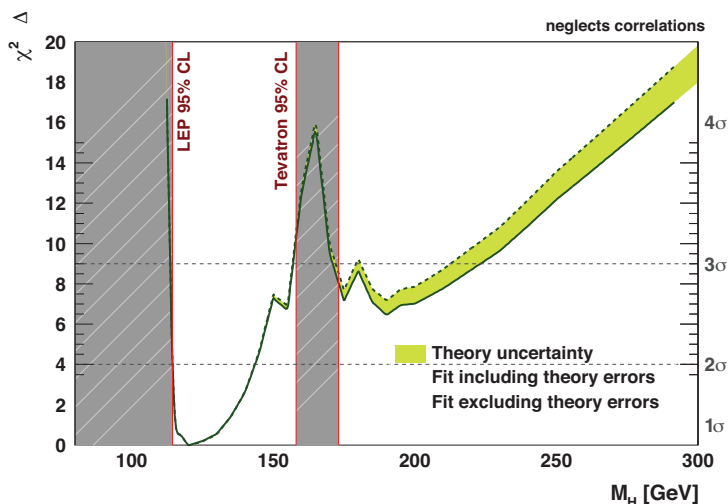


Figure 1.1: $\Delta\chi^2$ as a function of the Higgs mass. This plot includes data from direct searches. Taken from [20].

SM Fit to Electroweak Precision Data

The fit procedure is described in [20] and uses parameters as e.g. the coupling strengths of the electromagnetic (α), weak (G_F) and strong (α_s) interactions, as well as boson and fermion masses etc. as input variables. In some cases also experimental data from direct searches are included (i.e. LEP, Tevatron and 2010 LHC data).

The fit results are: 96^{+31}_{-24} GeV using only the electroweak precision data and 120^{+12}_{-5} GeV also including the data from direct searches. The 95% upper limit for m_H is 169 ± 8 GeV or 143 ± 8 GeV if direct searches are included. Figure 1.1 shows the $\Delta\chi^2$ of the fit which gives the most probable Higgs mass to be at around 120 GeV.

Experimental Constraints from Direct Searches

At the time of writing, the results from different experiments constrain the possible Higgs boson mass to basically a narrow window of only a few GeV.³ The lower bound is given by the combination of the LEP results [21] and limits the Higgs mass to be larger than 114.4 GeV at 95% confidence level using the total 2.5 fb^{-1} of e^+e^- -collision data. The experiments at the Tevatron presented their updated analysis using up to 9.7 fb^{-1} of $p\bar{p}$ -collision data [22]. The combination of the D0 and CDF exclusion limit at the 95% C.L. is excluding 100–106 GeV and 147–179 GeV with an expected limit of 100–120 GeV and 141–184 GeV. Finally, the exclusion limits from the two LHC experiments, using about 4.9 fb^{-1} each, are: 110–117.5 GeV, 118.5–122.5 GeV and 129–539 GeV from ATLAS [23] where the expected limit is 120–555 GeV, and 127.5–600 GeV from CMS [24–32] with the expected limit from 114.5–543 GeV. In the low mass region, the exclusion is weaker than expected, as there is an excess observed below around 130 GeV. A very significant excess of approximately 2.8σ significance is observed at around 125 GeV. This excess, although

³This snapshot of the current status of the SM Higgs boson searches is taken after the presentation of the most recent results on March 7th 2012 during the 47th *Rencontres de Moriond Electroweak Session* which is annually held in La Thuile, Italy.

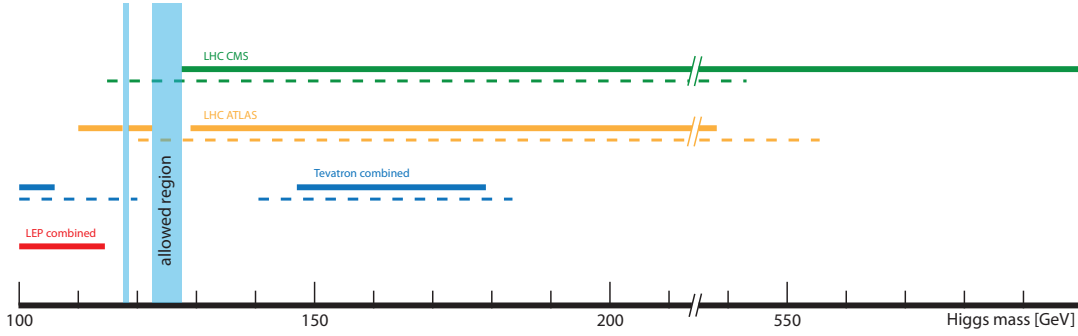


Figure 1.2: Summary of the experimental exclusion limits at the 95% confidence levels as of March 7th 2012. Solid lines correspond to the observed, dashed ones to the expected limits. The light blue areas show the remaining narrow mass regions (basically only 5 GeV in the region around 125 GeV) in which the Higgs boson is still allowed.

not exactly at the same mass, is also reported from the ATLAS results. Figure 1.2 tries to summarize these numbers from the different direct SM Higgs searches.

1.4 Quantum Chromo Dynamics

The strong interaction is described by quantum chromo dynamics (QCD). The underlying symmetry group used to describe the theory of strong interactions is $SU(3)$ with the corresponding conserved quantum number: *color*. The number of three colors (i.e. “green”, “blue” and “red”) are consistent with the experimental results and predicts the hadron content of the SM. The resulting gauge bosons are the eight massless *gluons*, which themselves carry color, as $SU(3)$ is a non-abelian group, and thus undergo *self interaction*.⁴ The QCD Lagrangian is similar to the one of the previously shown non-abelian gauge theories

$$\mathcal{L}_{\text{QCD}} = \bar{\psi}(i\not{D})\psi - \frac{1}{4}(F_{\mu\nu}^a)^2 - m\bar{\psi}\psi \quad (1.40)$$

where ψ is the quark field spinor and m the quark mass. $F_{\mu\nu}^a$ is the field strength tensor obtained from the gluon field. The fundamental parameters of the theory are the quark masses m_q and the strong coupling constant

$$\alpha_s = \frac{g_s^2}{4\pi}, \quad (1.41)$$

where g_s replaces g in Equation (1.14). T_{ij}^a are the generators of the Lie group. Neither quarks nor gluons are observed as free particles, which asymptotically have to form color neutral bound states.

For a more extensive discussion of QCD, see Refs. [2, 33].

⁴The $SU(3)$ algebra has eight generators, thus one obtains eight gluons and the symmetry remains unbroken and thus the gluons are massless.

1.4.1 The Running Coupling

In perturbative QCD, due to *ultraviolet divergencies*, predictions are made in terms of the *renormalized coupling* $\alpha_s(\mu_R^2)$. μ_R is a non-physical parameter called *renormalization scale*, which usually is chosen such that $\mu_R^2 \approx Q^2$, indicating the running strength of the coupling as a function of the momentum transfer Q^2 of a process. The strong coupling satisfies the *renormalization group equation*

$$\mu_R^2 \frac{d\alpha_s}{d\mu_R^2} = \beta(\alpha_s), \quad (1.42)$$

with $\beta(\alpha_s)$ the *beta function*

$$\beta(\alpha_s) = -(b_0\alpha_s^2 + b_1\alpha_s^3 + b_2\alpha_s^4 + \dots). \quad (1.43)$$

The first term of Equation (1.43) is $b_0 = 11 - \frac{2}{3}n_f$, with n_f the number of quarks lighter than μ_R .⁵ Equation (1.42) describes the evolution of $\alpha_s(Q)$ and the normalization of α_s is measured at the reference scale of e.g. the Z mass as $\alpha(m_Z) \approx 0.1184 \pm 0.0007$ [2]. The minus sign in Equation (1.43) is the origin of the *asymptotic freedom* — the strong coupling α_s is small for hard processes (i.e. with large momentum transfer Q^2). See Figure 1.3(a) for an illustration of the running coupling.

Usually, α_s is written as a function of Λ_{QCD} instead of $\alpha_s(m_Z)$, as

$$\alpha_s = \frac{2\pi}{b_0} \frac{1}{\log(Q/\Lambda_{\text{QCD}})}, \quad (1.44)$$

where Λ_{QCD} is defined via $\alpha_s(\mu_R^2)(b_0 \log(\mu_R^2/\Lambda_{\text{QCD}}^2)) = 1$. Here, Λ_{QCD} corresponds to a scale after which the coupling becomes divergent, i.e. after which one can not apply perturbation theory anymore. Λ_{QCD} is, experimentally, around ~ 200 MeV, and it is the energy scale at which the strong interaction gets strong. Consequently, $1/\Lambda_{\text{QCD}}$ is the distance (the time) at which (after which) a free quark starts to hadronize.⁶

1.4.2 The Parton Model and Parton Distribution Functions

The idea of the *parton*, referring to the quarks and gluons, was introduced by Feynman in 1969 as the basic constituents of hadrons in order to describe *deep inelastic scattering* data. In the picture of the *parton model*, an interaction does not happen with the proton as a whole, but with one of its constituent partons. This assumption is valid due to the asymptotic freedom. For this to happen, the incoming particle has to have a large enough energy to probe the inner structure of that proton, which consists of the valence quarks (uud) and a sea of $q\bar{q}$ -pairs and gluons (which carry about 50% of the total momentum). The hadron momentum is shared between the partons, each carrying only a fraction x of the total momentum. This distribution of the momenta of the partons inside the hadron is called the *parton distribution function* (PDF) $f_i^{(h_j)}(x_i)$, which corresponds to the probability density to find a certain parton i with a momentum fraction x_i in hadron j . The center of mass energy of the two partons actually undergoing the hard scattering is thus $\hat{s} = sx_1x_2$, with s the center of mass energy of the incoming hadrons p_1 and p_2 . An example of such an interaction is shown in Figure 1.3(b), where the two partons 1 and 2 interact without influence of the *spectator quarks*.

⁵Other terms can be found e.g. in Ref. [2].

⁶This corresponds to a distance of the order of femtometer and a time of the order of 10^{-23} s.

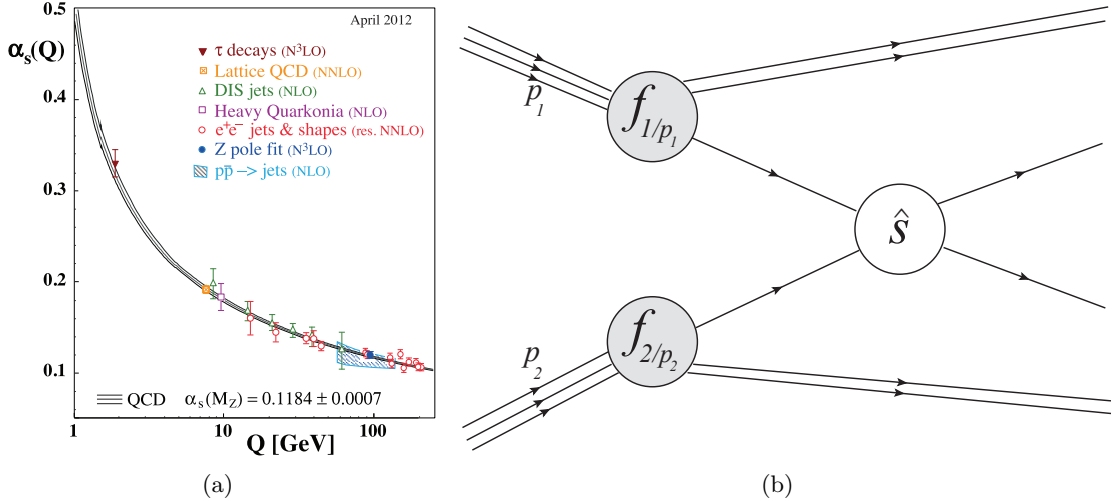


Figure 1.3: (a) Summary of α_s measurements illustrating the running coupling as a function of the momentum transfer Q^2 . [34] (b) Schematic view of parton interaction in a pp collision, where the hard scattering is *factorized* from the rest of the proton.

In order to make theoretical predictions of hadron scatterings, these PDFs have to be known over a large kinematic range; from a fractional momentum of $10^{-5} < x < 1$ and from a momentum transfer of $10 \text{ GeV} < Q^2 < 7 \text{ TeV}$. Figure 1.5 shows the kinematical ranges which different particle physics experiments cover. In order to evaluate the PDFs, different cross sections are measured in mainly deep inelastic scattering (DIS) processes as a function of Q^2 and x . To obtain the PDFs, these cross sections are then parametrized, fitted and extrapolated (through the so called DGLAP evolution equations) rendering the PDFs also Q dependent - called *scaling violation*. Figure 1.4 shows an example of a proton PDF, measured at HERA. The Q dependence is described by the *factorization scale* μ_F which acts as a cut-off removing divergent contributions and allows factorization of non-perturbative processes from the hard interaction.

1.4.3 The Hard Scattering

In terms of the parton model, the total pp cross section ($p_1 p_2 \rightarrow X$) can be written as the incoherent sum of the partonic cross sections $\hat{\sigma}$:

$$\sigma_{p_1 p_2 \rightarrow X} = \int_0^1 dx_1 dx_2 \sum_{1,2} f_1^{(p_1)}(x_1, \mu_F^2) f_2^{(p_2)}(x_2, \mu_F^2) \hat{\sigma}(x_1 x_2 s, \mu_F^2), \quad (1.45)$$

where $f_i^{(p_j)}(x_i, \mu_F^2)$ is the parton distribution function of the i^{th} parton (q, \bar{q} or g) in proton j . At leading order $f_i^{(p_j)}$ corresponds to the probability to find parton i with fractional momentum x_i in proton j . $\hat{\sigma}(x_1 x_2 s, \mu_F^2)$ is the partonic cross section of the interaction of parton 1 and 2. μ_F is the factorization scale. One can see that the cross section thus depends on the partonic cross section as well as on the PDF, which itself depends on the colliding type of hadrons and their energy, but also on the acceptance of the detector by restricting the x of the partons.

The partonic cross section $\hat{\sigma}$ depends on the partonic center of mass energy \hat{s} , the

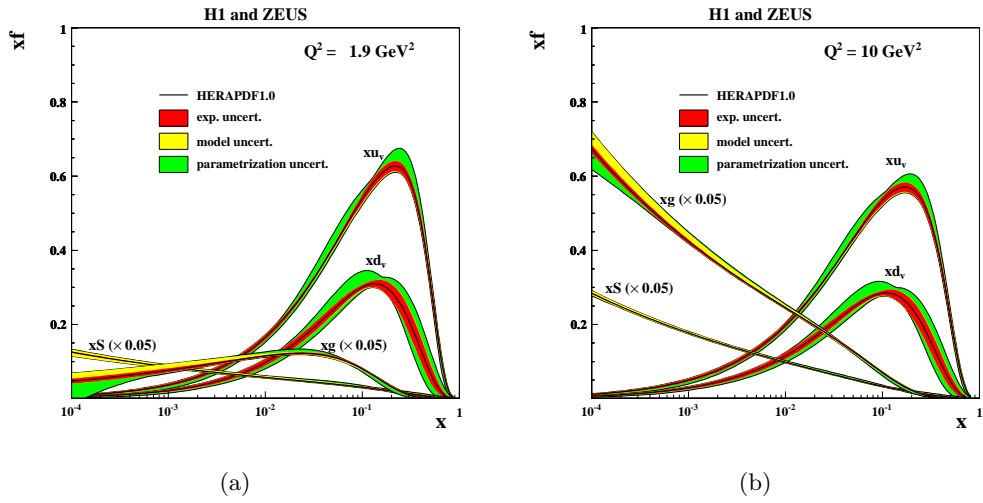


Figure 1.4: The parton distribution functions from HERAPDF1.0 for the valence (up: xu_v ; down: xd_v) and sea quarks (xS) and gluons (xg) at (a) $Q^2 = 1.9 \text{ GeV}^2$ and (b) $Q^2 = 10 \text{ GeV}^2$. The PDFs for the sea quarks and gluons are scaled down by a factor of 20. Different contributions to the uncertainties are shown as colored bands. Plots taken from [35].

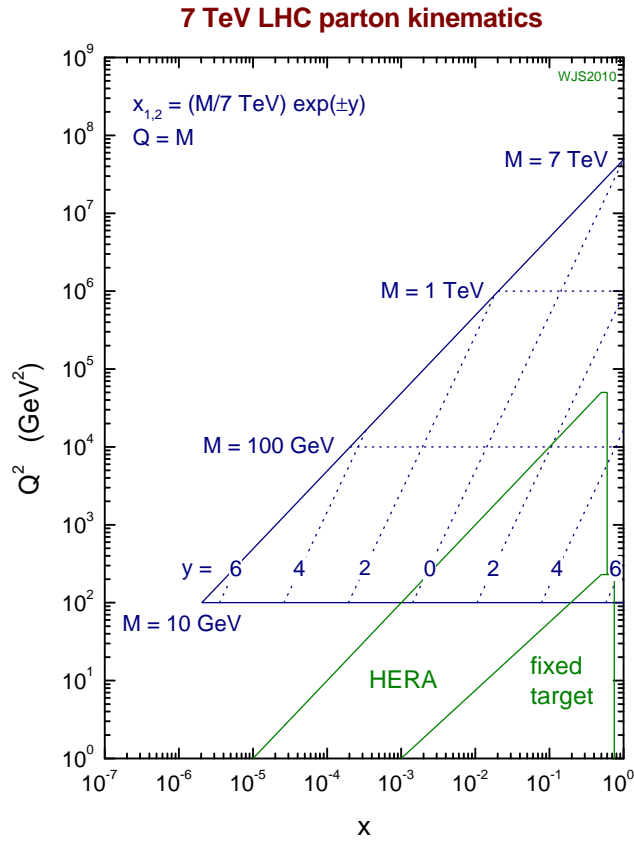


Figure 1.5: The kinematical ranges of particle physics experiments. Taken from [36].

factorization scale μ_F and on the final state phase space Φ_X :

$$\hat{\sigma} = \frac{1}{2\hat{s}} |\mathcal{M}_{1,2 \rightarrow X}|^2(\Phi_X, \mu_F^2). \quad (1.46)$$

$\mathcal{M}_{1,2 \rightarrow X}$ is the matrix element for the process of parton 1 and 2 going to X . To calculate the cross section of a given process (which is proportional to the amplitude squared), the amplitude can be described as a series of Feynman diagrams \mathcal{F}^i grouped according to the multiplicity of couplings $\sqrt{\alpha_s}$ they contain,

$$\mathcal{M}_{1,2 \rightarrow X} = \sum_i \mathcal{F}_{1,2 \rightarrow X}^i(\sqrt{\alpha_s}). \quad (1.47)$$

The simplest set of diagrams with the lowest order of α_s is called leading order (LO), the set of next higher order next-to-leading order (NLO), etc. Given a small coupling α_s , this series is expected to converge to the actual cross section.

1.5 Limitations of the Standard Model

The SM of particle physics is a remarkable theory and is describing most of the known physics with great success. But there are also some known missing pieces in the final theory, for example:

- *Neutrino oscillations:* In the context of the SM, neutrinos are thought to be massless, which is experimentally disproved by the observations of neutrino oscillations from one type of neutrino into a different one. This is only possible to happen if neutrinos themselves carry a mass.
- *Dark matter:* Gravitational effects hint to the existence of the so called dark matter which can not be accounted for in the SM, since neutrinos are not massive enough. Thus, a different model (e.g. supersymmetry) is needed to provide such a *weakly interacting massive particle*.
- *Gravity:* Gravitational forces are not included in the SM.
- *The hierarchy problem:* In the SM, the Higgs boson mass is expected to be of the order of $m_H \approx 100$ GeV. But its mass also gets contributions from virtual particles coupling to the Higgs boson, which depend on the cut-off scale Λ_C used for the regularization (i.e. physics processes which take place beyond this energy scale are ignored) of the appearing loop integrals. Thus, in order to conserve a low mass Higgs boson, one can expect new physics at a low enough scale (around few TeV), or one needs a so called fine tuning mechanism, which keeps the Higgs mass low.
- *Three families of fermions:* There is no explanation for the fact that there are three families of fermions.

Chapter 2

The Large Hadron Collider

Hadron colliders have meanwhile a tradition in experimental high energy particle physics and led to numerous important discoveries. The first of that kind was the Intersecting Storage Ring (ISR) at CERN back in the sixties of the last century where protons accelerated in the Proton Synchrotron (PS) were stored and brought to collision with a center of mass energy of 56 GeV — a large step in energy compared to the fixed target experiments available at the time. A next step was the SPS (Super Proton Synchrotron) again at CERN, operated from 1981-1984 with a center of mass energy of 800 GeV, which led to the noble prize winning discovery of the W and Z bosons. A high center of mass energy of almost 2 TeV, was realized at the Tevatron (1983-2011), a $p\bar{p}$ collider at Fermilab near Chicago (USA), whose experiments announced the discovery of the top quark in 1995.

The Large Hadron Collider (LHC), a pp collider at CERN, is the latest generation of this type of collider machine, surpassing its predecessors performance in all aspects. The main goals are the long awaited discovery of the since around 1960 predicted SM Higgs boson and to push the high energy physics frontier into the unknown and discover possible new physics.

The LHC has a circumference of 27 km and is installed in the former Large Electron Positron (LEP) collider tunnel, around 100 m below the earth's surface of the Franco-Swiss border near Geneva. Figure 2.1 shows a picture of the geographical situation in this area.

The four main experiments situated along the LHC ring are ATLAS, CMS, LHCb and ALICE. CMS, which will be described in more detail in the next Chapter, and ATLAS are so called general purpose detectors devoted to a wide physics program in which several thousands of physicists and technicians from all around the world are involved. LHCb is dedicated to b-physics and ALICE focuses on heavy ion collisions - lead nuclei which can be accelerated in the LHC.

This Chapter gives a short overview of the LHC. An extensive description of the LHC accelerator can be found in Refs. [37–39].



Figure 2.1: The geographical situation around Geneva with the perimeter of the LHC tunnel (yellow) and its experiments [40].

2.1 Experimental Needs - Energy and Luminosity

The composite structure of the colliding hadrons allows to probe a wide range of collision energies, making hadron colliders the ideal discovery machines for not yet observed particles, especially if their mass is not well predicted. But this comes at the price of a “less clean environment” due to the underlying event structure of hadron collisions, compared to e.g. an e^+e^- -collider as the LEP collider was. Another advantage of hadron colliders is the higher mass m of the accelerated particles. A proton is about 2'000 times heavier than an electron. This reduces the energy loss due to *synchrotron radiation*, compared to LEP, significantly, as it is proportional to $\Delta E \propto \frac{1}{Rm^4}$, with R the radius of the accelerator. The maximal energy of the proton beam and consequently the maximal center of mass energy is also limited by the magnetic field of the superconducting *dipole magnets*. Their fields have to be strong enough to deliver the centripetal force in order to keep the protons on their circular orbits. A technical problem with the power connections limits the actual running to 3.5 TeV (4 TeV during 2012) per beam, instead of the designed 7 TeV per beam.

Besides the center of mass energy E_{cm} , which has to be large enough to produce heavy particles, the main parameter is the *luminosity* \mathcal{L} which is related to the rate $\frac{d}{dt}N$ of produced events via the cross section σ of a certain process

$$\frac{d}{dt}N = \mathcal{L} \cdot \sigma. \quad (2.1)$$

In a collider with two identical beams travelling in opposite directions, the luminosity is

$$\mathcal{L} = \frac{N_b^2 \cdot n \cdot v/C}{A}, \quad (2.2)$$

Parameter	Designed	2010 running	2011 running
Circumference C [km]	27	27	27
Center of mass energy E_{cm} [TeV]	14	7	7
Luminosity \mathcal{L} [$\text{cm}^{-2}\text{s}^{-1}$]	10^{34}	$2 \cdot 10^{32}$	$3.6 \cdot 10^{33}$
Delivered Integrated Luminosity [fb^{-1}]	-	0.04	6.1
Number of bunches j	2'808	368	1'380
Bunch spacing [ns]	25	150	50
Number of protons per bunch N_b	$1.15 \cdot 10^{11}$	$1 \cdot 10^{10}$	$1.5 \cdot 10^{11}$

Table 2.1: LHC design, and best performance 2010 and 2011 running parameters for proton operation. Numbers taken from [37, 41, 42].

with n the number of colliding bunches each containing N_b particles in each beam traveling with velocity v in a ring of circumference C . $A = 4\pi\sigma_x\sigma_y$ is the cross-sectional area of the two beams in the interaction point and σ_x and σ_y are the Gaussian shapes of the beam along the x and y direction. The integral $\int \mathcal{L} dt$ is the *integrated luminosity*. As one can see from Equation 2.2, the goal is to minimize the beam cross section, maximize the number of particles per bunch as well as the number of bunches per beam and run for a long period of time in order to accumulate high statistics. This is especially true if one wants to study rare processes which have a rather small cross section σ as e.g. the production of the Higgs boson.

The nominal parameters for the Large Hadron Collider (LHC) are compiled in Table 2.1, for the 2010 as well as for the 2011 pp running periods.

2.2 LHC Design and Injection Chain

Two parallel beam pipes, each containing a ultra high vacuum, host the two proton beams which are traveling in opposite directions and cross each other in the interaction points. More than 1'200 superconducting *dipole magnets*, inducing a maximal magnetic field of more than 8 Tesla, keep the protons on the circular path. A few hundred additional superconducting *quadrupole magnets* are used to focus the beams in order to maximize the luminosity. Close to hundred tons of liquid helium are needed to cool the superconducting magnets to their operating temperature at 1.9 K.

The LHC is supplied with protons through the following injection chain, which is also shown in Figure 2.2: a linear accelerator, (Linac2, 50 MeV) provides the protons, which are obtained by ionization of hydrogen atoms, for the Proton Synchrotron Booster (PSB, 1.4 GeV), from which, via the circular Proton Synchrotron (PS, 25 GeV), they enter the Super Proton Synchrotron (SPS) which injects the protons with 450 GeV into the LHC, where they are accelerated to the final energy. Most of these facilities were already used in previous experiments, and were upgraded to meet LHC's needs.

2.3 Physics at the LHC

One of the main objectives of the LHC project is the discovery of the SM Higgs boson or the discovery of potential new physics beyond the SM. Figure 2.3 shows the predicted cross

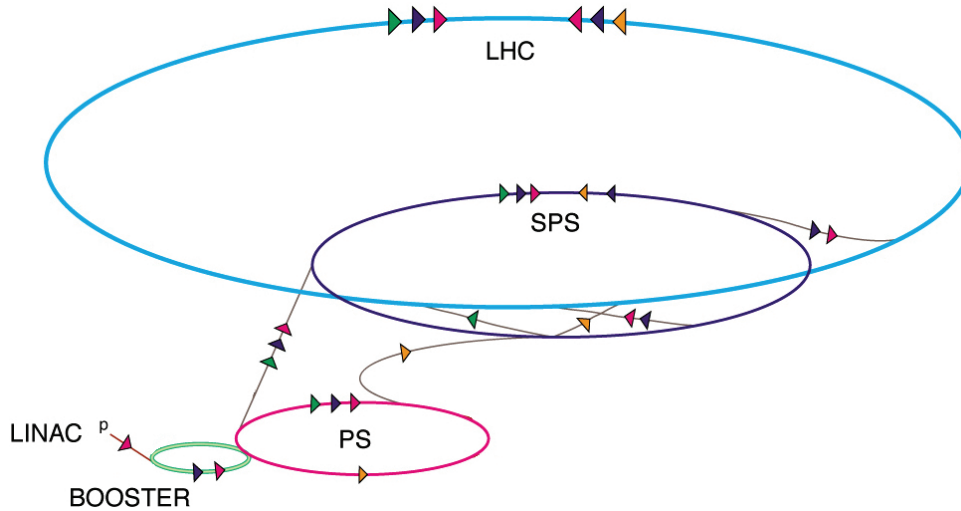


Figure 2.2: The LHC injection chain.

sections for different processes as a function of the center of mass energy. One can see, that the increase in center of mass energy of the LHC, compared to previous experiments, leads to a significant increase in the cross sections for practically all processes — for Higgs production, but also for already known SM processes. At a luminosity of $10^{33} \text{ cm}^{-2}\text{s}^{-1}$, this leads up to few tens of Higgs bosons per hour produced, depending on the actual Higgs boson mass.

While *en route* to the discovery of the Higgs or new phenomena as e.g. a Z' , many other processes can be studied by means of the LHC at the unprecedented 7 TeV center of mass energy. This allows to perform e.g. valuable cross checks of theoretical predictions or measurements of electroweak parameters, studies of the high momentum transfer Q^2 regime or the tuning of underlying event models used in simulations for future analyses.

Figure 2.4 summarizes for example some results of the measured and predicted cross sections for different electroweak processes. The W and Z boson production cross section have already been measured with good precision with the 2010 data, corresponding only to 36 pb^{-1} . The agreement between the measurements and the theoretical predictions is astonishingly good. The, up to two orders of magnitude smaller, di-boson cross sections have been measured with the data recorded during the first running period of 2011, corresponding to about 1 fb^{-1} . By the end of 2011, probably earlier than expected, the sensitivity for the Higgs production, depending on the mass hypothesis, was already reached.

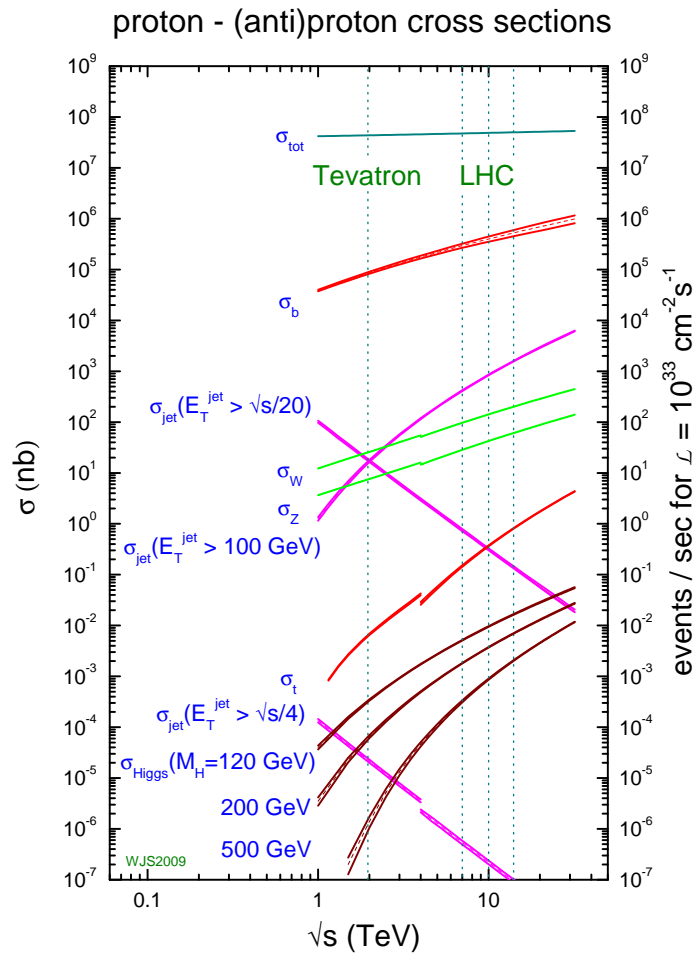


Figure 2.3: Cross section predictions as a function of the center of mass energy for different SM processes. One can clearly see the increase of cross section at the LHC compared to previous colliders. Taken from [36].

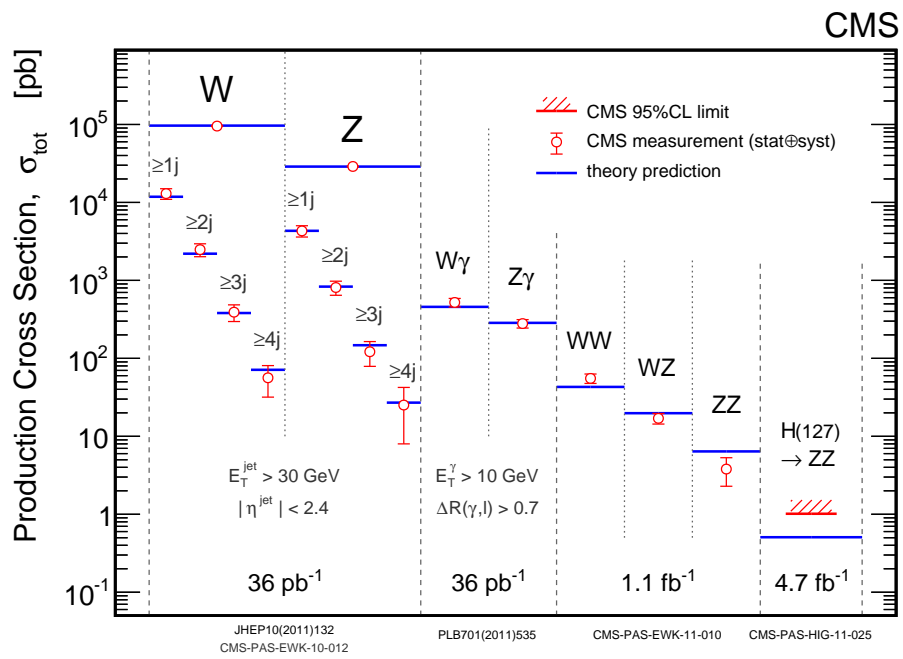


Figure 2.4: Predicted and measured electroweak cross sections from CMS. Taken from [43].

Chapter 3

The Compact Muon Solenoid Experiment

The primary goal of the LHC program is to investigate the nature of electroweak symmetry breaking and thus challenge the so far very successful SM of particle physics and/or discover new physics phenomena. The colliders performance as well as the desired accuracy of the measurements impose major challenges on the detector design and operation, and several novel techniques are used to fulfill the needs of a successful particle physics experiment at the LHC.

This Chapter gives a very short overview of the Compact Muon Solenoid (CMS) detector, its subdetector systems and the strategy which is applied for data taking.

3.1 Overall Design of the CMS Detector

The CMS detector is a *general purpose detector*, allowing the study of a large spectrum of physics processes. The overall length of the closed detector is 21.5 m with a diameter of 15 m. The total weight is 12'500 t, mainly due to the iron return yoke. CMS is located at point 5 on the perimeter of the LHC, around 100 m below the earth's surface. Several different physics processes are used to measure the different types of particles, emerging from the proton collisions which are taking place in the center of the detector. Thus, the different *subdetectors*, which provide the raw data needed for any successful particle identification, are set up in an "onion" like design as layers around the interaction point.

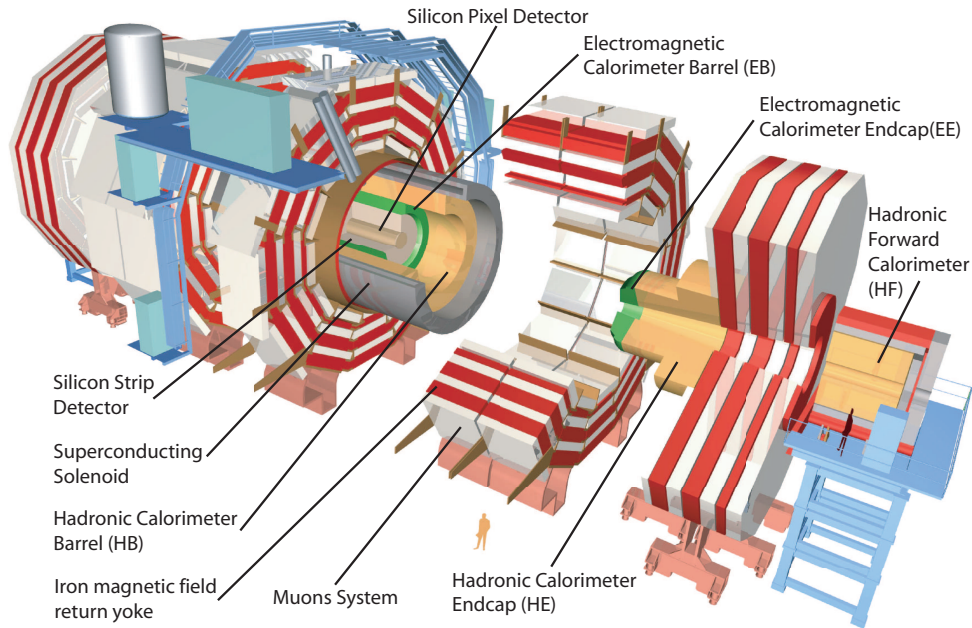


Figure 3.1: A schematic view of the (open) CMS detector.

These subdetectors are, from inside out:

- Tracking system
- Electromagnetic calorimeter
- Hadronic calorimeter
- Superconducting solenoid¹
- Muon system

Figure 3.1 shows a schematic view of the CMS detector and its components. One of the driving features towards this particular detector design is the superconducting solenoid and its magnetic field. This large field strength of almost 4 Tesla is needed to have the necessary bending of charged particles to measure their momenta with a high precision, with a focus on muons, and allows to maintain an overall compact design of the detector — hence the name Compact Muon Solenoid.

In the following Sections, a short description of the different subdetectors is given. A much more detailed description of the CMS detector can be found in [44, 45].

3.2 Tracker System

The innermost subdetector is the tracking system which is designed to provide precise measurements of the trajectories of charged particles down to a transverse momentum of

¹This is not exactly a subdetector, but a subsystem of big importance and thus discussed in the same way as the subdetectors.

about 100 MeV. It is divided into two regions: the *silicon pixel detector* close to the beam pipe and the surrounding *silicon strip detector*. It consists of a *barrel* and an *endcap* part, covering a total pseudorapidity range up to $|\eta| \leq 2.5$.² The tracker has a diameter of 1.1 m and a length of 5.6 m. Its operating temperature is around -20°C . Figure 3.2 shows an illustration of the cross section through the overall tracking system.

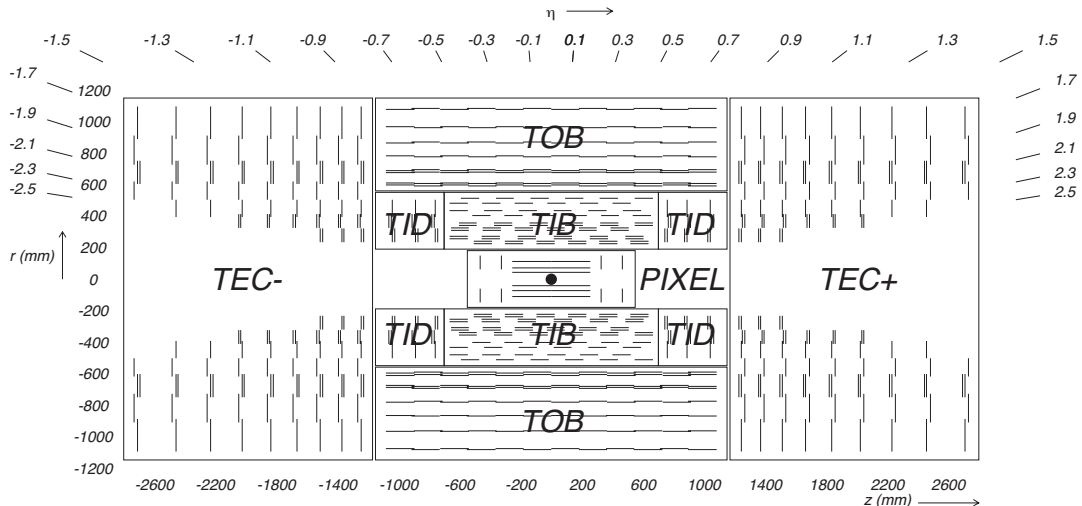


Figure 3.2: Schematic cross section through the CMS tracker. Each line corresponds to a silicon layer. The physical dimensions as well as the detector’s pseudorapidity acceptance are indicated. Taken from [45].

3.2.1 Pixel Tracker

The barrel pixel detector consists of three concentric cylindrical layers of silicon pixels, with radii from 4.4–10.2 cm around the beam pipe. The individual pixels have a size of $100 \times 150 \mu\text{m}^2$. The endcap part has two layers of pixels, giving a half length of the full pixel detector of approximately $|z| \approx 50$ cm. The CMS pixel detector has in total 66 million channels corresponding to an active area of $\sim 1 \text{ m}^2$. The spatial resolution is about $10 \mu\text{m}$ in r - ϕ and about $20 \mu\text{m}$ in z -direction.

3.2.2 Strip Tracker

The barrel part of the strip detector has 11 layers with radii from 20–110 cm. The inner 4 barrel layers (Tracker Inner Barrel, TIB) cover up to $|z| \leq 65$ cm and have strips of $320 \mu\text{m}$ width, separated by $\sim 100 \mu\text{m}$, whereas the outer 7 layers (Tracker Outer Barrel, TOB) extend up to $|z| = 110$ cm and the strip width is $500 \mu\text{m}$ with a separation of 100–200 μm . The endcap strip detector (Tracker End Cap, TEC) consists of 9 layers and covers the longitudinal distance of 120–280 cm from the interaction point. The smaller 3 layer inner discs (Tracker Inner Discs, TID) are filling the gap between TIB and TEC. The tracker

²The pseudorapidity of a particle is defined as $\eta = -\ln \left[\tan \left(\frac{\theta}{2} \right) \right]$, where θ is the angle between the particles momentum and the beam direction.

consists of around 15'000 modules corresponding to an active area of $\sim 200 \text{ m}^2$. The single point resolution of the silicon strip detector is around 20–50 μm in r - ϕ coordinates, depending on the subdetector part. The longitudinal resolution is between ~ 200 –500 μm .

For high momentum tracks of around 100 GeV, the transverse momentum resolution of the tracking system is 1–2%, up to $|\eta| < 1.6$.

More information on the tracking system can be found in Refs. [46,47].

3.3 Calorimetry

The energy of the final state particles is measured with a *calorimeter*. It is split in an *electromagnetic calorimeter*, measuring precisely the energies of electromagnetically interacting particles as e.g. photons or electrons, and a *hadronic calorimeter* measuring the energy of hadrons. In order to provide a precise measurement, the calorimeter system should be as hermetic as possible. The full containment of the energy is especially important for a precise measurement of the missing transverse energy \cancel{E}_T , due to the escaping neutrinos. The calorimeters are located outside of the tracker and inside the magnet.

3.3.1 Electromagnetic Calorimeter

The electromagnetic calorimeter (ECAL) plays, besides any measurement including photons or electrons, an essential role in the study of the electroweak symmetry breaking, by measuring the photons for the promising $H \rightarrow \gamma\gamma$ channel in which the Higgs boson is expected to be discovered if it has a light mass. The ECAL is also providing the calorimetric energy information used to reconstruct electrons from potential leptonic final states in many different analyses.

The ECAL consists of a barrel (EB) part, covering approximately $|\eta| < 1.5$ and an endcap (EE) part, covering approximately $1.5 < |\eta| < 3.0$. Figure 3.3 shows an illustration of the ECAL layout. ECAL is designed to have a very good energy resolution for photons and electrons. For photons, the energy resolution is around 0.2–0.9% depending on the ECAL region, while for electrons it is assumed to be around 2% [49].

Lead tungstate (PbWO_4) crystals are chosen as scintillating material. Its short scintillation decay time allows an emittance of 80% of the light within 25 ns and makes it possible to operate ECAL also at the high bunch crossing rates of 40 MHz. The scintillation light is blue-green with a wavelength of 420 nm. Because the light output is temperature dependent, ECAL is held at a constant temperature of $18 \pm 0.1^\circ\text{C}$.

The EB consists of 36 so called supermodules, 18 in each half of the subdetector, containing the total 61'200 lead tungstate crystals. The front faces of the crystals are located 1.3 m from the beam axis. The crystal front face has a cross section of $22 \times 22 \text{ mm}^2$ and the crystals are 23 cm long, corresponding to ~ 26 radiation lengths (X_0). The axes of the crystals are tilted by 3° from the direct line-of-sight to the interaction point in order to avoid energy leakage through the cracks between individual crystals. The small Molière radius of lead tungstate of approximately 2.2 cm allows a containment of 85% (95%) of the energy of an electromagnetic shower in one (a matrix of 3×3) crystal(s) [50]. The

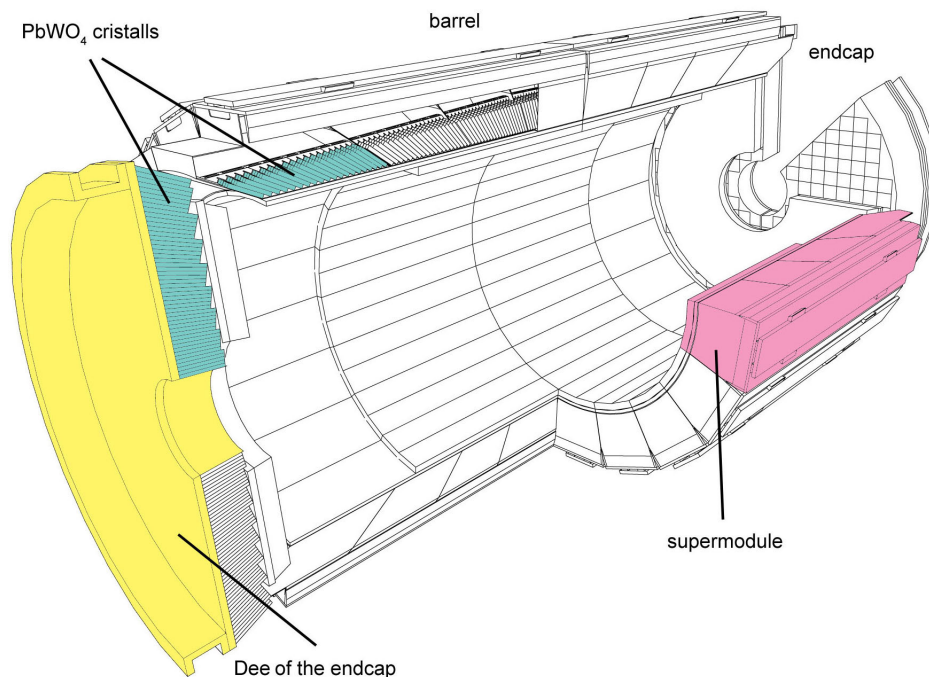


Figure 3.3: Illustration of the CMS ECAL layout. Taken from [48] and adapted.

light in EB is collected using *avalanche photodiodes* (APD) glued on the crystal's back face.

The energy resolution of the ECAL can be parametrized as

$$\left(\frac{\sigma}{E}\right)^2 = \left(\frac{S}{\sqrt{E}}\right)^2 + \left(\frac{N}{E}\right)^2 + C^2, \quad (3.1)$$

where S is the stochastic term, N is the noise term and C is the constant term.³ Typical values are obtained from test beams as $S \approx 2.8\%$, $N \approx 0.12$ and $C \approx 0.30\%$ [45].

The crystal front faces of the endcap are located around 3 m longitudinally from the interaction point. Each EE consists of 7'324 crystals. The crystal front face is $28.62 \times 28.62 \text{ mm}^2$ and are 22 cm long ($\sim 25X_0$). Due to the harsh radiation environment and the strong magnetic field, *vacuum phototriodes* (VPT) are used for the light collection.

In order to identify neutral pions in the approximate fiducial region of EE, a *preshower* (ES) *detector* is installed. It is a two layer sampling calorimeter consisting of lead absorbers and silicon sensors as active material. It is installed in front of EE.

More information about the ECAL can be found in [48, 51].

³The stochastic term describes e.g. event-by-event fluctuations and contributions from photostatistics, the noise term includes electronic noise and the constant term arises from non-uniformities, calibration errors and leakage at the back of the crystals.

3.3.2 Hadronic Calorimeter

Due to the large hadronic jet cross section in pp collisions, the hadronic calorimeter plays an important role in the reconstruction of jets. It is mainly made of brass (due to its short interaction length and because it is non-magnetic) and interleaved with plastic scintillator as an active medium, which is connected to the readout electronics by wavelength shifters. It consists of a barrel (HB) and endcap part (HE) as well as of a forward part (HF), covering a total pseudorapidity range up to $|\eta| \leq 5.3$. The radial size of the hadronic calorimeter is limited by the surrounding solenoid magnet. In order to contain the full hadronic energy, an additional detector layer is installed, in the central region outside of the magnet (Hadronic Outer calorimeter, HO). The total interaction length at $\eta = 0$ is $\sim 6X_0$, and ECAL adds about $\sim 1X_0$. An extensive discussion of the hadronic calorimeter can be found in the corresponding technical design report [52].

HCAL Barrel and Endcaps

The HB subdetector is made of 15 layers of brass which are approximately 5.5–7.5 cm thick, interleaved with ~ 4 cm thick scintillator plates. The HB covers an area of $-1.4 < \eta < 1.4$ in pseudorapidity and is assembled out of 2'304 ($\Delta\eta \times \Delta\phi = 0.087 \times 0.087$) towers which are read out as single calorimeter tower without a longitudinal sampling.

HE has a total of 2'304 towers with η -dependent ϕ -segmentations. It covers a pseudorapidity range of $1.3 < |\eta| < 3.0$. Figure 3.4(a) shows a picture of a wheel of the HB before its integration into CMS as of February 2007.

HCAL Forward

The HF subdetector takes the role of the electromagnetic and hadronic calorimeter in the pseudorapidity range it covers, i.e. $2.9 < |\eta| < 5.3$. Due to the high radiation field in the forward region (~ 100 Mrad/y at $|\eta| \approx 5$, [45]) a Čerenkov calorimeter is used, in contrast to the conventional scintillator used in HB and HE. HF uses steel as an absorber and quartz fibers for the readout. The signal originates from Čerenkov light emitted inside the quartz which is guided through the fibers to photomultipliers. The quartz fibers of 0.6 mm diameter are assembled in a square grid of 5 mm of distance inside the steel and are oriented parallel to the beam axis. Due to the fact that quartz is non-compensating, i.e. an electron induced shower produces twice as much light inside the fiber than the one induced by a pion with the same energy, two different lengths of fibers are used; the so called short (1.43 m) and long fibers (1.65 m), giving a very rough longitudinal sampling. The long fibers reach the front face of HF (towards the interaction point), whereas the short fibers are 22 cm shorter. This distance is longer than the average electromagnetic shower and corrects therefore the electron-to-hadron light ratio. The electromagnetic energy in HF is defined as

$$E_{electromagnetic} = E_{long\ fibers} - E_{short\ fibers}, \quad (3.2)$$

which can result in “negative” energies. The hadronic energy deposited in HF is

$$E_{hadronic} = 2 \cdot E_{short\ fibers}. \quad (3.3)$$

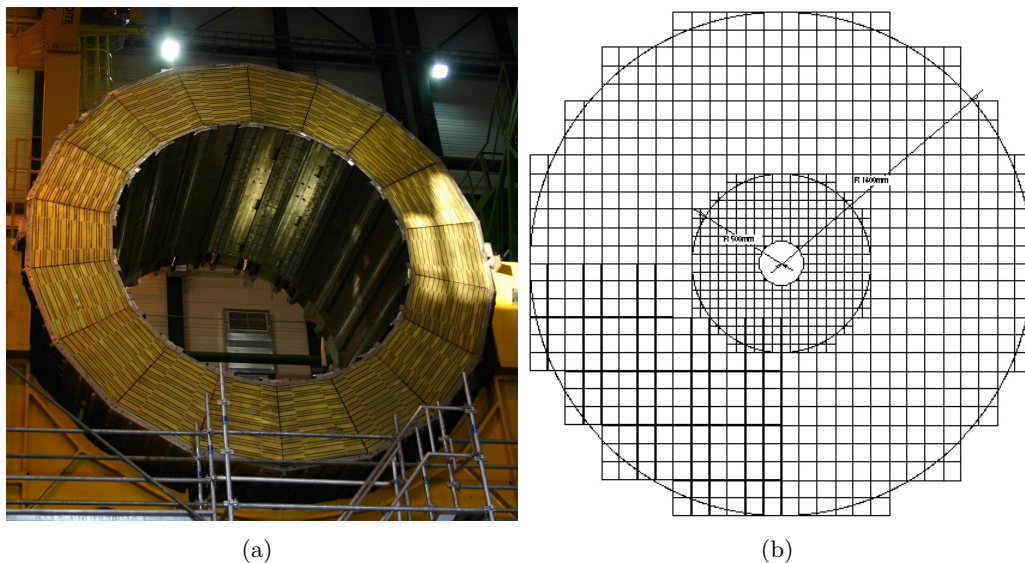


Figure 3.4: (a) Part of the HB before integration. (b) Layout of the towers in one HF endcap.

The total energy is the sum of the two: $E_{tot.} = E_{electromagnetic} + E_{hadronic}$.

HF is divided into 13 rings in η of $\Delta\eta \approx 0.175$ each, which have a segmentation of 10° in ϕ . The innermost and outermost rings deviate slightly from this pattern: the innermost ring has $\Delta\eta \approx 0.1$, the outermost has $\Delta\eta \times \Delta\phi \approx 3.0 \times 20^\circ$. This results in 900 towers, which corresponds to 1'800 read-out channels (long and short fibers).

Figure 3.4(b) shows the layout of the HF towers and the relative location of HF inside CMS can be seen from Figure 3.6.

3.4 Superconducting Solenoid

One of the most important design aspects of the CMS detector is the strong *magnetic field* used to measure the momenta of charged particles via the curvature of their tracks. The requirement to achieve an excellent momentum resolution and keep a compact design of the detector leads to the need of a very strong magnetic field. According to the *Glückstern formula*

$$\frac{\sigma_{pT}}{pT} \propto \frac{1}{BL^2}, \quad (3.4)$$

the momentum resolution can be improved by increasing the magnetic field B or the length of the track L [53].

CMS uses a *superconducting solenoid* of 13 m length and an inner diameter of 6 m. Figure 3.5 shows a picture of the wheel which is supporting the solenoid. The 3.8 Tesla field is parallel to the beam axis and allows precise momentum measurement up to $|\eta| \approx 2.5$. In order to increase the homogeneity of the field inside the tracker volume and reduce stray fields outside of the detector an *iron return yoke* is installed. At the same time the steel plates play the role of the absorber for the interleaved muon chambers [54].

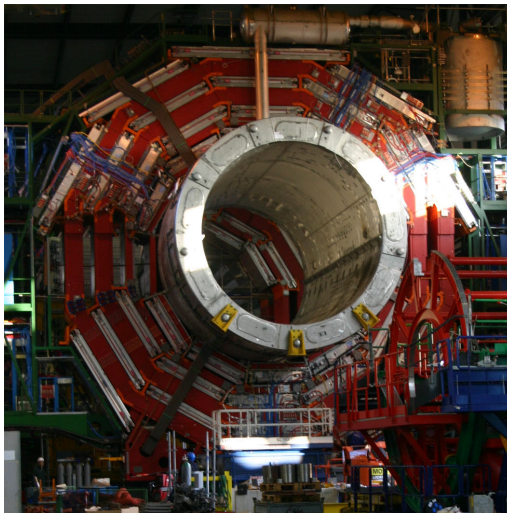


Figure 3.5: The CMS superconducting solenoid before being lowered into the experimental cavern in February 2007. The red colored areas are the iron plates from the return yokes, interleaved with the muon chambers (colored in white).

Many details of the magnet are described in Ref. [55].

3.5 Muon System

Muons, like electrons, are essential for analyses studying a leptonic final state, and are used in many SM precision measurements as well as in searches for new physics. Basically all processes can thus be studied in parallel in the electronic and muonic final states and allow thus a valuable cross check of the results. Muons have usually a significantly higher reconstruction efficiency compared to electrons and their reconstruction strategy is much simpler compared to the one of electrons.

CMS includes three types of gaseous detectors which are used for the muon reconstruction and momenta measurements. The muon system is hosted in the magnet return yokes and consists of a barrel ($|\eta| < 1.2$) and an endcap ($|\eta| < 2.4$) part. The barrel is divided into five coaxial wheels, which are further divided into four concentric stations. These stations are made of layers of *drift tube (DT) chambers* and *resistive plate chambers (RPCs)*. The endcaps are made of discs “closing” the barrel and consist of *cathode strip chambers (CSCs)* and RPCs. See Figures 3.1 and 3.6.

RPCs are made of double-gap bakelite chambers, filled with freon- and isobutane gas. The gaps are two millimeters. RPCs have a very fast response and are thus used as muon triggers in both, the barrel and endcaps.

Most drift tube chambers have the dimensions of $(2.0 \times 2.0 \times 0.4) \text{ m}^3$ and consist of 3 groups of 4 layers of DTs each. Two groups measure the $r\phi$ -coordinates, and the third group the z -coordinates. Single drift tubes are made of a cell, filled with Ar (argon) and CO_2 , aluminum cathodes and anode wires. In total, CMS has 172'000 DT channels. Hits from muons in the drift tubes are used as inputs for the muon track reconstruction.

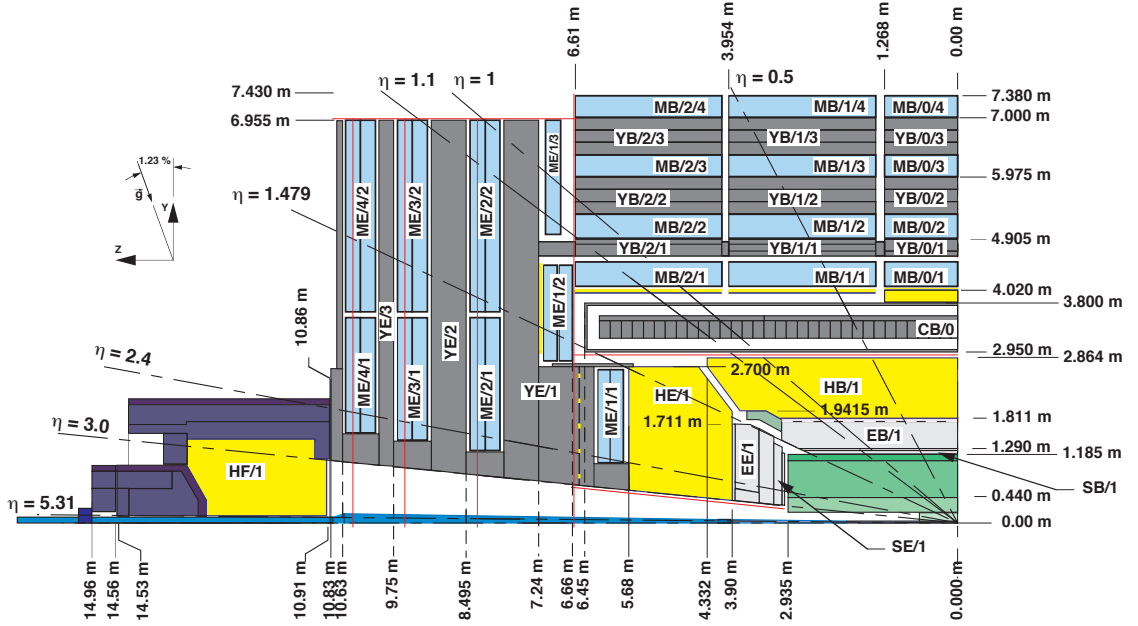


Figure 3.6: Longitudinal view of 1/4 of the CMS detector. The tracking system is shown in green, ECAL in light gray, HCAL in yellow, magnet and return yoke in dark gray and muon chambers in light blue. Taken and adapted from [56].

CMS has 468 CSCs of trapezoidal shape arranged in concentric rings around the beam pipe and in three layers per endcap. Each CSC consists of 6 gas gaps. Each gap has a layer of radial cathode strips and a plane of anode wires. The wires are perpendicular to the cathode strips. A charged particle traversing the CSC ionizes the Ar-CO₂-CF₄ gas in the gap, which results in an electron avalanche which produces a charge on the anode wire. By construction, all three space variables (r , ϕ , z) are measured in each CSC layer simultaneously.

The transverse momentum (p_T) resolution of muons with a $p_T < 100$ GeV varies from 1.3% to 2%, for muons in the barrel, depending on the pseudorapidity. The resolution for muons in the endcaps is better than 6%. The momentum resolution stays below 10% up to 1 TeV muons. The muon trigger efficiency is above 90% for the full acceptance. [57]

More information about the muon system can be found in [56].

3.6 Data Taking

3.6.1 Trigger System

The trigger is at the start of any event selection! At nominal LHC operation, a beam crossing occurs every 25 ns. Assuming a total pp cross section of ~ 100 mb, this results in an event rate of 10^9 Hz at a luminosity of 10^{34} cm⁻²s⁻¹. In order to record the data, this rate has to be reduced to ~ 100 Hz. The decision to keep or discard an event has to

be taken in an extremely short time interval of a few μs . CMS is doing this in two steps:

- i)* The *Level-1* (L1) *trigger* on hardware level, which is identifying leptons, jets etc. based on very coarse subdetector data only, stores the data for further processing. The trigger decision is taken by the subdetector electronics. The L1 has to be highly efficient and reduces the rate to ~ 75 kHz.
- ii)* If an event passes the L1 trigger, the data is transferred to the *High level trigger* (HLT) which accesses the full data and reduces the event rate down to ~ 100 Hz. The HLT uses data which was not yet available at the L1 stage (e.g. the tracker information) and can already apply partial object reconstruction and/or isolation.

An extensive description of the CMS trigger system can be found in Ref. [58].

Electron High Level Trigger

After passing the L1 trigger, the first step of the electron HLT is to reconstruct so called ECAL *super-clusters* which have to be in the fiducial region and have to pass certain energy thresholds. In a next step, the ECAL super-cluster gets matched with hits in the pixel detector. In a last step, the full event information, including reconstructed tracks, is used and different cuts are applied; e.g. on the ratio of the super-cluster energy and the extrapolated track momentum E/p , the fraction of hadronic activity in HCAL behind the super-cluster H/E or the matching of the reconstructed tracks with the super-cluster in $\Delta\phi$ and $\Delta\eta$. In addition, shower shape or isolation requirements are also applied. This gives the *HLT electron candidates*.

Muon High Level Trigger

The muon HLT selection has two steps: In the first, muons are reconstructed from hits in the muon chambers, in the second the muon chamber tracks are extended into the tracker, refining the muon p_T measurement. In each step, an isolation in a cone around the muon trajectory, is applied. In the first step using only calorimeter, in the second also tracker information.

Di-Lepton High Level Trigger

Di-electron triggers require two HLT electron candidates with loose shower shape and calorimeter isolation requirements on both candidates. In addition the leading electron has to match a L1 seed. For example, the main di-electron trigger during 2011 data taking, having minimum p_T thresholds of 17 GeV and 8 GeV respectively (HLT_E1e17_CaloIdL_CaloIsoVL_E1e8_CaloIdL_CaloIsoVL), has a trigger rate of approximately 13 Hz at an instantaneous luminosity of $1 \times 10^{33} \text{ cm}^{-2}\text{s}^{-1}$.

The di-muon trigger requires two HLT muon candidates above some p_T threshold and both have to match to a L1 seed.

3.6.2 Data Acquisition

The data acquisition (DAQ) system of CMS is designed to select and store collision data up to the design luminosity of a few times $10^{34} \text{ cm}^{-2}\text{s}^{-1}$. Given a total pp cross section of $\sim 100 \text{ mb}$, this leads to on average 20 pp interactions per bunch crossing — corresponding to approximately 1 MByte of data per bunch crossing! The trigger system described in Section 3.6.1 reduces the data flow to $\sim 100 \text{ MByte/s}$.

The data is stored for a short time in the Front-End System (FES) on the subdetector. After receiving the L1-trigger, the data is pushed into the Front-End Drivers (FED), where it is read by the Front-end Read-out Links (FRLs) and passed to the event builder. These event builders assemble the event fragments which belong to the same L1-trigger from the ~ 650 FEDs into a single and complete event which is transmitted to the filter farm in the surface building. The DAQ system is split into 8 *slices* which are redundant and each can manage an event rate of 12.5 kHz.

Back-pressure from any step in this chain can lead to buffer overflow and end in corrupted and lost data. The Trigger-Throttling System (TTS) protects against back-pressure by monitoring feedback from the FEDs and by throttling the trigger. This may lead to *dead-time* during data taking.

CMS splits the data taking into *luminosity sections* during which trigger thresholds and pre-scales are not changed and for which the average instantaneous luminosity is recorded.

The raw events contain the full detector information which is permanently archived in safe storage as *primary datasets* divided according to the different trigger, with a typical event size of about 1.5 MB/event.

3.7 Event Reconstruction

The raw data obtained from the detector is reconstructed by applying several levels of pattern recognition and compression algorithms to the raw data. This reconstruction is the most CPU-intensive step in the data processing chain of CMS. A reconstructed event contains reduced information and higher level “physics objects” and have a size of about 0.5 MB/event.

In the following Sections, the event reconstruction is briefly summarized.

3.7.1 Vertex Reconstruction

Due to multiple interactions per bunch-crossing (pileup), one obtains more than one vertex per event which has to be reconstructed offline from the recorded tracks. The vertex reconstruction is done using the deterministic annealing clustering algorithm which is described in more detail in [59].

3.7.2 Electron Reconstruction

Two complementary algorithms are used in CMS to reconstruct electrons [60]. In the more important *ECAL driven* seeding algorithm, a *super-cluster* of ECAL crystals is clustered first, starting from a single high energy crystal. Additional crystals are added to the cluster in order to recover energy lost due to *Bremsstrahlung*. In a next step, superclusters with a minimum transverse energy of 4 GeV, are matched to track seeds in the inner tracker layers. These hits are used as seeds for the electron track reconstruction using the Gaussian-sum filter (GSF) algorithm [61].

The electron identification is then based on: the energy-momentum match between the supercluster and the electron track E_{seed}/p_{in} , the spatial matching in $\Delta\eta_{in}$ and $\Delta\phi_{in}$ between supercluster and track, the hadronic leakage variable H/E and the shower shape variable $\sigma_{i\eta i\eta}$.⁴

Isolation variables are calculated using the tracker, the ECAL and the HCAL in a cone of $\Delta R < 0.3$ around the electron.

The transverse impact parameter and the number of missing tracker hits in the innermost tracker layers are used to reject electrons from conversions, as they are expected to have a large transverse distance from the beam and no hits in the innermost detectors.

3.7.3 Muon Reconstruction

The standard muon reconstruction in CMS uses independently reconstructed *tracker tracks* and *muon tracks*. Based on these two sets of tracks, muons are identified on a cut based approach.

After the reconstruction, three types of muons exist: *standalone muons* — having a reconstructed track in the muon system; *global muons* — which are seeded by standalone muons and having a track from a global fit using both, hits in the muon system and in the inner tracking system; and *tracker muons* — muons having a track from a fit on tracker hits only, which can be extrapolated to a hit in at least one muon segment (i.e. a track from DT or CSC hits).

Quality requirements for “good” muons include cuts on the number of hits in the tracker and the muon system, on the performance of the global track fit χ^2/ndof and are constrained to the primary vertex.⁵ In order to distinguish muons from hadron decays from muons emerging from the hard scattering process, muons have to be *isolated*. This is usually achieved by requiring that the summed energy in a cone around the muon trajectory is smaller than some fraction of the total muon momentum, typically 10-15%. The muon footprint is typically removed from this sum.

More details on muon reconstruction and the performance measured with 2010 data can be found in [62].

⁴The hadronic leakage variable H/E is the ratio of hadronic energy H and electromagnetic energy E in a cone around the electron direction, and $\sigma_{i\eta i\eta}$ describes the width of the supercluster in η .

⁵The variable ndof is the number of degrees of freedom of the fit.

3.7.4 Jet Reconstruction

The jets used in this thesis are the so called *Particle-Flow* jets [63]. The Particle-Flow algorithm is using information from all CMS sub-detectors to reconstruct individual particles (e.g. electrons, muons, photons, etc.). More information about this algorithm can be found in Ref. [64]. These particles are then used as input objects for the *jet reconstruction algorithm*. The used jet reconstruction algorithm is the anti- k_T algorithm [65] with a cone size of $R = 0.5$.

The measurement of the jet energy is experimentally more challenging than the lepton energy measurement, and it is a well known fact that the jet energy is underestimated, especially for low p_T jets, by a factor called the *jet energy scale* (JES). Thus, after jet reconstruction a JES correction [66, 67] is applied to correct for this effect. In CMS, a factorized approach was developed where each so called level (L1, L2, L3, etc.) is correcting for one particular effect at the time. The different levels are applied in a fixed order, each scaling the jet energy by a factor which is depending on different jet related variables (e.g. p_T, η , etc.). The most important JES corrections are:

- **L1: Offset correction:** Removes energy contributions from pileup events (Fast Jet correction according to Ref. [68]).
- **L2: Relative correction:** Corrects the jet energy response to be flat in η .
- **L3: Absolute correction:** Corrects the jet energy response to be flat in p_T .

These correction factors are measured using data driven techniques (e.g. Z/γ -jet balance).

By construction, electrons are automatically reconstructed as jets. To remove leptons from the jet collection a *jet cleaning* is applied by requiring that the jet is separated by $\Delta R > 0.3$ from any lepton.

3.7.5 Detector Simulation

The first *simulation* step, in order to produce a MC sample that can be used for an analysis, is the generation of a pp collision using one of the many available MC generators (e.g. PYTHIA, HERWIG, etc.). The outgoing particles from a certain process are then run through a full simulation of the CMS detector based on the GEANT4 simulation toolkit [69]. This includes the simulation of the subdetector response on the interaction with the simulated particles and the generation of electronic signals. These signals are then used for reconstruction in the same way as it is done for real data. The reconstructed samples can then be analyzed with the same analysis framework as the data and allows direct comparison of data and MC.

3.7.6 Luminosity Measurement

The correct measurement of the *luminosity* and a proper understanding of its systematic error is crucial for the overall normalization used in almost any physics analysis. The luminosity measurement is mainly based on the pixel subdetector (see Section 3.2.1).

The *pixel cluster counting* method [70] counts the number of occupied pixels per bunch crossing, which is linear to the number of pp interactions per bunch crossing. Due to the large number of pixels and their small area, it is very unlikely that one pixel is hit by two particles in one bunch crossing simultaneously. Thus by knowing the average number of pixels hit per pp interaction, one can estimate the number of pp interaction per crossing. The absolute normalization is obtained from *Van Der Meer scans* [71].

Additional methods which are based on the HF calorimeter (see 3.3.2) exist [72] and the luminosity measurement can also be cross checked offline using W and Z boson counting [73–75].

Part II

Observation of Diffractive W and Z Boson Production

Hadron-hadron scattering can be classified according to their final states: as *elastic* scattering, where no additional particles are produced and the incoming hadrons remain intact; but also as *diffractive* processes, in which the energy transfer between the two hadrons remains small, but one or even both hadrons dissociates into final states of many particles. A third class are *hard processes* which are characterized by a large momentum transfer.

Soft diffractive processes are well known since a long time, and are characterized by a low momentum transfer squared of the order of fractions of $(1 \text{ GeV})^2$. In a single soft diffractive process, the proton remains intact. First evidence for single *hard diffraction* has been observed in 1988 by the UA8 experiment [76] at CERN, where events with high transverse energy jets have been observed, which are containing an intact proton with more than 90% of the incoming beam energy in the final state.

This second Part of the thesis discusses the first observation of diffractive weak boson production at the LHC, which was published in Ref. [77]. One main aspect of this analysis is the study of the forward energy flow in W or Z events, which allows to select diffractive event candidates by the presence of large rapidity gaps.

The first Chapter of Part II gives a short introduction to diffraction in general, to diffractive weak boson production and summarizes the event selection. In Chapter 5, the forward energy flow is studied in these events, and different Monte Carlo tunes are verified with data. In parallel, the charged particle multiplicity in the central region of CMS is also studied.

Finally, in Chapter 6, a diffractive component in the weak boson production in pp collisions is observed and the fraction of diffractive events is estimated.

Chapter 4

Diffractive Production of W and Z Bosons

Diffractive weak boson production is a hard diffractive process, which can be observed in pp collisions. In the first Sections of this Chapter, a short introduction to diffraction is given and related concepts such as the diffractive parton distribution functions, the underlying event and the gap survival probability are introduced.

In the later Sections, the analysis strategy is outlined and the weak boson event selection is given.

4.1 Diffraction - A General Introduction

In high energy $pp \rightarrow XY$ collisions, a significant fraction (approximately 25%) of the total cross section is expected to arise from so called *diffractive* processes, which can be divided into three types of interactions:

- i)* in *elastic scatterings*, where X and Y denote the outgoing protons which remain intact during the interaction (i.e. $pp \rightarrow pp$), see Figure 4.1(a);
- ii)* in *single diffractive dissociation* (SD), where the final state X is the remnant of one dissociated proton, see Figure 4.1(b);
- iii)* and in *double diffractive dissociation* (DD), where the final states X and Y are the remnants of both dissociated protons, see (Figure 4.1(c)).

The total pp cross section for pp collisions at a $\sqrt{s} = 7$ TeV is approximately 100 mb [78], of which the total inelastic cross section is around 74 mb, which can further be divided in SD, DD and ND components. Table 4.1 summarizes the composition of the total inelastic pp cross section as it is predicted by PYTHIA6 [79].

For soft hadronic processes the coupling constant (α_s) becomes large and thus these processes can not be described by perturbative QCD. The *soft diffractive* reactions can be described in the framework of Regge theory [81]. In this picture the virtual exchange

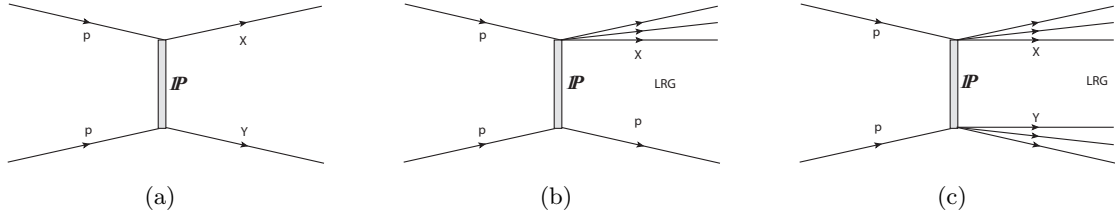


Figure 4.1: (a) Elastic pp scattering, (b) single diffractive dissociation and (c) double diffractive dissociation (c). The \mathbb{P} denotes the exchange of *vacuum quantum numbers*, p the incoming protons and X and Y correspond to the remnants of the dissociated protons. LRG stands for large rapidity gap devoid of particles.

Cross Section [mb]		Measured	PYTHIA6	Fraction [%]
Total pp		98.3 ± 2.81 [78]	-	-
Elastic pp		24.8 ± 1.22 [80]	-	-
Total Inelastic pp		73.5 ± 3.06	71.5	100%
Non-diffractive	$qq \rightarrow qq$	-	10.9	15.2
	$qg \rightarrow qg$	-	10.4	14.5
	$gg \rightarrow gg$	-	26.8	37.5
Diffractive	Single diffractive	-	14.0	19.6
	Double diffractive	-	9.4	13.2

Table 4.1: Total, elastic and inelastic pp cross section from TOTEM and CMS measurements [78, 80] (top part). Predicted total inelastic pp cross section from PYTHIA6 and divided into contributions from non-diffractive and diffractive processes, also from PYTHIA6. The 100% correspond to the total inelastic cross section.

particle carries the quantum numbers of the vacuum, which is often called *Pomeron* (\mathbb{P}). A diffractive interaction does not exchange quantum numbers between the colliding particles and the energy transfer between them remains small. Thus, the momenta of the final states X and Y are almost equal to the momenta of the incoming particles within a few percent, and as a consequence have only small transverse momenta.

The Pomeron exchange means that the color flow between the interacting particles is interrupted and no further particles are produced, resulting in a Large (pseudo)Rapidity Gap (LRG) — a “large” range in (pseudo)rapidity devoid of particles, which is separating the final states X and Y . In non-diffractive (ND) interactions there is an exchange of color charge and subsequently hadrons are produced, also in the central region of the detector.

The total pp cross section is given by the sum of all individual sub-processes

$$\sigma_{\text{tot}} = \sigma_{\text{el}} + \sigma_{\text{inel}} = \sigma_{\text{el}} + \sigma_{\text{SD}} + \sigma_{\text{DD}} + \sigma_{\text{ND}} + \sigma_{\text{rest}}.^1 \quad (4.1)$$

In the single diffractive (SD) case, where Y is the remaining proton, X corresponds to the underlying event and is composed of many low-transverse momentum hadrons. These hadrons are produced in parton showers and non-perturbative multi-parton interactions, in the range of rapidity where the color flow is not interrupted (see also Section 5.1.1).

¹The remaining contributions to the total cross section, denoted with σ_{rest} , which is $\ll 1$ mb, includes multi Pomeron exchanges as e.g. central diffraction etc.

A short introduction to diffraction for non-believers [sic] can be found in [82].

4.2 Detour: “Why is Diffraction Called Diffraction?”

The phenomenon that light shining on a circular disc gives a pattern which is characterized by a central maximum and concentric rings of further maxima and minima is called diffraction. For light with the wavelength λ and a disc of radius R , the intensity as a function of the scattering angle θ , is

$$I(\theta) = I_0 \frac{[2J_1(x)]^2}{x^2} \approx I_0 \left(1 - \frac{R^2}{4} k^2 \theta^2\right), \quad (4.2)$$

where J_1 is the Bessel function of the first order and $x = kR \sin(\theta) \approx kR\theta$ for small θ . $k = \frac{2\pi}{\lambda}$ is the wavenumber and I_0 is the intensity for $\theta = 0$. See Figure 4.2(a) for an illustration of the diffractive intensity pattern.

Given the *wave-particle duality*, which is saying that massive particles behave like waves with wavelength $\lambda = \frac{h}{p}$ (h is Planck’s constant and p the momentum of the particle), diffractive phenomena are expected for particles too.² Figure 4.2(b) shows the differential cross section for protons scattering off ^{40}Ca nuclei as a function of the scattering angle which shows a similar pattern as the diffraction of light.

The differential cross section $\frac{d\sigma}{dt}$ for elastic pp scattering can be described as

$$\frac{d\sigma}{dt}(t) \approx \frac{d\sigma}{dt}(t=0) \cdot e^{-b|t|} \approx \frac{d\sigma}{dt}(t=0) \cdot (1 - bP^2\theta^2), \quad (4.3)$$

which resembles strongly Equation (4.2). Here, $|t| \approx P^2\theta^2$ is the absolute value of the squared four-momentum transfer, P is the incident proton momentum and θ is the scattering angle. This pattern is observed for all diffractive processes mentioned in Section 4.1.

4.3 Diffractive Parton Distribution Functions

The HERA experiments have shown in electron-proton (ep) collisions that the QCD factorization theorem holds for interactions of the type $\gamma^*p \rightarrow pX$ which allows the introduction of diffractive parton distribution functions (dPDF). In this picture the dPDF can be interpreted as the probability density function $f_{\mathbb{P}/p}(x_{\mathbb{P}}, Q^2)$ to find a Pomeron \mathbb{P} with a certain momentum fraction $x_{\mathbb{P}}$ inside the proton, analogously to standard PDFs. Assuming that the dPDFs are process independent, like the standard parton PDFs, one can expect *hard-diffractive* scattering at even large momentum transfer Q^2 , like e.g. heavy quark or jet production [85, 86]. The hard-SD pp cross section is then

$$\sigma(\text{pp} \rightarrow \text{p} + X') = \int_0^1 dx_{\mathbb{P}} f_{\mathbb{P}/p}(x_{\mathbb{P}}, Q^2) \sigma(p\mathbb{P} \rightarrow X'), \quad (4.4)$$

with $\sigma(p\mathbb{P} \rightarrow X')$ the proton-Pomeron cross section. [87]

²After this statement, one might wonder if there are diffractive phenomena in e^+e^- scatterings. Diffraction is a hadronic process and thus suppressed in e^+e^- collisions where both electrons would have to radiate a virtual photon which both fluctuate into quark-antiquark pairs, which then can interact diffractively.

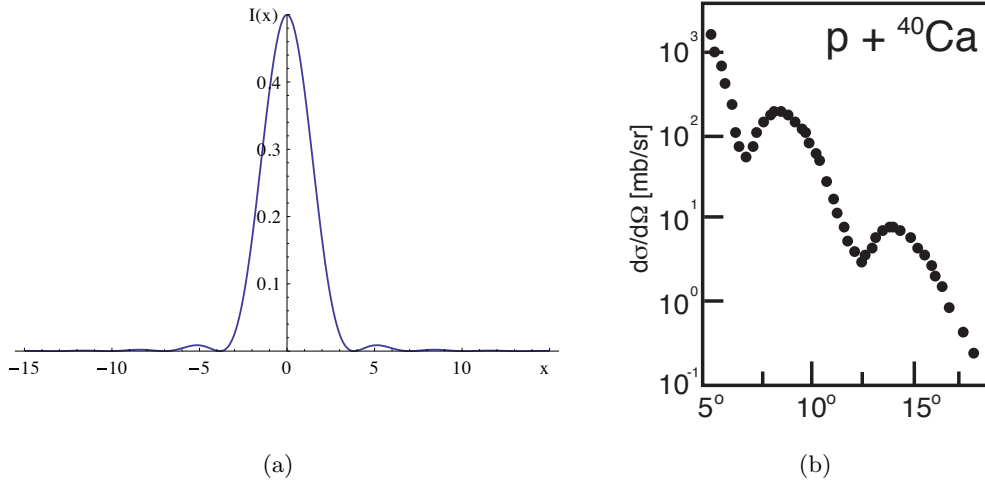


Figure 4.2: (a) The diffraction pattern of Equation (4.2) for $I_0 = 1$ and (b) the differential cross section of $p^{40}\text{Ca}$ scattering (taken from Ref. [83] which adapted the plot from Ref. [84]).

In the QCD picture, the Pomeron can be interpreted in lowest order as a two-gluon (or multi gluon at higher order) state, which is shown e.g. for diffractive W production in Figure 4.3.

The last term in Equation (4.4) can then further be factorized into

$$\sigma(p\mathbb{P} \rightarrow X') = \int_0^1 dx_1 dx_2 f_{p_1/p}(x_1, Q^2) f_{p_2/\mathbb{P}}(x_2, Q^2) \hat{\sigma} \quad (4.5)$$

with $f_{p_1/p}(x_1, Q^2)$ the standard proton PDF (i.e. the probability to find a parton p_1 with momentum fraction x_1 in the proton), $f_{p_2/\mathbb{P}}(x_2, Q^2)$ the Pomeron PDF (i.e. the probability to find a parton p_2 with momentum fraction x_2 in the Pomeron) and $\hat{\sigma}$ the partonic cross section.

The situation can be described as follows: One of the incoming protons radiates a Pomeron. A constituent of this Pomeron then interacts with a parton from the second proton and produces the diffractive system X' (containing XY and W in the example of Figure 4.3).

The dPDFs are obtained from fits to experimental data mainly from HERA [88–90] and by using evolution equations.

4.4 Underlying Event and Gap Survival Probability

In hadron-hadron collisions, only one parton per incoming hadron is participating in the hard scattering. The remaining spectator partons are generating a soft *underlying event* (UE) in which these quarks can undergo additional scatterings called *multi-parton interactions* (MPI). MPI can in principle also be a hard scattering, but are primarily soft interactions.

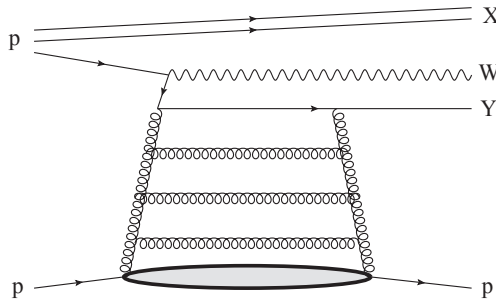


Figure 4.3: “Ladder diagram” for diffractive W production. The situation corresponds to the picture of a parton inside a Pomeron.

The UE description is based on phenomenological observations. Many details will not be discussed here, but can be found in Ref. [79]. In general it is assumed that the individual parton-parton interactions are described by QCD and that the additional number of MPIs follows a Poisson distribution of independent (except from the impact parameter and total momentum, color, charge, etc. conservation) parton-parton interactions. The hardness of an interaction is defined via the transverse momentum of the scattering. Due to the divergence of the QCD cross section for $p_T \rightarrow 0$, a minimum cutoff around $P_{T,0} \approx 2$ GeV is introduced. Only non-diffractive interactions are taken into account. Other simplifications are that e.g. initial- or final-state radiation and color connections are only taken into account for the hard interaction.

Most parameters in the UE model of PYTHIA are tuned to data from various experiments using the charged particle multiplicity in the central region of the detector, leading to different models called “tunes”.

For SD and DD processes, the UE is affecting the LRG structure by filling the LRG with additional particles from MPI and reducing the fraction of events having a LRG. The probability that the underlying event is not affecting the LRG signature, is called the *gap survival probability*. The relative fraction of the total cross section from hard diffractive processes gets reduced from approximately 10% at HERA to approximately 1% at the Tevatron, due to the gap survival probability [91].³

4.5 Diffractive production of W and Z Bosons

Because of the large cross section of vector boson production (see Section 2.3) many properties of W and Z bosons were studied during the 2010 data taking with sufficient statistics.

Diffractive vector boson production has been observed earlier at the Tevatron [92, 93], and the most recent analysis from CDF [94] found that the fractions of diffractively produced W and Z bosons are $1.00 \pm 0.11\%$ and $0.88 \pm 0.22\%$ respectively. Given that the full 2010 data delivered about 130'000 W and 20'000 Z bosons an observation of hard-SD vector boson production ($pp \rightarrow p + W(Z)$) seemed feasible at the LHC. This process

³The SD/ND ratio of around 1% stays approximately constant for different hard diffractive processes, as e.g. di-jets, J/ψ and W/Z production, measured at the Tevatron. This indicates that the gap survival probability is not process dependent.

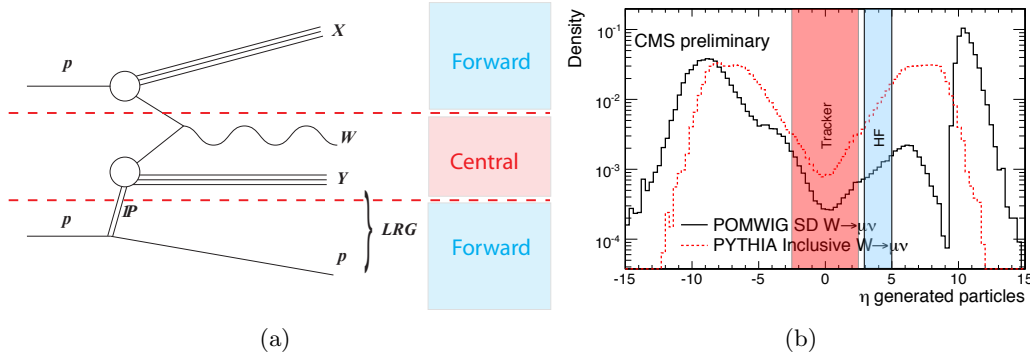


Figure 4.4: (a) Diffractive W production. The \mathbb{P} denotes the exchange of vacuum quantum numbers (*Pomeron*) interrupting the color flow (LRG) and keeping one proton (p) intact. The red and blue regions indicate the central (in which the W and the particles from multi-parton interaction can be detected) and forward regions in (pseudo)rapidity. (b) The normalized energy-weighted η distribution for SD and non-diffractive W production from MC. The η coverage of the central tracker is shown in red and the coverage of HF in blue. The muon from the W decay is not included. Taken from [95] and adapted.

is sensitive to the diffractive structure function (Section 4.3), and due to multi-parton interactions, to the gap survival probability. A first feasibility study for a CMS analysis was presented in Ref. [95]. A simplified diagram of diffractive W production is shown in Figure 4.4(a). The leptonic vector boson decays into electrons (and of course to muons; see [96] for a more detailed discussion of vector boson decay into muons) is discussed in more detail in this Part of the thesis.

4.6 Analysis Strategy

The selection of W bosons is based on the presence of a single central and isolated high transverse momentum lepton from the W decay and large missing energy from the escaping neutrino. Z bosons require two oppositely charged and isolated high p_T leptons.

The normalized and energy weighted particle pseudorapidity η distribution from SD and non-diffractive W production from simulation is shown in Figure 4.4(b). This plot includes only SD events with the LRG on the positive η side of CMS (i.e. the intact proton, which is the one radiating the Pomeron, escapes on the $+z$ side of CMS), giving the peak around $\eta \approx 10$. The non-diffractive distribution is symmetric. A gap survival probability of 0.05 was assumed for the SD MC. One can clearly see the reduced number of particles in the forward region for SD events which corresponds to the LRGs. Hence a diffractively enhanced sample of W events can be selected by asking low central and/or low forward particle multiplicity, e.g. in the HF.

It is obvious that in order to avoid particles from pile-up to fill the LRG or to increase the particle multiplicity shown in Figure 4.4(b), events with more than one vertex have to be rejected.

4.7 Datasets

The full 2010 pp collision data recorded with the CMS experiment is used for this diffractive analysis. A subset of “good” runs has been selected on the basis of the sub-detector states during data taking. The data taking was divided into two periods which were separated by a technical stop. The main difference between these two running periods is the rise of the instantaneous luminosity of the LHC beam, which results in an increased number of pileup events in data. The integrated luminosity corresponds to 36 pb^{-1} . The individual datasets used for the data (MC) are summarized in Table B.1 (B.2) of Appendix B.1.

4.8 Event Reconstruction

4.8.1 Event Triggers

During the 2010 running of the LHC, the instantaneous luminosity was still low enough, however with increasing instantaneous luminosity the lepton identification and isolation requirements had to become more stringent to keep a certain trigger un-pre-scaled. The single lepton triggers used for this analysis are summarized in Table C.1 of Appendix C.1. The logical OR of these individual triggers is required to accept an event.

4.8.2 Lepton Reconstruction

An official CMS electron identification working point was used, which provides a selection efficiency of approximately 80% for electrons coming from W decays.

Boson decays into muons are not discussed extensively in this Part of the thesis, but several distributions are shown combining electrons and muons. Details of the muon reconstruction can be found Ref. [96] and are summarized in Appendix A.

4.8.3 Jet Reconstruction

See Section 3.7.4 for details on jet reconstruction. Jets need to have a minimum corrected transverse momentum of $p_T > 30 \text{ GeV}$, and the pseudorapidity is restricted to central jets only, i.e. $|\eta| < 2.5$.

4.8.4 Charged Particle Tracks

The tracks used in this analysis have a transverse momentum above 1 GeV and, because of the limited tracker acceptance, $|\eta| < 2.5$.

A detailed study of the pion track reconstruction within the acceptance of the tracker [97] determined that the reconstruction efficiency rises from about 88% at a p_T of 0.5 GeV to about 95% for p_T between 1 – 10 GeV. Above 10 GeV, the efficiency decreases slowly to about 90% at 50 GeV. Furthermore, it was shown that the hadron track reconstruction

efficiency in the data agrees within 1 – 2% with the one in the MC simulation. The total systematic uncertainty of the tracking efficiency was estimated to be less than 3.9%.

4.8.5 Vertex Reconstruction for Pile-up Rejection

In order not to reject exclusive W or Z production, where the only tracks in the event come from the leptons from the boson decay itself, no vertex quality requirements as e.g. the minimum number of tracks, i.e. N_{dof} , are requested.⁴ The number of degrees of freedom is defined as $N_{dof} = 2 \cdot \sum_i w_i - 3$, where w_i is a weight assigned to the i^{th} track by the vertex finder algorithm.

The *primary vertex* is selected by a longitudinal matching of the charged lepton track(s) to the vertex. The closest vertex is defined as the primary vertex. This results in a fully efficient primary vertex definition.

Events with more than one vertex are rejected to avoid contributions from pile-up which fill the LRG and thus affect the fraction of LRG events significantly. In order not to reject an event based on the presence of a fake vertex, the *secondary vertices* have to fulfill quality cuts (i.e. a cut on N_{dof}). Events with such additional “good” vertices are rejected.

The secondary vertex reconstruction efficiency as a function of the longitudinal separation between the primary vertex and any secondary vertex as it is obtained from a $W \rightarrow e\nu$ MC including pile-up simulation and for different N_{dof} cuts is shown in Figure 4.5(a). The secondary vertex reconstruction efficiency is around 75% and flat in Δz for no additional quality requirements. With increasing N_{dof} cut, the efficiency decreases and is around 72%(68%) for $N_{dof} \geq 2(4)$.

Because of this vertex reconstruction inefficiency certain events which have pile-up do not get vetoed and thus can contaminate the LRG selection.

This reconstruction inefficiency of about 30% arises from a *soft diffractive* component in the pile-up, which produces low p_T particles which do not enter the pseudorapidity coverage of the tracker, and thus no vertex can be reconstructed, meaning that some fraction of events pass the vertex veto even though multiple interactions happened. This affects the forward energy flow and consequently the LRG signature.

Figure 4.6 helps to illustrate the origin of this inefficiency. It shows the vertex reconstruction efficiency in a minimum bias MC sample from PYTHIA6 with the D6T tune, split into different pp interaction processes: qq \rightarrow qq, qg \rightarrow qg, gg \rightarrow gg, SD (which is further divided into which proton is emitting the Pomeron) and DD. The relative contributions to the total pp cross section are listed in Table 4.1 and leads to the overall reconstruction efficiency of approximately 70%. While for qq, qg and gg interactions the vertex reconstruction efficiency is high (80–100%), it is very low for diffractive processes; around 30%, and thus reducing the overall efficiency.

Figure 4.5(b) shows the Δz distributions, between primary and any secondary vertex,

⁴In exclusive vector boson production, no additional particles are produced, except the boson itself. The protons remain intact and escape undetected down the beam pipe. In such a W event, the only detectable track would come from the lepton of the W decay, or from the two leptons in case of exclusive Z production.

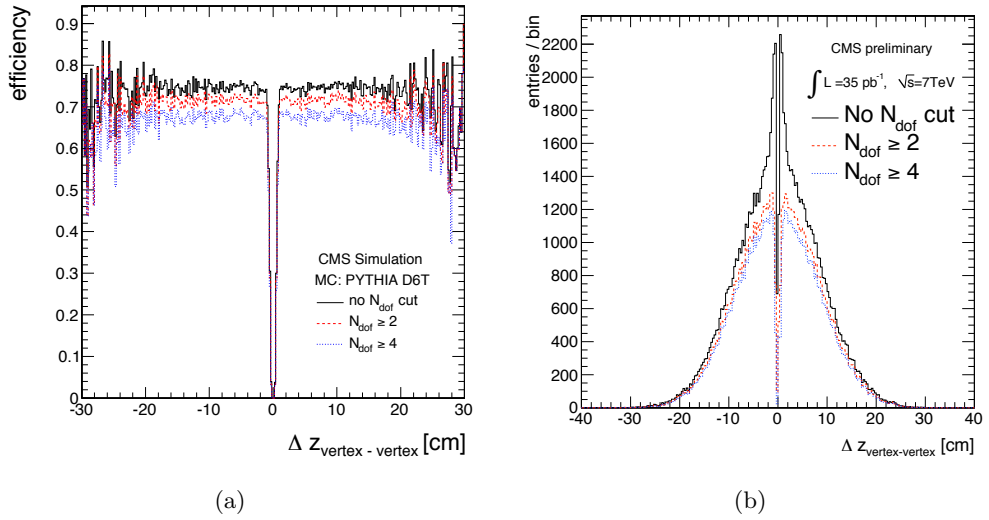


Figure 4.5: (a) The vertex reconstruction efficiency as a function of the distance between two vertices Δz from $W \rightarrow e\nu$ MC. (b) the Δz distribution from data for different N_{dof} cuts.

for the different N_{dof} cuts. The peaking structure at small $|\Delta z|$ is due to fake vertices. In order to keep a high reconstruction efficiency and not veto events with fake vertices, a $N_{dof} \geq 2$ cut, corresponding to more than 2 good tracks used in the vertex fitting, is chosen to define a good quality vertex. In addition, any vertex has to be within $|z| < 24$ cm from the interaction point and have a transverse impact parameter of $d_0 < 2$ cm. The dip at zero distance is due to the limited resolution of the vertex reconstruction. Vertices of a longitudinal separation of less than $\lesssim 1$ mm get merged and are reconstructed as one vertex. See also Section 6.1, where the separation between two vertices is again of some importance.

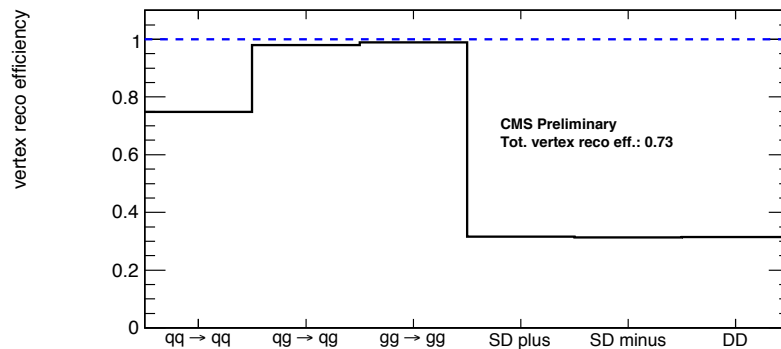


Figure 4.6: The vertex reconstruction efficiency for minimum bias MC (PYTHIA6, D6T tune) for the different types of pp interaction processes.

4.8.6 Forward Energy Deposit

The forward energy deposit is defined as the total energy deposited in one HF calorimeter and will be denoted as $\Sigma E_{HF\pm}$, depending on the z -coordinate. The Σ highlights the fact that the total energy in HF is the sum of individual HF calorimeter towers $\Sigma E_{HF\pm} = \Sigma E_i^{tower}$, above a threshold of $E_i^{tower} > 4$ GeV per tower, which corresponds to a transverse momentum of 0.07–0.4 GeV, depending on η . Figure 4.7 shows the energy of the hardest HF– calorimeter tower in one randomly selected run (i.e. 147757). One can see the “noise” peak at low energy, which is also present in non-crossing (i.e. unpaired) bunches, where no collisions take place, and thus is instrumental, motivating the 4 GeV minimum energy cut.

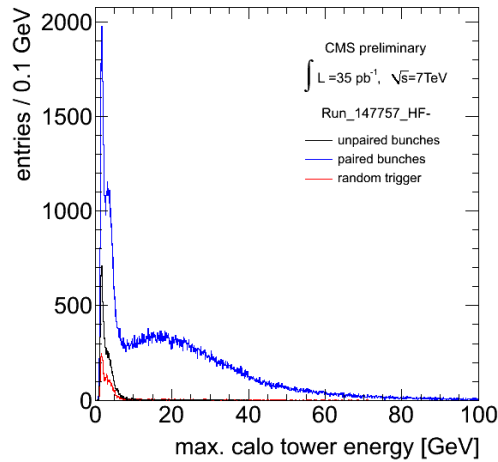


Figure 4.7: Highest HF– calorimeter tower in run 147757.

Consequently, a LRG of about 1.9 units in rapidity can now be defined if no energy is deposited in one side of HF, i.e. $\Sigma E_{HF\pm} = 0$ GeV, which corresponds to no HF calorimeter tower above threshold.

The uncertainty on the calorimeter tower energy is estimated to be $\pm 10\%$ [98]. The impact of the energy scale uncertainty on the forward energy flow is estimated by scaling the minimum energy cut to 3.6 GeV and 4.4 GeV in data and a subsequent re-summation of $\Sigma E_{HF\pm}$. This is the main systematic uncertainty.

4.8.7 Average Instantaneous Luminosity

As already mentioned earlier, in addition to the vector boson production, several simultaneous pp interactions can happen during the same bunch crossing. The number of such pile-up events per bunch crossing depends on the instantaneous luminosity, which is not constant with time. During the 2010 data-taking, the peak luminosity was steadily increasing. Figure 4.8(a) shows the mean average instantaneous luminosity L_{inst}^{avg} per bunch crossing for different runs. In order to separate different running conditions with a different number of expected pile-up events, the full 2010 data is split into three *periods* according to the average instantaneous luminosity. The red dashed horizontal lines in Figure 4.8(a) separates the data into three periods (PI, PII, PIII) of different average instantaneous

luminosity which are summarized in Table 4.2.⁵ Figure 4.8(b) shows the reconstructed

Period	$N_{\text{int.}}^{\text{avg.}}$	$L_{\text{inst.}}^{\text{avg.}} [\mu\text{b}^{-1}\text{s}^{-1}]$
PI	< 1	< 0.17
PII	$1 - 2$	$0.17 - 0.34$
PIII	> 2	> 0.34

Table 4.2: Definition of the three run periods with the corresponding range of average number of pile-up interactions $N_{\text{int.}}^{\text{avg.}}$ and average instantaneous luminosity per bunch crossing $L_{\text{inst.}}^{\text{avg.}}$.

number of vertices for the three different periods. The first period PI, with less than one pile-up event, contains much fewer events than PII and PIII.

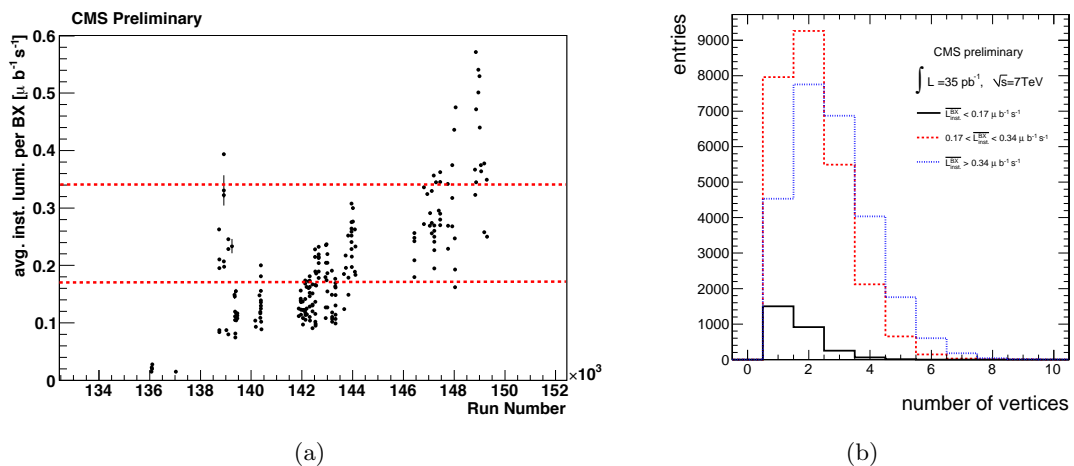


Figure 4.8: (a) The average instantaneous luminosity per bunch crossing for the 2010 data as a function of time (i.e. run number). The red dashed lines define the three periods. (b) The number of reconstructed vertices in $W \rightarrow e\nu$ events for three different periods of average instantaneous luminosity.

The vector boson reconstruction efficiency is independent of $L_{\text{inst.}}^{\text{avg.}}$, but the LRG signature is affected by particles from pile-up which are filling the gap. In order to get a correct MC simulation, pile-up is also simulated in the different MC samples. The MC samples have been generated using some average instantaneous luminosity which is not in agreement with the one in data. With a mean average instantaneous luminosity per bunch crossing of $0.32 \mu\text{b}^{-1}\text{s}^{-1}$ in the 2010 data taking, a minimum bias cross section of 71.5 mb and a revolution frequency of $f = 11.2 \text{ kHz}$, one expects an average of approximately 2 pile-up events. The MC is re-weighted such that the number of generated pile-up events matches a Poissonian distribution with an expected number of approximately 2 pile-up events corresponding to the mean average instantaneous luminosity observed in the data.

⁵Under the assumption that the total pp cross section is about 71.5 mb.

Period	$W \rightarrow e\nu$	$Z \rightarrow ee$
Full 2010 Data	13995 (25.8%)	1749 (25.7%)
PI	1502 (55.0%)	188 (53.0%)
PII	7961 (31.0%)	1018 (31.4%)
PIII	4532 (17.6%)	543 (16.8%)

Table 4.3: Single vertex W and Z event yields for the electron channel for different running periods. The relative fraction of single vertex events is given in brackets.

4.9 W and Z Event Selection

The leptonic (i.e. $\ell^\pm = e^\pm$ or μ^\pm) vector boson decays are studied in this thesis, and the W and Z event selection is based on the presence of leptons.

W Selection: An event is selected as a $W \rightarrow \ell\nu$ event, if the following requirements are fulfilled:

- exactly one isolated lepton, with
 - high transverse momentum, i.e. $p_T > 25$ GeV, and
 - in the central region, i.e. $|\eta| < 1.4$
- missing transverse momentum $\cancel{E}_T > 30$ GeV
- transverse mass $m_T > 60$ GeV.⁶

Figure 4.9 shows the transverse W mass and the electron p_T for $W \rightarrow e\nu$ events after full W selection except the m_T cut itself. The agreement between data and MC is reasonable.

Z Selection: An event is selected as a $Z \rightarrow \ell\ell$ event, if the following requirements are fulfilled:

- exactly two oppositely charged isolated leptons, with
 - high transverse momentum, i.e. $p_T > 25$ GeV, and
 - at least one central (i.e. $|\eta| < 1.4$) lepton,
- reconstructed invariant mass $m_{\ell\ell}$ between 60 and 120 GeV.

Table 4.3 summarizes the numbers of selected single vertex events. As expected, the relative fraction of single vertex events is decreasing with increasing $L_{\text{inst.}}^{\text{avg.}}$, and is independent of the hard scattering process.

⁶The transverse mass is $m_T = \sqrt{2E_T(\nu)E_T(\ell) - 2\vec{p}_T(\nu) \cdot \vec{p}_T(\ell)}$.

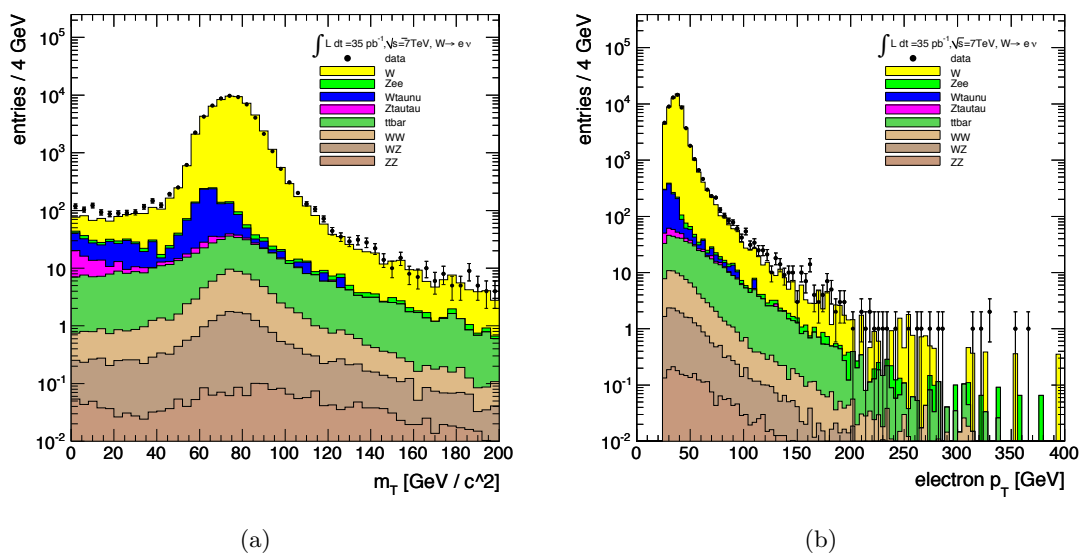


Figure 4.9: The (a) W transverse mass m_T and (b) electron transverse momentum p_T for $W \rightarrow e\nu$ events, after full W selection except the $m_T > 60$ GeV cut and single vertex selection.

Chapter 5

Forward Energy Flow and Central Track Multiplicity in W and Z Events

In the previously defined weak boson samples, a diffractive component can be selected by the presence of a LRG — one HF detector with no reconstructed energy deposit. This LRG emerges from the exchange of vacuum quantum numbers which interrupt the color flow and thus no hadrons are produced. This is expected also to affect the charged particle multiplicity in the central region of the detector. Thus one can also expect a correlation between the forward energy (which is somehow equivalent to the number of particles) and the number of particles in the central detectors.

In order to tag diffractive events with the help of LRGs, first the forward energy flow and the charged particle multiplicity in the central region of the detector, as well as their correlations are discussed in W and Z events. Later, in the last Section, the selection of W(Z) events with an enhanced diffractive component, based on the selection of LRGs is presented.

5.1 Forward Energy Flow

As mentioned in the previous Chapter, a possible diffractive W(Z) component would manifest itself in the presence of W(Z) events with a LRG. This LRG spans from the very forward region (i.e. from the intact proton) up to possibly more central regions. Experimentally, one can define a LRG as the range of pseudorapidity in which no particles are detected and which is preferentially starting as much forward as possible, because the Pomeron is emitted from one of the incoming protons. During the 2010 data taking, the sub-detector with the most forward coverage was the hadronic forward calorimeter (HF); see Section 3.3.2 for a detailed description of it.¹ HF covers the pseudorapidity range of $2.9 < |\eta| < 5.3$.

The average differential energy deposit in HF as a function of η (i.e. one bin in η

¹During 2011, CASTOR can be used which is extending the coverage up to $|\eta| < 8$ on one side of CMS. Later, TOTEM should also be included in the CMS data taking.

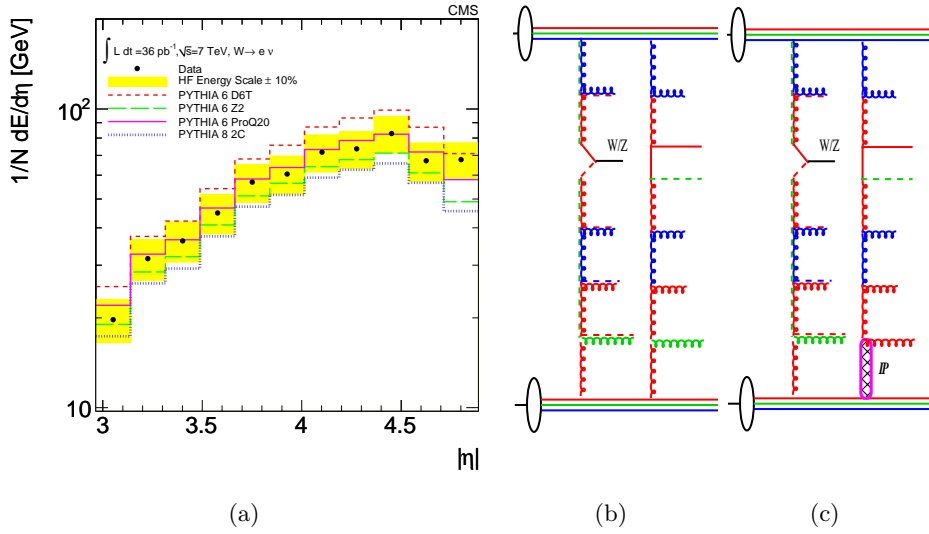


Figure 5.1: (a) Average forward energy deposit in single vertex $W \rightarrow e\nu$ events as a function of η and for different MC tunes. The yellow band indicates the 10% energy scale uncertainty on energy measurements in HF. (b) and (c) Sketches of the process $pp \rightarrow W(Z)X$. The vector boson is produced in the hard interaction (shown as the *left* color connection between the interacting partons) accompanied by multi-parton interactions (shown as the *right* color connection). (b) Shows a non-diffractive multi-parton interaction. (c) Shows a diffractive multi-parton interaction. The colored straight (curly) lines correspond to quarks (gluons) and the black lines to protons and vector bosons. The \mathbb{P} depicts the vacuum quantum number (Pomeron) exchange.

corresponds to one HF ring of $\Delta\eta \approx 0.175$) in single vertex $W \rightarrow e\nu$ events is shown in Figure 5.1(a). The drop in energy for higher rapidity is where the material budget increases due to the beam pipe. The last ring (number 13), covering $4.9 < |\eta| < 5.3$ is not used in this analysis due to its improper implementation in the simulation. The yellow (shaded) band illustrates the main systematic uncertainty due to HF energy scale uncertainty, which was assumed to be 10% during 2010. The simulation events were generated with PYTHIA6 with different tunes: D6T, Z2 and ProQ20, and PYTHIA8 [99] with the 2C tune. The energy flow from PYTHIA6 D6T (Z2 and 2C) is systematically 10–15% higher (lower) than the data. PYTHIA6 with the ProQ20 tune is describing the differential energy flow best.

The total forward energy flow ΣE_{HF} deposited in HF in $W \rightarrow e\nu$ events is shown in Figure 5.2. The observed energies vary from 0 GeV (i.e. no HF calorimeter tower above the 4 GeV threshold) to approximately 2 TeV. Only a few events have an energy deposition above 2 TeV (approximately 0.05%). The data points compare the HF+ and HF–, which are consistent within the energy scale uncertainty.

In Table 5.1, the mean energy deposits in HF+ and HF– per $W \rightarrow \ell\nu$ event, which differs between approximately 3–5% depending on the period, are summarized. Also the average number of calorimeter towers above threshold is listed. The increase in energy and multiplicity is related to the increase of instantaneous luminosity (see Section 5.1.3). The MC energy deposits, summarized in Table 5.2, are completely symmetric by construction,

Period	Mean Energy [GeV]		Average HF Tower Multiplicity	
	HF+	HF-	HF+	HF-
Full 2010 Data	311.8 ± 2.0	300.1 ± 1.9	30.9 ± 0.2	30.0 ± 0.1
PI	298.3 ± 5.9	284.7 ± 5.8	29.2 ± 0.5	28.5 ± 0.5
PII	308.2 ± 2.6	296.6 ± 2.5	30.5 ± 0.2	29.6 ± 0.2
PIII	322.6 ± 3.5	313.6 ± 3.5	32.1 ± 0.2	31.2 ± 0.3

Table 5.1: Mean of the total energy deposit in HF+ and HF- per event and average number of calorimeter tower multiplicities per event for the 2010 data and divided into the three running periods in $W \rightarrow e\nu$ events.

MC Tune	Mean Energy [GeV]	Average HF Tower Multiplicity
D6T	370.8 ± 1.6	35.1 ± 0.1
Z2	269.3 ± 1.4	26.9 ± 0.1
ProQ20	311.5 ± 1.0	29.5 ± 0.1
PYTHIA8 2C	249.4 ± 1.1	24.5 ± 0.1

Table 5.2: Mean of the total energy deposit in HF± per event and average number calorimeter tower multiplicities per event for different MC tunes in $W \rightarrow e\nu$ events.

but show large discrepancies compared to the data (as already observed in Figure 5.1(a)).

The average HF energy deposit in data is around 310 GeV with an r.m.s. of 235 GeV, with an average of approximately 30 HF calorimeter towers above threshold. In MC simulations, PYTHIA6 D6T has a approximately 60 GeV higher average energy, whereas PYTHIA6 Z2 and PYTHIA8 2C predict a similar but significantly too low forward energy flow. PYTHIA6 ProQ20 has on average a correct prediction of the total forward energy in HF.

The observed differences in the forward energy flow between data and MC arise from several sources:

- i)* Different UE models lead to different results and some of them might not describe the data correctly.
- ii)* Experimental effects like noise from beam-gas interactions are missing in the simulation.
- iii)* An imperfect description of pile-up in the simulation can affect the forward energy and/or
- iv)* a soft pile-up contribution which can not be controlled by the additional vertex veto as it is described in Section 4.8.5.

These issues are discussed in the following Subsections.

5.1.1 Underlying Event Modeling

Only one parton per proton takes part in the hard interaction. The remaining spectator quarks undergo multiple interactions which is called the underlying event. A description

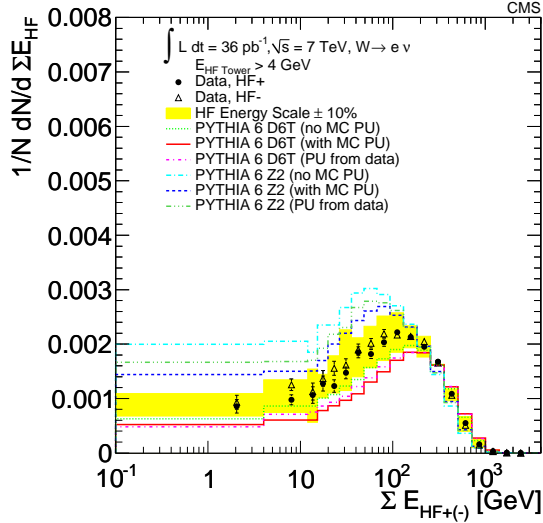


Figure 5.2: Forward energy deposit for HF+ (data points) and HF- (data triangles) in data and MC. Two tunes are shown (PYTHIA6 D6T and Z2) with no pile-up, simulated pile-up and pile-up from data. The yellow band corresponds to the energy scale uncertainty of 10%.

of the UE is given in Section 4.4. The consequence of such an UE event is the increased hadron multiplicity as illustrated in Figure 5.1(b), which will affect the central charged particle multiplicity as well as the forward energy flow.

PYTHIA uses different tunes (or models) to describe the UE. The main differences between these models are the ordering of the MPIs according to their virtuality or the transverse momentum respectively. The “old” PYTHIA6 D6T and the ProQ20 tunes are virtuality-ordered and the “new” PYTHIA6 P0, Pro-PT0, Z2, and the PYTHIA8 2C tunes are p_T -ordered.

Only non-diffractive interactions are taken into account in the UE simulation, and thus there is no diffractive component described by PYTHIA, which may result in observable differences (as illustrated in Figure 5.1(c)).

5.1.2 Experimental and Pile-up effects on the Forward Energy Flow

In order to study effects on the forward energy deposit from pile-up and its accuracy in the simulation, a pile-up contribution obtained from data is added to a MC simulation without pile-up. Figure 5.3 shows the energy distribution per HF calorimeter tower for towers with $\eta < -4$ (i.e. HF-), in *zero bias* events from data. The only event selection requirements are:

- *paired bunches*, i.e. two bunches cross inside CMS and collisions are possible to happen
- *zero bias trigger*, i.e. randomly triggered events
- no reconstructed good vertices

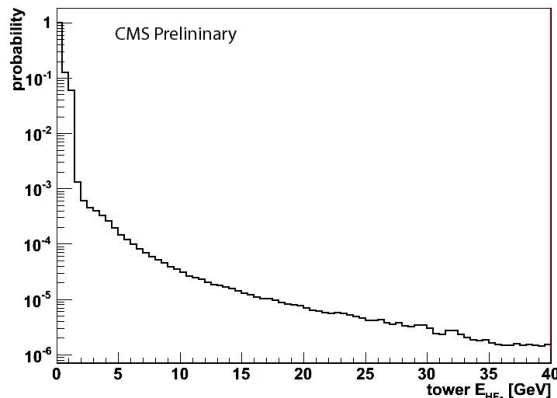


Figure 5.3: Normalized energy per HF calorimeter tower ($\eta < -4$) in data.

Zero vertex events are required because one is interested in the energy contribution from pile-up to single vertex $W(Z)$ events, leading to zero reconstructed vertices from pile-up.

The histogram in Figure 5.3 is normalized to unity and used as a probability density function, according to which in MC, event-by-event a random energy is added to each calorimeter tower. Analogous distributions are used for the full HF coverage in different η bins. A possible ϕ dependence is ignored and the distributions, as the one in Figure 5.3, are averaged over ϕ . Using zero bias events from the full 2010 data taking, experimental effects such as e.g. beam-gas interactions or other LHC machine dependent effects, which are not included in the simulation, are by construction taken into account.

Figure 5.2 shows the total forward energy flow ΣE_{HF} obtained from PYTHIA6 with D6T tune including the simulation of pile-up. It is shifted significantly to higher energies with respect to the distribution obtained from the same generator and tune, but without pile-up. The forward energy flow with the addition of energy from pile-up obtained from data, using the method described above, is also shown and the MC description of the pile-up contribution to the forward energy flow is reasonably well described, as the two histograms are in agreement (i.e. solid red and dashed purple histograms). Only the MC simulation of pile-up will further be used for simplicity.

A second set of three histograms show the same procedure for the Z2 tune. The D6T and Z2 tunes are the most commonly used tunes for simulation with the PYTHIA generator for 2010 data analyses.

5.1.3 Soft Pile-up Contributions

With increasing luminosity the effect of the soft pile-up is expected to increase. In Table 5.1 one can see an increase in the average HF energy (tower multiplicity) of approximately 10 ± 5 GeV (1 ± 0.2) from PI to PII and of 15 ± 5 GeV (2 ± 0.2) from PII to PIII. This increase in forward energy is due to a *soft pile-up* component, which gives only low p_T particles, which either do not enter the tracker acceptance at all or do not give a reconstructed track, and thus are not vetoed by the additional vertex veto.

Similarly as in Section 5.1.2, this soft pile-up contribution can be studied in a single vertex zero bias sample from paired bunches and can be divided into the following three

components:

- i) quasi-elastic pp scattering* where no energy is deposited in either HF,
- ii) soft pp scattering* where some energy can be measured in one of the HFs (i.e. has a LRG) and
- iii) soft-inelastic pp scattering* with measurable energy deposits in both HFs.

Figure 5.4 shows the fraction of zero bias events with energy deposits in one or both HFs as a function of the number of reconstructed vertices and for the different periods. One can see that both fractions increase with increasing average instantaneous luminosity (especially the soft-inelastic part) and thus reduces the quasi-elastic component and increases the forward energy flow in zero vertex events. Table 5.3 summarizes the relative contributions for the individual periods and zero vertices.

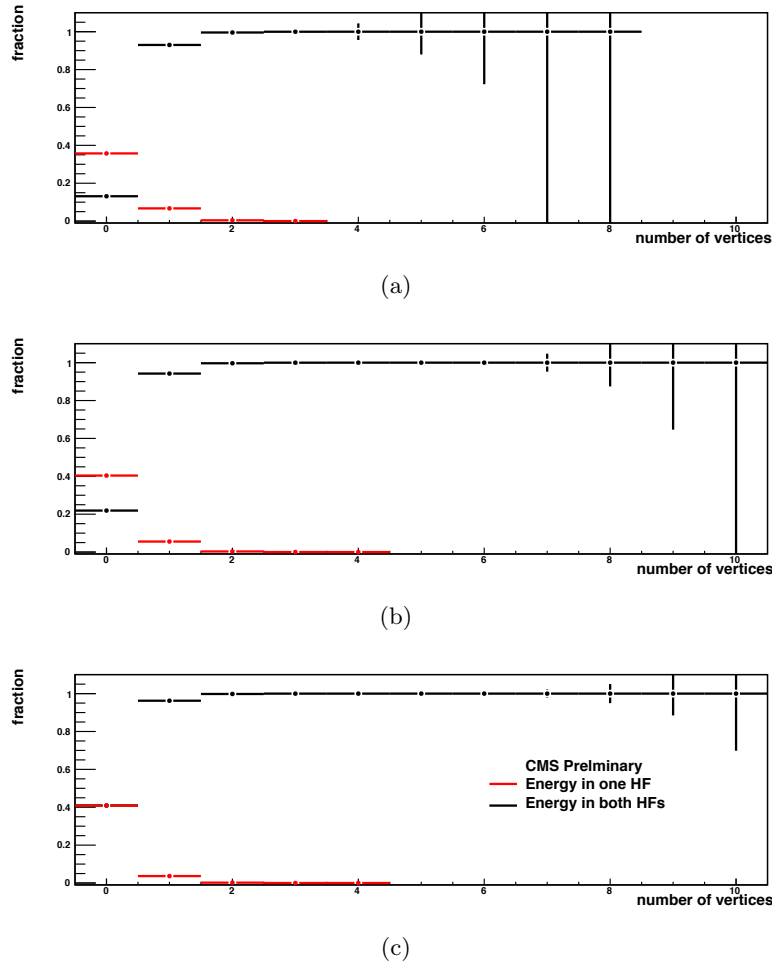


Figure 5.4: Fraction of zero bias events with energy (i.e. at least one HF calorimeter tower above threshold) in one HF (red) and both HFs (black) for (a) PI, (b) PII and (c) PIII as a function of the number of reconstructed vertices.

As consequence of this observation, one can expect that the fraction of vector bosons in association with LRGs are affected by this soft pile-up component.

Process	PI	PII	PIII
quasi-elastic scattering	0.512 ± 0.002	0.377 ± 0.001	0.183 ± 0.001
soft scattering	0.357 ± 0.002	0.404 ± 0.001	0.408 ± 0.001
soft-inelastic scattering	0.131 ± 0.001	0.219 ± 0.001	0.409 ± 0.001

Table 5.3: Relative composition of soft pp interactions in single vertex zero bias events for the three different periods.

5.2 Central Charged Particle Multiplicity

The charged particle multiplicity in the central region of the CMS detector depends, like the forward energy flow, on the UE modeling and its tuning. Like the forward energy deposit, the multiplicity can be verified in data. The central multiplicity is tuned to data using central tracking information and the forward energy flow description is a consequence of this tuning. Thus one can also expect a certain correlation between the central multiplicity and the forward energy flow.

The charged particle multiplicity (i.e. the number of tracks) for $W \rightarrow e\nu$ events is shown in Figure 5.5(a). The minimum track p_T is 1 GeV. The lepton track from the boson decay is not included. PYTHIA8 with 2C tune and PYTHIA6 with Z2 tune give the best charged particle multiplicity description compared to data, even though both predict too many events with very low multiplicity. PYTHIA6 with ProQ20 tune has a too high multiplicity.

Due to the fact that the tuning of the UE modeling depends on the track selection in the data used for tuning, Figure 5.5(b) shows the charged particle multiplicity for the lower minimum track p_T threshold of 0.5 GeV in $W \rightarrow \mu\nu$ events [96]. The PYTHIA8 2C tune has worse agreement with the data, when the minimum track p_T cut is lowered to 0.5 GeV. PYTHIA6 with D6T tune predicts a harder particle momentum spectrum for UE particles and thus a higher multiplicity when applying a 1 GeV threshold. Applying the same thresholds, no difference can be observed in the multiplicity comparing electronic or muonic decays.

5.3 Correlations between Forward Energy Flow and Central Charged Particle Multiplicity

The correlation between the forward energy flow and the central charged particle track multiplicity is measured and compared to different MC simulations. The W sample is divided into three groups depending on their energy deposit in HF–:

- i)* low energy deposit, 20 – 100 GeV,
- ii)* medium energy deposit, 200 – 400 GeV and
- iii)* high energy deposits, > 500 GeV.

The forward energy flow and track multiplicity for the different HF– energy bins are shown in Figure 5.6. In these three energy bins, the forward energy deposit in HF+ as well as

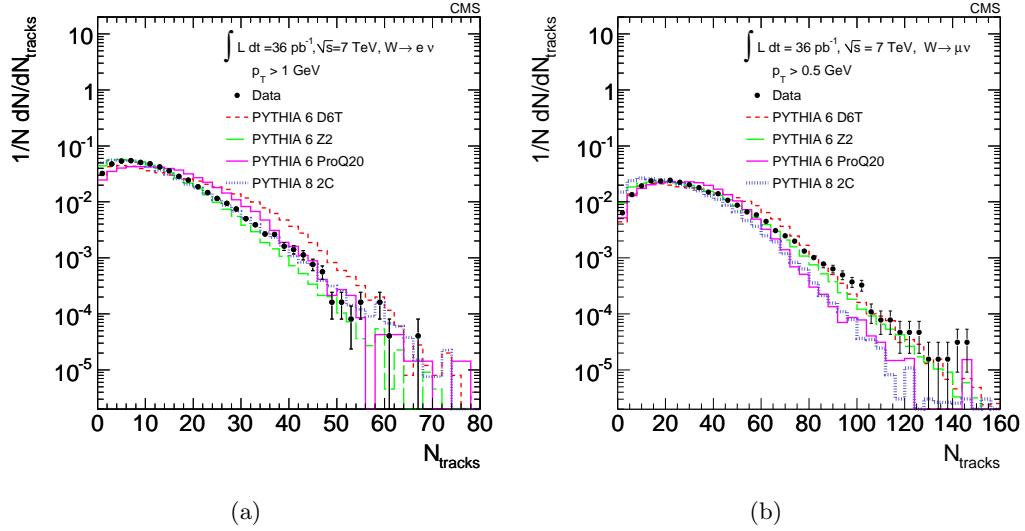


Figure 5.5: (a) Charged particle multiplicity with (a) minimum track $p_T > 1$ GeV (in $W \rightarrow e\nu$ events) and with (b) minimum track $p_T > 0.5$ GeV (in $W \rightarrow \mu\nu$ events).

the central track multiplicity are studied for the different tunes, leading to the following observations in comparison with data:

PYTHIA6 D6T: The PYTHIA6 D6T tune describes the forward energy flow for the low bin quite accurately, but is significantly larger for the higher energy bins. The track multiplicity is too low for the low energy bin and too high for the higher two energy bins. With the lower p_T threshold, the inclusive track multiplicity is reasonably well described [77].

PYTHIA6 Z2: The PYTHIA6 Z2 tune provides a good description of the inclusive charged particle multiplicities, but predicts too many events with very low charged-particle multiplicities. For the HF energy distributions, too many events with low-energy depositions are predicted. The correlations between charged-particle multiplicity and HF energy are well described.

The HF+ energy distribution obtained for the low energy interval is not well modeled, and the MC prediction is significantly lower than the data. However, the correlations are well described for the two higher energy intervals.

PYTHIA6 ProQ20: This tune provides the best description of the HF energy distributions and the charged-particle multiplicities with the $p_T > 0.5$ GeV threshold [77]. The inclusive charged-particle multiplicity for the $p_T > 1.0$ GeV threshold is not well described, though still closer to the data than the D6T tune. In terms of correlations, the central charged-particle multiplicities are reasonably well described. The fraction of events with large multiplicity and a large HF energy deposition is underestimated. Too many events with low-energy depositions in HF+ are predicted for the low energy bin. For the other HF energy bins this tune provides a rather good description of the data.

PYTHIA8 2C: In the inclusive case, this tune predicts too many events with low HF energy depositions, whereas the central charged-particle multiplicity distributions are well described. The HF+ energy distributions for the low and medium energy bins are shifted towards lower values compared to data, whereas for the high-energy bin good agreement is found.

Table 5.4 summarizes qualitatively the abilities of the different tunes to describe the correlations between the forward energy flow and the central charged particles multiplicity. This Table combines all results of the study as they are presented in Ref. [77]. None of the studied MC tunes provides an overall consistent description of the forward energy flow, the inclusive charged particle multiplicity and their correlation simultaneously.

Distribution	Energy bin	D6T	Z2	ProQ20	Pythia 8
Forward Energy Flow	inclusive	X	X	O	X
	low	O	X	—	X
	medium	X	O	—	—
	high	X	—	—	O
Tracks $p_t > 0.5$ GeV	inclusive	—	—	—	X
	low	—	—	O	—
	medium	O	—	—	—
	high	X	—	X	—
Tracks $p_t > 1.0$ GeV	inclusive	X	—	X	O
	low	X	X	X	X
	medium	—	—	X	O
	high	X	O	—	O

Table 5.4: Qualitative summary of the quality of the MC description of the track multiplicity, the forward energy and their correlation (for different minimum p_T cuts) with various tunes. “O” indicates a good agreement, “—” a marginal agreement and “X” a strong disagreement between data and MC.

The main reason for this, is the fact that the different models are mainly tuned according to the central charged particle multiplicity, ignoring the forward energy flow. The observations shown in Figures 5.2, 5.5 and 5.6 as well as the summary from Table 5.4 can be used for a future preparation of new tunes based on LHC data.

5.4 Selection of W Events with a LRG

The minimum and maximum energy deposit on either side in HF are shown Figures 5.7(a) and 5.7(b). Both sides of the detector are combined, reducing the statistical fluctuations and enhancing the disagreement observed in Figure 5.2. W events with a LRG signature cumulate in the first bin. This is equivalent to no HF calorimeter tower above the 4 GeV threshold. The minimum and maximum number of calorimeter towers in HF \pm are shown in Figures 5.7(c) and 5.7(d) respectively. In total 100 $W \rightarrow e\nu$ events are observed with zero reconstructed HF energy depositions (Figure 5.7(c)). Table 5.5 summarizes the vector boson production yields with LRG for different final states and also in the different periods.

Intuitively one could assume the presence of a diffractive vector boson production

Period	$W \rightarrow e\nu$	$Z \rightarrow ee$	$W \rightarrow \mu\nu$	$Z \rightarrow \mu\mu$
Total 2010 data	100 (0.71%)	19 (0.80%)	145 (0.81%)	23(0.79%)
PI	17 (1.13%)	7 (2.7%)	31 (1.61%)	3 (0.91%)
PII	57 (0.72%)	9 (0.59%)	91 (0.86%)	16 (0.93%)
PIII	26 (0.57%)	3 (0.55%)	23 (0.42%)	4 (0.46%)

Table 5.5: Number of leptonically decaying single vertex vector boson events with a LRG. The relative percentage to all selected single vertex vector boson events are given in brackets.

component, and its fraction, by comparing the PYTHIA6 D6T prediction in the first bin of Figure 5.7(a) or 5.7(c). This is the method used for the observation of diffraction in minimum bias events from CMS [100]. But the fact that different MC tunes predict a too large number of LRG events purely from fluctuations in the UE, resulting in no forward energy in one HF, requires a different approach to measure a diffractive component. This is the main topic of the next Chapter.

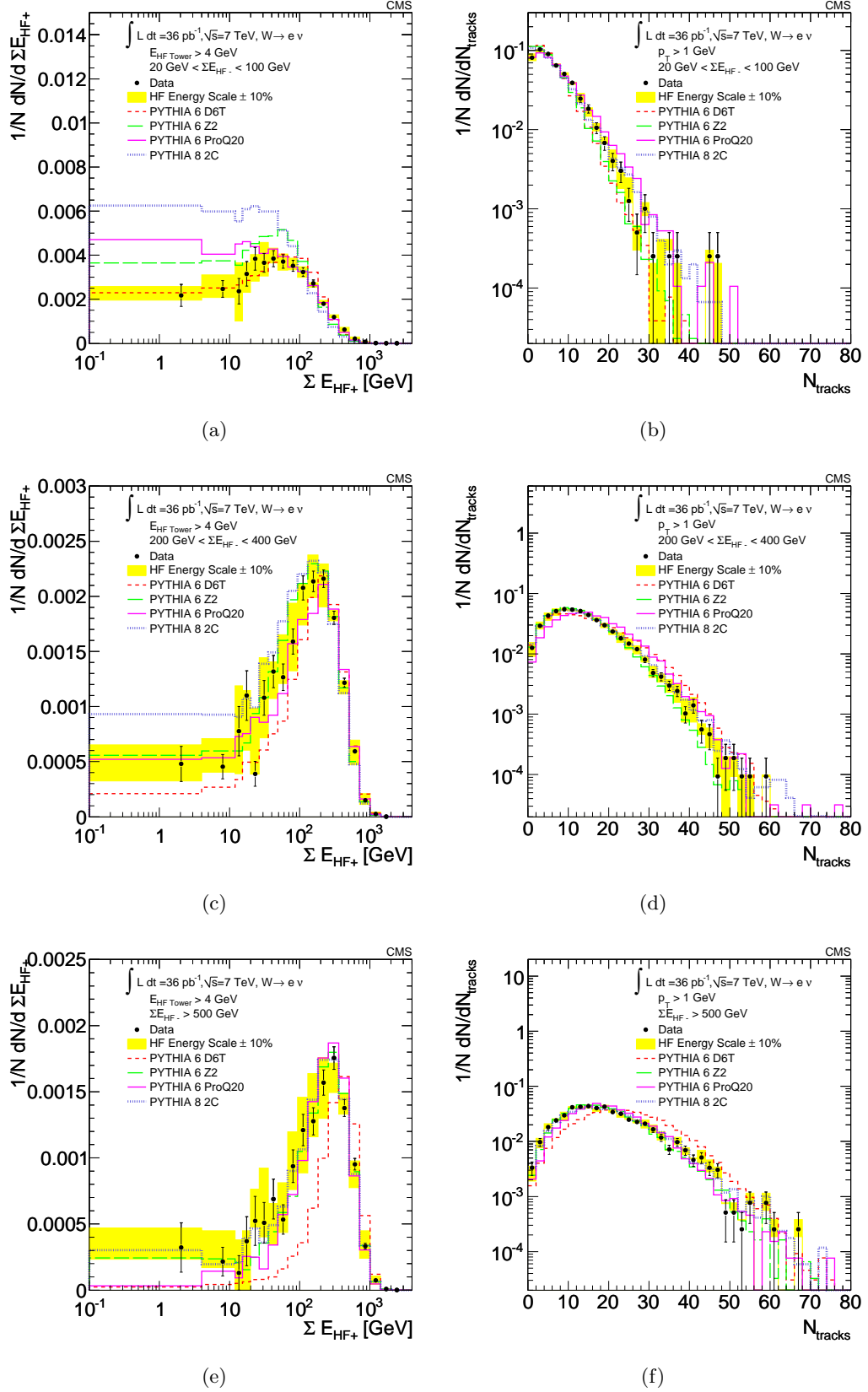


Figure 5.6: The forward energy flow (left column) and the central charged particle multiplicity (right column) for the three energy bins; (a) and (b): low, (c) and (d): medium, (e) and (f): high.

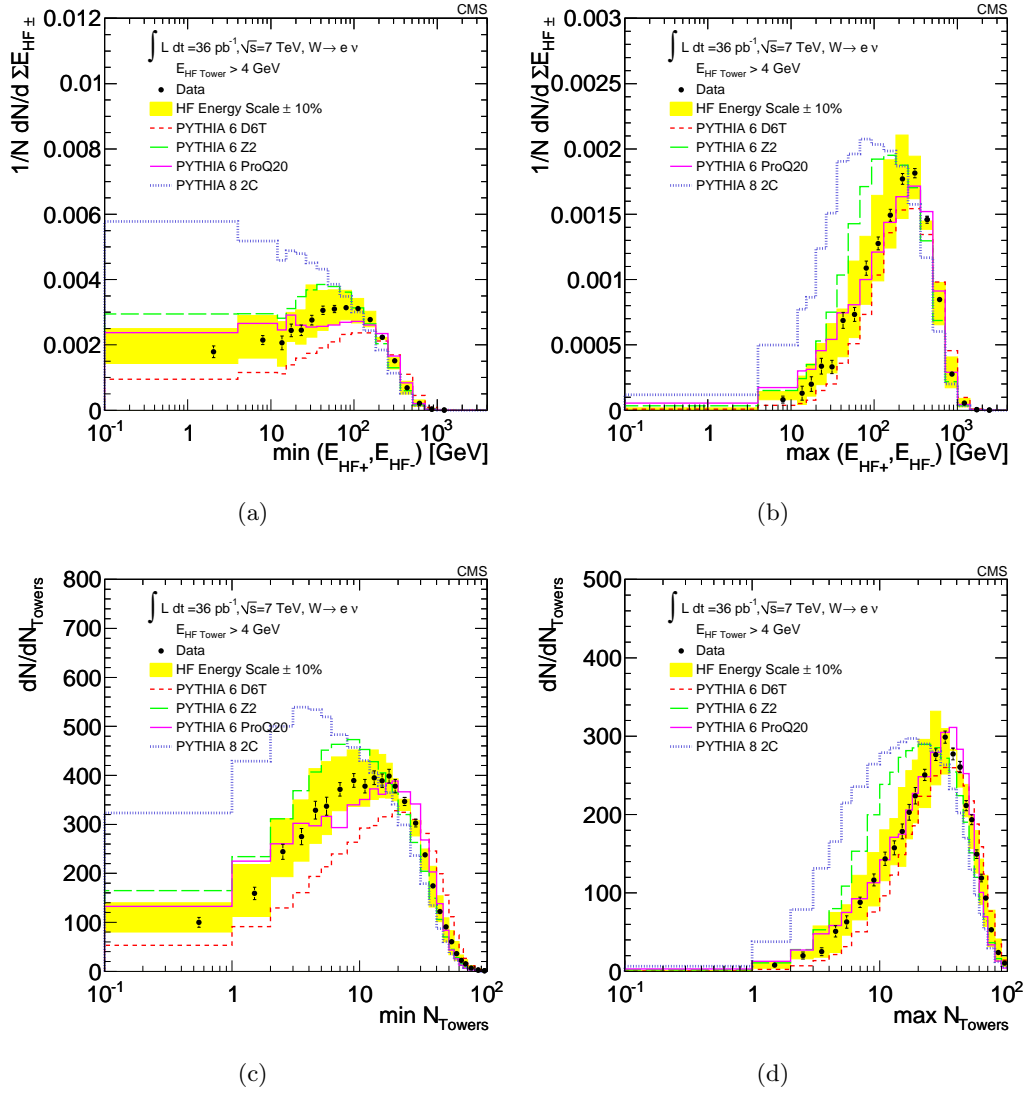


Figure 5.7: The (a) minimum and (b) maximum forward energy deposit $\Sigma E_{HF\pm}$ and the (c) minimum and (d) maximum number of HF calorimeter towers.

Chapter 6

Observation of Diffractive Weak Boson Production

This Chapter presents the analysis of the selected weak boson events having a LRG, which is defined as no reconstructed forward energy in one of the two HF calorimeters, corresponding to a LRG of at least 1.9 units. The goals of this analysis are the observation of diffractive weak boson production and the measurement of the fraction of such diffractive events.

In the first part of this Chapter, the effect of soft pile-up on the fraction of LRG events is discussed and a correction is presented. In a second step, the forward energy flow, the central charged particle multiplicity and the size of the LRGs are discussed in order to get a handle on a diffractive component. In the last Section of this Chapter, the extraction of a diffractive component is presented which leads to the first observation of a diffractive component in weak vector boson production at the LHC.

6.1 LRG Events and Invisible Pile-up Correction

In the 2010 data, 245 W events and 42 Z events with a LRG are selected.¹ One can see in Table 5.5 that the relative fraction of LRG events is decreasing with the three periods of increasing average instantaneous luminosity by a factor of 2–5.

This decrease can again be explained by an “invisible” soft component in the pile-up, as already discussed in Section 5.1.3, which is “filling” the LRG, without having a reconstructed vertex. These events thus migrate from the first bin, with no energy in one HF (i.e. $\Sigma E_{HF\pm} = 0$), in a higher energy bin containing events with a non-zero HF energy deposit, thus reducing the relative fraction of LRG events. Three effects contribute to this

¹Decays into electrons and muons combined.

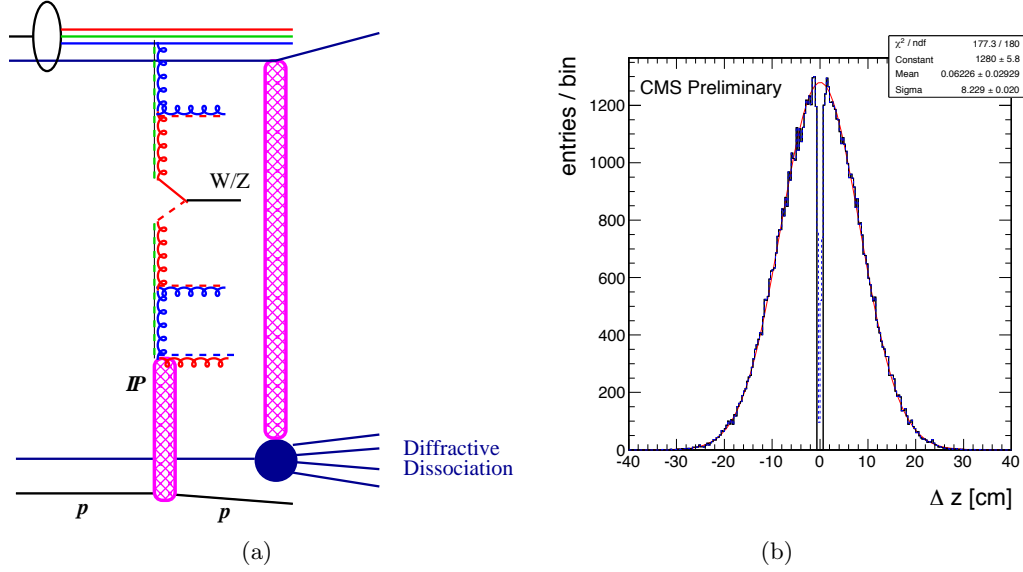


Figure 6.1: (a) Sketch of a primary diffractive pp interaction in which a weak boson is produced, accompanied by a LRG, and a second diffractive pp interaction (pile-up), which is “filling” the LRG and thus destroying the signature. The colored straight (curly) lines correspond to quarks (gluons) and the black lines to protons and vector bosons. The \mathbb{P} depicts the vacuum quantum number (Pomeron) exchange.

	Process	PI	PII	PIII
p_{SD}	single diffractive scattering	0.357 ± 0.002	0.404 ± 0.001	0.408 ± 0.001
$p_{inelastic}$	soft-inelastic scattering	0.131 ± 0.001	0.219 ± 0.001	0.409 ± 0.001

Table 6.1: Fractions of single diffractive and soft-inelastic pp scatterings measured in zero vertex zero bias data.

invisible pile-up:

- i)* A *soft SD pp scattering* component which gives energy deposits in one of the HFs. Such events may fill the LRG if the two energy deposits are on opposite sides of the detector. Figure 6.1(a) shows a sketch of a diffractive pile-up event together with the diffractive $W(Z)$ production.
- ii)* A *soft-inelastic* component which leads to energy deposits in both HFs and thus can fill a LRG.
- iii)* A *non-soft pile-up* component whose vertices are not reconstructed and thus cannot be vetoed.

For the first two effects, the probabilities of soft SD and soft-inelastic pp scatterings to fill the LRG (defined as p_{SD} and $p_{inelastic}$), can be measured in zero vertex, zero bias data the same way as described in Section 5.1.3. The relative fractions of these processes were already shown in Figure 5.4, and are re-summarized for zero vertices in Table 6.1. These fractions correspond to the probability that a LRG in a single vertex boson event gets destroyed. The value of p_{SD} stays approximately constant while the value of $p_{inelastic}$ increases as a function of the average instantaneous luminosity.

ε	0.72		
$\varepsilon_{\text{close}}$	0.033		
f [s ⁻¹]	11245.5		
σ_{pp} [mb]	71.5		
	PI	PII	PIII
L_{inst} [$\mu\text{b}^{-1}\text{s}^{-1}$]	0.13	0.27	0.42
λ	0.84	1.72	2.68
p_{close}	0.015	0.016	0.012
f_{corr}	1.48 ± 0.008	1.78 ± 0.016	2.67 ± 0.043

Table 6.2: Different input parameters and the final correction factors f_{corr} for the three periods. The error includes statistical and systematic uncertainties on the input parameters, except HF energy scale uncertainty.

By measuring p_{SD} and $p_{\text{inelastic}}$ in data, vertex reconstruction inefficiencies for non-soft pile-up events are automatically included, except for inefficiencies due to vertex reconstruction resolution. If two vertices are too close in Δz , i.e. closer than $\lesssim 1$ mm, they get merged and can be reconstructed as one single vertex, resulting in some probability p_{close} that a non-soft pile-up event is filling the LRG. Figure 6.1(b) shows the longitudinal separation Δz of two vertices. Assuming a Gaussian shape for the Δz distribution, the fraction of vertices where Δz is too small to reconstruct both vertices $\varepsilon_{\text{close}}$ is estimated from a fit to the Δz distribution to be $(3.3 \pm 0.3)\%$. With this inefficiency one gets the probability that a LRG gets filled because of closely located vertices as

$$p_{\text{close}} = \varepsilon_{\text{close}} \cdot P(1, \lambda) + 2\varepsilon_{\text{close}} \cdot P(2, \lambda) \cdot (1 - \varepsilon) + \varepsilon_{\text{close}} \cdot P(3, \lambda) \cdot (1 - \varepsilon)^2 + \dots \quad (6.1)$$

where $\varepsilon = 72\%$ is the vertex reconstruction efficiency and $P(n, \lambda)$ is the Poisson probability to have n vertices for an expected number of vertices of λ , which is given by

$$\lambda = \sigma_{\text{pp}} \cdot L_{\text{inst}} \cdot \frac{1}{f}, \quad (6.2)$$

with σ_{pp} the total pp cross section, L_{inst} the average instantaneous luminosity and f the revolution frequency of the beam.

The first term in (6.1) corresponds to one additional vertex which is not reconstructed because it is too close to the primary one. The second term corresponds to 2 additional vertices, where one is not reconstructed and the second one is missed because it too is close, etc. Contributions from 4 vertices and terms proportional to $\varepsilon_{\text{close}}^2$ are neglected.

The final correction factor for the number of events with a LRG is then

$$f_{\text{corr}} = \frac{1}{1 - (p_{\text{inelastic}} + 0.5 \cdot p_{\text{SD}} + p_{\text{close}})}. \quad (6.3)$$

The factor 0.5 comes from the fact that the LRG in single diffractive events can be on either the plus or the minus side.

In Table 6.2 the input parameters used to calculate f_{corr} are summarized and it lists the resulting correction factors for the three different periods.

By applying the correction factors to the LRG event yields, the instantaneous luminosity dependence is reduced and the fraction of LRG events is more stable over time.

Table 6.3 summarizes the corrected relative fraction of weak boson events with LRG. Combining the results from electrons and muons and taking the main systematic uncer-

Period	$W \rightarrow e\nu$ [%]	$Z \rightarrow ee$ [%]
Total 2010 data	$1.37 \pm 0.14(\text{stat.}) \pm 0.06(\text{syst.})$	$1.73 \pm 0.43(\text{stat.}) \pm 0.07(\text{syst.})$
P I	$1.68 \pm 0.41(\text{stat.}) \pm 0.01(\text{syst.})$	$5.52 \pm 2.08(\text{stat.}) \pm 0.04(\text{syst.})$
P II	$1.27 \pm 0.17(\text{stat.}) \pm 0.02(\text{syst.})$	$1.57 \pm 0.52(\text{stat.}) \pm 0.03(\text{syst.})$
P III	$1.53 \pm 0.30(\text{stat.}) \pm 0.07(\text{syst.})$	$1.47 \pm 0.85(\text{stat.}) \pm 0.06(\text{syst.})$

Table 6.3: Corrected relative fraction of weak vector boson events ($W(Z) \rightarrow e\nu(ee)$) with a LRG. Only the systematic error from the invisible pile-up correction is given. The main systematic uncertainty from energy scale uncertainty is approximately 25%.

tainty from HF energy scale uncertainty into account, the relative fraction of W with a LRG signature of at least 1.9 units is

$$1.46 \pm 0.09(\text{stat.}) \pm 0.38(\text{syst.})\%.$$

The relative fraction of Z events with LRGs is

$$1.57 \pm 0.25(\text{stat.}) \pm 0.42(\text{syst.})\%.$$

These fractions from data are different to the ones obtained from the ND MC tunes studied: e.g. for $W \rightarrow e\nu$ with PYHTIA6 D6T: 0.4%, PYTHIA6 Z2: 1.2% and PYTHIA8 2C: 2.3%. This has mainly two reasons: *i*) no diffractive W(Z) production is included in the simulation and *ii*) LRGs can arise from fluctuations in the particle multiplicity in the hard scattering and simultaneously in the UE, which can vary strongly between different tunes. Again one can not distinguish a diffractive component in data.

6.2 Forward Energy Flow and Charged Particle Multiplicity in LRG Events

Similarly to the previous Chapter, the forward energy flow and the track multiplicity in LRG events is studied. Figure 6.2 shows the forward energy deposit (i.e. the HF energy deposit opposite to the gap) and central charged particle multiplicity in W LRG events. Due to statistical limitations decays to electrons and muons are combined. The average forward energy deposit in the HF opposite to the LRG is 150 GeV. Given the low statistics, the different predictions describe the data reasonably well for high $\Sigma E_{HF\pm}$ above ~ 50 GeV. The MC predicts much lower $\Sigma E_{HF\pm}$ opposite to the LRG. One expects a low forward energy deposit opposite to the LRG for ND W production, where the LRG only arises due to fluctuations in the UE. For SD W production, the forward energy deposit opposite to the LRG can also be of high energy. Given the observed relative shift of the data compared to the ND MC, this can be interpreted as a first hint of the presence of a diffractive component, as the diffractive production can result in very high $\Sigma E_{HF\pm}$ opposite to the gap.

In addition, the central charged particle multiplicity ($p_T > 0.5$ GeV for electrons and muons) tends to slightly higher multiplicities in data compared to the MC. In ND W production, the fluctuations in the UE, which are giving the LRG, are expected also to

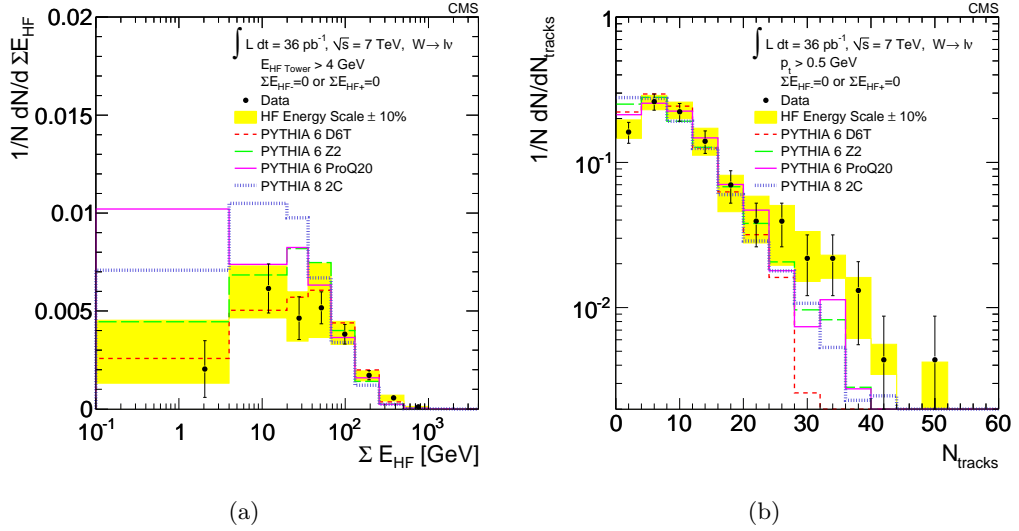


Figure 6.2: (a) Forward energy deposit in the HF opposite to the LRG and (b) central charged particle multiplicity for LRG events. W decays to electrons and muons combined.

have low central multiplicity. In contrast, the SD events can have a larger multiplicity despite the presence of the LRG.

This can be interpreted as a first sign of a diffractive component, because fluctuations in the UE are expected to have low central multiplicity, whereas SD events can have a larger multiplicity despite the presence of the LRG.

Figure 6.2(b) also shows hints for a diffractive component in the UE. This leads to a higher track multiplicity in the central region, while the two LRGs, one from the boson production and one from the UE, overlap and thus preserve the LRG.

Thus, the shift to lower energy opposite to the LRG and the lower central charged particle multiplicity in MC indicate the presence of a diffractive W production component and/or a diffractive component in the MPI, but are by far not significant enough to draw a solid conclusion.

6.3 Size of the LRG

The diffractive W component can be enhanced by requiring a larger LRG extending more into the central region of the detector as one can conclude from Figure 4.4(b). The size of the LRG is measured using particle flow (PF) candidates with the following minimal cut requirements:

- $E_{\text{cand.}}^{\text{PF}} > 1.5 \text{ GeV}$ if $|\eta| < 1.5$
- $E_{\text{cand.}}^{\text{PF}} > 2 \text{ GeV}$ if $1.5 < |\eta| < 2.85$
- $E_{\text{cand.}}^{\text{PF}} > 4 \text{ GeV}$ if $|\eta| > 2.85$
- $p_{T, \text{cand.}}^{\text{PF}} > 0.5 \text{ GeV}$ if charged

The PF candidate with the largest η_{max} (smallest η_{min}) is the most forward particle in HF+ (HF-) and defines thus the size of the LRG. To select the most forward particle in the event one can define $\tilde{\eta} = \min(\eta_{max}, -\eta_{min})$. The minimal LRG size is thus defined by the detector acceptance as $\Delta\eta_{LRG}^{HF} = 4.9 - \tilde{\eta}$, where 4.9 is the maximal η coverage of the HF.² Figure 6.3(a) shows the $\tilde{\eta}$ distribution in data and MC. The fraction of events with LRG decreases rapidly with increasing gap size. An excess of events at $\tilde{\eta} < 3$ is observed in data compared to PYTHIA6 D6T, but not for the other tunes (PYTHIA 6 Z2, ProQ20, PYTHIA8 2C). The systematic uncertainty on the energy scale of the PF candidates was estimated to be around 10%. By applying a scaling of 10%, the uncertainty due to energy scale is of the order of the statistical uncertainty.

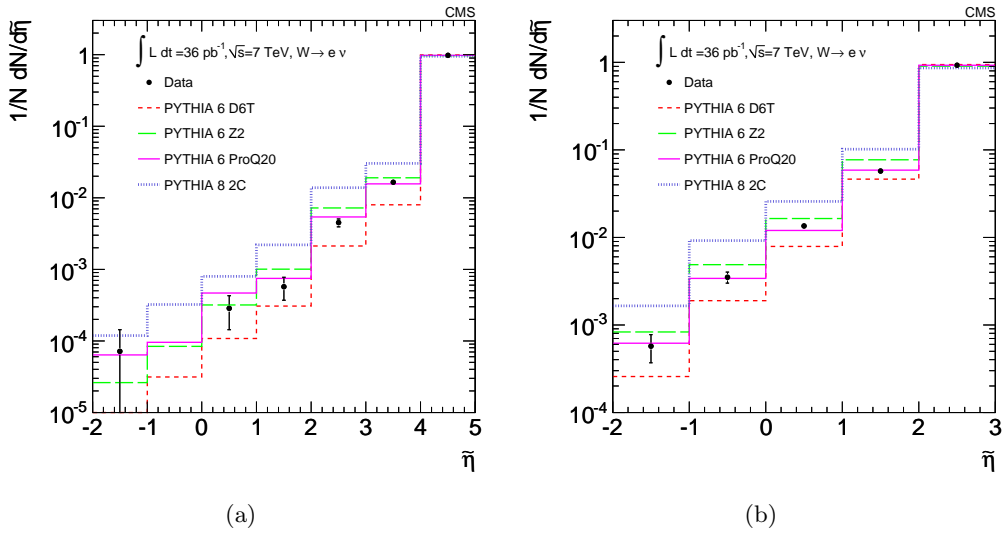


Figure 6.3: The $\tilde{\eta}$ distribution for $W \rightarrow e\nu$ events. (a) Including HF and (b) without HF.

If $\tilde{\eta} < 0$, all PF candidates in the event are contained in one hemisphere leaving the other one “empty”. One $W \rightarrow e\nu$ event with an empty hemisphere is found in data. The MC simulation predicts different values, depending on the tune: 0.8 for PYTHIA 6 D6T, 3.5 for PYTHIA 6 Z2 and 2.2 for PYTHIA 6 ProQ20.

As discussed in Section 6.1, a certain fraction of events include soft pile-up where the vertex cannot be reconstructed and remains in the LRG selection. These events are not increasing significantly the overall central particle multiplicity (otherwise this would lead to a reconstructed vertex). Thus one can define the size of the LRG by using only the central detector as $\Delta\eta_{LRG}^{central} = 2.85 - \tilde{\eta}$, where 2.85 is the maximal η coverage of the central detectors (i.e. up to EE). The number of LRG events in this detector region, when ignoring the information from the HF sub detector, should mainly depend on the amount of very low MPI activity and thus on the number of low multiplicity events. The $\tilde{\eta}$ distribution without HF is shown in Figure 6.3(b). The data shows an excess compared to PYTHIA6 D6T for low $\tilde{\eta}$; corresponding to LRG size of ≈ 1.85 . The fraction of such events is reasonably described by PYTHIA6 D6T and PYTHIA6 ProQ20, while PYTHIA8 2C predicts too large a fraction.

²This gives only the minimal size of the LRG, because one does not have any information of more forward particles, which could limit the size of the LRG.

No conclusion about the existence of a diffractive component in weak vector boson production can be drawn from the measurement of $\Delta\eta$.

6.4 Hemisphere Correlations in LRG Events

No evidence for a diffractive W production can be found in any of the studied distributions so far. Only a slight indication is found in the shifts of the forward energy deposit and central track multiplicities in LRG events (see Section 6.2).

The observation of a diffractive component in minimum bias events [100] is possible due to the clear diffractive peak in the $\Sigma E_{HF\pm}$ distribution and its comparison to SD and ND MC predictions. The $\Sigma E_{HF\pm}$ distributions from W production do not show such a clear diffractive peak. In addition, the different MC tunes give very different results, which can not be used to distinguish a SD and a ND component. Thus one has to follow an alternative way to find a discriminating variable which allows a separation between SD and ND weak boson production.

One possibility is to exploit the kinematical properties of diffractive production. Figure 6.4(a) shows an example of a standard parton PDF and a diffractive PDF. The dPDF has on average a smaller fractional momentum x than the standard parton PDF. In an interaction as shown in Figure 4.4(a), a low x parton inside the Pomeron interacts with a higher x parton from the incoming proton and the final state gets boosted in the direction of the parton with higher x . In the case of diffractive W production, the boson is expected to be boosted in the direction opposite to the LRG.

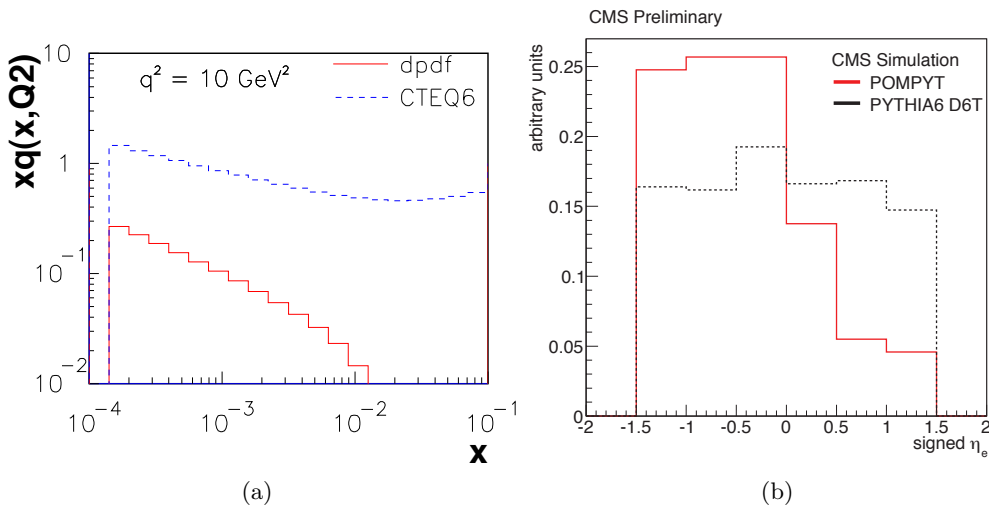


Figure 6.4: (a) Standard (dashed blue) and diffractive (solid red) parton distribution function. The cutoff at low x is artificial. (b) Signed lepton pseudorapidity (signed η_ℓ) in $W \rightarrow e\nu$ events with a LRG as it is obtained from purely diffractive MC (POMPYPY) and non-diffractive MC (PYTHIA6 D6T).

The signed lepton pseudorapidity η_ℓ in W events with a LRG, obtained from MC for purely SD and purely ND W production is shown in Figure 6.4(b). The signed η_ℓ is defined

as

$$\text{signed } \eta_\ell = \eta_\ell \cdot \text{sgn}(\text{LRG}), \quad (6.4)$$

where $\text{sgn}(\text{LRG})$ is +1 (−1) if the LRG is on the +(−) side of the detector. Thus, the sign of signed η_ℓ is defined to be positive (negative) if the LRG and the reconstructed lepton are in the same (opposite) hemisphere of the CMS detector. As expected, the SD W production shows a strong tendency that the reconstructed lepton is in the opposite hemisphere than the LRG. For the ND MC signed η_ℓ is flat.

In $W \rightarrow \ell\nu$ events (where $\ell = e, \mu$ combined) from data, see Figure 6.5, one can again see a strong asymmetry in this variable: 147 W events with the charged lepton and the LRG in different hemispheres and 96 with the charged lepton and the LRG in the same hemisphere.

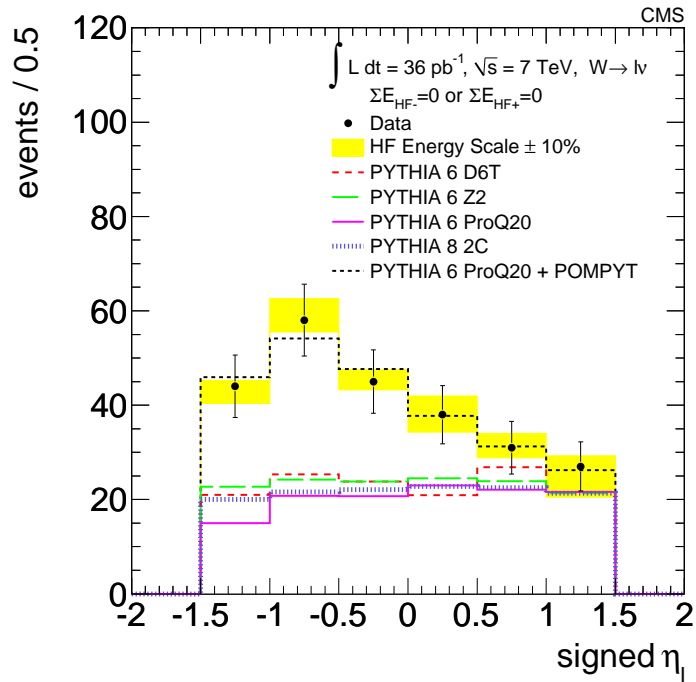


Figure 6.5: Signed lepton pseudorapidity η_ℓ in $W \rightarrow \ell\nu$ events with a LRG from data (data points) and MC (histograms). The colored histograms show the ND component only, the black dashed histogram shows the combined SD and ND MC as it is obtained from the fit.

Defining an asymmetry $A = \frac{N_{\text{opposite}} - N_{\text{same}}}{N_{\text{opposite}} + N_{\text{same}}}$, where N_{same} (N_{opposite}) is the number of events with signed $\eta_\ell > 0$ (signed $\eta_\ell < 0$). The different values are summarized in Table 6.4. The statistical errors are rather large due to the very low statistics after LRG event selection, even in MC.

Assuming that the data can be described as a “mixture” of SD and ND processes, the relative fraction of the two components can be estimated by a binned maximum likelihood template fit. The templates (Figure 6.4(b)) are taken from SD MC and the ND MC with the relative fraction as the free parameter. The black dashed histogram in Figure 6.5 corresponds to a mixture of SD and ND MC according to the fit result using PYTHIA6

	Asymmetry [%]
Data	-21.0 ± 6.4
PYTHIA6 D6T	0.4 ± 3.3
PYTHIA6 Z2	3.7 ± 2.5
PYTHIA6 ProQ20	6.9 ∓ 5.7
PYTHIA8 2C	6.1 ∓ 2.3
SD MC	-47.7 ± 10.8

Table 6.4: Asymmetry values and statistical errors for the data and the MC in %.

ProQ20. The fraction of SD W events in the LRG sample, as obtained from the fit, is

$$50.0 \pm 9.3(\text{stat.}) \pm 5.2(\text{syst.})\%$$

for electrons and muons combined. For simplicity, only the non-diffractive components for the different tunes are shown in Figure 6.5, but similar results are obtained for all studied tunes. The observed significance of the data compared to the purely non-diffractive hypothesis, including the statistical and systematic uncertainties, the uncertainties from the fit and for all bins, as well as for muons and electrons combined, is approximately 5.6σ . The p-value, which is the probability that the non-diffractive hypothesis fluctuates in a way that it describes the observed data, is $1.07 \cdot 10^{-8}$.

Figure 6.6 shows the signed η_ℓ in $W \rightarrow e\nu$ for events without LRG. Instead of requiring zero energy in one HF, events are selected according to the minimum energy to be within 20–100 GeV (Figure 6.6(a)) or 200–400 GeV (Figure 6.6(b)). In the low energy bin, a small (not significant) residual asymmetry of $(-3.5 \pm 1.1)\%$ persists. With increasing energy, the correlation weakens to $(-2.7 \pm 1.0)\%$ in the medium energy bin to $(0.9 \pm 2.3)\%$ for events with more than 500 GeV in one HF (plot not shown). The residual asymmetry could be explained by diffractively produced W events in which the LRG signature is destroyed by multi-parton interaction or invisible pile-up, and is supporting the strong evidence for the observation of a diffractive weak boson production component.

6.5 Diffractive W Boson Production

In Section 6.1 the corrected fraction of W events to have a LRG signature is found to be around 1.5%. One can assume that the LRG signature gets destroyed with the same probability by soft invisible pile-up, independent if it arises from SD W production or from ND W production accompanied by fluctuations. Thus the relative composition of the total LRG sample is not affected. This leads to the conclusion that the SD component in W production is 50% as obtained from the fit, independent of the instantaneous luminosity.

This gives a final fraction of diffractively produced W bosons of $(0.73 \pm 0.34)\%$ at the LHC, which is compatible with the observed fraction of $(1.0 \pm 0.11)\%$ at the Tevatron.

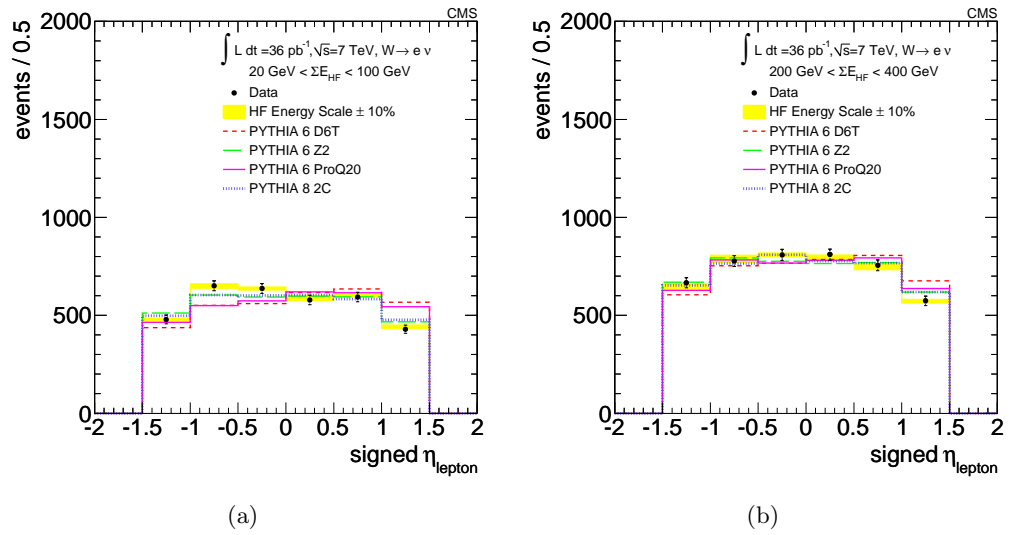


Figure 6.6: Signed lepton pseudorapidity η_{ℓ} in $W \rightarrow \nu$ events without LRG. (a) shows η_{ℓ} for events with low HF energy of 20–100 GeV and (b) for events with medium HF energy of 200–400 GeV.

Part III

Standard Model Higgs Boson Search

The Standard Model of particle physics predicts, as a consequence of spontaneous symmetry breaking which leads to massive W and Z bosons, the existence of a neutral scalar particle — the Higgs boson. In Part III of this thesis, the search for the Standard Model Higgs boson is presented in the fully leptonic final state of the $H \rightarrow WW$ decay channel.

After an introduction in Chapter 7, which discusses the possible Higgs production modes and summarizes the expected experimental signatures which are expected to be observed, Chapter 8 discusses different Monte Carlo simulations used in the analysis. The study of the simulation of the gluon-fusion Higgs production mode was performed to achieve a better understanding of the Higgs signal modeling. Differential weights in order to re-weight the Higgs transverse momentum spectrum in simulated events to the most up-to-date theoretical prediction (at NNLO) are derived.

In the following chapters (Chapters 9-11), the Higgs boson search strategies and the results using 2011 data are presented. Chapter 9 gives an overview of the different methods used in the analysis and discusses the event selection. In Chapter 10, the different sources of systematic uncertainties are discussed which enter the upper limit calculation on the Higgs production cross section. This study was done in the context of the limit calculation using a statistical method which is based on the information from the shapes of the distributions of discriminating variables which are obtained using multivariate techniques. The limit calculation, based on the CL_S method, is discussed in Chapter 11 where also the results are presented.

A study of the SM Higgs boson production in the gluon-fusion process with the application of a jet veto is presented in Chapter 12. This topic will again become more important future precision measurements of e.g. the Higgs decay branching fractions.

Chapter 7

Higgs Production and the $H \rightarrow WW \rightarrow \ell\nu\ell\nu$ Signature

Electroweak symmetry breaking predicts, as a consequence of spontaneous symmetry breaking which leads to massive W and Z bosons, the existence of a neutral scalar particle — the Higgs boson. The discovery, or exclusion of the Higgs boson is one of the main physics goals of the LHC project. Most of the Higgs bosons properties are predicted by the theory, except its mass, which allows to assess the existence of such a particle experimentally. In order to do so, this Chapter gives a summary of the different Higgs production mechanisms and their relative contributions to the total Higgs cross section as well as the different decay modes of the Higgs boson. The cross section times branching ratios of the experimentally accessible decay modes are discussed in more details. At the end of this Chapter, a summary of the $H \rightarrow WW \rightarrow \ell\nu\ell\nu$ signature which can be observed with the CMS experiment, in case the Higgs exists, is given.

7.1 The Standard Model Higgs Boson at the LHC

As discussed in Chapter 1, the Higgs boson coupling to fermions and vector bosons is proportional to the mass of the fermions and proportional to the square of the mass of the bosons. Thus the Higgs boson couples predominantly to heavy particles such as to W and Z bosons or top quarks and, much less of course, to bottom quarks. The Higgs cross sections and branching ratios are thus fully determined by the particles masses. Due to the fact that the heavy quark PDFs in the proton are small, the direct contribution via heavy sea quarks to the total Higgs production cross section remains small and can be neglected for all practical purposes.

The four main Higgs production mechanisms, at a pp collider like the LHC, in the

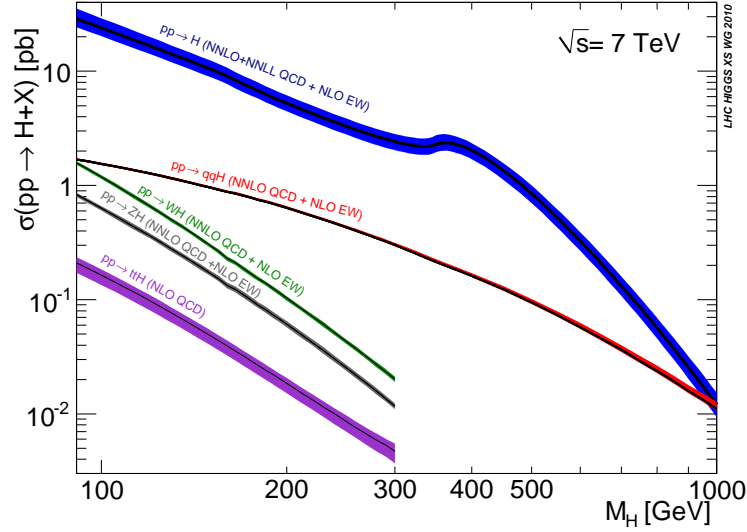


Figure 7.1: The theoretical SM Higgs boson production cross sections for different processes as a function of the Higgs mass at $\sqrt{s} = 7$ TeV pp collisions. The labels on the curves indicate the type of higher order radiative QCD corrections that are taken into account. Plot taken from [101].

order of their contribution to the total cross section, are:

- Gluon-fusion
- Vector-boson-fusion
- Associated production
- Higgs-strahlung

The individual production cross sections, at the center of mass energy of 7 TeV, for these channels are summarized in Figure 7.1.

7.1.1 Higgs Production Mechanisms

Gluon-Fusion: $gg \rightarrow H$

The coupling to an incoming gluon pair is induced by a heavy (mainly top) quark loop, i.e. the Higgs boson does not couple directly to the massless gluons. The corresponding Feynman diagram is shown in Figure 7.2(a). Due to the large gluon PDF in the proton (see Figure 1.4), this is the main Higgs production process for the LHC.

Vector-Boson-Fusion: $q\bar{q} \rightarrow q\bar{q}H$

In the vector-boson-fusion (VBF) process, the Higgs boson couples, at leading order, to a vector boson linking two quark lines, see Figure 7.2(b), which shows the leading order

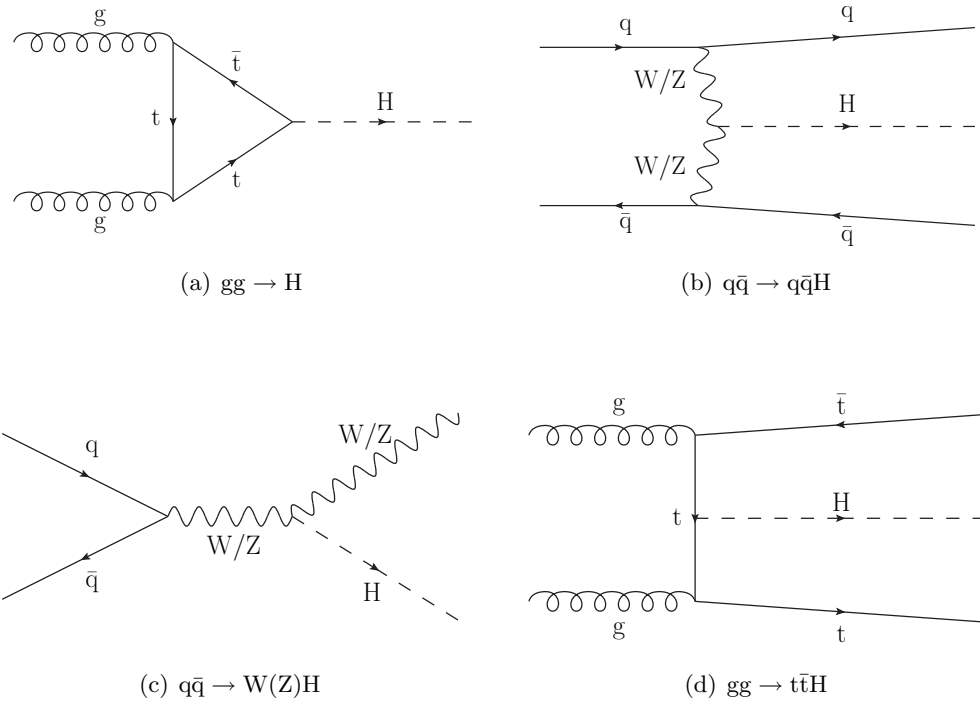


Figure 7.2: Feynman diagrams of the main Higgs production mechanisms at the LHC.

Feynman diagram. The outgoing quarks result in two forward-backward jets with a large separation in pseudorapidity. This large central pseudorapidity gap gives a rather strong handle to suppress the backgrounds to this process. The VBF cross section is, up to a Higgs mass of approximately 500 GeV, around 10 times smaller than the gluon-fusion cross section.

Associated Production: $q\bar{q} \rightarrow W(Z)H$

Also called Higgs-strahlung due to the fact that the Higgs boson is radiated off a vector boson. See Figure 7.2(c) for the leading order Feynman diagram. At very low Higgs masses, i.e. around 100 GeV associated production with vector bosons has a similar cross section as VBF production, but decreases rapidly at higher masses and e.g. for 300 GeV, it is around 10 times smaller than the one via VBF, and thus not relevant for high mass Higgs searches at the LHC. Higgs-strahlung was the main production mechanism searched for at the LEP collider.

Associated Production: $q\bar{q}/gg \rightarrow t\bar{t}H$

In this process, the Higgs gets radiated off a top quark (see Figure 7.2(d)). This process contributes only a small fraction to the total cross section.

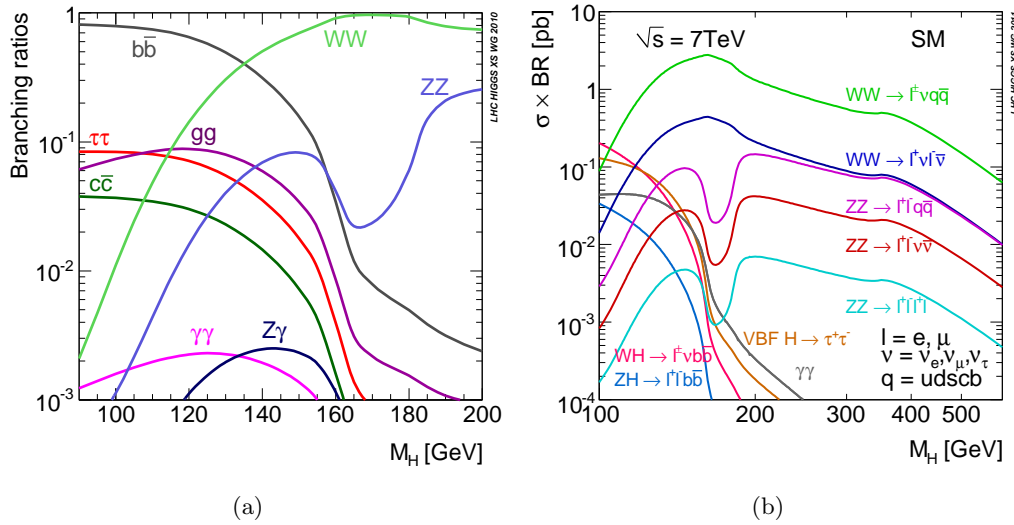


Figure 7.3: (a) The theoretical SM Higgs boson branching ratios as a function of the Higgs mass. (b) The SM Higgs boson cross section times branching ratio as a function of the Higgs mass. Both plots taken from [101].

7.1.2 Higgs Decay Modes

The different Higgs decay modes with their corresponding branching ratios are summarized in Figure 7.3(a).

For low Higgs masses, i.e. around 100 GeV, the main decay mode is $H \rightarrow b\bar{b}$. Its branching ratio is decreasing with increasing mass, whereas the decay to a W pair is becoming dominant. At the Higgs mass of 160 to 180 GeV, the $H \rightarrow WW$ branching ratio is close to 1. For high Higgs mass, the decay into Z pairs has a significant contribution. Decays to gluon pairs or light massive particles as taus or charm quarks only play a role for masses which are smaller than 150 GeV. Despite its rather small branching ratio, the $H \rightarrow \gamma\gamma$ has a very clear experimental signature of two high p_T and isolated photons, and is a very crucial channel for a discovery of a *light*, around 120-140 GeV, Higgs boson.

To experimentally detect a potential Higgs boson in one of the mentioned channels, the relevant parameter is not only the production cross section but rather the product of the cross section with the branching ratio ($\sigma \times \text{BR}$) of the decay channel of interest; this quantity is shown in Figure 7.3(b). This branching ratio is further divided into the individual decay channels of the Higgs decay products which ultimately will be detected with the help of a detector.

Due to the high hadronic jet background cross section in pp collisions, the cleaner leptonic final states such as $H \rightarrow WW \rightarrow \ell\nu\ell\nu$ or $H \rightarrow ZZ \rightarrow 4\ell$ are preferred over hadronic final states. The $H \rightarrow ZZ \rightarrow 4\ell$ and the $H \rightarrow \gamma\gamma$ channels give a narrow mass resonance which is relatively straight forward to detect. The mass of the Higgs boson in the $H \rightarrow WW$ channel can not be reconstructed directly due to the escaping neutrinos. This fact also affects the precision of the Higgs boson mass that can be inferred with the $H \rightarrow WW$ channel, and it can be expected to be around 20-30 GeV for a Higgs mass of 100-150 GeV, compared to the resolution of the di-photon channel which is of the order of 1 GeV.

As the $H \rightarrow WW$ mass resolution is not very good, the large $\sigma \times \text{BR}$ compensates for this, and it is thus the most sensitive search channel in the *intermediate mass range* of 140-180 GeV. [102]

A detailed summary of Higgs production cross sections, decay modes and the most up-to-date theoretical calculations can be found in Ref. [101], which is intended to unify as well as document the theoretical assumptions and give recommendations for the numbers to be used by the experimental community at the LHC.

7.2 The $H \rightarrow WW \rightarrow \ell\nu\ell\nu$ Signature

The gluon-fusion channel is the most dominant SM Higgs production mechanism at the LHC. In the mass range from 160 to 190 GeV, the $H \rightarrow WW$ channel has the largest branching fraction, making it the most sensitive channel in this intermediate mass range.

The W s, from the $H \rightarrow WW$ decay, decay further into charged-lepton-neutrino pairs ($\text{BR} = 10.8 \pm 0.09\%$ [2]) or jets ($\text{BR} = 67.6 \pm 0.27\%$ [2]). The leptonic final state gives an experimentally cleaner signature, of an oppositely charged, high transverse momentum lepton pair, compared to hadronic final states. $W \rightarrow \tau\nu_\tau$ decays have the same signature, if the τ decays leptonically, plus an additional τ -neutrino. The neutrinos in the final state escape any detection and are experimentally manifest in the form of missing transverse momentum, further called missing transverse energy \cancel{E}_T .

Consequently, the most basic and most promising signature to identify a Higgs decay via this channel, consists of:

- two oppositely charged leptons, and
- large missing transverse energy.

But other processes, often with much higher production cross sections, exist, which have the same or a very similar final state signature and thus “mimic” Higgs events. Such processes are further called *backgrounds*. See Table 7.1, which lists some backgrounds and compares their cross sections to the signal cross sections for different mass hypotheses.

The main background process is the $q\bar{q} \rightarrow WW \rightarrow \ell\nu\ell\nu$ continuum which has basically the same signature as the signal process, from which it is thus especially difficult to distinguish. WW production is a *irreducible* background. The $q\bar{q}/gg \rightarrow t\bar{t} \rightarrow WWb\bar{b}$ has also a similar signature in the case the two b -jets are not reconstructed. W +jets production leads to one prompt lepton and \cancel{E}_T , and a second lepton arises from a misidentified jet. Drell-Yan processes give two isolated, high p_T leptons, and the missing energy results from not reconstructed jets.

In the following Section, the rejection of these backgrounds is discussed.

7.2.1 Signal Event Selection and Background Rejection

The basic strategy consists of selecting events containing two high p_T leptons with opposite charge coming from the WW decays with large \cancel{E}_T from the escaping neutrinos.

Process (pp \rightarrow)	$\sigma \times \text{BR}$ [pb]	Remarks
$\text{WW} \rightarrow \ell\nu\ell\nu$	4.9	irreducible, i.e. exactly the same signature
$t\bar{t} \rightarrow \text{WW}b\bar{b} \rightarrow \ell\nu\ell\nu + 2\text{Jets}$	17.1	missed b-jets
$\text{W} + \text{jets} \rightarrow \ell\nu + \text{Jets}$	31314	fake leptons from jets
$\text{Z}/\gamma^* \rightarrow \ell\ell$	14956	fake \cancel{E}_T from badly reconstructed jets
$\text{H} \rightarrow \ell\nu\ell\nu$ ($m_H = 120$ GeV)	2.3	-
$\text{H} \rightarrow \ell\nu\ell\nu$ ($m_H = 160$ GeV)	8.2	-
$\text{H} \rightarrow \ell\nu\ell\nu$ ($m_H = 200$ GeV)	3.9	-

Table 7.1: The main backgrounds to the $\text{H} \rightarrow \text{WW} \rightarrow \ell\nu\ell\nu$ channel. In the lower part of the table, the Higgs production cross sections for three different mass hypotheses are given for comparison. The values for the cross sections (σ) and branching ratios (BR) are taken from [103] and [101].

Contributions from Drell-Yan are by construction rejected by the requirement of large \cancel{E}_T . In addition Drell-Yan contributions can be reduced by vetoing events with an invariant mass close to the Z mass and by requiring that the two leptons are not exactly back-to-back.

The $t\bar{t}$ background is best rejected by the selection of events with no (or only one) central high p_T jet(s), as there are two b-jets in top-pair events from b-quark decays. A $t\bar{t}$ contribution in the zero- or one-jet bin can be removed by vetoing any event containing a b-jet.

W+jets can be controlled by applying a high purity lepton identification and a tight lepton isolation. This is especially important for electrons which are more likely to be “faked” by a mis-reconstructed jet than muons.

A signal extraction from the by orders of magnitude larger WW-continuum background was only conceivable after the study presented in Ref. [104], where for the first time the spin correlations and the more central production of the WW system from the signal, compared to the WW continuum, was studied and efficient cuts against the WW background were proposed:

Spin Correlations: The SM Higgs boson has spin 0 and the W bosons have spin 1. Due to angular momentum conservation, the spin of the W^+ and W^- have to be anti-correlated. In the further decay of the W bosons, the right-handed $\bar{\nu}_{\ell^+}$ (left-handed ν_{ℓ^-}) has to be preferentially emitted in the same (opposite) direction of the W^+ (W^-) spin. Consequently, the right-handed ℓ^- (left-handed ℓ^+) has the same (opposite) direction of the W^+ (W^-) spin. This results in the two charged leptons having preferentially the same direction. This can be experimentally observed as a small azimuthal opening angle between the two final state charged leptons in the transverse plane for the signal. For the WW background, the initial state is not polarized, and thus the angular preference between the two charged leptons is different — even tending to larger opening angles for WW production. See Figure 7.4(a) for an illustration of this fact.

Centrality of the WW-System: The WW-system from gluon-fusion Higgs production has a smaller boost (i.e. is more central) than the predominantly $q\bar{q}$ -produced system from

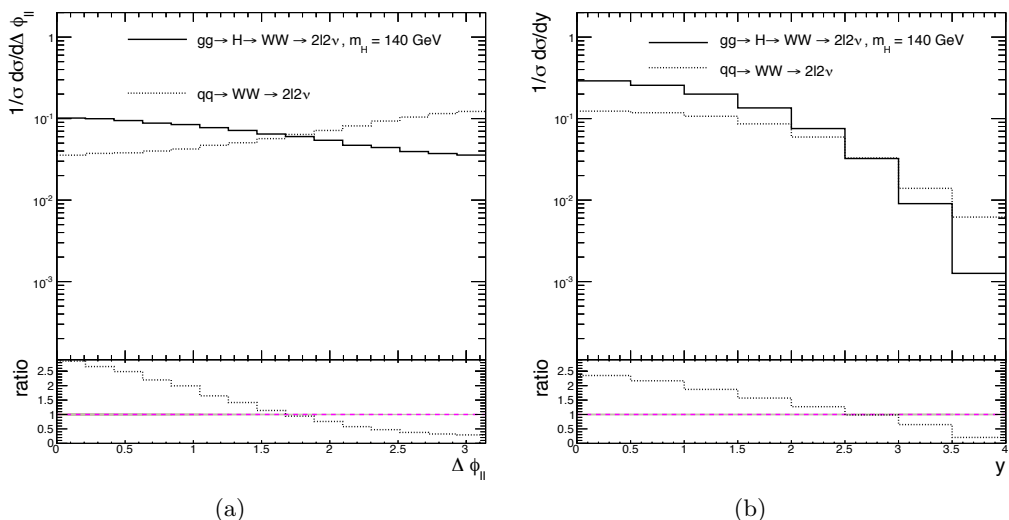


Figure 7.4: (a) Azimuthal opening angle $\Delta\phi_{\ell\ell}$ between the two charged leptons; for a $m_H = 140$ GeV gluon-fusion Higgs signal (solid line) and the WW continuum background (dashed line). (b) Rapidity distribution for the W^- from the Higgs signal (solid line) and the WW continuum (dashed line).

the WW continuum. This is a consequence from the larger momentum imbalance between the valence- and sea-quark, compared to the two interacting gluons (see also Figure 1.4). Figure 7.4(b) shows the rapidity distribution of the W^- from the signal and from the WW continuum. Figure 7.5(a) shows the lepton pseudorapidity, which shows consequently the same trend.

Other variables which can be exploited to distinguish a signal from the backgrounds are:

- the transverse m_T^H Higgs mass, which can not be larger than the hypothetical Higgs mass for the signal, or
- the transverse momenta of the leptons, which are also Higgs mass dependent. Figure 7.5(b) shows the leading charged lepton transverse momentum.

The above criteria give a first qualitative description of the Higgs signal selection and background rejection strategy, which can be used in order to increase the ratio of signal over background. The exact event selection will be discussed in more details in Section 9.

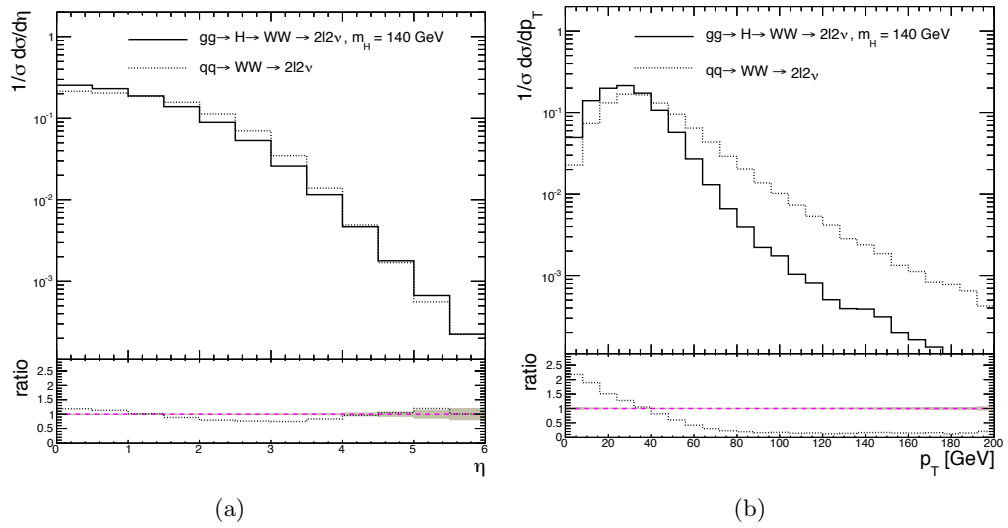


Figure 7.5: The leading charged lepton (a) pseudorapidity and (b) transverse momentum.

Chapter 8

Monte Carlo Simulation of the Gluon-Fusion Higgs Production

Simulations of high energy physics processes are an indispensable tool to understand the underlying signature, plan the required analysis strategy in great details and predict the discovery potential of an experiment. In addition, it is the only feasible way to compare the theory predictions with measured data in an efficient way by generating large samples of realistically simulated events with the help of Monte Carlo (MC) generators.¹ These simulated events can then be analyzed in the same way as the measured data and can be directly compared to it.

In the first part of this Section the basic concepts of Monte Carlo simulations are briefly mentioned. In the second part, different event generators (POWHEG and MC@NLO) are studied and compared for the gluon-fusion Higgs production.

8.1 Event Generators

Mainly two ways of addressing higher order QCD effects in a cross section calculation for a MC simulation exist:

Fixed order MC generators include all Feynman diagrams up to a fixed order of α_s , which can lead to very complicated calculations. This gives a precise description of the hard jets (or partons) in an event up to the considered order, but fails to describe the internal jet structure.

Parton shower MC generators simulate the event in its entirety taking also non-perturbative effects into account and give a hadronic final state which can be interfaced with a detector simulation (see Section 3.7.5) and compared directly to data.

In the case of a parton shower MC, the event generation can be split into the following

¹The term Monte Carlo is often used to refer to event generators because they use Monte Carlo integration techniques.

steps:

- i)* generation of the hard process using (N)LO matrix elements and PDFs,
- ii)* showering of primary partons to produce final state partons, which then
- iii)* get hadronized.

8.1.1 The Hard Process

The generation of the hard process makes use of the calculation of the partonic scattering cross section as described in Section 1.4.3. Together with the PDFs (see Section 1.4.2), the pp interaction cross section of the hard process can be calculated.

Depending on the order which is used in the calculation (i.e. LO, NLO,...) this gives a certain number of primary final state partons. These partons can undergo parton showering and get hadronized into observable final states of hadrons.

8.1.2 Parton Shower and Hadronization

The incoming partons as well as the final state partons which are involved in a scattering can radiate virtual gluons. This is true for any colored particle, in a similar way as an accelerated charged particle is emitting photons via Bremsstrahlung. These secondary gluons, which carry also color charge, can further radiate gluons or produce quark-antiquark pairs. This repeating process is leading to a *parton shower*, which is evolving down to an energy scale of ~ 1 GeV per particle. These showers compensate for the missing higher order QCD corrections in the matrix element calculation.

The formation of hadrons out of these final state partons, emerging from the hard scattering and the subsequent showering, is a non-perturbative process; i.e. the coupling is large because the energy of the individual partons from the shower is small. Due to the absence of analytical calculations the hadronization is based on phenomenological models.

Two important models exist: the *string model* which is implemented in PYTHIA and the *cluster model* used in HERWIG.²

String model: One can imagine a separating $q\bar{q}$ -pair to be connected by a color string which gets stretched as the partons move apart. The potential energy between the partons is increasing linearly and due to the confinement at large distances (~ 1 fm) the string breaks under creation of an additional $q\bar{q}$ -pair (given the energy stored inside the string is large enough to produce the quark pair, otherwise the splitting stops). At the end of this string splitting, the partons are combined into color neutral hadronic final states.

²PYTHIA and HERWIG are two general purpose MC event generators which will be discussed later in more detail.

Cluster model: In the cluster model, after the parton shower, all “final” state gluons are further decayed into $q\bar{q}$ -pairs. The quarks then form clusters of $q\bar{q}$ -pairs which later are decayed into hadrons.

Ref. [79] gives a very complete overview of MC generators.

8.2 Comparison of Different Event Generators

As discussed in Chapter 7, gluon-fusion is the main Higgs production mechanism. In order to provide an accurate simulation of any process, the production cross section has to be known at a high precision. For example in a leading order (LO) calculation, where no additional particles are produced besides the Higgs boson itself, the Higgs transverse momentum p_T^H would be zero. To get a more realistic description, higher order (e.g. NLO or NNLO) calculations have been performed from different groups giving more precise results.

Thanks to the developments during the last few years, such NLO parton shower MC generators have become the state-of-the-art simulation tools, especially for the Higgs signal production at the LHC.

Different such generators exist and give different results. While the matrix element calculation is in principle unique, the main differences occur due to different approaches used in the implementation of the parton shower and hadronization models which are used and additional parameter tuning.

The goal of this section is an estimation of the theoretical uncertainties by comparing two different NLO parton shower generators. The studied generators are POWHEG [105–107] and MC@NLO [108]. For the parton shower and the hadronization step, POWHEG is interfaced with PYTHIA [79] and MC@NLO with HERWIG [109, 110].

There are several sources of uncertainties affecting a result from a NLO parton shower MC and the following items will be studied in this Section:

- factorization and renormalization scale dependence
- parton shower and hadronization models
- underlying event structure
- parton distribution functions
- parameter tuning

All plots in this Section are at particle level and no detector simulation has been applied.

8.2.1 The Higgs Transverse Momentum Spectrum

The rest frame of the Higgs boson is fully defined by three variables: the transverse momentum p_T , the pseudorapidity η and the azimuthal angle ϕ . Higgs production is

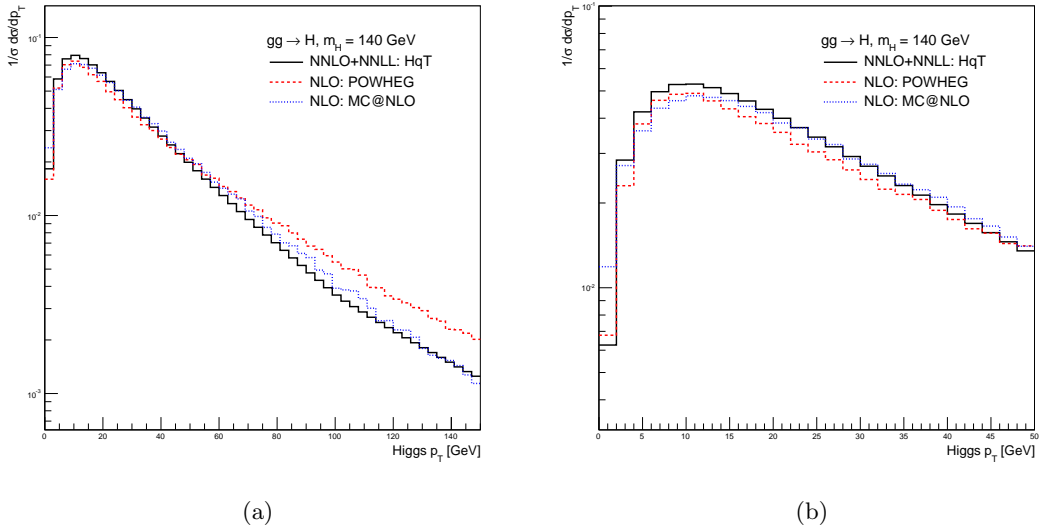


Figure 8.1: Higgs transverse momentum as obtained with POWHEG and MC@NLO compared to the NNLO+NNLL prediction from HqT. The Higgs boson mass is $m_H = 140$ GeV. The plot on the right side shows a zoom into the low p_T region.

symmetric in ϕ , thus only p_T and η affect the kinematical distributions of the Higgs decay products.

The Higgs p_T spectrum generated by POWHEG and MC@NLO in comparison to the most detailed theoretical calculation available so far at NNLO+NNLL (NNLL: next-to-next-to-leading logarithm), which was performed using HqT [111–113], is shown in Figure 8.1. The PDF set used for POWHEG and MC@NLO is CTEQ6m (NLO) and MSTW2008 (NNLO) for HqT. It can be seen that both, POWHEG and MC@NLO, have a harder p_T spectrum than the NNLO+NNLL prediction. The difference is most visible in the high p_T region. Due to the fact that the analysis is not very sensitive to high p_T Higgs, the low p_T region is of more importance and still shows sizable differences, see Figure 8.1(b).

It is important to get a realistic prediction of the Higgs transverse momentum, because most kinematical variables of detectable final states are directly correlated to the p_T of the Higgs. Any slight difference will result in a modified acceptance and influence the result. In order to illustrate this, Figure 8.2 shows a comparison of different variables on generator level obtained from POWHEG and MC@NLO respectively.

8.2.2 Re-weighting to NNLO+NNLL

It has become a standard procedure to re-weight the LO or NLO Higgs p_T spectrum to the NNLO+NNLL spectrum using differential K-factors. The method was described in Ref. [114] and the ideas will be summarized briefly here.

The number N of observed events at a given integrated luminosity \mathcal{L} depends on the

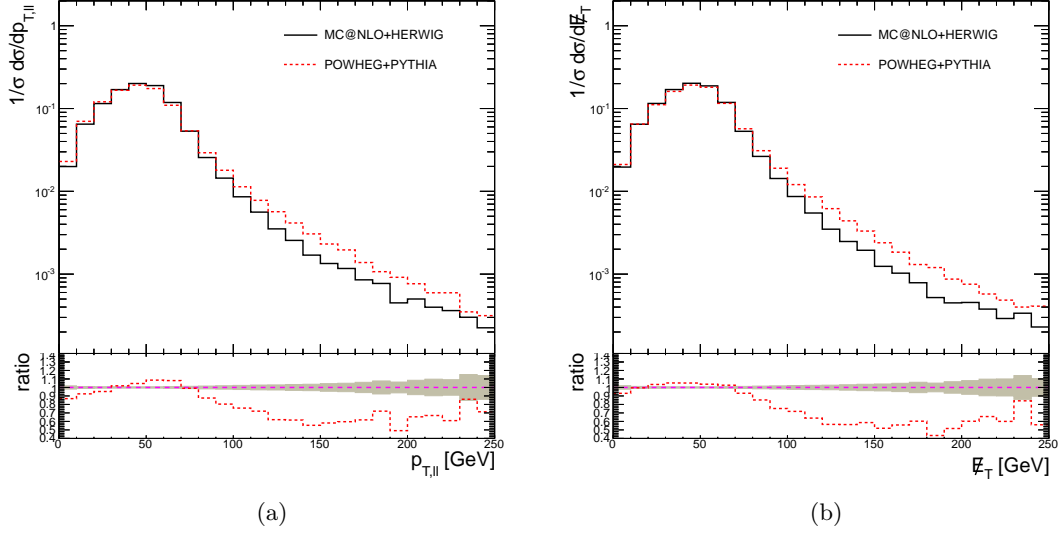


Figure 8.2: The transverse momentum of the di-lepton system (left) and the missing transverse energy (right) obtained by MC@NLO (solid black) and POWHEG (red dotted). The \cancel{E}_T is the p_T of the two escaping neutrinos. The gray area corresponds to the statistical uncertainty.

NNLO cross section σ_{NNLO} :

$$N = \sigma_{NNLO} \cdot \mathcal{L} = K_{incl.} \cdot \sigma_{NLO} \cdot \mathcal{L}. \quad (8.1)$$

In terms of the NLO cross section σ_{NLO} one gets an inclusive K-factor $K_{incl.}$, which is the ratio of the NNLO and the NLO cross section, $K = \frac{\sigma_{NNLO}}{\sigma_{NLO}}$.

Due to the missing higher order QCD corrections at NLO, the inclusive gluon-fusion Higgs production cross section is smaller by a factor $K_{incl.}$. In addition, the Higgs p_T spectrum (or the jet p_T spectrum) is not described correctly compared to the one obtained from higher order calculations. If now a e.g. jet veto is applied, one needs to take into account these higher orders of corrections.

This can be achieved by applying a differential K-factor which is correcting the differential NLO cross section to the differential NNLO cross section. These K-factors are defined as

$$K(p_T) = \frac{\left(\frac{d\sigma_{NNLO}(p_T)}{dp_T}\right)}{\left(\frac{d\sigma_{NLO}(p_T)}{dp_T}\right)}. \quad (8.2)$$

To factorize the correction of the shape of the p_T spectrum and the correction of the inclusive cross section one can write

$$K'(p_T) = \frac{\sigma_{NLO}}{\sigma_{NNLO}} \frac{\left(\frac{d\sigma_{NNLO}(p_T)}{dp_T}\right)}{\left(\frac{d\sigma_{NLO}(p_T)}{dp_T}\right)} = \frac{1}{K_{incl.}} \frac{\left(\frac{d\sigma_{NNLO}(p_T)}{dp_T}\right)}{\left(\frac{d\sigma_{NLO}(p_T)}{dp_T}\right)}. \quad (8.3)$$

Figure 8.3(a) shows the differential K-factor K' as a function of p_T for a Higgs mass of 118 GeV.³ The K-factors are obtained by the division of the NNLO+NNLL Higgs p_T

³In principle, the K-factor can be defined as a function of other kinematical variables. e.g. for η the improvement is expected to be small due to the already reasonable agreement.

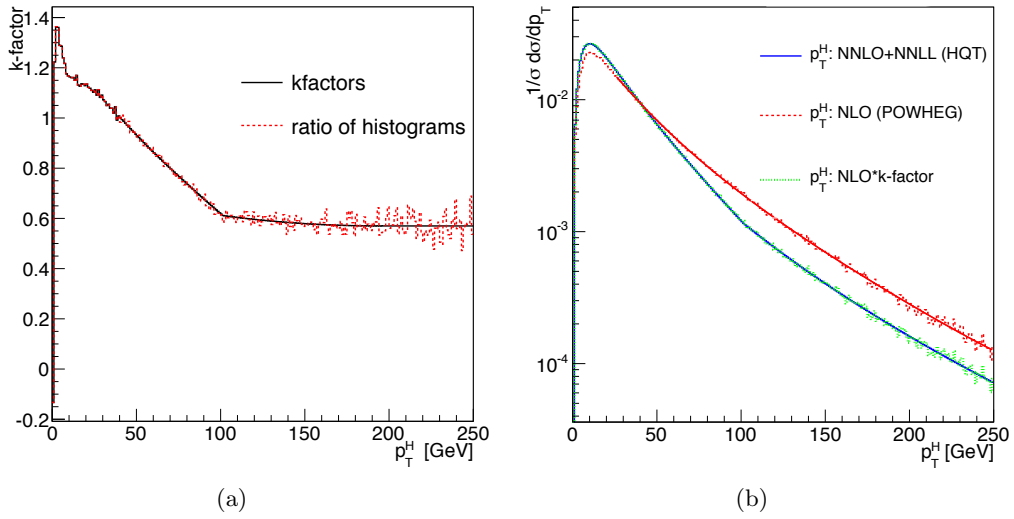


Figure 8.3: Differential K-factors for a Higgs mass of 118 GeV. The black line shows the actual K-factors (using a fit in the high p_T region), the red dotted line the ratio of the NNLO+NNLL and NLO (obtained with POWHEG) Higgs p_T spectra. On the right side, the input p_T spectra and the fit (red solid line) are shown as well as the re-weighted spectrum.

spectrum by the NLO p_T spectrum. In order to avoid large statistical fluctuations in the tails of the p_T spectrum, the high p_T region of the NLO spectrum is fitted, using a function of the form

$$a_0 \frac{1}{x} + a_1 \frac{1}{x^2} + a_2 \frac{1}{x^3} + a_3 \frac{1}{x^4} + a_4 \frac{1}{x^5} + \dots \quad (8.4)$$

The exact form of the fit function, as well as starting and end points of the fit and starting point of the division with the fit are Higgs mass dependent. The shape of the fit is then used for the K-factor calculation. For the very high $p_T \geq m_H$ region the K-factor is set to a constant value.

These K-factors can now be used to re-weight (i.e. to apply an event-by-event weight) the NLO Higgs p_T spectrum to the NNLO+NNLL spectrum, leading to a more precise simulation. This affects also the kinematic distributions of the Higgs decay products. Figure 8.4 shows the same variables as in Figure 8.2 but after re-weighting. As expected the two distributions now agree better, illustrating the importance of having a precise description of the Higgs transverse momentum. Compared to Figure 8.2, the statistical uncertainty is larger above 150 GeV, which is due to the migration of events from the high p_T (\cancel{E}_T) to lower values.

8.2.3 Jet distributions

Depending on the analysis, the jet transverse momentum spectra and jet multiplicities play a vital role; as for example in the $H \rightarrow WW$ analysis, where the events are separated into different jet bins to suppress e.g. the $t\bar{t}$ background.

Jets are complicated objects and their definition is not unambiguous, as they are

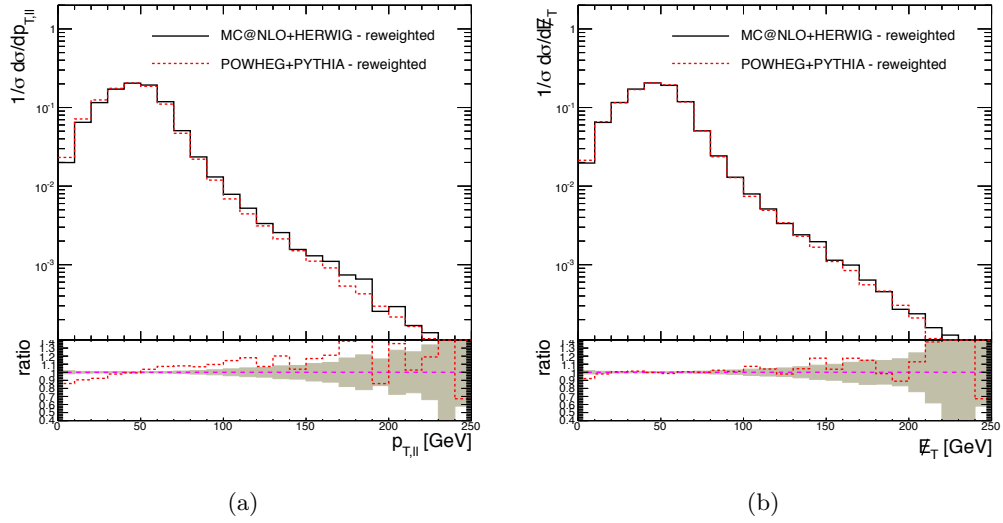


Figure 8.4: The transverse momentum of the di-lepton system (left) and the missing transverse energy (right) obtained by MC@NLO (solid black) and POWHEG (red dotted) after re-weighting the Higgs p_T to NNLO+NNLL. The \cancel{E}_T is the p_T of the two escaping neutrinos.

collimated sprays of particles (hadrons), which can be assigned to the final state partons of the hard scattering. The jet clustering algorithm used in this Section is the so called anti- k_T algorithm with a cone size of $\Delta R = 0.5$, in analogy to the jet definition used in the analysis of the data. See 3.7.4 for more details. The acceptance of the jets is similar to the experimental one in CMS, i.e. $|\eta| < 5$ and the minimum transverse momentum is 30 GeV.

Figure 8.5 shows the transverse momentum of the hardest and second hardest jet for MC@NLO+HERWIG and POWHEG+PYTHIA. Even though the Higgs p_T is re-weighted here, the jet p_T spectrum of POWHEG+PYTHIA is in general still harder than the one from MC@NLO+HERWIG. This also affects the jet bin fraction, which is shown Figure 8.5(c).

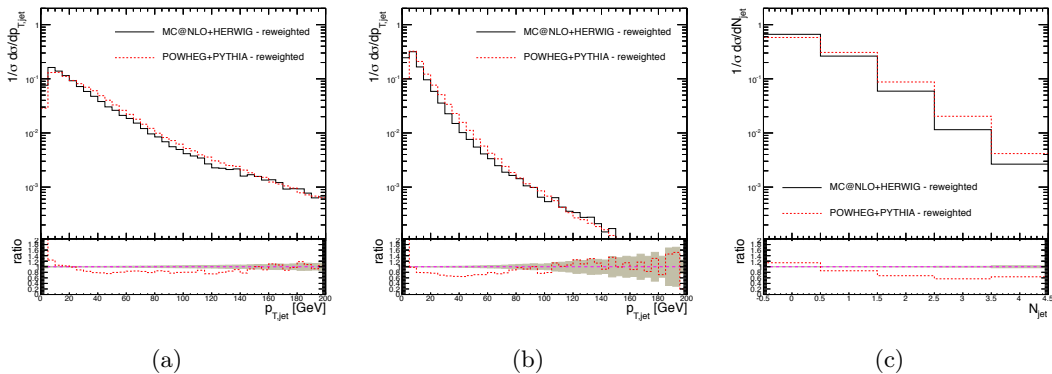


Figure 8.5: The transverse momentum of the hardest (a) and second hardest (b) jet for MC@NLO (solid black) and POWHEG (red dotted), after re-weighting of the Higgs p_T . (c) shows the jet bin fraction. The jet definition is: $p_T > 30$ GeV and $|\eta| < 5$

8.2.4 Factorization and Renormalization Scale Dependence

The cross section given in Equation (1.45) depends on the factorization μ_F and renormalization μ_R scale and there is no fundamental law which tells which is the correct scale to choose. As a guidance, the scales are often chosen such that $\mu_F = \mu_R \approx Q^2$, where Q^2 is the physical hard scale, but the exact value depends on the generator, on the order of the QCD corrections included and on the personal choice.

To evaluate the scale dependence of a cross section calculation, the standard procedure is to vary the factorization and renormalization scales simultaneously by a factor of 2, while all other parameters are kept constant,

$$\frac{1}{2}\mu_0 \leq \mu_F = \mu_R \leq 2\mu_0. \quad (8.5)$$

The nominal scale was set to be half the Higgs boson mass, i.e. $\mu_0 = \frac{m_H}{2}$. This variation gives an estimate of the effect due to missing higher order QCD corrections in the cross section calculation.

The not-re-weighted Higgs transverse momentum ($m_H = 140$ GeV) is shown in Figure 8.6(a). The red band corresponds to a factorization and renormalization scale variation of a factor of 2 and can be interpreted as a residual theoretical uncertainty due to missing higher order corrections. It results in an overall theoretical uncertainty due to the scale variation on the total Higgs cross section of about 16%.

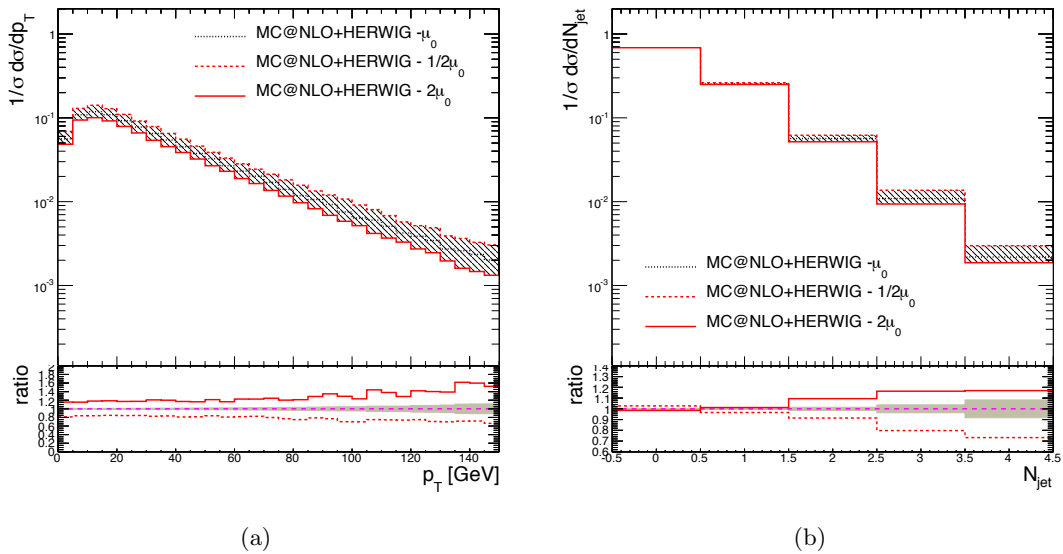


Figure 8.6: (a) Higgs ($m_H = 140$ GeV) transverse momentum obtained with MC@NLO. The band corresponds to a factorization and renormalization scale variation by a factor of 2 up and down, including the change of the total cross section. (b) Jet multiplicity obtained by MC@NLO and with a scale variation by a factor of 2.

The scale variation also has an impact on the jet bin definitions. Figure 9.2(b) shows the jet multiplicity obtained from MC@NLO for a Higgs mass of 140 GeV. The uncertainty on the jet bin fraction for the zero-jet bin is around 3%. It is approximately 4% and 10% for the 1 and 2 jet bin respectively and increasing with larger number of jets.

8.2.5 Effects of the Parton Shower and the Hadronization

So far, two different Monte Carlo generators were studied. Both of them are interfaced to different parton shower and hadronization models; i.e. PYTHIA and HERWIG. In order to understand the effects of these models, a private version of MC@NLO which is interfaced to PYHTIA is compared to the default setup of MC@NLO+HERWIG.

Figure 8.7 shows a comparison of the Higgs p_T as predicted by MC@NLO+HERWIG and by MC@NLO+PYTHIA. The parton shower simulated by PYTHIA results in a softer Higgs p_T spectrum compared to the one from HERWIG. Given the fact that the same matrix element calculation is used for the hard scattering, the difference is due to differences between the parton shower models used. Possible sources are different shower models or a different underlying event (UE) structure.

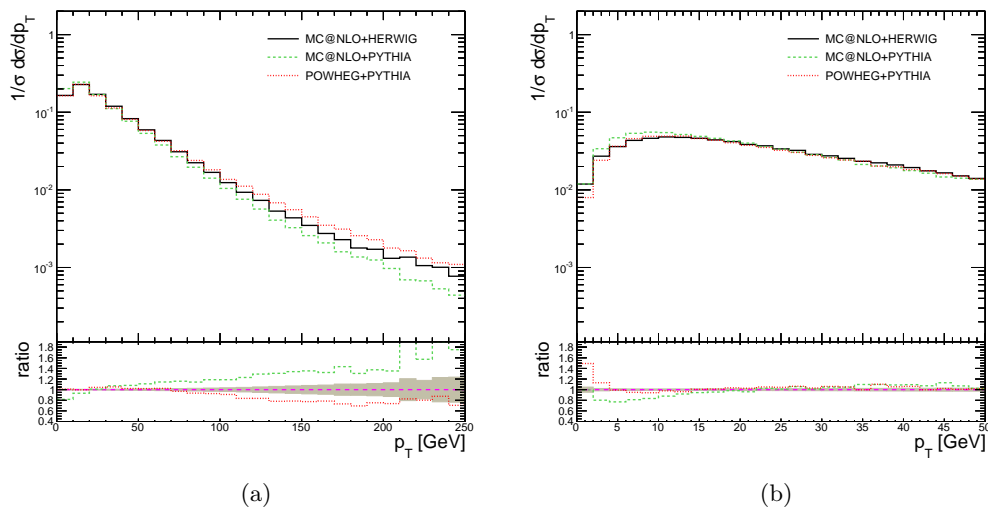


Figure 8.7: (a) Higgs transverse momentum as predicted by MC@NLO+PYTHIA and MC@NLO+HERWIG for $m_H = 140$ GeV. As a reference, the prediction from POWHEG+PYTHIA (with $h_{fact} = m_H/1.2$; see Section 8.2.8 for an explanation of this parameter) is also shown. (b) Zoomed to lower p_T .

The p_T and η distributions of the leading jet after re-weighting to NNLO+NNLL are shown in Figures 8.8(a) and 8.8(b). This allows a direct comparison of the effect of the two parton shower models. PYTHIA results in a softer jet spectrum than HERWIG. The observed differences in η are mainly due to the parton shower modeling; the two PYTHIA lines being very close compared to HERWIG.

8.2.6 Underlying Event

In hadron collisions, typically only one parton per incoming hadron is participating in the hard scattering. The remaining spectator partons are generating a soft underlying event. See Section 5.1.1 for more details on underlying events. The effect of such an underlying event is rather small for most practical purposes of the Higgs search. This is not true in the case of the study of the forward energy flow presented in Part II of this thesis.

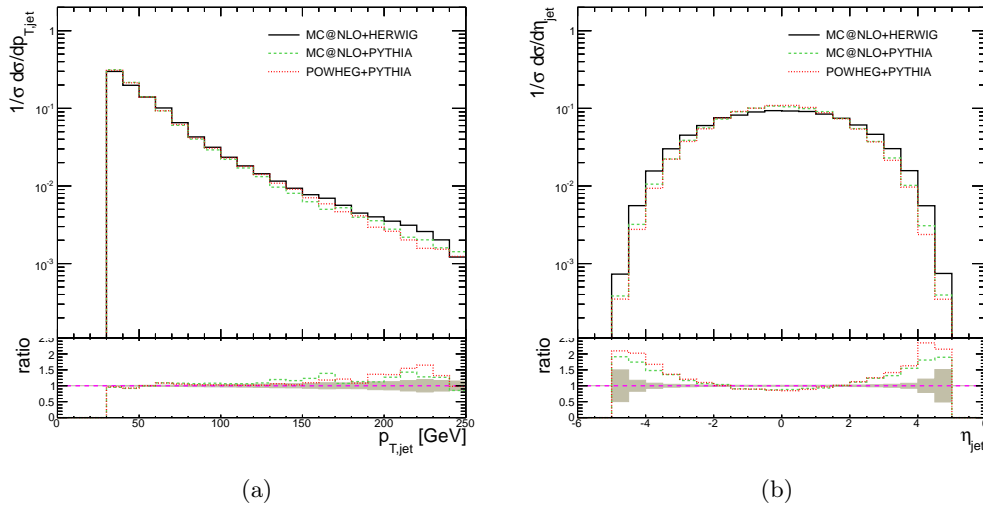


Figure 8.8: Leading jet (a) p_T and (b) η for MC@NLO+HERWIG and MC@NLO+PYTHIA. As a reference, the prediction from POWHEG+HERWIG (with $h_{fact} = m_H/1.2$; see Section 8.2.8 for an explanation of this parameter) is also shown. The Higgs p_T has been re-weighted to the NNLO+NNLL prediction.

A comparison of the leading jet p_T and the jet multiplicity using MC@NLO+HERWIG, with and without UE structure (the spectator quarks are not interacting any further) is shown in Figure 8.9. The effect is in this case very small, i.e. of the order of the statistical uncertainty.

8.2.7 Parton Distribution Functions

The choice of the PDF sets (see Section 1.4.2) used in the generation of events is not unique. To study its effects on the simulation of the Higgs signal, different NLO PDFs are compared to the standard choice in this thesis, which is CTEQ6m (also used the central MC production in 2011 of CMS). Figure 8.10 shows the Higgs transverse momentum and rapidity for MRST2004nlo and HERAPDF01 parton distribution functions.

The effect on the Higgs transverse momentum is not very large (1 – 2% for low p_T) but more significant for the Higgs rapidity distribution.

8.2.8 Parameter Tuning for the POWHEG Generator

Following the recommendations in Ref. [115], some parameters can be changed to improve agreement between the POWHEG prediction of the Higgs p_T and the one obtained from NNLO+NNLL. One of these parameters is the h parameter which is a dump factor for high p_T radiation. By default there is no such factor set, but a better agreement is achieved by setting this factor to $h_{fact} = \frac{m_H}{1.2}$. A change of this parameter is not feasible for the analysis of the 2011 data anymore, but is studied for the future production for the 2012 analysis (N.B. at a center of mass energy of 8 TeV), see also Section 13.2.2.

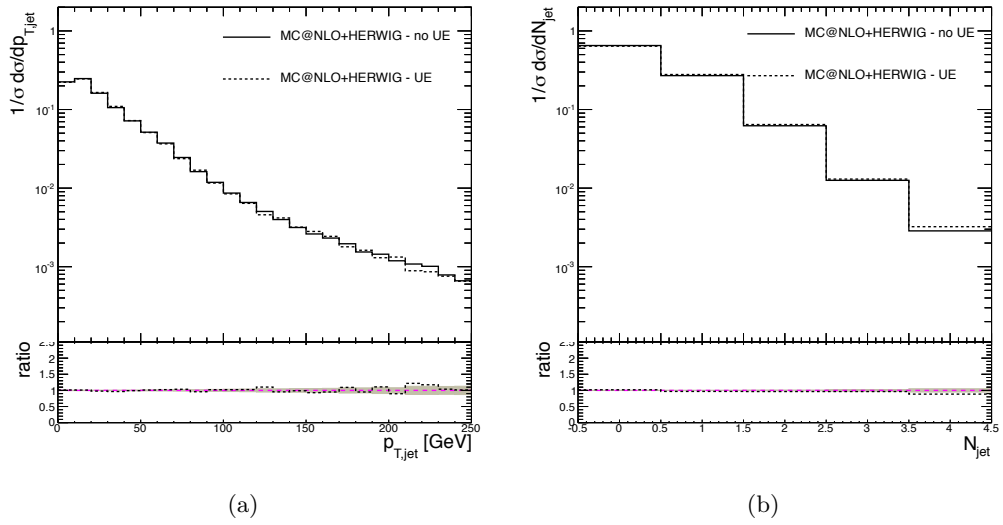


Figure 8.9: (a) Leading jet p_T and jet multiplicity ($p_T > 30$ GeV) (b) with and without underlying event structure from MC@NLO+HERWIG.

Figures 8.11(a) and 8.11(b) show the comparison of the Higgs transverse momentum between the NNLO+NNLL prediction from HRres [116] and the NLO result from POWHEG.⁴ The mentioned h_{fact} parameter in POWHEG is set to $h_{fact} = \frac{m_H}{1.2}$, and consequently, the agreement between POWHEG and NNLO+NNLL is improved and is within the factor of 2 scale variation uncertainties, over the full p_T spectrum. The corresponding plot for the Higgs rapidity is shown in Figure 8.11(c). Again, the two predictions agree within the scale variation bands. The same behavior can be observed for higher Higgs mass hypotheses.

Given the improved agreement obtained by the tuning of the h_{fact} parameter, a differential re-weighting of the NLO Higgs transverse momentum to the NNLO+NNLL prediction is not applied anymore for the 2012 analysis.

⁴HRres is the successor of Hqt, allowing a differential cross section calculation. It was checked that HRres gives equal predictions as Hqt.

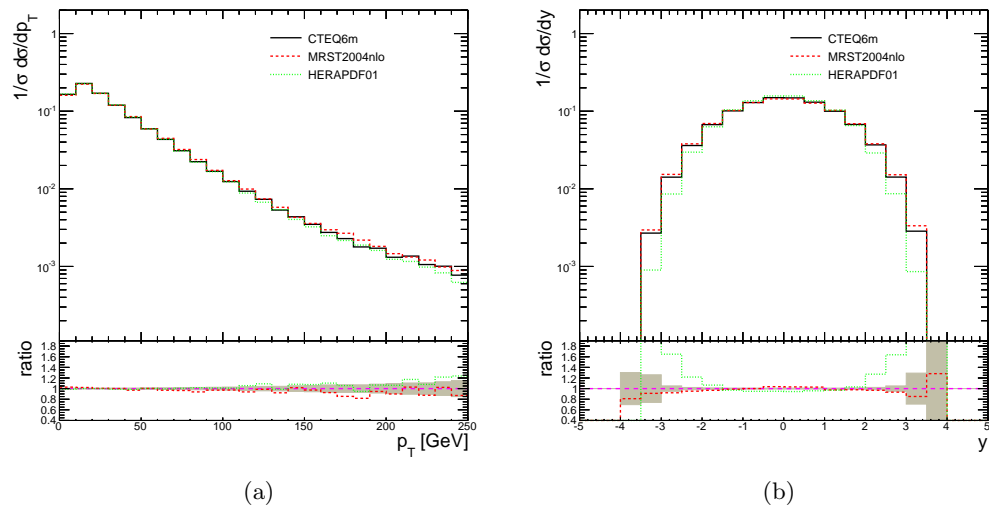


Figure 8.10: Higgs transverse momentum (a) and rapidity (b) for different PDFs.

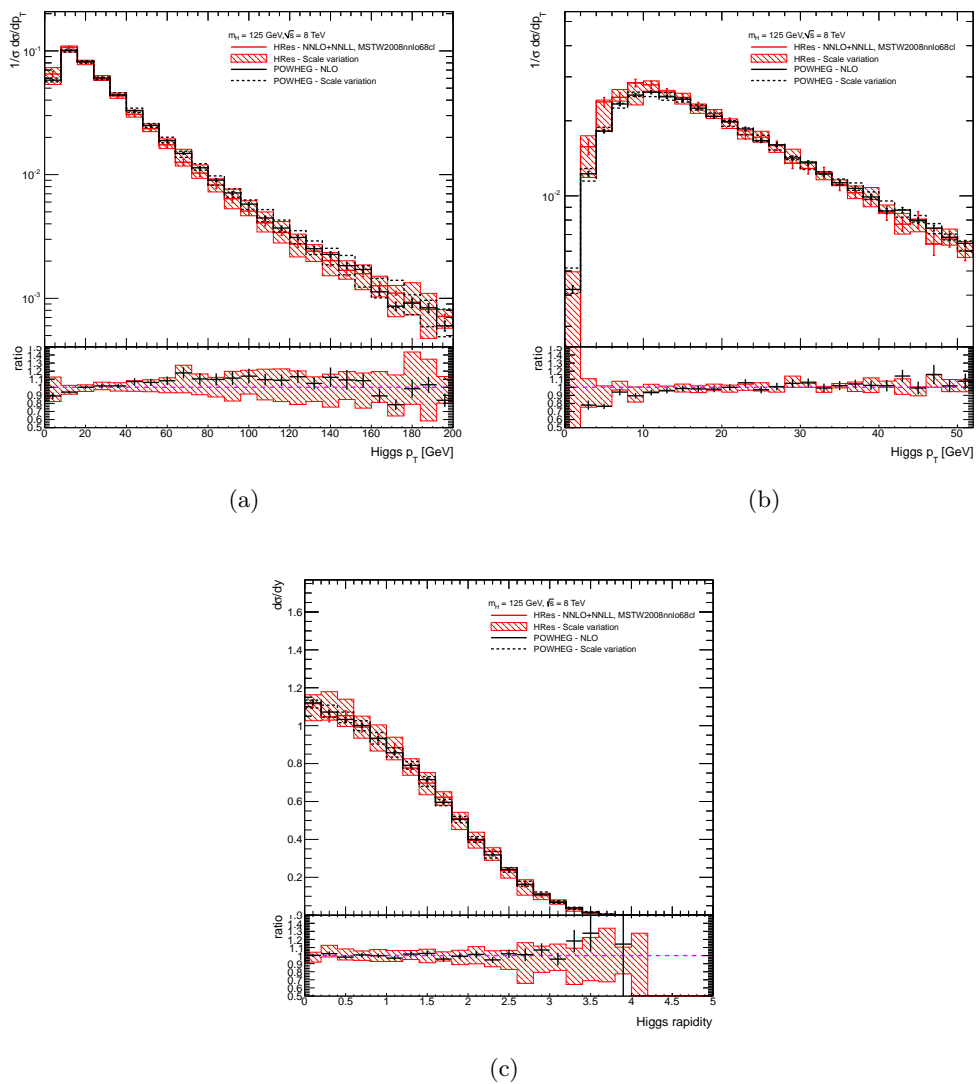


Figure 8.11: Higgs transverse momentum (a) from 0 to 200 GeV and (b) from 0 to 50 GeV. (c) Higgs rapidity. The red histogram shows the NNLO+NNLL central value, the red dashed area the scale variation. The black solid histogram gives the normalized NLO p_T from POWHEG and the area between the two dashed histograms corresponds to the scale variation.

Chapter 9

H \rightarrow WW \rightarrow $\ell\nu\ell\nu$ Analysis

The search for the standard model (SM) Higgs boson can be performed in many different channels with different sensitivity, depending on the Higgs mass hypothesis. Within the CMS experiment, the most promising channels are the $H \rightarrow \gamma\gamma$ and $H \rightarrow ZZ \rightarrow 4\ell$ channels for the *low* Higgs mass around 120 GeV. For an *intermediate* Higgs mass of approximately 140-180 GeV, the $H \rightarrow WW \rightarrow \ell\nu\ell\nu$ channel has the largest expected sensitivity.

In this Chapter, the search for the SM Higgs boson in the $H \rightarrow WW$ channel, using 4.92 fb^{-1} of 2011 pp collision data from the LHC at a center of mass energy of $\sqrt{s} = 7 \text{ TeV}$ recorded with the CMS detector, is described. The analysis presented in this thesis was performed in the context of the CMS publication of Ref. [117]. More documents exist describing the CMS $H \rightarrow WW$ analysis [118–126].

9.1 Analysis Strategy

The search for the Higgs boson is mainly a *hypothesis testing* procedure, where the two hypotheses, to which the data is compared, are a *background only* standard model hypothesis and a *background plus signal* standard model hypothesis. Due to the fact that the Higgs mass is not predicted by the theory, many Higgs mass dependent hypotheses have to be tested individually. Because of the by several orders of magnitude lower signal cross section, and in order to compare the measured data to the possible hypotheses, a sample of events has to be pre-selected according to the $H \rightarrow WW$ signature described in Chapter 7. In order to distinguish with some statistical significance between the background only and a background plus signal hypothesis, the ratio S/\sqrt{B} has to be maximized, i.e. the number of signal events S has to be larger than the uncertainty on the number of background events B , including only statistical uncertainties to first approximation.

Before any event selection can be applied, the basic experimental observables such as e.g. leptons, jets and missing transverse energy etc. have to be defined, which are presented in Section 9.3. The basic experimental event selection can be divided into the

following points:

- The event has to pass one of the lepton triggers (Section 9.3.1), and
- has to contain two isolated high p_T , good quality and oppositely charged leptons (Section 9.3.3).
- The event has to have large missing transverse momentum from the neutrinos (Section 9.3.5).
- The leptons have to be kinematically inconsistent with leptons coming from Z decays (Section 9.3.4).
- The events are divided according to their number of jets (i.e. zero- or one-jet) in order to reduce background from $t\bar{t}$ and because the background composition is different in the different jet bins (Section 9.3.6).
- Higgs mass dependent event selection in order to maximize S/\sqrt{B} .

Section 9.5 gives the details of the final event selection.

The analysis is split into different channels, according to the flavor of the leptons: the *same flavor* channel, which includes di-electron and di-muon final states and the *mixed flavor* channel including final states with one lepton from each flavor, i.e. $e\mu$ and μe , where the ordering of the leptons is according to their transverse momenta. Additionally, the analysis is split according to the jet multiplicity in the *zero-* and *one-jet* bins. These divisions are motivated by the different background compositions in different bins/channels, and in order to independently optimize the event selection.

Several options exist in order to extract the final result from the data: the most simple and robust is a *cut based* approach, where a set of dedicated and optimized selection cuts is applied, in order to achieve a large S/\sqrt{B} . The final observed number of selected events enters the hypothesis testing against the number of expected events from the background only hypothesis and the background plus signal hypothesis, which are obtained from MC simulation. The CMS Higgs searches use this approach as a baseline.

A second method includes the information from the shapes of the different distributions, further called *shape analysis*. Such a shape analysis can be applied on any discriminating distribution e.g. any kinematic variable which is used in the cut based analysis or on the distribution of a *multivariate analysis* output, which merges different input distributions into one single variable. The analysis presented in this thesis follows the latter approach. Due to the additional information of the shapes of the different distributions and the correlations between them, the expected significance of the result increases.

Due to the lack of a narrow mass peak in the $H \rightarrow WW$ channel, one is relying rather strongly on MC simulations of the backgrounds and the signal, in order to perform the hypothesis testing. This requires detailed simulations and thorough comparisons of the MC predictions with the measured data. To avoid a strong dependence on the theoretical predictions of the production cross sections, the different backgrounds are normalized using so called *data driven* methods, wherever this is possible. Section 9.4 summarizes these background estimates.

In order to estimate the significance of a possible excess, systematic uncertainties have to be taken into account. This requires a detailed study of the different effects and a thorough estimate of its impact on the final results. A study of the systematic uncertainties used in this analysis is presented in Chapter 10.

Finally, the statistical significance for the shape analysis are computed and the results are summarized in Chapter 11.

9.2 Datasets

The full 2011 pp collision data recorded by the CMS experiment is used in this $H \rightarrow WW$ analysis. The data taking started on March 12th 2011 with run number 160329 and ended on October 30th 2011 with run number 180252. A subset of “good” runs has been selected on the basis of the sub-detector states during the actual data taking. The data taking was divided into two main periods, called **Run2011A** and **Run2011B**, which were separated by the technical stop of the LHC at the beginning of July. The main difference between these two running periods is the instantaneous luminosity of the LHC beam, which results in an increased number of pileup events in the second data taking period.

The integrated luminosity of both running periods together is $4.92 \pm 0.11 \text{ fb}^{-1}$. The individual datasets used for the data (Monte Carlo) are summarized in Table B.3 (B.4) of Appendix B.2.

9.3 Event Reconstruction and Pre-Selection

The event reconstruction follows mainly the ideas presented in Section 3.7, but several details can be optimized in order to increase the performance in different aspects of a certain analysis. The following Sections summarize the details for this $H \rightarrow WW$ analysis.

9.3.1 Trigger

Due to the di-lepton signature of a possible Higgs signal and the fact that single lepton triggers require tight identification and isolation requirements in order to control the rate at high instantaneous luminosities [127], *di-lepton triggers* are used to trigger events for this analysis.

Besides the presence of a lepton pair and the need for a high trigger efficiency, an additional requirement is to trigger on lowest possible lepton p_T to maintain sensitivity for a possible low Higgs mass signal. Due to the increasing instantaneous luminosity of the LHC beams, individual triggers became *pre-scaled* during data taking, and thus the used trigger path had to be adjusted to remain un-prescaled with the lowest possible lepton p_T .¹ In addition to the di-lepton triggers, single lepton triggered events are selected to recover events from a possible residual inefficiency of the di-lepton triggers.

¹If a trigger is pre-scaled by a factor n , only every n^{th} event passing the trigger requirements gets actually triggered.

Mass [GeV/c ²]	120	140	160	200	400
Di-muon ($p_T > 20/15$ GeV/c)	96.96	97.63	98.36	98.76	99.63
Di-electron ($p_T > 20/15$ GeV/c)	97.28	97.78	98.12	98.39	99.34
Mixed ($p_T > 20/10$ GeV/c)	94.67	95.04	95.39	95.96	98.12

Table 9.1: Trigger efficiencies in percent for the signal and for different Higgs mass hypothesis. The efficiencies are split in the di-electron, di-muon and mixed flavor case. Besides lepton identification and isolation, only a minimum p_T cut (leading/trailing lepton p_T) is applied.

The used triggers are summarized in Tables C.2 and C.2 of Appendix C and a detailed description of the used triggers can be found in [125].

Trigger Efficiency

The trigger efficiencies for the signal at different mass hypotheses are given in Table 9.1. The efficiency is averaged over the full 2011 data taking. The only requirement on the lepton (after identification and isolation) is a minimum p_T cut of 20 GeV for the leading and 15 GeV for the trailing lepton in the same flavor channel and a 10 GeV cut in the mixed flavor channel.

In the MC simulation no trigger requirements were applied due to the fact that some trigger paths have not been simulated. To account for trigger inefficiencies, the MC events have been re-weighted according to the trigger efficiencies shown in Table 9.1, and similarly for all MC samples.

9.3.2 Vertex Reconstruction

Reconstructed vertices have to be within 24 cm from the center (0, 0, 0) of the CMS detector in longitudinal direction, and within 2 cm in radial direction from the actual beam-spot position. The number of degrees of freedom for the vertex is $N_{\text{dof}} > 4$, which corresponds to at least four tracks assigned to the vertex.

After vertex reconstruction, the primary vertex is defined as the one with the largest summed squared- p_T of the associated tracks (due to the high p_T leptons from the hard scattering originating from this vertex).

In the MC simulation, pileup is simulated with additional (simulated) minimum bias events which are overlapped with the hard scattering. Because the instantaneous luminosity was varying continuously during the 2011 data taking, it is not possible to simulate the exact number of pileup events in advance. To get around this fact, the simulation was generated with a flat number of pileup vertices up to 10 and a subsequent Poissonian tail. To match the simulated number of vertices to the one in data, the MC is re-weighted to the observed number of vertices [128]. Figure 9.1 shows the number of vertices for triggered di-electron, leading (trailing) electron $p_T > 20(10)$ GeV, events in data and MC before and after re-weighting the MC. The MC is normalized to the luminosity of 4.92 fb^{-1} and the relative contributions are from the theoretical cross sections.

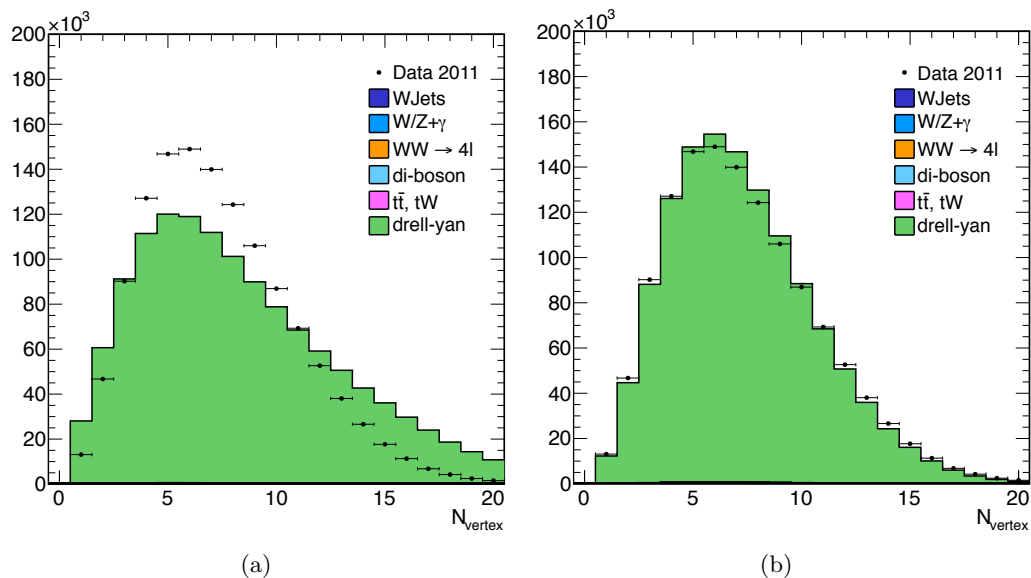


Figure 9.1: Number of vertices in data and in MC (a) before and (b) after re-weighting the pile-up distribution in MC. Only the di-electron channel is shown.

9.3.3 Lepton Reconstruction

In contrast to the cut based electron identification described in Section 3.7.2, a multivariate technique is used in this analysis. A Boosted Decision Tree (see Section 9.5.1 for a general description) is trained on a sample of prompt electron candidates from Z decays and on a fake electrons enriched sample, both from data. The input variables are the same as are used in the cut based electron identification plus some additional impact parameter related variables. The background rejection improves by 40-50%, compared to the cut based approach, using this multivariate electron identification, while the signal efficiency is kept constant [129].

The lepton reconstruction efficiencies are measured using the *tag and probe* method [130, 131]. The electron reconstruction efficiency for electrons with a p_T above 20 GeV is approximately 80% (65%) for electrons in the barrel (endcaps) of ECAL. For electrons with lower p_T , the reconstruction efficiency is reduced to approximately 40% (20%) [124]. The differences of the identification efficiencies between data and MC are corrected by applying a scale factor, event by event, to the MC. Table 9.2 contains these scale factors, which are all close to one, for electrons.

Muons used in this analysis have to be reconstructed as global muons (see also Section 3.7.3) plus additional cut based quality requirements which are summarized in Appendix A.3. The muon efficiency scale factors, used to correct differences in the reconstruction efficiencies between data and MC are summarized in Table A.1.

9.3.4 Z and Low Mass Resonances Veto

To reject the Z-background in the same flavor channels, events with the invariant mass $|m_{\ell\ell} - m_Z| < 15$ GeV are rejected. To avoid backgrounds from low mass resonances (e.g.

			p_T [GeV]				
			0 – 15	15 – 20	20 – 25	25 – 50	> 50
η	Run2011A	< 1.44	1.009	0.987	0.959	0.990	0.986
		1.44 – 1.55	0.792	0.859	1.041	1.014	1.012
		> 1.55	1.179	1.038	1.015	1.006	1.014
	Run2011B	< 1.44	0.916	0.933	0.947	0.988	9.824
		1.44 – 1.55	1.024	1.130	0.950	1.007	0.992
		> 1.55	0.898	1.026	1.006	1.010	0.999

Table 9.2: Electron efficiency scale factors as a function of electron p_T and η . The upper part of the table is for the Run2011A and the lower one for the Run2011B running period.

$\Upsilon, \mathbf{J}/\Psi$) an additional invariant mass cut of $m_{\ell\ell} > 20$ GeV ($m_{\ell\ell} > 12$ GeV) is applied in the same flavor (mixed flavor) channel. The motivation for the higher 20 GeV cut in the same flavor channel is motivated to suppress low invariant mass contributions from Drell-Yan events which are not perfectly simulated by the MC. Figure 9.2 illustrates the need for a Z mass veto in the same flavor channel, in contrast to the mixed flavor channel, where the residual Z contribution is removed by the cut on the missing transverse momentum (see Section 9.3.5).

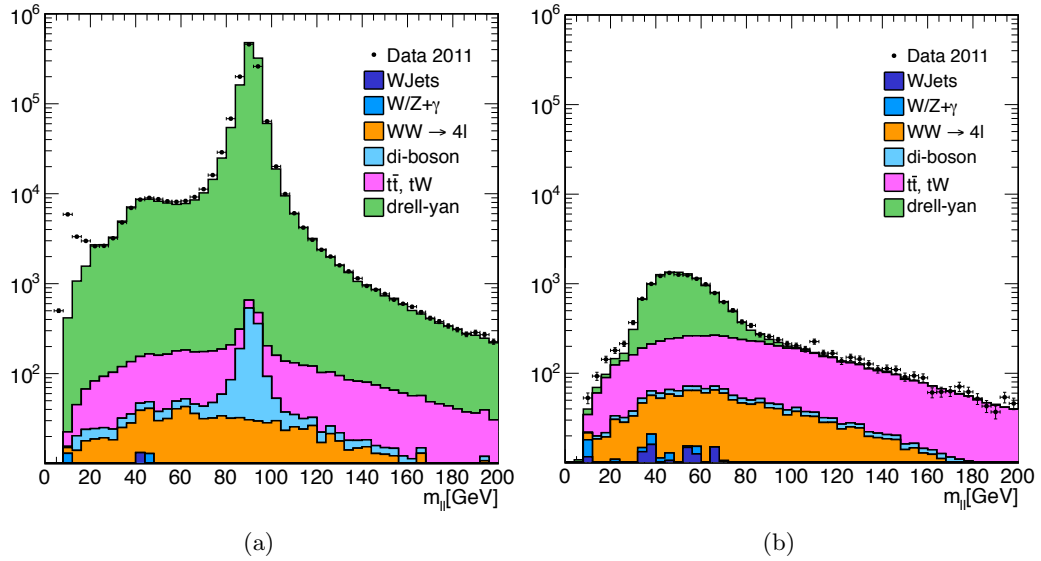


Figure 9.2: Invariant mass of the (a) di-electron and (b) electron-muon system. The leading (trailing) lepton has $p_T > 20(10)$ GeV. The disagreement in the low $m_{\ell\ell}$ region of Figure (a) motivates the cut at 20 GeV for the same flavor channels.

9.3.5 Missing Transverse Energy

Due to the two neutrinos in the $\mathbf{H} \rightarrow \mathbf{WW} \rightarrow \ell\nu\ell\nu$ final state, which escape any detection, the summed energy perpendicular to the beam axis gets imbalanced and leads to *missing transverse energy*. A minimum cut on this missing transverse energy \cancel{E}_T , can be used to suppress backgrounds which do not have any real missing transverse energy; e.g. Drell-

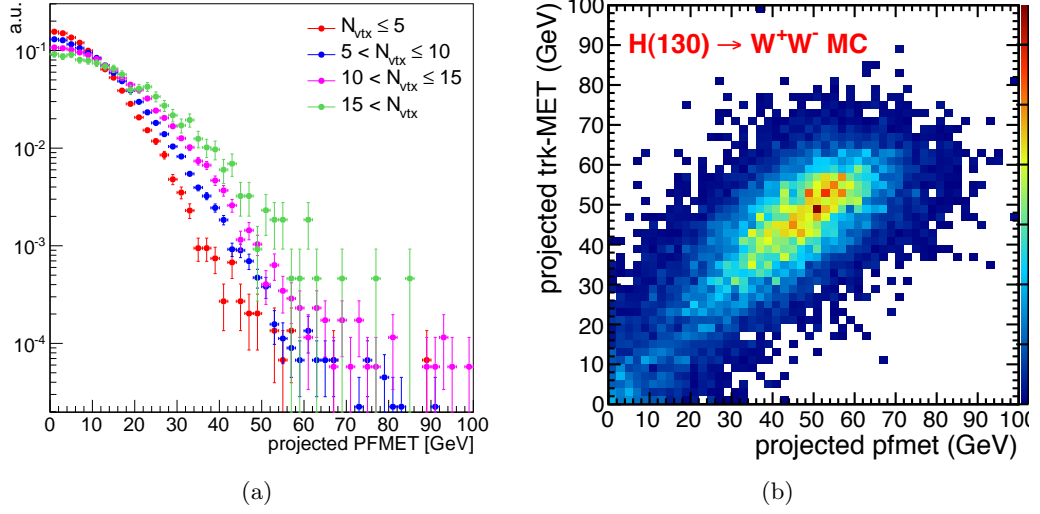


Figure 9.3: (a) Projected particle flow missing transverse energy $\cancel{E}_T^{\text{proj.}}$ in $Z/\gamma^* \rightarrow \ell\ell$ events for different number of reconstructed vertices. (b) Correlation between projected particle flow $\cancel{E}_T^{\text{proj.}}$ and projected trk-MET for a $m_H = 130$ GeV Higgs signal. Plot taken from [125].

Yan or QCD processes. Still, such events can receive a fake missing transverse momentum component due to mis-reconstructed energy, and might thus survive the cut and contribute to the final number of background events.

A background with real missing energy is $Z/\gamma^* \rightarrow \tau^+\tau^- \rightarrow \bar{\nu}_\tau\nu_\tau\ell^+\bar{\nu}\ell^-\nu$. Due to the large difference between the Z mass and the τ lepton mass, the τ s from the Z decays get strongly boosted. The τ decay products (e or μ plus ν s) are thus aligned in the same direction. Therefore, the transverse component of the missing energy projected onto the lepton direction is large, compared to events with no real \cancel{E}_T . This, further called, projected $\cancel{E}_T^{\text{proj.}}$ is defined as

$$\cancel{E}_T^{\text{proj.}} = \begin{cases} \cancel{E}_T & \text{if } \Delta\phi_{\min} > \frac{\pi}{2}, \\ \cancel{E}_T \cdot \sin(\Delta\phi_{\min}) & \text{if } \Delta\phi_{\min} < \frac{\pi}{2}, \end{cases} \quad (9.1)$$

with

$$\Delta\phi_{\min} = \min(\Delta\phi_{\ell_1, \cancel{E}_T}, \Delta\phi_{\ell_2, \cancel{E}_T}), \quad (9.2)$$

and $\Delta\phi_{\ell_j, \cancel{E}_T}$ is the azimuthal angle between lepton ℓ_j and the missing transverse energy \cancel{E}_T .

Figure 9.3(a) shows the normalized particle flow missing transverse energy \cancel{E}_T distribution for $Z/\gamma^* \rightarrow \ell\ell$ events. The different colors correspond to different numbers of reconstructed vertices N_{vtx} . The events were selected to be in the Z mass peak with $|m_{\ell\ell} - m_Z| < 15$ and with minimum transverse momentum $p_{T, \ell} > 20$ GeV for the leptons. One can see, that the tail in the $\cancel{E}_T^{\text{proj.}}$ increases with increasing number of vertices due to pile-up.

In order to remove the pile-up dependence in the projected $\cancel{E}_T^{\text{proj.}}$, the so called *tracker missing transverse momentum* (trk-MET) has been developed, where the missing trans-

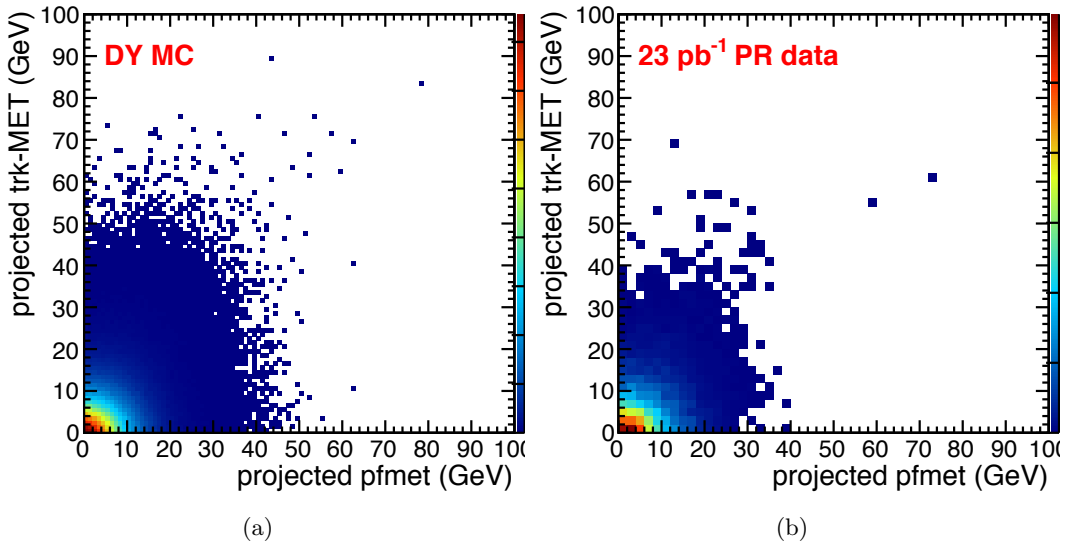


Figure 9.4: Correlation between projected particle flow $\cancel{E}_T^{\text{proj.}}$ and projected trk-MET for $Z/\gamma^* \rightarrow \ell\ell$ events in (a) MC and (b) data. Both plots taken from [125].

verse momentum is calculated only from particles originating from the same vertex as the selected lepton pair. See Ref. [117] for a detailed description of the algorithm. The trk-MET and the *normal* transverse missing energy are weakly correlated for processes with no real \cancel{E}_T and strongly correlated in processes with real \cancel{E}_T ; Figures 9.3(b) and 9.4(a). (Figure 9.4(b) shows the same plot for Z events in data.) Thus the event selection is based on

$$\min \cancel{E}_T^{\text{proj.}} = \min(\cancel{E}_{T \text{ track}}^{\text{proj.}}, \cancel{E}_{T \text{ PFMET}}^{\text{proj.}}), \quad (9.3)$$

which improves the S/\sqrt{B} ratio and reduces the pile-up dependence of the selection efficiency.

The $\min \cancel{E}_T^{\text{proj.}}$ selection is different for the same flavor channel than for the mixed flavor channel, because of the different Drell-Yan contributions.

9.3.6 Jets and Jet Counting

Jets are reconstructed as described in Section 3.7.4. The minimum jet p_T threshold is 30 GeV for high p_T jets. The acceptance in pseudorapidity is $|\eta| < 5$. According to the number of jets, the events are divided into the zero- and one-jet bins, in order to take advantage of the different background contributions: the zero-jet bin is dominated by the WW continuum, whereas the one-jet bin gets a large $t\bar{t}$ contribution. Two- and more-jet events are vetoed, except in the dedicated vector boson fusion analysis [117], which is not further discussed here.

Jets with a p_T between 15 and 30 GeV are called *low p_T jets*, but are not counted as jets and are only used for Drell-Yan and top background rejection.

9.3.7 Top Veto

Top backgrounds have, due to their relatively large cross section, a big contribution to the overall background yield. This is especially true in the one-jet bin. Top backgrounds are rejected using two methods:

- **Soft muon veto:** events with a soft muon from b-quark decays are vetoed.
- **b-jet tagging:** events with a low p_T jet (see Section 9.3.6) which is *b-tagged*, using the TrkCountingHighEff algorithm [132], get vetoed. This procedure is also applied in the zero-jet bin, which can contain events with low p_T jets, as these are not counted as jets. The signal efficiency for this b-tagging method is approximately 98%, whereas it is around 50% for the $t\bar{t}$ background, reducing significantly the top background.

9.3.8 Summary: Pre-Selection of a WW Enriched Sample

Using the above reconstruction and background rejection methods, a WW enriched sample can be selected.

The event selection down to a W^+W^- dominant subsample is:

1. **Di-lepton pre-selection:**
 - triggered event
 - two opposite sign leptons
 - from the same vertex
 - leading (trailing) $p_T > 20(10)$ GeV in the mixed flavor channel
 - leading (trailing) $p_T > 20(15)$ GeV in the same flavor channel
 - $|\eta| < 2.5(2.4)$ for electrons (muons)
 - both leptons have to fulfill the identification and isolation requirements described in sections 3.7.2 and 3.7.3
2. **Extra lepton veto:** events with a third good (with lower p_T) lepton are vetoed, reducing WZ contributions
3. **Missing transverse momentum pre-selection:** $\cancel{E}_T > 20$ GeV
4. **Z mass and low mass resonances veto:** $|m_{\ell\ell} - m_Z| > 15$ GeV and $m_{\ell\ell} > 12(20)$ in the same (mixed) flavor channel
5. **Min. projected transverse momentum:**
 - $\min \cancel{E}_T^{proj.} > 20$ GeV in the mixed flavor channel
 - $\min \cancel{E}_T^{proj.} > 37 + N_{vertex}/2$ GeV for the same flavor channel (N_{vertex} is the number of vertices)
6. **Soft muon veto:** no additional soft muon from b-quark decays

7. **Top veto:** events with a b-tagged jet are vetoed
8. **Azimuthal di-lepton-jet angle:** the azimuthal angle $\Delta\phi_{\ell\ell\text{-jet}}$ between the lepton system and any leading jet above 15 GeV should be smaller than 160° , rejecting Drell-Yan events which are balanced by a jet
9. **Kinematics:** the di-lepton transverse momentum is larger than $p_T^{\ell\ell} > 45$ GeV
10. **Jet counting:** the events are separated in zero- and one-jet bins

This stage of event selection is further called WW selection level. Figures 9.5 and 9.6 show some kinematic variables at the WW selection level for data and MC. The WW level pre-selection is not mass dependent. For illustration purposes, a hypothetical Higgs signal for $m_H = 160$ GeV is also shown. The agreement between the data and the MC is very good. This selection does not entirely consist of WW events only. There is always a large amount of background processes which survive this selection. The normalizations of the background contributions shown in Figures 9.5 and 9.6 are done using *data driven background estimation* methods, wherever this is possible.

9.4 Background Estimates

The background processes for which data driven background estimates can be used are:

- W+jets, where one of the jets *fakes* a lepton
- $Z/\gamma^* \rightarrow \ell\ell$, where large missing transverse energy appears from wrongly reconstructed hadronic activities.
- Top backgrounds.
- Di-boson backgrounds with a Z boson (WZ or ZZ); the *peaking* di-boson component where the selected lepton pair originates from the Z decay
- WW continuum, which has the identical signature as the signal and thus cannot be fully rejected.

The background composition depends on the separation into the different jet bins; in the zero-jet bin, the main background is from the WW continuum, whereas in the one-jet bin $t\bar{t}$ has the largest contribution, and WW is the second largest.

9.4.1 W+Jet Background

In any analysis selecting leptons in the final states, jets contribute to the backgrounds, due to the fact that jets can fake leptons. This is more strongly the case for electrons. In the $H \rightarrow WW$ analysis, W+jets has the largest contribution to backgrounds from fake leptons, where one lepton is a real isolated, prompt lepton from the W decay and where the “second” lepton arises from a misidentified jet. Other sources of non-prompt leptons are leptonic decays of heavy quarks, misidentified hadrons or electrons from photon conversions.

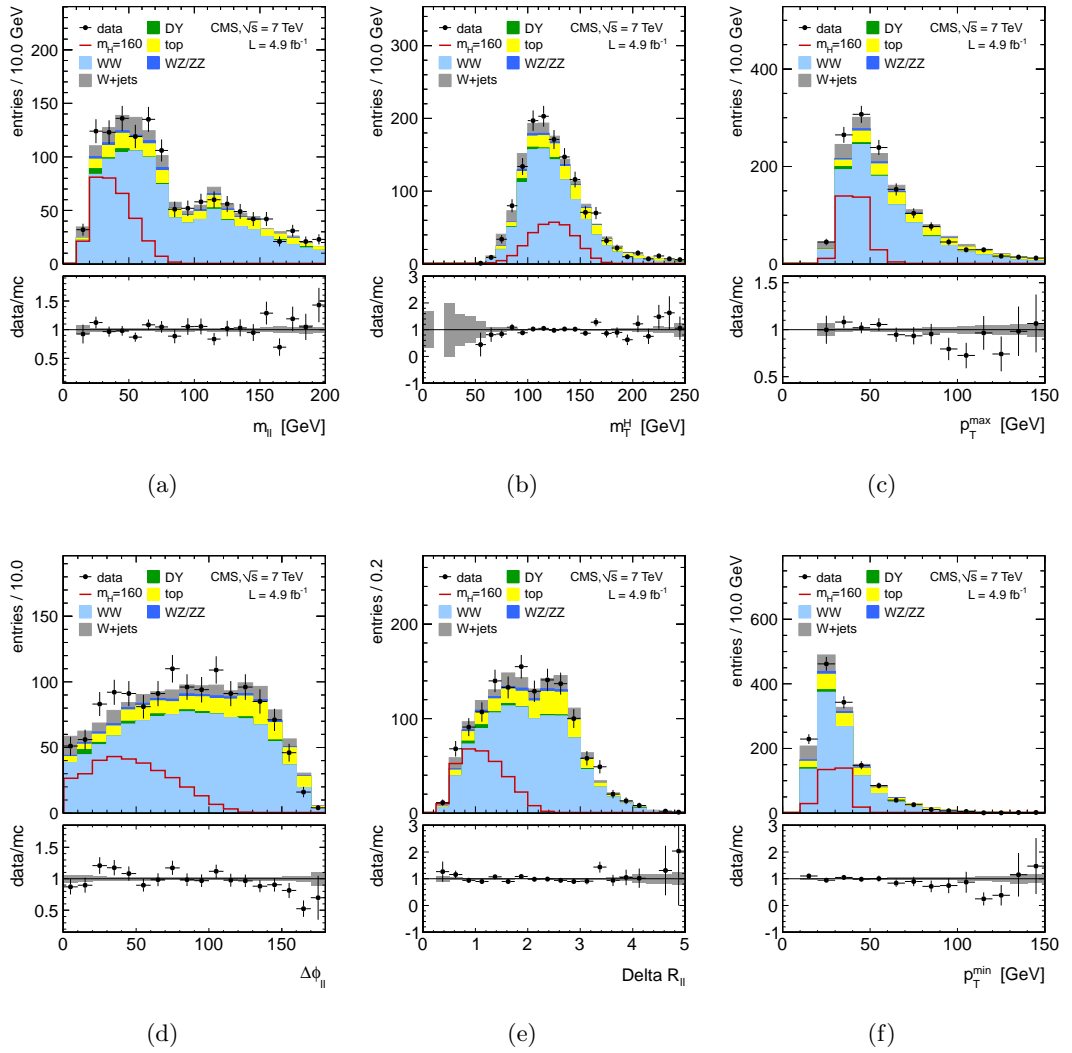


Figure 9.5: Kinematic distributions at WW selection level. (a) invariant mass $m_{\ell\ell}$, (b) transverse mass m_T^H , (c) leading lepton p_T , (d) $\Delta\phi_{\ell\ell}$ and (e) $\Delta R_{\ell\ell}$ between the charged leptons, (f) trailing lepton p_T , all for the zero-jet bin and all flavor channels combined.

The detailed description of the data driven method used in this analysis can be found in Refs. [133] and [134], and only a short summary is given here.

The strategy is the following: in a di-jet enhanced sample, *fakeable objects* are selected — objects that pass a loose lepton definition and which can fake a lepton. The efficiency for these objects to pass the full lepton identification criteria is then measured, and is called the *fake rate* $\varepsilon_{\text{fake}}$ of the background. $\varepsilon_{\text{fake}}$ is then used as a weight to extrapolate the background yield of a loose control sample to the full signal region.

The control region, where $\varepsilon_{\text{fake}}$ is measured, is dominated by QCD di-jet events. Leptons from W and Z bosons are suppressed by requiring $\cancel{E}_T < 20$ GeV and not more than one reconstructed lepton. In order to measure the electron fake rate, a minimum jet p_T of 35 GeV is required with $\Delta R > 0.1$ between the jet and the fakeable object. The fake rate is then ratio of the number of fakeable objects passing the full selection divided by

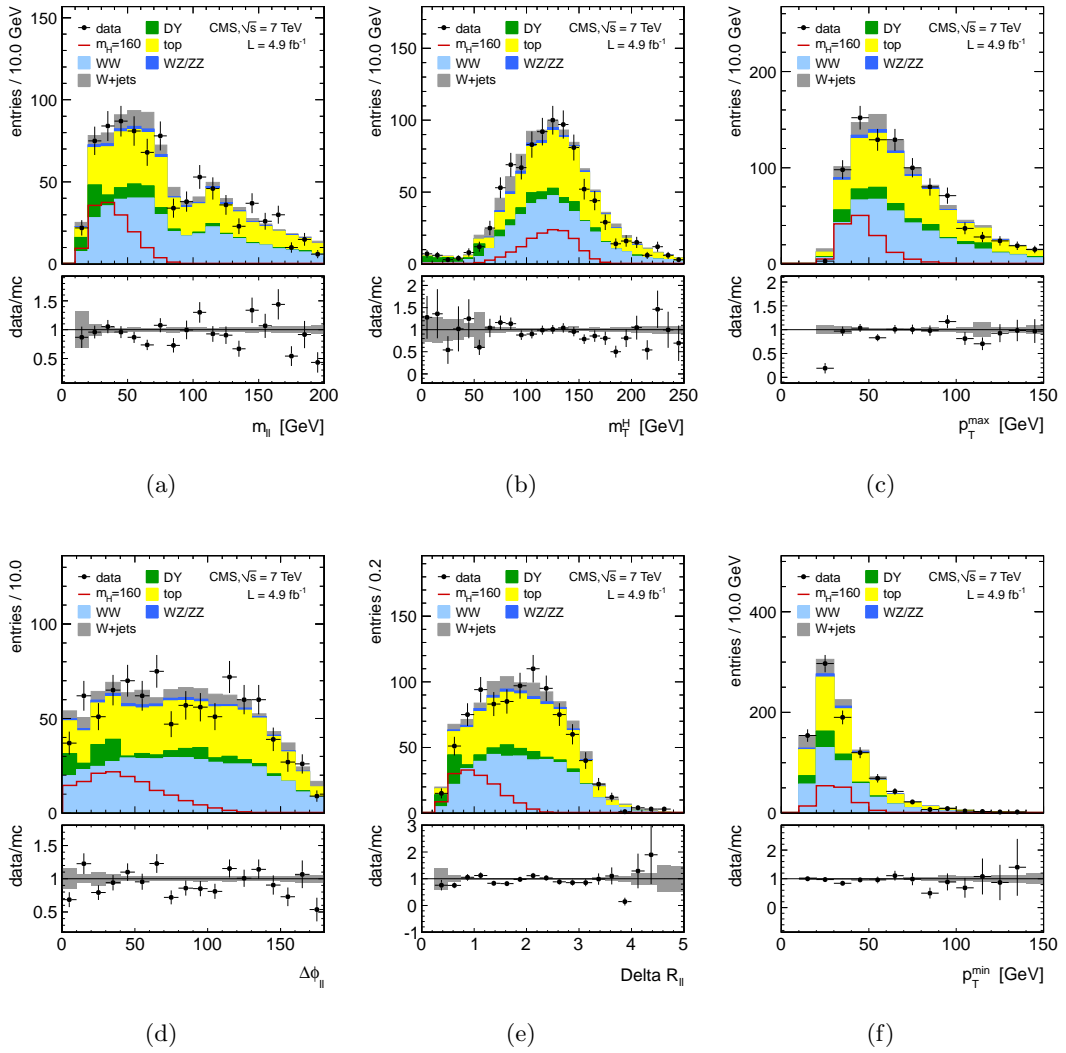


Figure 9.6: Kinematic distributions at WW selection level. (a) invariant mass $m_{\ell\ell}$, (b) transverse mass m_T^H , (c) leading lepton p_T , (d) $\Delta\phi_{\ell\ell}$ and (e) $\Delta R_{\ell\ell}$ between the charged leptons, (f) trailing lepton p_T , all for the one-jet bin and all flavor channels combined.

the number of fakeable objects

$$\varepsilon_{\text{fake}} = \varepsilon_{\text{fake}}(p_T, \eta) = \frac{N_{\text{fakeable}}^{\text{tight}}(p_T, \eta)}{N_{\text{fakeable}}^{\text{loose}}(p_T, \eta)}, \quad (9.4)$$

and is measured as functions of p_T and η of the fakeable object, in order to include kinematical dependences. For the muon fake rate, the minimum jet p_T requirement is relaxed to 15 GeV.

The background yield is estimated in a so called *tight+fail* sample which fulfills the full selection requirements but only one fully tight selected lepton (the *tight* object). The second lepton only has to pass the fakeable object definition (the *fail* object). Each event i in this tight+fail sample gets the weight

$$w_i^{tf} = \frac{\varepsilon_{\text{fake}}(p_T^f, \eta^f)}{1 - \varepsilon_{\text{fake}}(p_T^f, \eta^f)}, \quad (9.5)$$

where the f denotes the fail object and p_T^f and η^f are the fail objects p_T and η . The sum of all weights $\sum w_i^{tf}$ gives the jet induced fake background yield.

This method double counts events with two fakeable objects which get fully reconstructed. To correct for this, a *fail+fail* sample, similar to the tight+fail sample, where both leptons fail the tight selection is selected. Each event gets again a weight

$$w_i^{ff} = \frac{\varepsilon_{\text{fake}}(p_T^{f1}, \eta^{f1})}{1 - \varepsilon_{\text{fake}}(p_T^{f1}, \eta^{f1})} \cdot \frac{\varepsilon_{\text{fake}}(p_T^{f2}, \eta^{f2})}{1 - \varepsilon_{\text{fake}}(p_T^{f2}, \eta^{f2})}, \quad (9.6)$$

where $f1$ ($f2$) is the first (second) failing object. The total background estimate is then

$$N_{\text{fake}} = \sum w_i^{tf} - \sum w_i^{ff}. \quad (9.7)$$

The exact object definition, used for the background estimate can be found in Ref. [125].

The main systematic uncertainties enter due the differences in the jet p_T spectra in the QCD dominated di-jet sample, where the fake rate is measured as a function of the jet p_T , and the tight+fail sample, dominated by W+jets, to which the fake rate is applied. A second source of uncertainty is the different structure of the fakeable object in the two samples. The overall systematic uncertainty is found to be 36%. [125]

9.4.2 Top Background Estimation

Top backgrounds originate from $t\bar{t}$ and tW (single top) production. $t\bar{t}$ contributes mainly to the one-jet bin, whereas single top is more important for the zero-jet bin. The top background estimation is based on the measurement of the b-tagging efficiency, which is used to suppress top events. Knowing the top-tag efficiency (i.e. the b-tag and soft muon veto efficiency combined), the residual top event yield can be estimated from a control region in data.

For the zero-jet bin, the top-tag efficiency is measured in an almost pure $t\bar{t}$ enriched control sample, which is selected by requiring one b-tagged jet above 30 GeV. The top-tag efficiency is the efficiency that an event in this sample gets top-tagged

$$\varepsilon_{\text{top-tag}} = \frac{N_{\text{top-tagged}}^{\text{control sample}}}{N_{\text{control sample}}}. \quad (9.8)$$

Because in $t\bar{t}$ both top legs can be the tagged, and tW only has one top leg, $\varepsilon_{\text{top-tag}}$ has to be corrected according to the relative fractions of the two processes

$$\varepsilon_{\text{top-tag}}^{\text{data}} = f_{t\bar{t}} (1 - (1 - \varepsilon_{\text{top-tag}})^2) + (1 - f_{t\bar{t}}) \varepsilon_{\text{top-tag}}, \quad (9.9)$$

where $f_{t\bar{t}}$ is the fraction of $t\bar{t}$ events, which is estimated from MC.

The final number of top background events at WW selection level is then

$$N_{\text{top}}^{\text{WW-level}} = \left(N_{\text{top-tagged}}^{\text{WW-level}} - N_{\text{other backgrounds}}^{\text{WW-level}} \right) \frac{1 - \varepsilon_{\text{top-tag}}^{\text{data}}}{\varepsilon_{\text{top-tag}}^{\text{data}}}, \quad (9.10)$$

with $N_{\text{top-tagged}}^{\text{WW-level}}$ the number of top-tagged events for the zero-jet bin at WW selection level in data, and $N_{\text{other backgrounds}}^{\text{WW-level}}$ the number of other background events in this very same control region. The efficiencies for further event selection, past the WW selection level is taken from MC.

9.4.3 Drell-Yan Background Estimate

The Drell-Yan background is estimated by counting the number of Z events in a predominantly signal free control region and extrapolating this number into the signal region [135]. This extrapolation factor $R_{out/in}$ is the ratio of the number of Z events outside the control region and the number of Zs inside it, where the control region is defined by the invariant mass range of ± 7.5 GeV around the Z mass, on top of the concerned selection level. The extrapolation factor

$$R_{out/in} = \frac{N_{DY}^{\text{control}}}{N_{DY}^{\text{signal}}} \quad (9.11)$$

is estimated using MC and cross-checked with data.

The number of Drell-Yan events inside the signal region $N_{DY}^{\text{signal, data}}$ is estimated through

$$N_{DY}^{\text{signal, data}} = \left(N_{\ell\ell}^{\text{control, data}} - k \cdot N_{e^\pm\mu^\mp}^{\text{control, data}} - N_{\text{di-boson}}^{\text{control, MC}} \right) \cdot R_{out/in}, \quad (9.12)$$

where contributions from non-Drell-Yan processes to the number of events inside the control region, $N_{\ell\ell}^{\text{control, data}}$, are addressed by subtracting the number $N_{e^\pm\mu^\mp}^{\text{control, data}}$ of $e^\pm\mu^\mp$ events in data. The peaking di-boson contribution (i.e. WZ and ZZ) $N_{\text{di-boson}}^{\text{control, MC}}$ is purely taken from MC and again subtracted from the control region. k is a correction factor to normalize the relative electron-to-muon efficiency. For the same flavor final state (i.e. di-electron *and* di-muon events together) it is

$$k_{\text{sf}} = \frac{1}{2} \cdot \sqrt{\frac{N_{ee}^{\text{control}}}{N_{\mu\mu}^{\text{control}}} + \frac{N_{\mu\mu}^{\text{control}}}{N_{ee}^{\text{control}}}}, \quad (9.13)$$

while for the single flavor final states k is

$$k_{ee} = \frac{1}{2} \cdot \sqrt{\frac{N_{\mu\mu}^{\text{control}}}{N_{ee}^{\text{control}}}} \quad \text{or} \quad k_{\mu\mu} = \frac{1}{2} \cdot \sqrt{\frac{N_{ee}^{\text{control}}}{N_{\mu\mu}^{\text{control}}}}, \quad (9.14)$$

respectively.

$R_{out/in}$ is evaluated as a function of $\min(\cancel{E}_T^{\text{proj.}})$ in which it is roughly flat, showing that the $\cancel{E}_T^{\text{proj.}}$ dependence is reasonably well modeled in MC.

Figure 9.7 shows the $R_{out/in}$ at the WW selection level for different channels and jet bins as it is obtained from MC and from data. The $R_{out/in}$ value used for the background estimation is the one for $\cancel{E}_T^{\text{proj.}} > 37$ GeV as used in the analysis itself. For the signal extraction with the shape analysis, the $R_{out/in}$ (and the Drell-Yan background) are estimated at the mass dependent BDT-level. In order to reduce the statistical uncertainty, the $\min(\cancel{E}_T^{\text{proj.}})$ cut on the Drell-Yan MC has been relaxed to 20 GeV, which is possible due to the fact that $R_{out/in}$ is independent of $\min(\cancel{E}_T^{\text{proj.}})$ and the transverse mass m_T cuts have been removed.

Tables 9.3 and 9.4 summarize the results at the WW selection level.

The systematic uncertainty on the Drell-Yan background estimation method is taken as the maximum difference between two $R_{out/in}$ in each channel/jet bin (see also Figure 9.7). These uncertainties are of the order of 20 – 60% for the zero-jet bin and 5 – 15% in the 1-jet bin at the WW selection level (Tables 9.4).

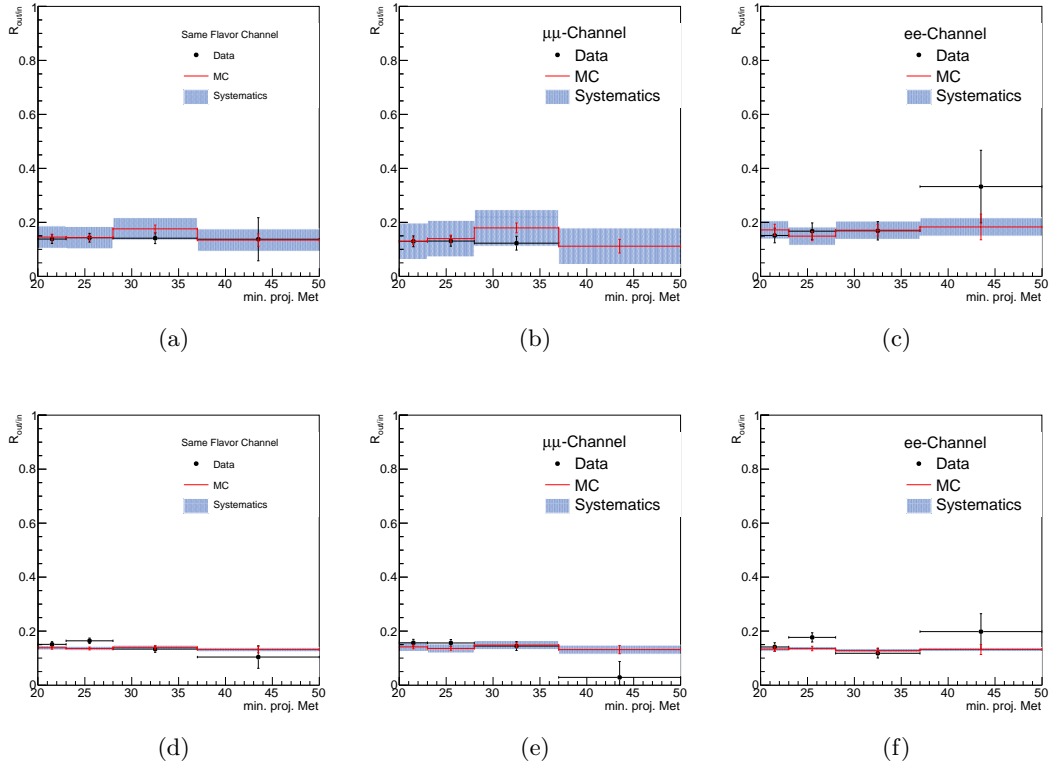


Figure 9.7: $R_{out/in}$ at the WW selection level for different channels (from left to right: sf, $\mu\mu$, ee) and different jet bins (from top to bottom: zero-jet, one-jet) as it is obtained from MC and from data. The systematic uncertainty is the maximum difference between two $R_{out/in}(\cancel{E}_T^{\text{proj.}})$ cuts.

9.4.4 WW Background Normalization

The $qq/gg \rightarrow W^+W^-$ continuum, having the same signature as the signal, is irreducible and thus the most dominant background in this analysis. The WW background yield is estimated in two ways, depending on the Higgs mass hypothesis: *i*) normalized in an almost signal free control region for Higgs mass hypotheses below 200 GeV or *ii*) directly taken from MC for Higgs masses $m_H \geq 200$ GeV, because the signal starts to enter control region significantly.

In the first case, an almost signal free control region can be defined, by selecting events with an invariant mass $m_{\ell\ell} > 100$ GeV, and passing the full event selection (except for m_T^H cuts used in the signal extraction. This cut efficiency is taken from MC and applied afterwards). From the data event yield in the control region, other background contributions are subtracted, using the above methods. This corrected yield is then extrapolated from the control region into the signal region using control-to-signal-region ratios $R_{c/s}$ from MC simulation.

Possible uncertainties arise from the generator dependence of $R_{c/s}$, as well as from the m_T^H cut efficiency which is also taken from MC, but mainly of course from the uncertainties on the normalizations of the other backgrounds in the control region.

Final State	$R_{out/in}$	k	$N_{\ell\ell}^{\text{ctrl, data}}$	$N_{e\pm\mu^\mp}^{\text{ctrl, data}}$	$N_{\text{di-boson}}^{\text{ctrl, MC}}$
sf	$0.134 \pm 0.023(\text{stat.}) \pm 0.042(\text{syst.})$	1.035 ± 0.307	257	45	117.5 ± 10.8
ee	$0.183 \pm 0.047(\text{stat.}) \pm 0.034(\text{syst.})$	0.385 ± 0.185	106	45	47.3 ± 6.9
$\mu\mu$	$0.112 \pm 0.025(\text{stat.}) \pm 0.068(\text{syst.})$	0.650 ± 0.393	151	45	70.1 ± 8.4
sf	$0.132 \pm 0.012(\text{stat.}) \pm 0.008(\text{syst.})$	1.017 ± 0.156	384	59	47.00 ± 6.86
ee	$0.131 \pm 0.019(\text{stat.}) \pm 0.008(\text{syst.})$	0.416 ± 0.112	164	59	19.00 ± 4.36
$\mu\mu$	$0.131 \pm 0.015(\text{stat.}) \pm 0.017(\text{syst.})$	0.601 ± 0.190	220	59	28.00 ± 5.29

Table 9.3: Values used for the Drell-Yan background estimation at the WW selection level. Upper part of the table for the zero-jet bin, lower for the one-jet bin. Errors are statistical except where explicitly stated.

Final State	$N_{DY}^{\text{signal, data}}$	$N_{DY}^{\text{signal, MC}}$	data/MC
sf	$12.50 \pm 0.61(\text{stat.}) \pm 3.92(\text{syst.})$	3.00 ± 0.86	4.17
ee	$7.57 \pm 0.39(\text{stat.}) \pm 1.42(\text{syst.})$	1.24 ± 0.50	6.12
$\mu\mu$	$5.77 \pm 0.49(\text{stat.}) \pm 3.50(\text{syst.})$	1.76 ± 0.72	3.28
sf	$36.45 \pm 1.71(\text{stat.}) \pm 2.22(\text{syst.})$	15.82 ± 2.01	2.30
ee	$15.89 \pm 1.33(\text{stat.}) \pm 0.97(\text{syst.})$	7.80 ± 1.47	2.04
$\mu\mu$	$20.56 \pm 1.14(\text{stat.}) \pm 2.66(\text{syst.})$	8.01 ± 1.37	2.57

Table 9.4: Drell-Yan background estimates at the WW selection level. The estimate from MC and its ratio to data is also given. Upper part of the table for the zero-jet bin, lower for the one-jet bin.

In the zero-jet bin, the theoretical uncertainties from missing higher order corrections are found to be negligible compared to the uncertainties from the data driven methods. For the one-jet bin, the WW scale factor is taken from the zero-jet WW background estimate, but adding additionally the jet bin uncertainty, which is about 21%, to the overall systematic uncertainty. [124]

9.4.5 Other Backgrounds

WZ and $W+\gamma^*$ contribute as backgrounds if the third lepton is not reconstructed. The $W+\gamma^*$ process has been observed in a control region and validated in MC. The agreement between data and MC is found to be good. The ratio of the event yields in data and MC are applied to the MC background prediction in order to estimate the $W+\gamma^*$ background after event selection. [124]

The non-peaking WZ and ZZ backgrounds are taken from MC, as well as $W+\gamma$, where the γ is faking an electron. Also the $Z \rightarrow \tau\tau$ Drell-Yan contribution is normalized using the prediction from MC simulation.

9.5 Signal Extraction

In a cut based approach, events are accepted or rejected from the event selection by applying cuts on several discriminating variables in order to increase the S/\sqrt{B} ratio of the final selection. This reduces the statistics significantly and most of the information of the actual shape of the distribution is not used to discriminate between signal and back-

m_H [GeV]	$m_{\ell\ell} <$ [GeV]	$m_T >$ [GeV]	$m_T <$ [GeV]
120	70	80	120
140	90	80	140
160	100	80	160
200	130	80	200
400	400	80	400

Table 9.5: Summary of the Higgs mass dependent BDT-level selection for a selection of Higgs mass points.

ground. This information can be better exploited using a multivariate analysis technique, which combines different input variables without losing statistics and including shape information as well correlations between the different input variables.

9.5.1 Multivariate Analysis

The multivariate analysis used in the CMS SM Higgs search is a Boosted Decision Tree (BDT) as it is provided by the TMVA [136] toolkit. BDTs are widely used in high energy physics, are rather simple, robust and faster than other MVA techniques. A BDT is a binary tree structure where at each branching a pass/fail decision is taken, based on a single variable at the time. This is similar to a cut based analysis, with the difference that a failing event is not thrown away. This procedure splits the phase space into a large number of regions which will be labeled as signal or background like, depending on the results of the training where it is known if an event belongs to the signal or background sample. Boosting means that several parallel trees are used, which are then combined by an individual weighting of each tree, into one single discriminator. Boosting makes the decision tree more stable against fluctuations and enhances its performance.

The BDT combines the information stored in the different distributions of the input variables into one single variable (the BDT output) which allows to perform a shape analysis based on a single discriminating variable.

The event selection for the BDT input requires some Higgs mass dependent cuts on the invariant mass $m_{\ell\ell}$ and transverse mass m_T^H on top of the WW selection, in order to enhance the S/\sqrt{B} ratio. The transverse Higgs mass is the transverse mass of the di-lepton system, $m_T^H = \sqrt{2 \cdot p_T^{\ell\ell} \cdot \cancel{E}_T \cdot (1 - \cos(\Delta\phi_{\ell\ell-\cancel{E}_T}))}$, where $\Delta\phi_{\ell\ell-\cancel{E}_T}$ is the azimuthal angle between the di-lepton direction and the missing energy. This selection is further called BDT-level. These cuts are summarized for some mass points in Table 9.5.

The event yields for the different flavor channels and jet bins are summarized in Tables 9.6, 9.7, 9.8 and 9.9 for a selection of Higgs mass points. The full tables can be found in Appendix D.1.

The different input variables for the calculation of the BDT discriminating variable

m_H	$Z/\gamma^* \rightarrow \ell\ell$	Top	W+jets	VV	gg \rightarrow WW	qq \rightarrow WW	Σ Bkg.	Signal	Data
120	0.3 ± 0.4	11.7 ± 2.2	24.7 ± 9.0	8.0 ± 1.3	6.6 ± 0.7	143.3 ± 14.7	194.6 ± 17.4	14.5 ± 1.8	202
140	0.3 ± 0.5	26.5 ± 4.7	37.9 ± 13.7	11.2 ± 1.6	14.8 ± 1.5	275.4 ± 28.0	366.1 ± 31.6	81.3 ± 8.1	361
160	0.3 ± 0.5	40.2 ± 7.1	42.9 ± 15.5	13.2 ± 1.8	21.4 ± 2.2	354.8 ± 36.1	472.7 ± 40.0	172.4 ± 14.9	467
200	0.3 ± 0.5	66.0 ± 11.6	51.7 ± 18.7	17.7 ± 2.0	26.1 ± 0.4	397.6 ± 2.8	559.3 ± 22.2	83.5 ± 6.4	612
400	0.3 ± 0.5	104.8 ± 18.3	62.1 ± 22.4	21.3 ± 2.3	31.6 ± 0.5	511.7 ± 3.1	731.8 ± 29.2	22.1 ± 0.6	785

Table 9.6: Estimated background and signal event yields and data yields for 4.92 fb^{-1} of integrated luminosity at BDT-level and for different Higgs mass points in the **mixed flavor zero-jet bin**. The data driven background estimates are used.

m_H	$Z/\gamma^* \rightarrow \ell\ell$	Top	W+jets	VV	gg \rightarrow WW	qq \rightarrow WW	Σ Bkg.	Signal	Data
120	8.0 ± 10.8	6.8 ± 1.3	7.4 ± 2.7	3.6 ± 1.1	4.2 ± 0.4	94.8 ± 9.7	124.9 ± 14.9	6.4 ± 1.2	128
140	10.7 ± 11.8	15.8 ± 2.8	12.7 ± 4.6	6.7 ± 1.9	9.3 ± 1.0	170.4 ± 17.3	225.6 ± 21.7	50.2 ± 6.4	238
160	11.2 ± 11.7	22.7 ± 4.0	14.3 ± 5.2	8.1 ± 2.2	13.0 ± 1.3	205.7 ± 21.1	274.9 ± 25.1	132.2 ± 13.7	279
200	13.4 ± 14.1	35.8 ± 6.3	16.1 ± 5.8	13.0 ± 3.1	16.6 ± 0.3	239.9 ± 2.2	334.9 ± 16.9	54.2 ± 5.7	376
400	14.4 ± 15.7	60.5 ± 10.6	19.5 ± 7.1	24.5 ± 3.1	20.4 ± 0.4	324.0 ± 2.6	463.2 ± 20.6	14.5 ± 0.5	522

Table 9.7: Estimated background and signal event yields and data yields for 4.92 fb^{-1} of integrated luminosity at BDT-level and for different Higgs mass points in the **same flavor zero-jet bin**. The data driven background estimates are used.

are:

- $m_{\ell\ell}$ — di-lepton invariant mass: The signal $m_{\ell\ell}$ distribution tends to much smaller masses, especially for low Higgs mass hypotheses. This is the most discriminating variable.
- p_T^{leading} — transverse momentum of the leading lepton:
- p_T^{trailing} — transverse momentum of the trailing lepton:
- $\Delta\phi_{\ell\ell}$ — azimuthal angle between the leptons: Due to spin correlations, the opening angle for the signal is smaller than for the background.
- $\Delta R_{\ell\ell} = \sqrt{(\Delta\phi_{\ell\ell})^2 + (\Delta\eta_{\ell\ell})^2}$ — angular separation between the leptons: $\Delta\eta_{\ell\ell}$ is the pseudorapidity difference between the two charged leptons. For the signal, this variable tends, similarly as $\Delta\phi$, to smaller angles.
- m_T — di-lepton transverse mass: the transverse mass of the signal has a cutoff at the Higgs mass and the distribution has a different shape for the background.
- flavor channel: (ee, e μ , μe , $\mu\mu$)

The following two variables are in addition used for the one-jet case:

- $\Delta\phi_{\ell\ell\text{-jet}}$ — azimuthal angle between di-lepton system and leading jet:
- $\Delta\phi_{\ell\ell\text{-}\cancel{E}_T}$ — azimuthal angle between di-lepton system and \cancel{E}_T :

Figure 9.8 shows the $\Delta\phi_{\ell\ell\text{-jet}}$ and $\Delta\phi_{\ell\ell\text{-}\cancel{E}_T}$ distributions for a $m_H = 160 \text{ GeV}$ hypothesis at the WW selection level.

m_H	$Z/\gamma^* \rightarrow \ell\ell$	Top	W+jets	VV	gg \rightarrow WW	qq \rightarrow WW	Σ Bkg.	Signal	Data
120	0.6 ± 1.0	29.7 ± 1.9	13.4 ± 4.9	4.8 ± 1.4	2.7 ± 0.7	44.7 ± 10.9	95.9 ± 12.3	6.5 ± 0.6	105
140	0.9 ± 1.5	70.2 ± 4.3	22.5 ± 8.1	7.0 ± 1.8	5.4 ± 1.3	89.3 ± 21.9	195.2 ± 23.9	34.0 ± 2.2	192
160	0.9 ± 1.5	104.4 ± 6.3	25.4 ± 9.2	8.1 ± 2.0	7.9 ± 1.9	121.0 ± 29.6	267.8 ± 31.8	79.0 ± 4.3	250
200	2.2 ± 2.2	157.8 ± 9.4	32.1 ± 11.6	9.8 ± 2.4	10.0 ± 0.3	145.5 ± 1.6	357.3 ± 15.4	44.7 ± 2.3	350
400	4.2 ± 3.7	223.8 ± 13.2	41.4 ± 14.9	13.0 ± 2.8	12.8 ± 0.3	200.5 ± 2.0	495.8 ± 20.6	16.2 ± 0.3	479

Table 9.8: Estimated background and signal event yields and data yields for 4.92 fb^{-1} of integrated luminosity at BDT-level and for different Higgs mass points in the **mixed flavor one-jet bin**. The data driven background estimates are used.

m_H	$Z/\gamma^* \rightarrow \ell\ell$	Top	W+jets	VV	gg \rightarrow WW	qq \rightarrow WW	Σ Bkg.	Signal	Data
120	13.1 ± 2.8	15.9 ± 1.1	3.9 ± 1.4	2.4 ± 1.2	1.2 ± 0.3	21.5 ± 5.3	58.0 ± 6.3	2.3 ± 0.4	58
140	26.8 ± 5.7	35.9 ± 2.3	6.3 ± 2.3	3.8 ± 1.7	3.1 ± 0.8	43.8 ± 10.7	119.8 ± 12.7	17.6 ± 1.6	120
160	26.9 ± 4.1	51.7 ± 3.2	6.9 ± 2.5	4.5 ± 2.0	4.6 ± 1.1	58.6 ± 14.4	153.3 ± 15.6	54.1 ± 3.9	152
200	37.9 ± 8.2	78.4 ± 4.7	9.1 ± 3.3	6.8 ± 2.8	5.9 ± 0.2	74.9 ± 1.2	213.0 ± 10.5	25.7 ± 1.8	220
400	42.3 ± 9.4	116.6 ± 6.9	12.2 ± 4.4	10.8 ± 2.5	7.6 ± 0.2	108.6 ± 1.4	298.1 ± 12.8	9.2 ± 0.2	320

Table 9.9: Estimated background and signal event yields and data yields for 4.92 fb^{-1} of integrated luminosity at BDT-level and for different Higgs mass points in the **same flavor one-jet bin**. The data driven background estimates are used.

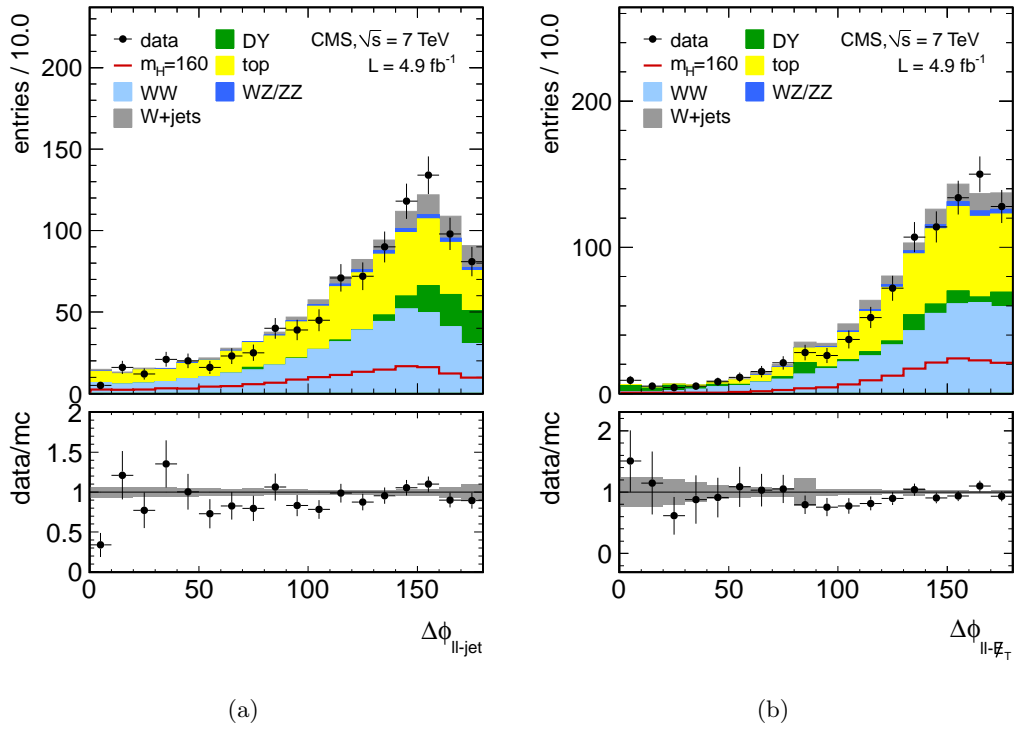


Figure 9.8: (a) $\Delta\phi_{\ell\ell-jet}$ and (b) $\Delta\phi_{\ell\ell-\cancel{E}_T}$ distributions at the WW selection level.

The BDT was trained using these variables in order to discriminate the Higgs signal against the main and irreducible background from the WW continuum. For each mass point the training was done individually.

Figures 9.9 and 9.10 show the BDT discriminator for two different Higgs masses in the different flavor channels and jet bins. The different ranges of the discriminators are

a consequence of the training which was performed at different times during the analysis, but does not affect the result of the shape analysis.

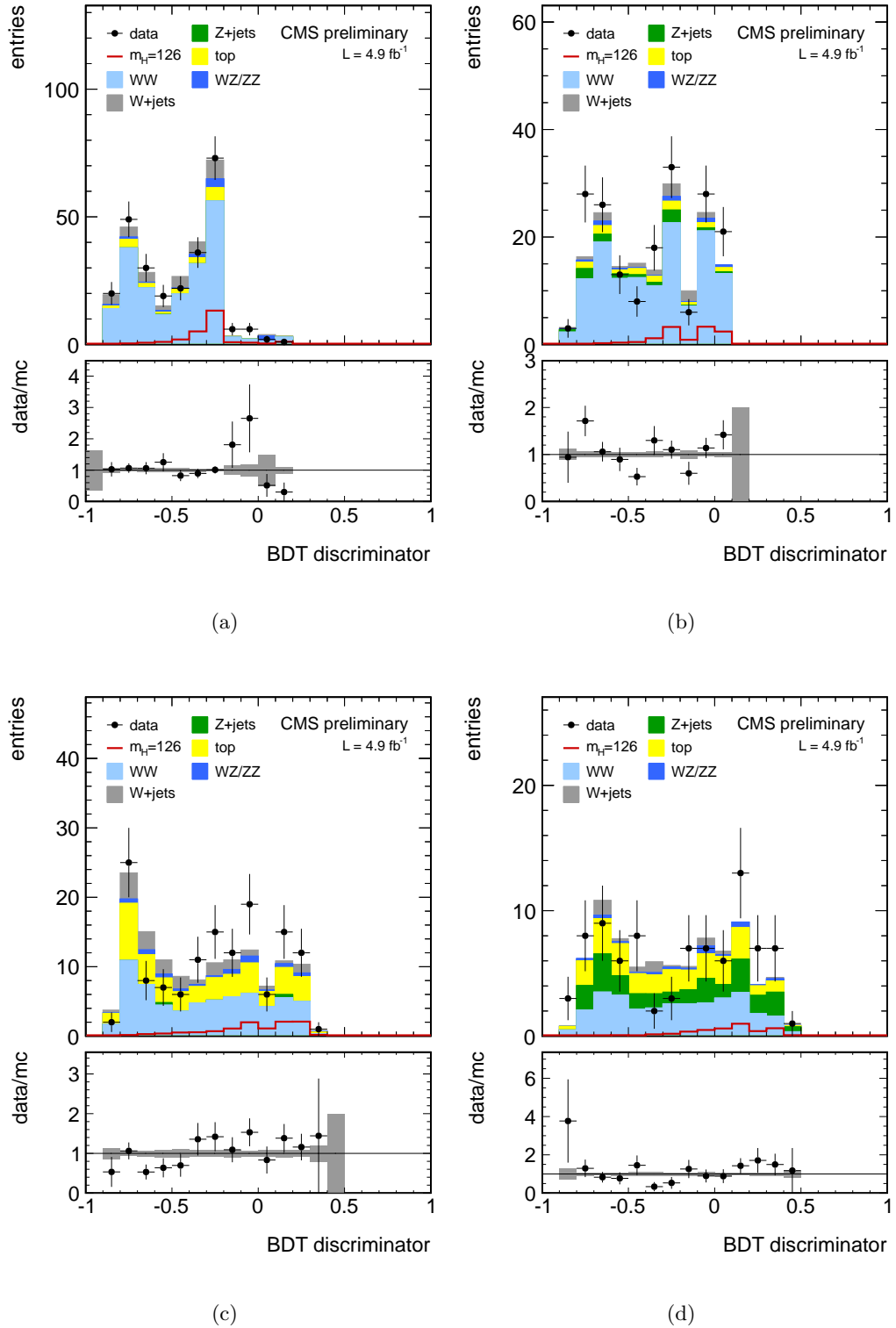


Figure 9.9: BDT discriminator output for a Higgs mass of 126 GeV. (a) mixed flavor, 0-jets; (b) same flavor, 0-jets; (c) mixed flavor, one-jet; (d) same flavor, one-jet.

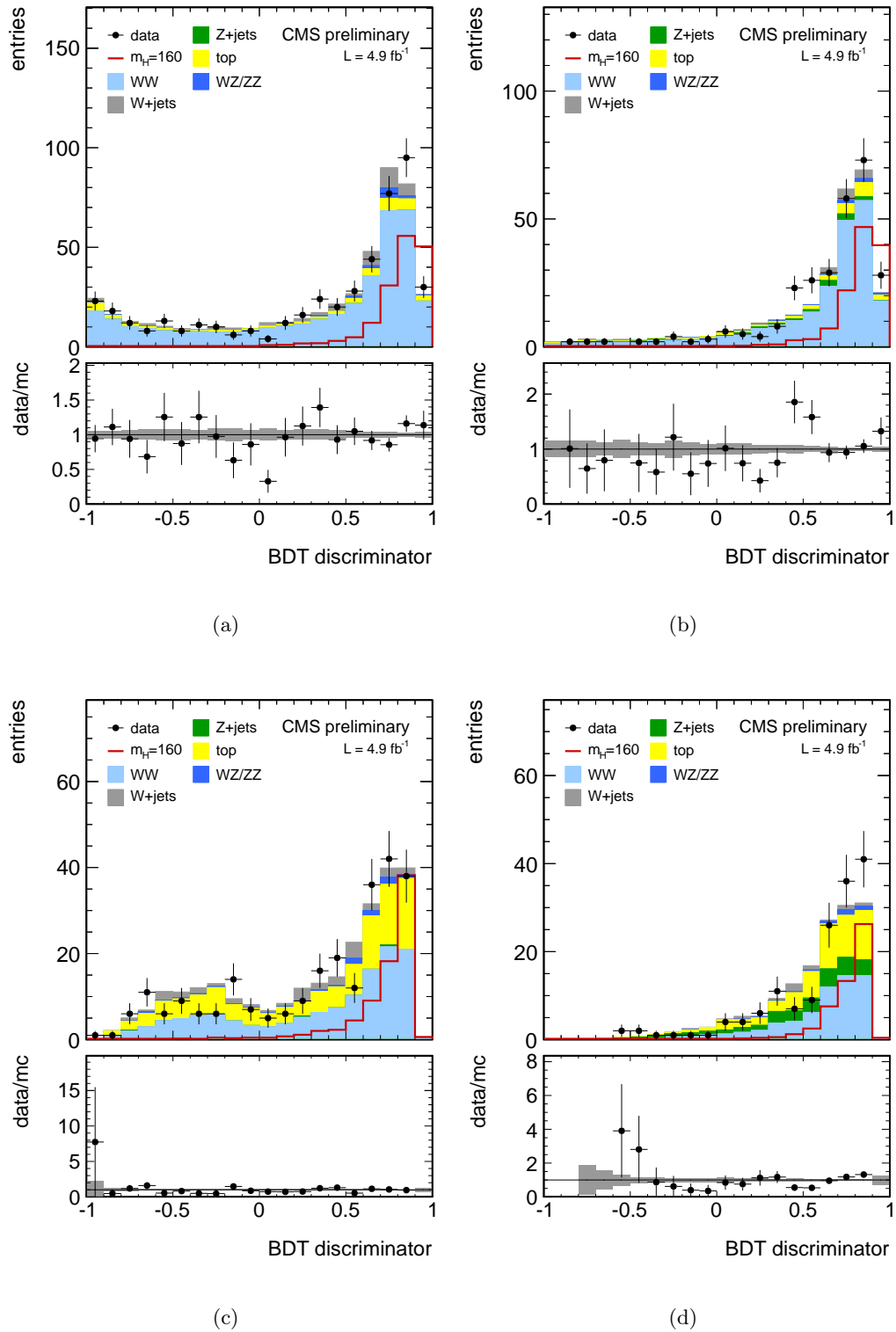


Figure 9.10: BDT discriminator output for a Higgs mass of 160 GeV. (a) mixed flavor, 0-jets; (b) same flavor, 0-jets; (c) mixed flavor, one-jet; (d) same flavor, one-jet.

Chapter 10

Systematic Uncertainties for the $H \rightarrow WW \rightarrow \ell\nu\ell\nu$ Analysis

The understanding of systematic uncertainties is of great importance, as they affect the event selection efficiencies, of the signal and the background as well, and thus the significance of the result of an analysis. This is especially true if the expected background is of the same order as the signal itself. Additionally, in shape analyses, uncertainties do not only affect the overall normalization but also the shape of the discriminating variable. Thus, good understanding of the numerous systematic effects is needed.

In this Chapter, the systematic uncertainties which are taken into account in the $H \rightarrow WW \rightarrow \ell\nu\ell\nu$ shape based analysis and their treatments, with respect to the shape analysis, where the full information of the distribution of a discriminant variable is used, are summarized.

10.1 Sources of Systematic Uncertainties

The main sources of systematic uncertainties and the ones discussed in the following Sections are:

- i)* theoretical uncertainties,
- ii)* experimental effects,
- iii)* statistical uncertainties.

Theoretical uncertainties enter by the limitations and simplifications of the model used to describe the physics processes which are used in the MC simulation. Experimental uncertainties are driven by the performance of the detector to measure the observables used in the analysis. Statistical uncertainties govern due to the finite sizes of the MC samples used.

Furthermore, all uncertainties can be separated in two types:

- i) normalization uncertainties*, where a systematic effect is changing the overall normalization (i.e. number of selected events), assuming that the shape of any distribution is not affected, and
- ii) shape uncertainties*, which effectively change the shape of a distribution.

Normalization uncertainties enter the shape analysis as a constant normalization scale factor. Shape uncertainties, on the other hand, enter the analysis in form of a set of three histograms: the *nominal shape* of a distribution and the $+1\sigma$ and -1σ *variation shapes* of the same variable. (See Chapter 11 for more details on the statistical method used to calculate the significance of the result.) The goal of this Chapter is to estimate the normalization uncertainties and, where applicable, to find the $\pm 1\sigma$ shapes.

By construction, shape uncertainties include always also the uncertainty on the normalization. The two types of uncertainties can be factorized by normalizing the $\pm 1\sigma$ shapes to the nominal one. Thus, one obtains the pure shape uncertainty only in form of the histograms.

10.2 Theoretical Uncertainties

The following theoretical uncertainties have been studied:

- Higgs signal cross section uncertainty
- Jet bin fraction uncertainty
- Uncertainties on α_s and PDFs
- Generator effects on WW background MC simulation

10.2.1 Uncertainty on the Higgs Signal Cross Section

The uncertainties on the Higgs signal cross sections $\sigma_{\text{gg}\rightarrow\text{H}}$ arise mainly from missing terms of higher order QCD corrections in the partonic cross section calculation (see Section 1.4 for more details). The customary method to estimate the size of this effect is the systematic variation of the factorization and renormalization scale. The uncertainties on the Higgs signal cross section are summarized for a few mass points in Table 10.1. The full set of uncertainties can be found in Ref. [101]. The uncertainty on the Higgs production cross section from scale variations is of about $\pm 12\text{-}17\%$, depending on the Higgs mass. The uncertainty on the Higgs cross section is treated as a normalization uncertainty, as it changes the number of expected Higgs events.

Higgs Mass [GeV]	$\sigma_{gg \rightarrow H}$ [pb]	$\Delta\sigma_{x\text{-sec.}}^+$ [%]	$\Delta\sigma_{x\text{-sec.}}^-$ [%]	$\Delta\sigma_{\text{scale}}^+$ [%]	$\Delta\sigma_{\text{scale}}^-$ [%]	$\Delta\sigma_{\text{PDF}}^+$ [%]	$\Delta\sigma_{\text{PDF}}^-$ [%]
120	16.63	19.7	-15.1	11.9	-7.9	7.8	-7.2
140	12.13	18.8	-14.9	11.0	-7.4	7.8	-7.5
160	9.080	18.6	-15.0	10.9	-7.2	7.7	-7.8
200	5.249	17.2	-15.2	9.4	-7.2	7.8	-8.0
400	2.032	15.7	-16.3	6.8	-7.7	8.9	-8.7

Table 10.1: Summary of the total theoretical (relative) uncertainties $\Delta\sigma_{x\text{-sec.}}$ on the Higgs signal cross section, for a few Higgs mass points. The individual uncertainties from factorization and renormalization scale variation $\Delta\sigma_{\text{scale}}$ and from PDF uncertainties $\Delta\sigma_{\text{PDF}}$ are also listed. All numbers are provided in Ref. [101].

Higgs Mass [GeV]	f_0	f_1	f_2	$\Delta\sigma_{\text{scale}}^{\geq 1}$ [%]	$\Delta\sigma_{\text{scale}}^{\geq 2}$ [%]
120	0.64	0.25	0.11	± 24	± 9
140	0.61	0.26	0.12	± 32	± 11
160	0.58	0.29	0.14	± 25	± 12
200	0.49	0.34	0.18	± 24	± 15
400	0.44	0.31	0.25	± 21	± 19

Table 10.2: Jet bin fractions f_i for some Higgs mass points. The relative scale uncertainties on the one- and two-jet Higgs signal cross sections are also listed.

10.2.2 Uncertainties on PDFs and the Strong Coupling α_s

The uncertainties on the PDFs and on the QCD coupling constant α_s are an additional and important source for uncertainties on the cross sections and the acceptance, both for the signal and background. The PDF and α_s uncertainties for the Higgs signal are taken from Ref. [101]. The PDF uncertainties are also listed in Table 10.1. This leads together with the uncertainties from scale variations to a total uncertainty of about $\pm 15\text{-}20\%$, depending on the Higgs mass. For background processes, without data driven normalization, the PDF and α_s uncertainty is assumed to be 4%. For the backgrounds which are estimated using data driven methods, these uncertainties cancel out. The uncertainty on the signal acceptance is 2% for both gluon-fusion and vector boson fusion Higgs production.

10.2.3 Uncertainty on the Jet Bin Fraction

In this analysis, the events are divided into different jet bins, and consequently, the uncertainty on these fractions has to be taken into account. For the jet counting, a minimum $p_T > 30$ GeV cut is applied. The one (two) jet cross section and its scale uncertainties $\Delta\sigma_{\text{scale}}^{\geq 1(2)}$, which are listed in Table 10.2, have been calculated with MCFM. Following a recipe presented in Ref. [101] the jet bin fractions, summarized in Table 10.2, are calculated. f_0 , f_1 and f_2 are the fractions of events having 0, 1 and 2 or more jets. The exact formulas for the calculations can be found in Ref [124]. The uncertainties on the jet bin fractions are large, up to 40%, and are summarized, also for background processes, in Table 10.3.

10.2.4 Effects of Different Generators on the WW background

Due to the fact that the WW background shape is entirely taken from MC simulations, the analysis is fully relying on the theoretical models and thus can easily be affected by their uncertainties. Especially missing higher order QCD radiation effects are expected to have the largest influence on the generated WW shape. To take these effects into account, the shapes of the distributions obtained from MadGraph (the default event generator for WW production used in this analysis and a LO generator) are compared to the shapes obtained from MC@NLO. Figures 10.1 are showing the comparisons of some of the input variables used in the BDT analysis.

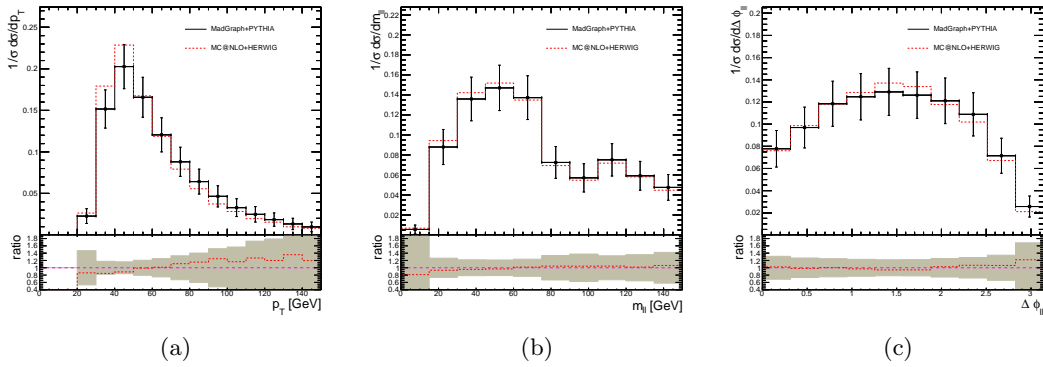


Figure 10.1: The (a) leading lepton p_T , (b) invariant mass $m_{\ell\ell}$ and (c) $\Delta\phi_{\ell\ell}$ for the WW background at the mass independent WW selection level as obtained from MadGraph (dots) and MC@NLO (histogram). These histograms are normalized to unity.

The bin-wise difference of the discriminating BDT-output variables between the two generators is interpreted as the $\pm 1\sigma$ uncertainty, and is applied on the MadGraph shape. This gives the $\pm 1\sigma$ shapes of the BDT output, as shown in Figure 10.2(a). The $\pm 1\sigma$ difference is about 10% in the signal dominated region.

An additional way to study effects of missing higher order QCD corrections is by a simultaneous variation of the factorization and renormalization scale by a factor 2 up and down. This was performed on events generated with MC@NLO. The difference between the nominal MC@NLO and varied MC@NLO shape is interpreted as the $\pm 1\sigma$ uncertainty and is applied on the MadGraph nominal shape to obtain the shape uncertainty. An example for such $\pm 1\sigma$ shapes are shown in Figure 10.2(b) in the case of the BDT analysis. The $\pm 1\sigma$ difference is about 10%.

10.3 Experimental Effects

The experimental uncertainties taken into account cover mainly the different energy scales of e.g. jets or leptons, or their energy resolutions, which affect the selection efficiencies. These effects are studied by the application of a scaling and/or smearing of the variable to study by $\pm 1\sigma$ and is followed by a recalculation of the correlated variables. This

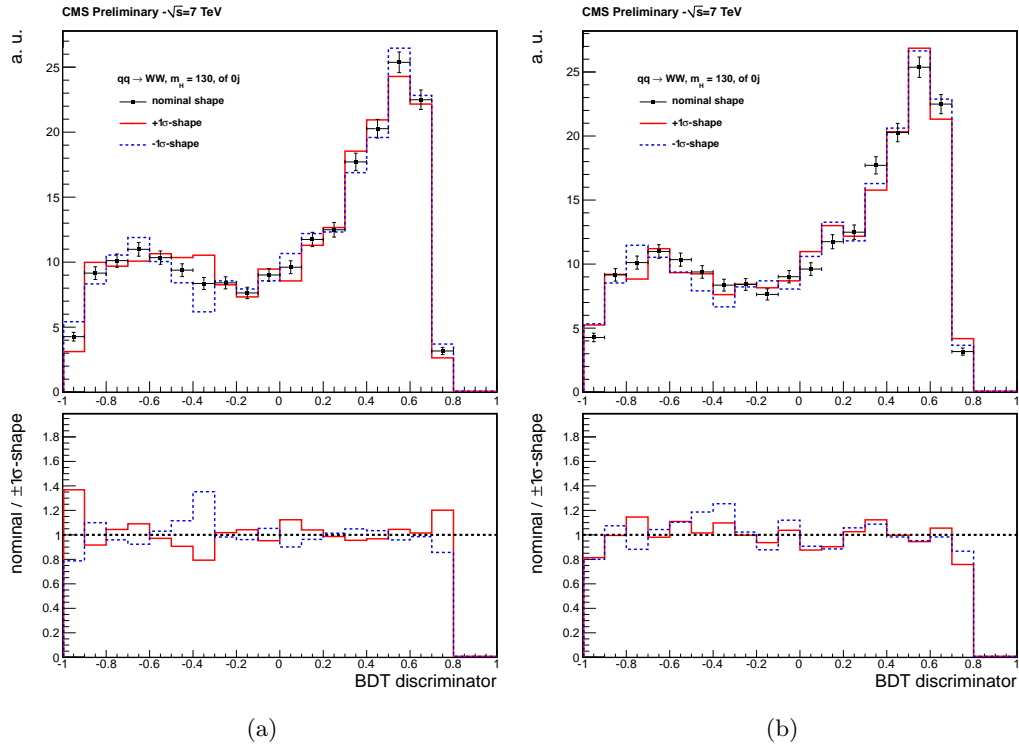


Figure 10.2: The nominal and $\pm 1\sigma$ -shapes for the WW background in the mixed flavor channel, zero-jet bin. (a) shows the shape uncertainty obtained by the comparison of MadGraph (nominal generator) with MC@NLO. (b) shows the shape uncertainty from MC@NLO factorization and renormalization scale variations.

procedure is done for the MC simulation and the scaled and/or smeared samples are re-analyzed in order to quantify the net effect of the uncertainty on the selection. The studied experimental effects are:

- Lepton identification efficiencies
- Lepton momentum scale uncertainty
- Electron energy resolution
- Jet energy scale uncertainty
- \cancel{E}_T -resolution
- Luminosity
- Pile-up
- Uncertainties on the background estimates

In the following Sections, these points are discussed in detail.

Theoretical Effect	Shape	Avg. Normalization Uncertainty [%]			
		$gg \rightarrow H$	$qq \rightarrow WW$	$gg \rightarrow WW$	di-boson
Jet bin fraction - 0 jet	no	12 – 17	4	30	3
Jet bin fraction - 1 jet	no	5 – 40	13 – 24	-	-
Jet bin fraction - 2 jet	no	5 – 15	9	-	-
PDF+ α_s - gg	no	1 – 20	-	4	-
PDF+ α_s - qq	no	-	4	-	4
Signal acceptance	no	2	-	-	-
WW scale uncertainty	yes	-	0	-	-
WW generators	yes	-	0	-	-

Table 10.3: Summary of the theoretical systematic uncertainties for different processes. A range is given in case the differences between individual channels or mass points are large.

10.3.1 Uncertainties on Lepton Identification Efficiencies

The lepton identification efficiencies were measured with the tag and probe method [130, 131] using data. A scale factor was applied event by event to MC to correct for the different lepton identification efficiencies in data and MC. The effect of the lepton identification efficiency uncertainty is estimated by shifting the applied scale factor by its statistical error up and down (all bins in the same direction). Due to a residual uncertainty of the tag and probe method, the minimum uncertainty on the scale factor is kept at 1%, even though the statistical error might be smaller. Figure 10.3(a) shows the normalization uncertainty due to the lepton identification efficiency uncertainty for the Higgs signal MC at BDT-level, as a function of the Higgs mass. The uncertainty is mass dependent for low

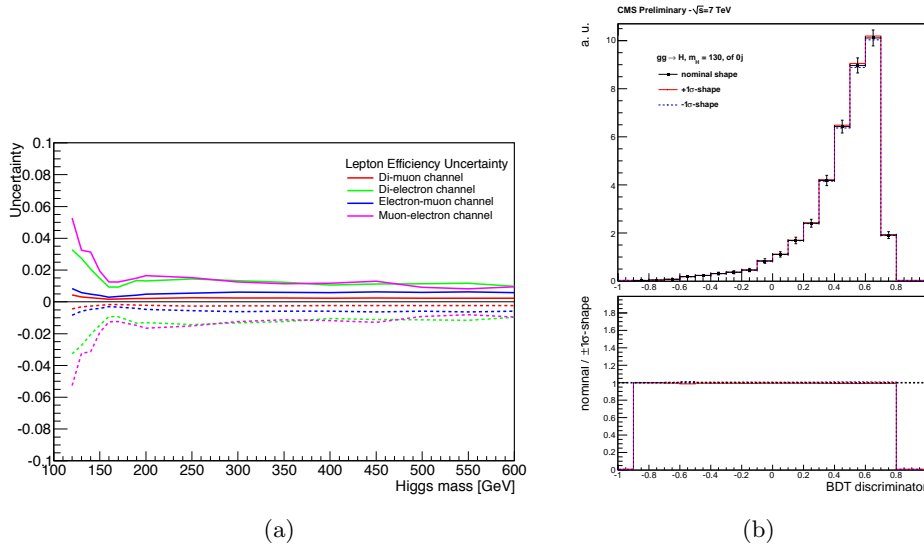


Figure 10.3: (a) The normalization error on the lepton identification efficiency for Higgs signal as a function of the Higgs mass for the zero-jet case at BDT-level. The different colors show different lepton flavor channels. (b) The nominal and $\pm 1\sigma$ shapes for the BDT shape analysis in the mixed flavor channel, zero-jet bin, $m_H = 130$ GeV.

Higgs masses and becomes roughly constant, above 150-200 GeV, around 1.5-2%. This

is mainly due to the fact that the statistical error on the scale factor is larger for low p_T leptons. For the single variable shape analysis (as well for the cut based analysis) this effect is further enhanced due to the lower lepton p_T cuts in the low mass event selection. The differences between the nominal and the varied $\pm 1\sigma$ -shapes are rather small, as can be seen in the example shown in Figure 10.3(b). The lepton identification efficiency uncertainty is treated as a shape uncertainty including by construction a normalization uncertainty.

10.3.2 Lepton Momentum Scale Uncertainty

The lepton momentum scales have relatively large uncertainties due to different detector effects. One example is the transparency loss of the ECAL crystals, due to damage to the crystal structure caused by their exposure to radiation, affecting the momentum scale of the electrons. Figure 10.4 illustrates the invariant mass of di-electron events for different run periods during Run2011A data taking. The plot shows the world average Z invariant mass and width [2] (red and green lines) and the average invariant mass (data points) and width (red band) obtained from a crystal ball fit to the data. The first bin is the average over the full Run2011A; the other bins show different periods of approximately similar luminosities. One can clearly see the trend of decreasing mass with increasing time (corresponding to an increased irradiation of the crystals). See e.g. Ref. [137] for more details on this topic and possible solutions to avoid such problems in a future upgrade of ECAL. A re-calibration was applied during the period of the third bin, hence the agreement between data and MC. This calibration is based on built in lasers which can be used to measure the response of the ECAL crystals as a function of the LHC irradiation time. [138]

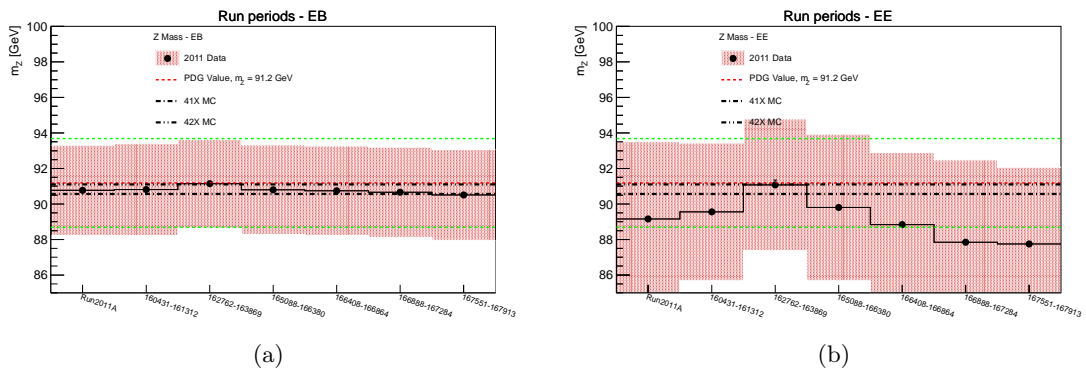


Figure 10.4: Invariant mass of di-electron events for different run periods of the Run2011A data taking. The invariant mass decreases due to the transparency loss of the crystals with increasing irradiation time. The first bin corresponds to the overall Run2011A period. The agreement in the third bin is due to fact that the correction of the data has been evaluated in that period. The transparency loss is more severe in the endcaps due to the harsher radiation environment. The red and green dashed lines indicate the Z mass and width as published in Ref. [2]. The red bands show the width obtained from a crystal ball fit of the data.

For electrons a scale uncertainty of 2% for the barrel and 4% for the endcaps respec-

tively is assigned over the full 2011 data taking.¹ For muons the scale uncertainty is assumed to be 1% independent of the pseudorapidity. The effect of the lepton scale uncertainty is estimated by scaling the lepton p_t up and down by the assigned uncertainty. In addition all correlated variables, as e.g. the invariant and transverse mass, the di-lepton p_T and the \cancel{E}_T , are recalculated. Figures 10.5(a) and 10.5(b) show the normalization uncertainties as a function of the Higgs mass for the WW background.

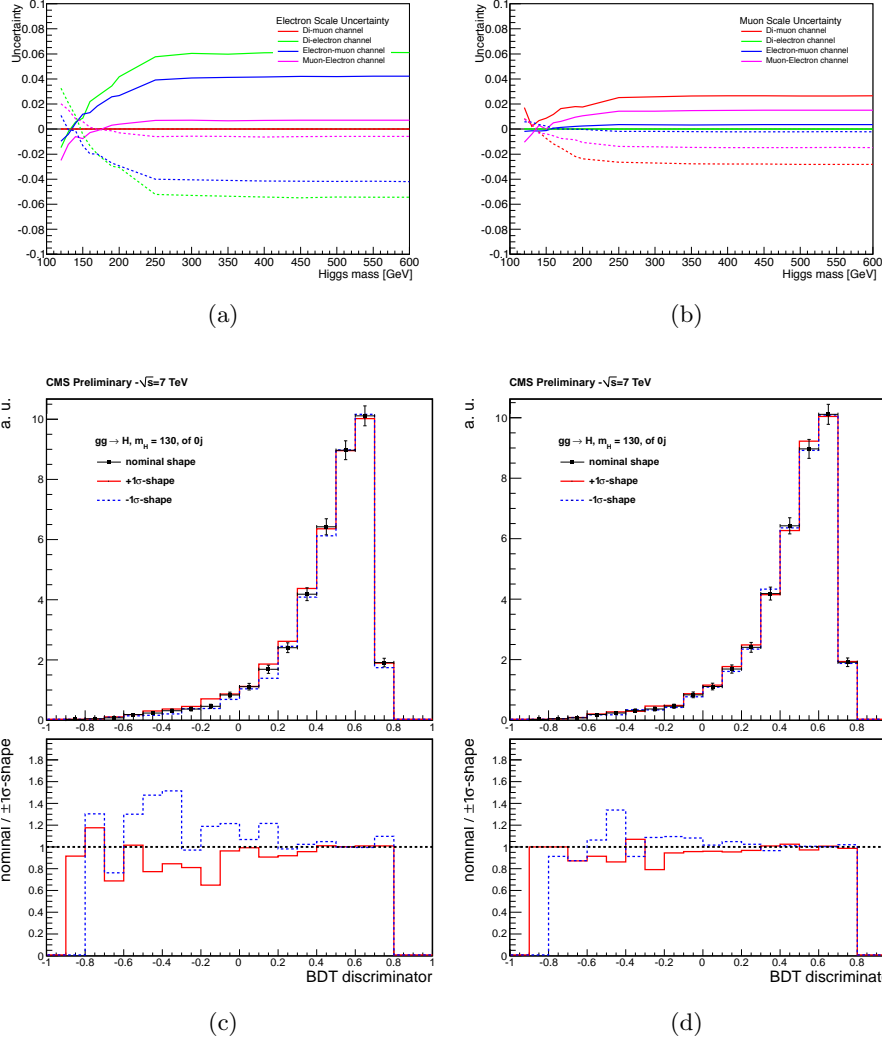


Figure 10.5: The normalization error due to the lepton scale uncertainty for the WW background MC as a function of the Higgs mass for the zero-jet case at BDT-level. For (a) electrons and (b) muons. The different colors show different lepton flavor channels. The three (nominal $\pm 1\sigma$) BDT discriminator shapes for (c) electrons and (d) muons. Mixed flavor channel, zero-jet bin, $m_H = 130$ GeV.

The normalization uncertainty is larger for electrons than for muons, due to the already mentioned transparency loss in the ECAL crystals. The lepton scale uncertainty is increasing with the Higgs mass and remains fairly constant above a Higgs mass of approximately 200 GeV. The magnitude of the uncertainty is driven by the leading lepton; i.e. a larger

¹The effect shown in Figure 10.4 was enhanced during the Run2011B period of data taking, due to the increase in luminosity.

uncertainty due to the electron scale uncertainty in the di-electron and electron-muon channel than in the channels with a muon as leading lepton. Figures 10.5(c) and 10.5(d) show examples for the nominal and $\pm 1\sigma$ -shapes. In the shape analysis, the lepton scale uncertainties are treated as a shape uncertainty.

10.3.3 Electron Energy Resolution

A 2%(4%) uncertainty is assigned to the energy of electrons in the barrel (endcaps) due to resolution effects. The impact due to this uncertainty is studied by applying a random smearing of the electron p_T using a Gaussian p.d.f. with a width of 2%(4%) of the actual electron momentum. All correlated variables, e.g. invariant mass etc., are recalculated. The uncertainty is around 1% for all channels containing at least one electron in the final state, independent of the Higgs mass. The electron resolution uncertainty is treated as a shape uncertainty, where the -1σ shape is obtained by a *mirroring* of the $+1\sigma$ shape at the nominal shape, i.e. the bin-wise addition of $d_i = y_i^{nominal} - y_i^{+1\sigma}$ to the nominal bin content $y_i^{nominal}$ in bin i , where $y_i^{+1\sigma}$ is the bin content of bin i in the smeared histogram.

10.3.4 Jet Energy Scale Uncertainty

Jets do not enter the evaluation of the discriminator directly, but are used to separate events into different jet bins. Thus, the jet energy scale (JES) uncertainty enters mainly as a normalization uncertainty on the jet bin fraction due to migration of events between different jet bins. Additionally, this migration can alter the distributions of some kinematical variables.

The JES uncertainties are estimated elsewhere [139]. These uncertainties are p_T - and η -dependent. The effect of JES uncertainty on the event selection efficiency is studied by scaling the jet momentum (up and down individually) by a p_T - and η -dependent factor, which varies between 2 to 5%. Again, after scaling, all correlated variables are recalculated. The uncertainty arises mainly due to jet bin migration between the 0 and 1 jet bin, and causes an only slightly Higgs mass dependent uncertainty of about 2 – 4% on the event selection efficiency, depending on the process. The effect of the jet energy scale uncertainty on other variables, e.g. missing transverse momentum etc., is very small. The JES uncertainty is treated as shape uncertainty. Figure 10.6 shows two examples of the shapes for the Higgs signal in the zero- and one-jet bin.

10.3.5 \cancel{E}_T -Resolution

The effect of the missing transverse momentum (\cancel{E}_T) resolution is studied by applying a Gaussian smearing of 10% on the x - and y -components of the \cancel{E}_T . All correlated variables, e.g. the transverse mass etc, are recalculated. For the same flavor channel at BDT-level, the effect of the \cancel{E}_T -resolution is found to be around 2% for high Higgs masses and around 4–6% for lower Higgs mass points. For the mixed flavor channel the uncertainty is smaller, around 1%, and constant for all Higgs mass points. \cancel{E}_T -Resolution uncertainty is treated as a shape uncertainty. The smeared distribution corresponds to the $+1\sigma$ shape and the -1σ shape is again obtained by mirroring.

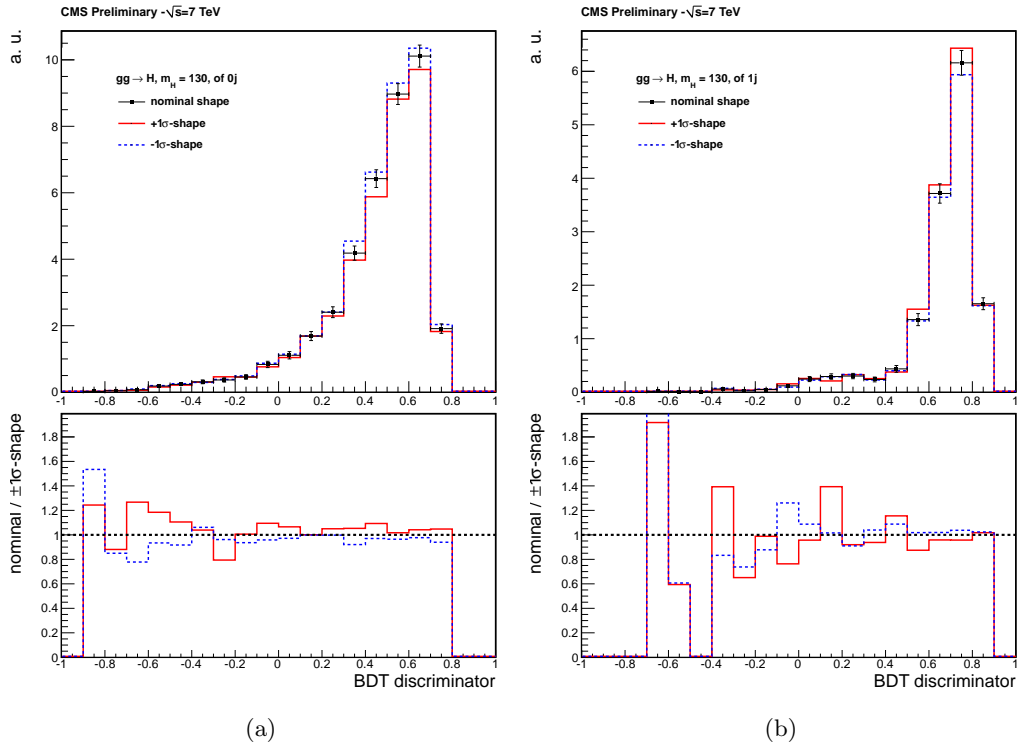


Figure 10.6: The nominal and $\pm 1\sigma$ -shapes for jet energy scale uncertainty for the gluon-fusion Higgs signal in the mixed flavor channel, (a) zero- and (b) one-jet bin. $m_H = 130$ GeV.

10.3.6 Luminosity

A 2.2% uncertainty is assumed on the measured luminosity [140]. The luminosity uncertainty is treated as a normalization uncertainty for the signal and the backgrounds whose estimates depend on MC, i.e. Drell-Yan, WW (above $m_H = 200$ GeV), all other di-boson processes. For the backgrounds with a purely data driven estimate, this uncertainty cancels out.

10.3.7 Pile-up

The number of pile-up events is measured in data, and is thus affected by two sources of uncertainties: the instantaneous luminosity per bunch crossing and the total pp cross section.

The MC simulation is reweighted to the measured number of interactions in data. A conservative approach to estimate the effect of the pile-up is to compare the reweighted with the non-reweighted MC (see also Figure 9.1 for illustration). The estimated uncertainty is found to be around 1 – 2% for most processes. Table 10.4 summarizes for the Higgs signal and some mass points the normalization uncertainty. The uncertainty on the pile-up is a normalization uncertainty.

Channel / Mass [GeV]	120	140	160	200	400
$gg \rightarrow H$					
mixed flavor, 0 jets [%]	3.6	2.7	2.7	2.7	2.3
mixed flavor, 1 jet [%]	1.1	0.3	0.5	1.5	0.7
same flavor, 0 jets [%]	4.2	3.3	3.5	3.6	2.8
same flavor, 1 jet [%]	1.8	1.2	1.32	1.2	1.3

Table 10.4: Overview of the uncertainties from pile-up for the Higgs signal for some mass points.

Background Estimate	Shape	Normalization Uncertainty [%]				
		qq \rightarrow WW	gg \rightarrow WW	W+jets	top	DY
qq \rightarrow WW	no	10	–	–	–	–
gg \rightarrow WW	no	–	50	–	–	–
W+jets	no	–	–	36	–	–
Top	no	–	–	–	15	–
DY	no	–	–	–	–	5 – 60

Table 10.5: Summary of the normalization uncertainties on the data driven background estimates. A range is given in case the differences between individual channels are large.

10.3.8 Uncertainties on Background Estimates

The systematic uncertainties for the different data driven background estimates have already been described in the corresponding Sections in Chapter 9. For completeness, Table 10.5 summarizes these uncertainties.

10.4 Statistical Uncertainties

Statistical uncertainties are taken into account in two ways: Once as a normalization uncertainty coming from the statistical error on the event yield at a certain selection level, i.e. at BDT-level. The statistical uncertainty is of the order of 1 – 2% for almost all processes, masses and channels. Secondly, the $+1\sigma$ (-1σ) shapes are constructed by a bin-wise addition (subtraction) of the statistical error in the corresponding bin, and a subsequent renormalization to the nominal histogram. This procedure has the drawback that the variation in shape is only taken into account in the case of a simultaneous upward (downward) fluctuation of all bins at the same time, while the bin-wise fluctuations are, in principle, uncorrelated. An alternative approach would be the upward only fluctuation in the left half of the histogram accompanied by a downward only fluctuation in the right half, which would probably lead to a too extreme shape uncertainty. Figure 10.7 shows two examples of the shapes for the statistical uncertainties used in the BDT analysis. Table 10.6 summarizes for some processes the statistical errors.

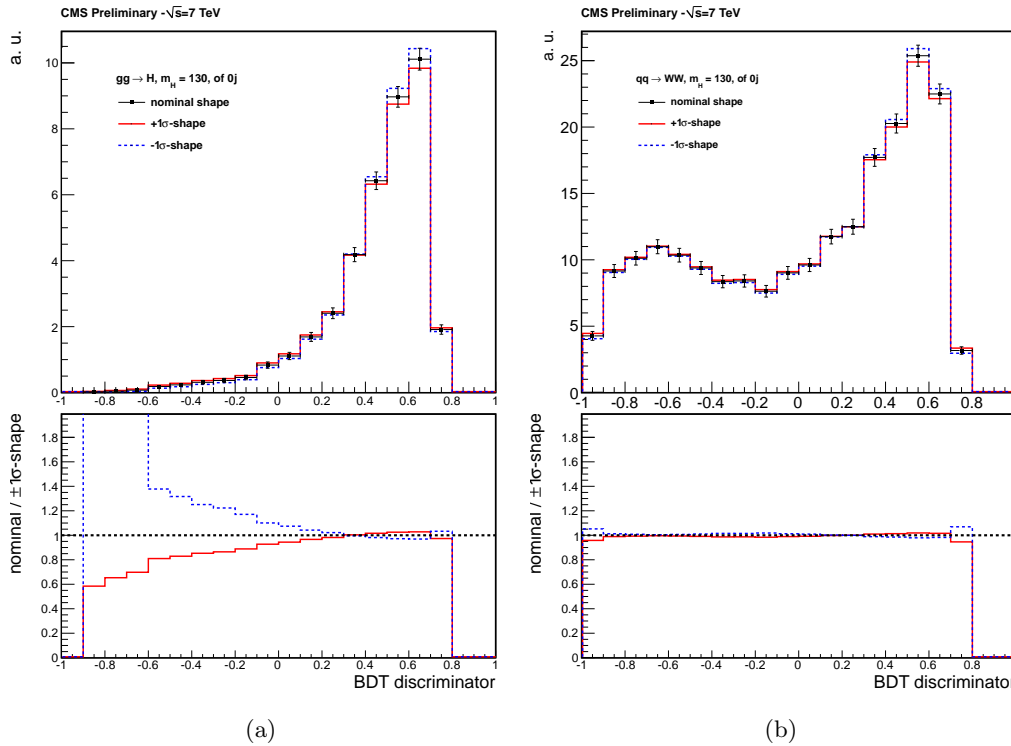


Figure 10.7: The nominal and $\pm 1\sigma$ -shapes from statistical uncertainties for (a) the Higgs signal (Higgs mass scenario of 130 GeV) and (b) the WW background, in the mixed flavor channel with no jets.

Effect	Shape	Avg. Normalization Uncertainty [%]					
		$gg \rightarrow \text{H}$	$qq \rightarrow \text{WW}$	$gg \rightarrow \text{WW}$	di-boson	top	DY
MC Statistics - 0 jet	yes	1 – 2	-	-	1 – 3	-	100
Statistics* - 0 jet	yes	-	1 – 5	20 – 50	-	5 – 55	-
MC Statistics - 1 jet	yes	1 – 5	-	-	2 – 3	-	40 – 70
Statistics* - 1 jet	yes	-	0.5 – 3	20 – 50	-	2 – 30	-

Table 10.6: Summary of the statistical uncertainties for different processes. A range is given in case the differences between individual channels or mass points are large. Be aware that this table does not contain the exact values, but illustrates the sizes of statistical uncertainties. * This is the statistical uncertainty from the data driven background estimate.

Chapter 11

Cross Section Limits and Statistical Significance

After an event selection which favors the selection of signal over background events and a corresponding estimate of the background contribution, the obtained results have to be interpreted. This is basically a statistical hypothesis testing of the observed data against the *background only* (B) and the *background+signal* (S+B) hypotheses. The method used at the LHC is called CL_s (or modified frequentist) method, which has been developed during the combination of the results from the different LEP experiments. With this method it is possible to estimate the expected signal significance, calculate $\sigma \times \text{BR}$ of a hypothetical signal or give exclusion limits for certain mass hypotheses.

In this Chapter, the statistical method used is briefly described and the results of the analysis are presented.

11.1 Statistical Method

11.1.1 Introduction to the CL_s Method

In order to discriminate the *signal-like* or *background-like* outcome of N counting experiments (i.e. N bins i), one has to define a test statistics; an optimal choice is the *likelihood ratio*

$$X = \prod_i X_i = \prod_i \frac{L(d_i | s_i + b_i)}{L(d_i | b_i)}, \quad (11.1)$$

where the likelihood function is

$$L(d_i | n_i) = \frac{n_i^{d_i} \cdot e^{-n_i}}{d_i!}, \quad (11.2)$$

which is the Poisson probability $p(d_i | n_i)$ to observe d_i events when n_i is expected. Here, d_i is the number of observed events in data in bin i , s_i is the number of signal events expected and b_i the expected number of background events. $n_i = s_i + b_i$ for the S+B and $n_i = b_i$ for the B hypothesis. The likelihood ratio for the combination of independent channels is the product of the individual likelihood ratios.

The S+B confidence level (CL_{S+B}), if d_i events are observed in bin i , is defined as

$$CL_{S+B} = P_{S+B}(X \leq X_{\text{observed}}) = \sum_{X(d'_i) \leq X(d_i)} \prod_i L(d_i | s_i + b_i), \quad (11.3)$$

where $X(d_i) = X_{\text{observed}}$ is the likelihood ratio for the observed set of values d_i and the sum runs over all likelihood ratios $X = X(d'_i)$ which are not greater than X_{observed} .

Similarly, CL_B (which can be used to quantify a discovery) is defined as

$$CL_B = P_B(X \leq X_{\text{observed}}) = \sum_{X(d'_i) \leq X(d_i)} \prod_i L(d_i | b_i). \quad (11.4)$$

With this, the confidence level for exclusion is

$$CL_S = \frac{CL_{S+B}}{CL_B}. \quad (11.5)$$

CL_S is used instead of CL_{S+B} to avoid exclusion of zero signal. A *five sigma discovery* corresponds to $1 - CL_B < 2.8 \cdot 10^{-7}$, and a signal hypothesis is called *excluded at the 95% confidence level* (95% C.L.), when $CL_S < 0.05$.¹

Note that the above method is strictly valid only if there are no systematic uncertainties on the values of d_i , s_i and b_i .

11.1.2 Limit Setting with the CL_S Method Including Systematic Uncertainties

In the more practical scenario where the different sources of uncertainties have to be included in the limit setting, the likelihood function from (11.2) gets extended to

$$L(\text{data} | \mu, \theta) = \text{Poisson}(\text{data} | \mu \cdot s(\theta) + b(\theta)) \cdot p(\tilde{\theta} | \theta) = \prod_i \frac{(\mu s_i + b_i)^{d_i} \cdot e^{-(\mu s_i + b_i)}}{d_i!} \cdot p(\tilde{\theta} | \theta). \quad (11.6)$$

The variable μ is the so called signal strength modifier, a scale factor on the signal cross section; θ is the set of nuisance parameters used to take all systematic uncertainties into account; and $p(\tilde{\theta} | \theta)$ is a p.d.f. assigned to a given nuisance parameter $\tilde{\theta}$. Often, p is chosen to be a log-normal distribution in order to obtain positively defined variables.

In analogy to the likelihood ratio in (11.1) the new test statistics is the profile likelihood ratio²

$$q_\mu = -2 \log \frac{L(\text{data} | \mu, \hat{\theta}_\mu)}{L(\text{data} | \hat{\mu}, \hat{\theta})}. \quad (11.7)$$

The numerator corresponds to the maximum likelihood (i.e. the likelihood got maximized) for some given “data” and a fixed signal strength μ , while the nuisance parameters are profiling (“left floating” within the uncertainties). $\hat{\theta}_\mu$ corresponds to those values of the nuisance parameters maximizing the numerator. In the denominator, the likelihood is

¹The $1 - CL_B < 2.8 \cdot 10^{-7}$ is the Gaussian probability to observe a 5σ deviation from the mean.

²The factor -2 and the logarithm are just conventional and do not change the result. Its origin is that the right hand side of Equation (11.7) converges to $\Delta\chi^2$, which is the difference between the χ^2 of a S+B and the χ^2 of a B only fit to a distribution, in the high statistics limit.

maximized for both μ and θ . Similarly $\hat{\mu}$ and $\hat{\theta}$ are the values maximizing the likelihood in the denominator. One can again define CL_{S+B} and CL_B

$$CL_{S+B} = P(q_\mu \leq q_\mu^{\text{observed}}) \quad \text{and} \quad CL_B = P(q_\mu \leq q_\mu^{\text{observed}}), \quad (11.8)$$

where q_μ^{observed} is the test statistics for the observed values in data. And thus again

$$CL_S = \frac{CL_{S+B}}{CL_B}. \quad (11.9)$$

As previously, if $\mu = 1$ and $CL_S < \alpha$, the signal is rejected at the $(1 - \alpha)$ confidence level; the results are often quoted in terms of the signal strength $\hat{\mu}$, which will be $\sigma/\sigma_{\text{SM}}$ in the following Section. The same method is used to derive the expected limits by replacing q_μ^{observed} from data with the mean expected values of S+B and B respectively obtained from pseudo experiments thrown around the expected yields from MC simulation.

An extensive discussion of the CL_s method can be found in Refs. [141–144].

11.2 Results for the SM Higgs Boson Search

The CL_S method described in Section 11.1 is used to compute upper limits on the Higgs boson production cross section times the branching ratio: $\sigma_{\text{SM Higgs}} \times \text{BR}(H \rightarrow WW \rightarrow \ell\nu\ell\nu)$. The limit is expressed with respect to the expected SM Higgs cross section $\sigma/\sigma_{\text{SM Higgs}}$. The limit is calculated using the shapes of the BDT discriminator output obtained at BDT-level selection. The sources of systematic uncertainties (e.g. theoretical uncertainties on cross sections, experimental effects as energy scales and resolutions or statistical uncertainties etc.) as discussed in Chapter 10 are taken into account.

The 95% C.L. expected median upper limit on the cross section is shown in Figure 11.1 for all flavor channels and jet bins combined. The flavor channels and jet bins are orthogonal data sets which are statistically combined. The green and yellow bands correspond to the 1σ and 2σ uncertainty around the median expected limit, as obtained from variation of the background expectation by 1σ or 2σ respectively. In the mass range from 140-200 GeV, the expected limit is around 0.2-0.3 times the SM cross section. The expected limit in the background only SM hypothesis excludes a SM Higgs boson in the range from 125-230 GeV. The sensitivity is degrading rapidly in the low Higgs mass region due to the steeply falling $\text{BR}(H \rightarrow WW)$ from almost 1 at $m_H = 170$ GeV to about 0.2 at $m_H = 125$ GeV (see also Figure 7.3).

The observed limit, also shown in Figure 11.1, excludes the existence of a SM Higgs boson in the range 134-211 GeV at the 95% C.L. In the intermediate Higgs mass range from 160-200 GeV, the observed limit is approximately 1σ higher than the expected limit. For the low mass region below about 160 GeV this excess increases to approximately 2σ . For high Higgs masses above 200 GeV, the observed limit is in agreement with the expected limit to within 1σ .

Due to the large mass resolution of the $H \rightarrow WW$ channel, the mass dependent event selection is very similar and thus one event (signal or background) is shared across a few different mass points.

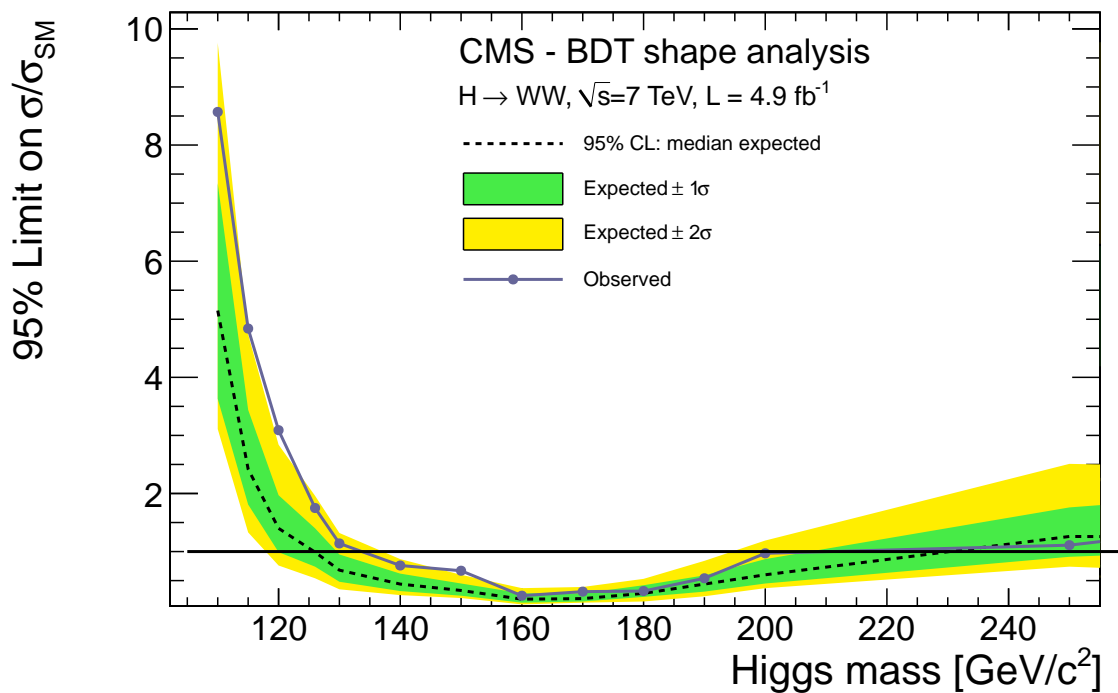
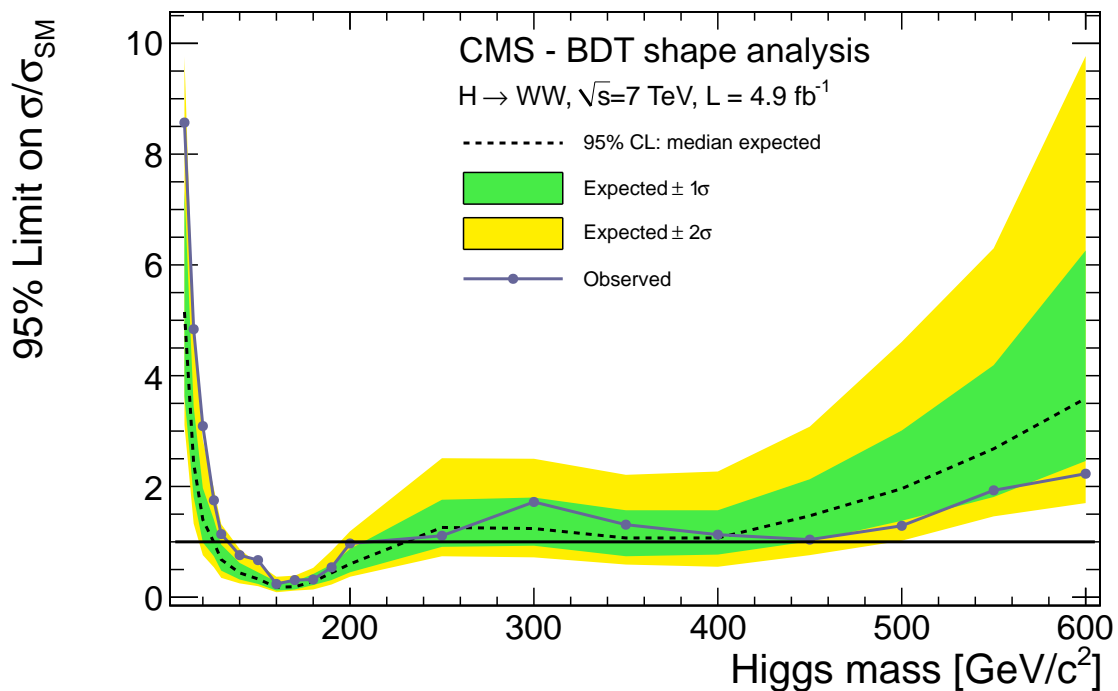


Figure 11.1: Expected and observed limits for the BDT discriminator shape analysis. All flavor channels and jet bins combined (i.e. same flavor, mixed flavor channel, zero- and one-jet bin). For (a) the full mass range and (b) the low mass region.

m_H [GeV]	Observed σ/σ_{SM}	Expected σ/σ_{SM}	1σ Range	2σ Range
110	8.57	5.15	[3.63 , 7.34]	[3.11 , 9.76]
115	4.84	2.42	[1.81 , 3.44]	[1.33 , 4.74]
120	3.09	1.40	[0.99 , 1.97]	[0.76 , 2.84]
126	1.75	0.99	[0.74 , 1.40]	[0.54 , 1.96]
130	1.14	0.68	[0.48 , 0.95]	[0.35 , 1.32]
140	0.76	0.44	[0.32 , 0.62]	[0.25 , 0.87]
150	0.67	0.33	[0.24 , 0.45]	[0.20 , 0.60]
160	0.24	0.18	[0.12 , 0.28]	[0.09 , 0.37]
170	0.31	0.19	[0.14 , 0.28]	[0.12 , 0.39]
180	0.32	0.28	[0.22 , 0.42]	[0.14 , 0.53]
190	0.54	0.44	[0.31 , 0.59]	[0.23 , 0.84]
200	0.97	0.60	[0.45 , 0.87]	[0.37 , 1.19]
250	1.11	1.26	[0.91 , 1.76]	[0.74 , 2.51]
300	1.72	1.24	[0.93 , 1.80]	[0.72 , 2.50]
350	1.31	1.07	[0.74 , 1.57]	[0.59 , 2.21]
400	1.13	1.07	[0.77 , 1.57]	[0.55 , 2.27]
450	1.04	1.47	[1.01 , 2.13]	[0.76 , 3.08]
500	1.29	1.96	[1.38 , 3.01]	[1.02 , 4.61]
550	1.93	2.68	[1.81 , 4.19]	[1.46 , 6.30]
600	2.23	3.59	[2.46 , 6.26]	[1.70 , 9.77]

Table 11.1: Observed and median expected 95% C.L. limits (σ/σ_{SM}) for the BDT shape analysis. The 1σ and 2σ ranges are also given. All flavor channels and jet bins combined (i.e. same and mixed flavor, as well as zero- and one-jet bins).

The numerical values of the expected and observed limits are summarized in Table 11.1. For a hypothetical Higgs mass of 126 GeV, the 95% C.L. expected limit is $0.99 \sigma/\sigma_{SM}$ while the observed limit is $1.75 \sigma/\sigma_{SM}$, which is approximately 1.5σ higher. Similarly for $m_H = 160$ GeV, the expected limit is $0.18 \sigma/\sigma_{SM}$ and the observed one is $0.24 \sigma/\sigma_{SM}$ — almost 1σ higher.

The corresponding local p -values are shown in Figure 11.2. The p -value corresponds to the probability of the background model to fluctuate in a way such that it describes the observed data. One can see the $\sim 2\sigma$ excess around 120 GeV Higgs mass, while there is no significant excess for higher Higgs masses. All channels and bins combined have a slightly lower significance than the one-jet combination alone because there is no significant excess in the zero-jet bin. The $> 2\sigma$ excess at $m_H = 150$ GeV is mainly driven by the zero-jet bin.

11.2.1 Channel Compatibility

The best signal cross section fit value for a Higgs mass hypothesis of $m_H = 126$ GeV and for all channels combined is $\sigma/\sigma_{SM} = 0.76_{-0.51}^{+0.52}$, shown in Figure E.2(a). In order to obtain the blue line, a simultaneous fit in all channels is performed, keeping the signal strength modifier equal in all channels at the same time, which gives one best signal cross section for all channels. The light blue band indicates the uncertainty on this best fit value.

For the black points, the signal strength modifier is left floating for each channel individually. The error bars represent the uncertainties on the fit result. The one-jet bins tend to higher signal strength, whereas the zero-jet bins are below one (as already seen

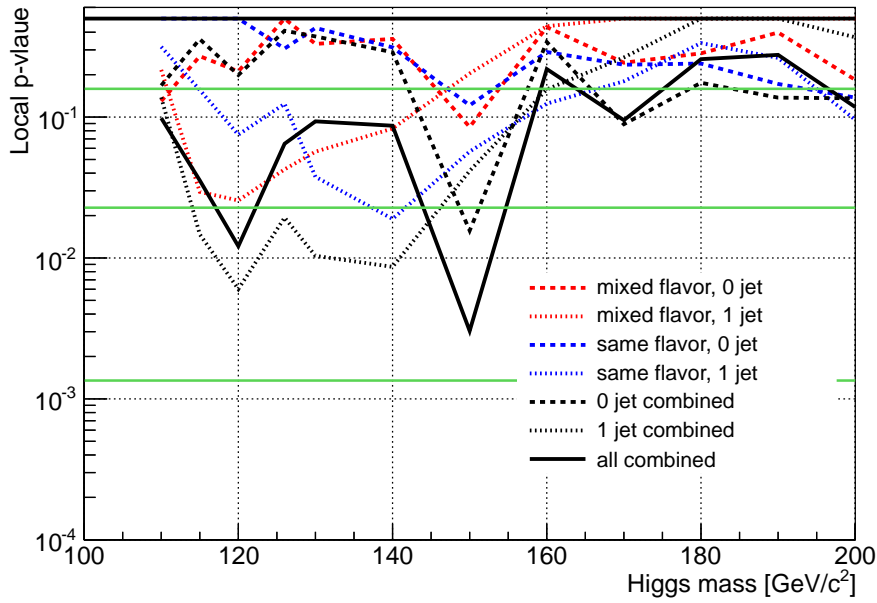


Figure 11.2: Local p -values for the low Higgs mass region. The horizontal green lines indicate (from top to bottom) the significance in terms of 1σ , 2σ and 3σ .

from the p -value plot). All individual channels are compatible with the best fit within their uncertainties, which can be interpreted such that the different channels give statistically compatible results.

For a Higgs mass hypothesis of $m_H = 160$ GeV, the best signal cross section fit value is $\sigma/\sigma_{SM} = 0.07^{+0.09}_{-0.07}$ as it is shown in Figure E.2(b) and the different channels are compatible. The same observation is true for all Higgs mass hypotheses.

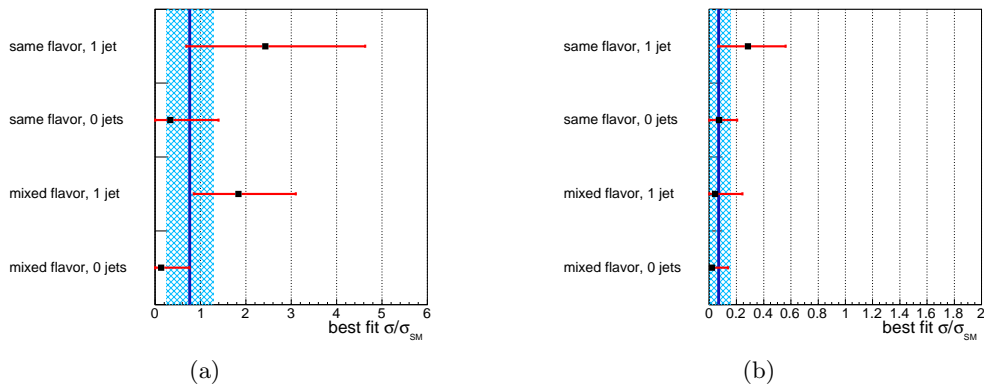


Figure 11.3: Channel compatibility. (a) for $m_H = 126$ GeV and (b) for $m_H = 160$ GeV. N.B. The two plots have different scales on the x -axis.

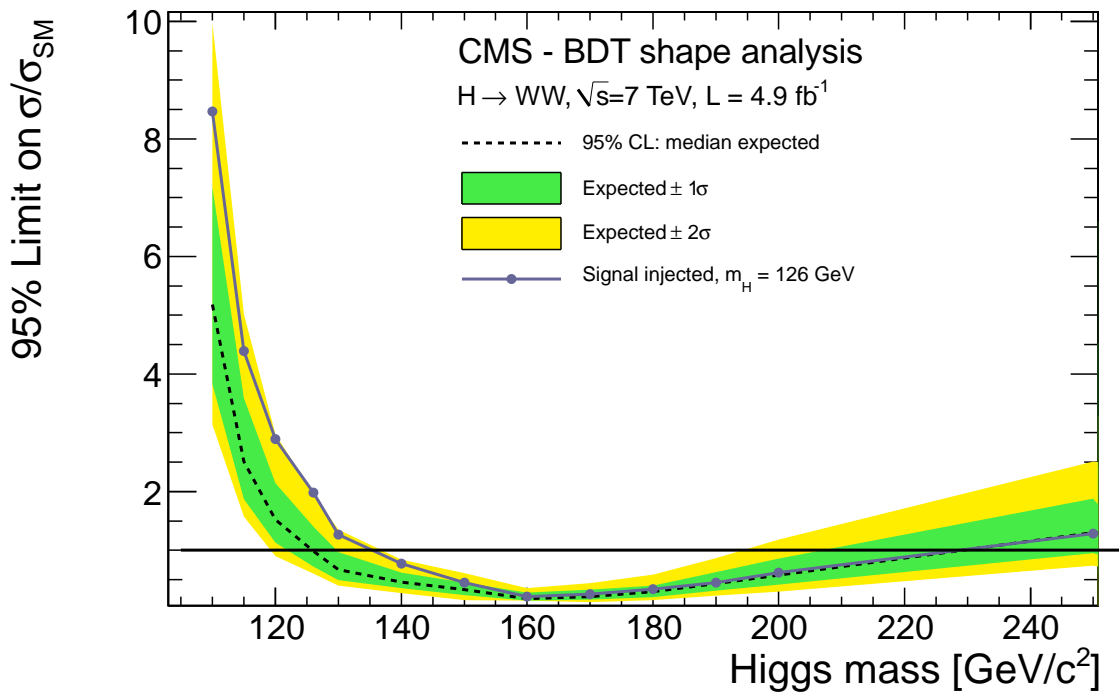


Figure 11.4: Expected limits for the BDT discriminator shape analysis. The data points show the expected limits from MC simulation in case of the presence of a Higgs boson with a mass of $m_H = 126$ GeV (no data!). All flavor channels and jet bins combined (i.e. same flavor, mixed flavor channel, zero- and one-jet bin).

11.2.2 Expected Limits in the Presence of a Signal

Due to the escaping neutrinos in the $H \rightarrow WW$ channel, no narrow mass peak can be reconstructed. This limits the mass resolution to approximately 20-30% depending on the Higgs mass. Even though the BDT-level selection is slightly Higgs mass dependent, there is a significant overlap in the event selection at the different mass points. An excess at a given Higgs mass will thus be smeared out over several Higgs mass hypotheses. In order to estimate this effect, the expected limit in case of the presence of a $m_H = 126$ GeV signal is calculated. The observed data from Figure 11.1 is replaced with the total background prediction plus a Higgs signal is injected.

The expected limits in the presence of a Higgs signal with $m_H = 126$ GeV are shown in Figure 11.4. In the mass region above approximately 170 GeV the signal injected and the expected limits are identical even though $m_H = 126$ GeV Higgs events enter the mass dependent event selection at the BDT-level for high mass. With increasing mass, more background is selected and in addition the signal cross section is expected to increase strongly with mass and thus the significance of a $m_H = 126$ GeV Higgs signal is too small to be distinguished.

The excess observed in data around 150 GeV is not observed here. In the low Higgs mass region, an approximately 2σ excess can be observed from 110-140 GeV, similarly to the one observed in data. One can see that a Higgs signal is spread over about 35 GeV.

11.2.3 Pre- and Post-Fit Normalization

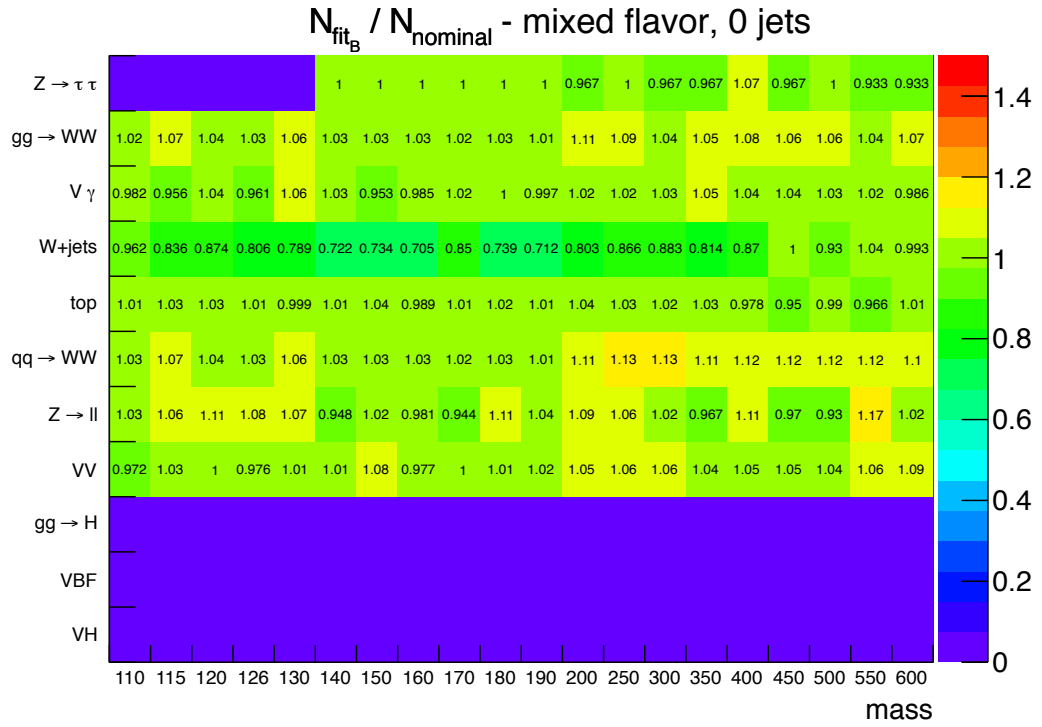
In the profile likelihood ratio method, see Section 11.1.2, the nuisance parameters are profiled. This means that the different normalizations of the background and signal components in MC are left floating within their assigned uncertainties for the limit calculation. The maximum likelihood fit of the total MC to the data thus changes the normalization of the MC (post-fit normalization) with respect to the input normalization (pre-fit normalization), which is estimated with the data driven estimates described in Section 9.4.

In order to estimate the change of normalization due to the fit, Figure 11.5 shows the ratio of the pre- and post-fit normalization of the different MC samples and for the different mass hypotheses (for the mixed flavor channel, zero-jet bin). In the background only (B) fit, the background MC only is fit to the data (Figure 11.5(a)). Light green (or 1) corresponds to no change in normalization, i.e. the background model describes the data without rescaling. Values different from 1 mean that this particular MC sample gets re-normalized.

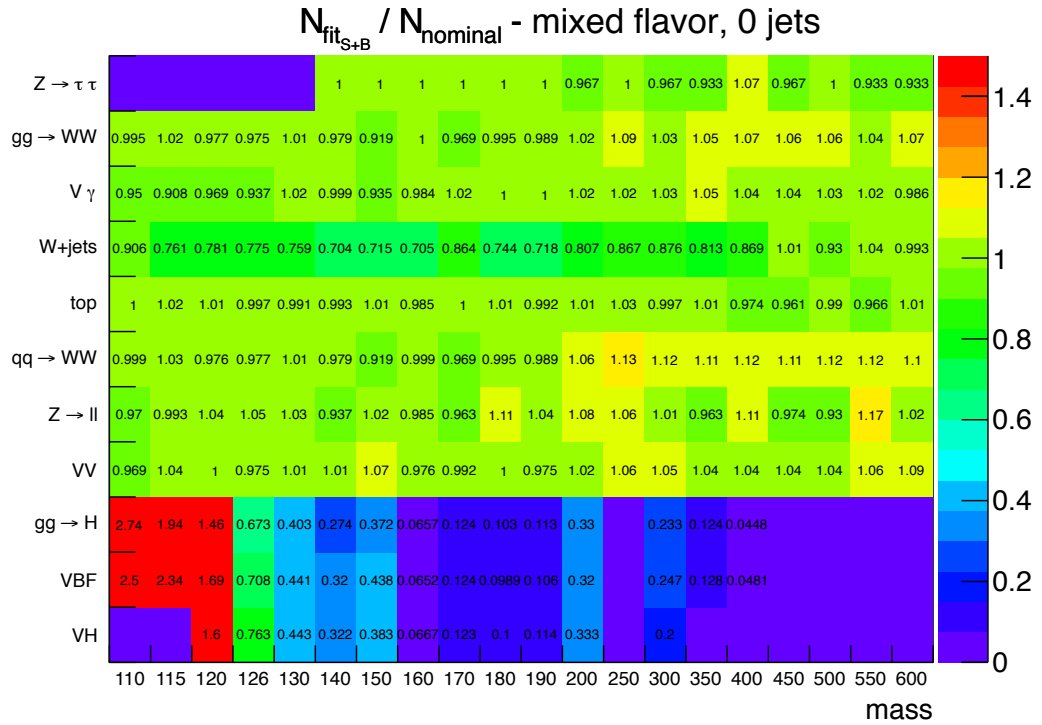
The empty bins in the $Z \rightarrow \tau\tau$ channel are because no events survive the event selection (BDT-level). The bins for the signal are empty too, because the fit does not include the signal. For the $qq \rightarrow WW$ background, the change in normalization is around 2-3% for Higgs mass hypotheses below 200 GeV, and around 10-13% above 200 GeV. This is because the WW normalization is taken from MC, without data driven correction, above 200 GeV — the WW cross section is observed to be larger in data than it is predicted by the MC, see also Refs. [145,146] for a dedicated WW cross section measurement. The same feature can be observed for the $gg \rightarrow WW$ background, but less pronounced.

In Figure 11.5(b) the same ratios for the signal plus background (S+B) fit are shown. As expected, the change in normalization of the main backgrounds is smaller, because parts of it get compensated by the Higgs signal. For the Higgs signal, the normalization ratio is significantly above 1 below ~ 120 GeV, is closest to 1 between $m_H = 120$ GeV and $m_H = 126$ GeV and decreases rapidly with increasing Higgs mass. In other words, a small Higgs mass hypothesis has a too small cross section to describe the observed data, hence gets re-normalized by a large factor. A large Higgs mass hypothesis has a large cross section and thus gets scaled down.

In general, the pre- and post-fit normalization ratios are close to one for all backgrounds which indicates that the background estimates are reasonably well understood, and similar observations can be made for the same flavor channels and the one-jet bin (see Appendix D.2 for the full set of plots.)



(a)



(b)

Figure 11.5: Pre- and post-fit normalization ratio for the different background and signal processes and as a function of the Higgs mass for the mixed flavor channel, zero-jet bin. (a) For the background hypothesis only fit, and (b) for the signal plus background hypothesis fit. Empty bins correspond to a ratio of 0.

Chapter 12

Higgs Boson Production with a Jet Veto

As mentioned in Chapter 9, the $H \rightarrow WW \rightarrow \ell\nu\ell\nu$ analysis is split into different bins according to the number of hadronic jets in the event. The main reason for that is the different background contribution in the different jet bins: i.e. the main background in the zero-jet bin is the WW background, whereas in the one-jet bin the contribution from top-pairs, which also decay in W -pairs but are accompanied by two jets from top-quark decays, increases. Thus, in order to reduce ($\varepsilon \approx 50 - 60\%$ depending on the jet p_T) contributions from top pair production, events with jets are vetoed.

The main difficulty in this separation into different jet bins is the fact that jets not only arise from b-quark decays (from the $t\bar{t}$ decay), but also from QCD radiation. This is important in the case of gluon-fusion Higgs production, as the gluons also tend to radiate additional partons. Thus, by dividing into jet bins (or by vetoing jet events), which reduces the $t\bar{t}$ background, a fraction of signal events migrate into the one-jet bin (get vetoed). Thus it is important, in order to estimate the uncertainty on the jet veto efficiency, to understand the jet veto better.

In the first Section of this Chapter, the jet veto efficiency is studied using the NLO parton shower MC program. In the second Section these results are compared to data and to the POWHEG MC program.

12.1 Simulation of the Jet Veto Efficiency in Parton Shower Monte Carlo

The jet veto efficiency is defined as the ratio

$$\varepsilon(p_T^{\text{jet veto}}) = \frac{\sigma_{0\text{-jet}}(p_T^{\text{leading}} < p_T^{\text{veto}})}{\sigma_{\text{incl.}}}, \quad (12.1)$$

where $\sigma_{0\text{-jet}}$, which depends on the jet transverse momentum $p_T^{\text{jet veto}}$, is the production cross section without additional jets above $p_T^{\text{jet veto}}$, and $\sigma_{\text{incl.}}$ is the inclusive cross section. The jet veto efficiency depends strongly on the jet transverse momentum p_T , but in principle also on the cone size R and the clustering algorithm of the jet [147]. In case of MC

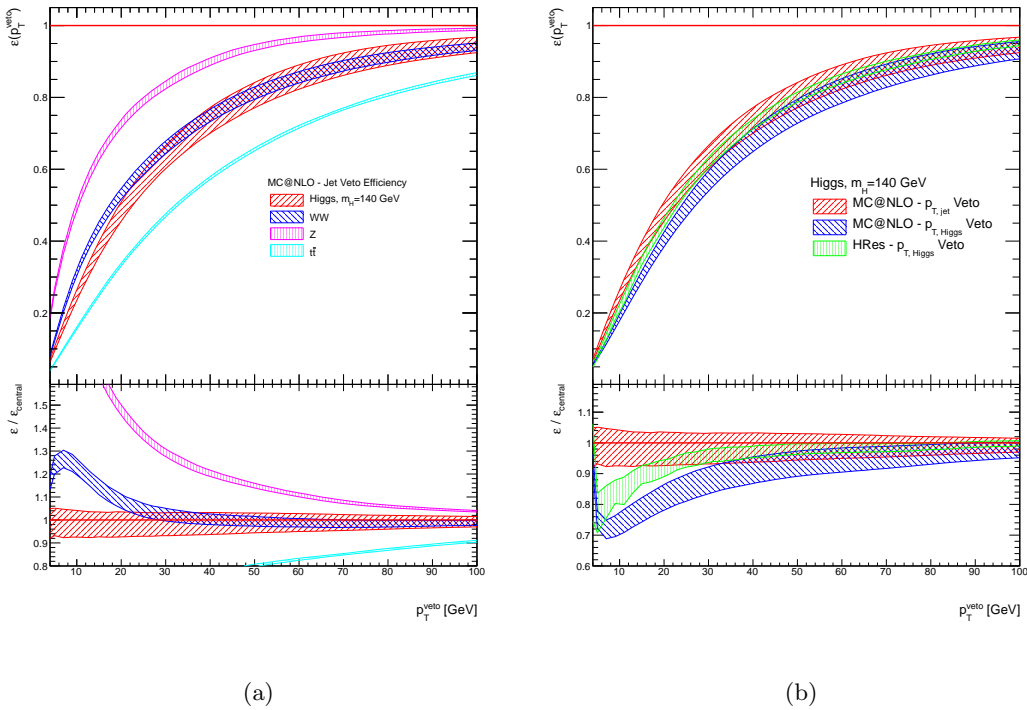


Figure 12.1: (a) Jet veto efficiency for a Higgs signal with $m_H = 140$ GeV and the WW , Z and $t\bar{t}$ backgrounds, obtained from MC@NLO. The bands are obtained from factorization and renormalization scale variations by factors $1/4\mu_{ref} < \mu_{ref} < 4\mu_{ref}$. (b) Comparison of the jet veto efficiency (red) and the Higgs p_T veto efficiency (blue), both from MC@NLO. The green band shows the Higgs p_T veto at NNLO+NNLL obtained from HRes.

simulations, it also depends on the higher order QCD corrections that are included in the theoretical calculations. See also Figure 8.6(a), where the scale uncertainty on the Higgs cross section is shown, estimated from factorization and renormalization scale variation.

Figure 12.1(a) shows the jet veto efficiency as a function of the leading jet p_T for a Higgs signal of mass $m_H = 140$ GeV obtained from MC@NLO interfaced with HERWIG for the hadronization (red band). As the jet veto efficiency depends on the hadronic activity in the event, the dependence on the factorization μ_{fac} and renormalization μ_{ref} scale is also shown, in form of bands. The scale variation was performed by a simultaneous variation (i.e. $\mu_{fac} = \mu_{ren}$) by a factor of 4; i.e. $1/4\mu_{ref} < \mu_{ref} < 4\mu_{ref}$, where μ_{ref} is the reference scale, which is summarized in Table 12.1. The PDFs used are MSTW2008NLO and jets are reconstructed using the anti- k_T algorithm with a cone size of $R = 0.5$, which clusters the generated particles into jets. Prompt leptons are excluded from the jet clustering and no detector simulation is applied (i.e. this analysis is done at *particle level*). Jets are limited to the acceptance of $|\eta| < 5$, similar to the experimental acceptance of CMS.

Figure 12.1(b) compares the jet veto efficiency (red band) with a veto on the Higgs transverse momentum (blue band), as obtained from MC@NLO. One would expect an overlap of the two bands, since the Higgs p_T is balanced by the jets. The shift between the two bands arises from hadronic activity which is not clustered in the jet, but which contributes to the Higgs transverse momentum and due to the fact that the veto is applied on the leading jet only. Thus the jet veto efficiency increases more steeply than the

Parameter	Value
Center-of-mass Energy E_{cm}	7 TeV
Heavy Quark Mass m_t	172.5 GeV
Higgs Mass m_H	140 GeV
Higgs Width Γ_H	0.00814
μ_{ref} ($gg \rightarrow H$)	$m_H/2$
μ_{ref} ($qq \rightarrow Z$)	$m_Z/2$
μ_{ref} ($qq \rightarrow WW$)	m_W
μ_{ref} ($gg/qq \rightarrow t\bar{t}$)	m_t

Table 12.1: Summary of parameters used for MC@NLO.

Higgs transverse momentum veto curve. Figure 12.1(b) also shows the Higgs transverse momentum veto as it is obtained from HRes (green band). The POWHEG Higgs p_T is slightly harder as the Higgs p_T from HRes (HqT gives the same results), which is in agreement with the study of the Higgs transverse momentum described in Chapter 8. For $p_T > 60$ GeV, the overlap is good.

Figure 12.1(a) also shows the jet veto efficiencies for the following processes: $qq \rightarrow Z + X \rightarrow \ell\ell + X$, $qq \rightarrow WW + X \rightarrow \ell\nu\ell\nu + X$ and $gg/qq \rightarrow t\bar{t} + X \rightarrow WbWb + X \rightarrow \ell\nu\ell\nu b\bar{b} + X$. The leading jet p_T spectra are expected to be different for different processes and consequently the jet veto efficiencies are different. By parametrizing the relation of the jet veto efficiencies between these processes, the jet veto efficiency measured in a well known and clean process (e.g. Drell-Yan) can be used to predict the jet veto efficiency for a Higgs signal. This makes it possible to correct the final event selection for the jet veto efficiency, based on a measurement in data.

Note that, for the $t\bar{t}$ band, the jets from b-quarks are ignored in this plot, and only jets from additional QCD radiation are counted as jets, in order to compare the jet veto efficiencies for the different processes.

As one can see from Figure 12.1(a), the jet veto efficiencies are ordered according to the invariant mass of the produced system, here: $m_Z < m_H < m_{WW} < m_{t\bar{t}}$. WW and Higgs signal overlap as the invariant masses are of a similar magnitude, despite the fact that Higgs production is a gluon-fusion process whereas for WW production only $q\bar{q}$ scattering is simulated. The higher the invariant mass of the system is, the harder the radiation of the initial-state partons. This mass dependence can be “removed” by normalizing the jet veto transverse momentum $p_T^{\text{jet veto}}$ by the invariant mass m_{inv} of the system

$$x = \frac{p_T^{\text{jet veto}}}{m_{\text{inv}}}, \quad (12.2)$$

where $m_{\text{inv}} = m_Z, m_H, 2m_W$ and $2m_t$ respectively. Figure 12.2(a) shows the jet veto efficiencies for the four processes as a function of x . The overlap between the different curves improves significantly. A minimum jet p_T of 30 GeV corresponds, in the case of the Higgs signal, to $x \approx 0.21$.

The qq induced processes, which are WW and Z production, overlap most, down to $x \sim 0.15$, whereas $t\bar{t}$ and Higgs production still shows some differences. The different initial states are expected to radiate differently: gluons radiate harder than quarks due to

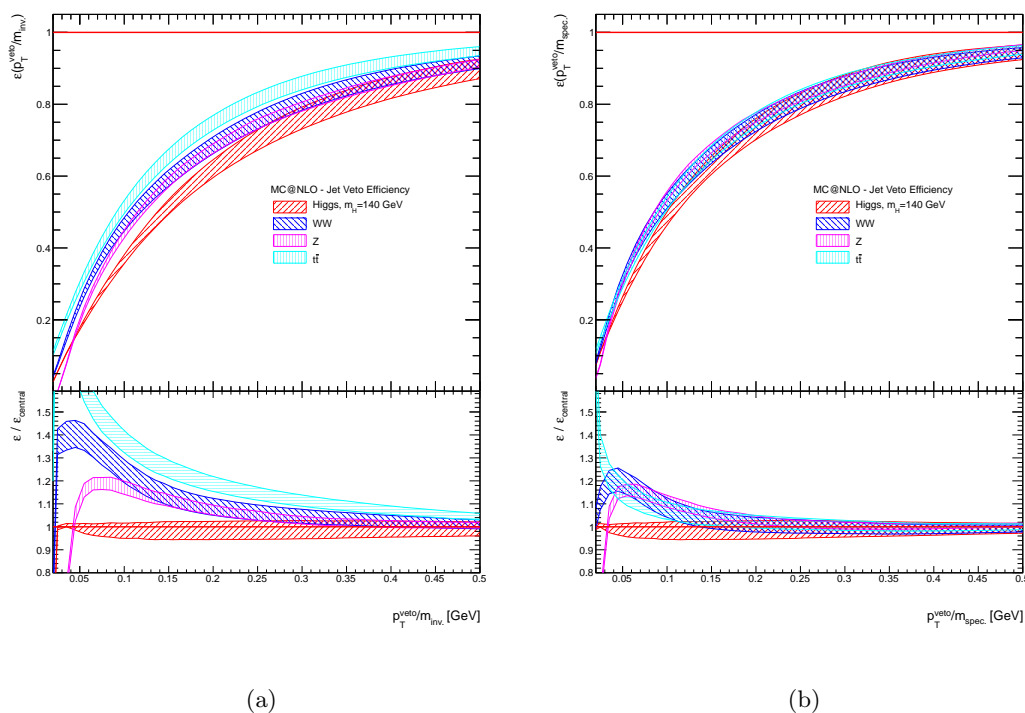


Figure 12.2: Jet veto efficiency for a Higgs signal with $m_H = 140$ GeV and the WW, Z and $t\bar{t}$ backgrounds, obtained from MC@NLO. The bands are obtained from factorization and renormalization scale variations by factors $1/4\mu_{ref} < \mu_{ref} < 4\mu_{ref}$. The lower pad shows the ratio, where $\varepsilon_{\text{central}}$ denotes the Higgs jet veto efficiency with central factorization and renormalization scales. (a) As a function of the dimensionless variable x . (b) As a function of the dimensionless variable x' .

Process	m_{inv} [GeV]	$\langle p_T \rangle$ [GeV]	m_{special} [GeV]
$gg \rightarrow H + X \rightarrow WW + X \rightarrow \ell\nu\ell\nu + X$	140	50	190
$qq \rightarrow WW + X \rightarrow \ell\nu\ell\nu + X$	160.8	35	195.8
$qq \rightarrow Z + X \rightarrow \ell\ell + X$	91.2	30	121.2
$qq/gg \rightarrow t\bar{t} + X \rightarrow WWbb + X \rightarrow \ell\nu\ell\nu bb + X$	347	10	357

Table 12.2: Summary of the different numerical values to define the dimensionless variables x and x' . The X denotes the production of possible additional jets.

Process	$\varepsilon(p_T^{\text{jet veto}} > 30 \text{ GeV})$	$\varepsilon(x > 0.2)$	$\varepsilon(x' > 0.16)$
Higgs, $m_H = 140 \text{ GeV}$	$0.66^{+0.02}_{-0.05}$	$0.63^{+0.02}_{-0.03}$	$0.64^{+0.02}_{-0.04}$
WW	$0.67^{+0.01}_{-0.02}$	$0.70^{+0.02}_{-0.03}$	$0.69^{+0.02}_{-0.03}$
Z	$0.84^{+0.01}_{-0.01}$	$0.68^{+0.01}_{-0.01}$	$0.64^{+0.02}_{-0.01}$
$t\bar{t}$	$0.48^{+0.01}_{-0.001}$	$0.76^{+0.02}_{-0.03}$	$0.70^{+0.02}_{-0.02}$

Table 12.3: Jet veto efficiencies for a leading jet $p_T > 30 \text{ GeV}$. The normalized jet veto efficiencies are at the corresponding x and x' values.

the QCD color factors. In order to compensate for a recoil of the produced system, which is process dependent, one can define another dimensionless variable

$$x' = \frac{p_T^{\text{jet veto}}}{m_{\text{special}}}, \quad (12.3)$$

where $m_{\text{special}} = m_{\text{inv}} + \langle p_T \rangle$. $\langle p_T \rangle$ is of the order of the average transverse momentum of the produced system. Table 12.3 summarizes the values used to define x' . With these numbers, one obtains the jet veto efficiencies as a function of x' as shown in Figure 12.2(b). In the case of Higgs production, a jet definition of 30 GeV corresponds to $x' \approx 0.16$. The overlap between the four different bands is further improved. At low x' , the backgrounds overlap most, whereas the Higgs signal shows some differences of 10-20%.

12.2 Ratios of Jet Veto Efficiencies

The ratios shown in Figures 12.1(a), 12.2(a) and 12.2(b) allow to determine the Higgs signal jet veto efficiency, given it is measured in one of the other processes. The only experimentally feasible process is $pp \rightarrow Z + X \rightarrow \ell\ell + X$, since it will be almost background free, especially compared to WW or $t\bar{t}$ production, where it is not possible to disentangle the two components completely.

In these ratios, some of the systematic uncertainties from parton shower and hadronization models can be expected to cancel. A simple check allows the comparison of this ratio between MC@NLO+HERWIG and POWHEG+PYTHIA. These two generator setups show some differences in the Higgs transverse momentum, as well as in the leading jet p_T . As we have seen in Section 8.2.5, the main differences between the two parton shower MCs arises from the parton shower and hadronization model used. The comparison of the leading jet p_T distributions are shown in Figure 8.8(a).

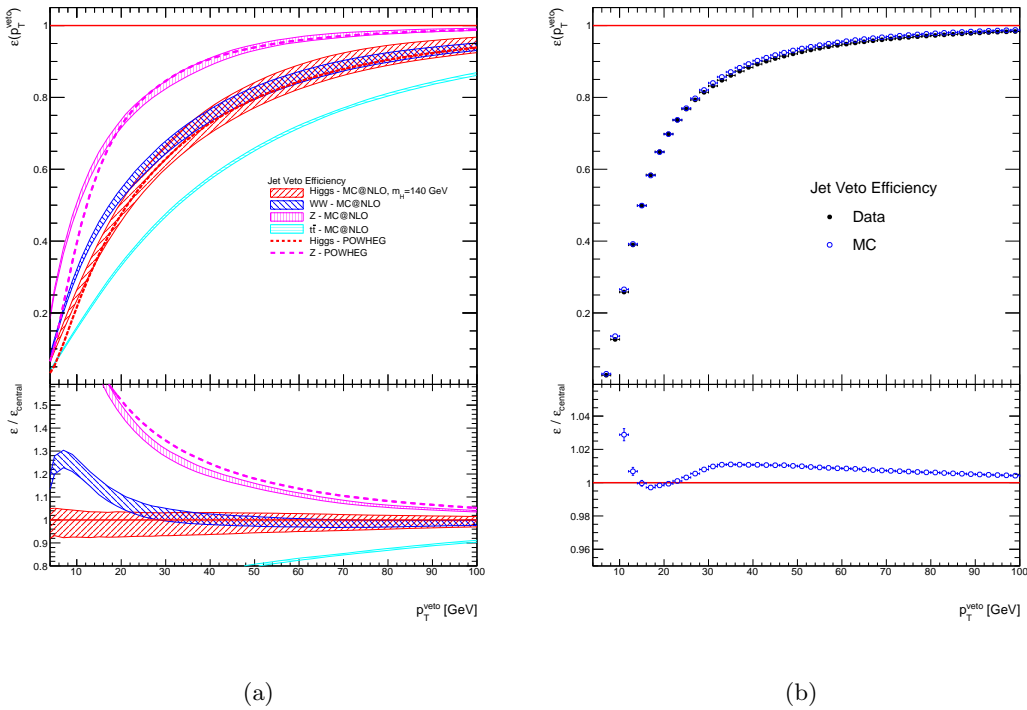


Figure 12.3: (a) Same plot as in Figure 12.1(a), but with Z and Higgs signal from POWHEG+PYTHIA. In the ratios, the systematic uncertainties are supposed to cancel. The POWHEG Z-Higgs ratio is slightly shifted compared to the MC@NLO Z-Higgs ratio. (b) Comparison of data and MC jet veto efficiency in a $Z \rightarrow ee$ sample.

Figure 12.3(a) shows a comparison of the jet efficiency ratios obtained from MC@NLO+HERWIG and POWHEG+PYTHIA. For POWHEG+PYTHIA, only the central values of the jet veto efficiencies and their ratios are shown. The Higgs p_T from POWHEG+PYTHIA is re-weighted in order to agree more or less with the MC@NLO Higgs p_T . The intrinsic harder Higgs p_T spectrum in POWHEG+PYTHIA remains reflected in a slightly steeper turn on of the Higgs jet veto efficiency. A similar trend can be observed for Z production. Above approximately 20 GeV, the POWHEG+PYTHIA jet veto efficiency curve is enclosed in the MC@NLO+HERWIG scale variation envelope.

The ratio $\epsilon_Z / \epsilon_{Higgs}$ has a similar shape, both for MC@NLO+HERWIG and POWHEG+PYTHIA, but are slightly shifted, and is thus not completely inside the band of the MC@NLO+HERWIG ratio. This indicates that not all uncertainties cancel and thus some bias is introduced. One can assume that the scale uncertainty on this ratio is of similar order as the one from MC@NLO+HERWIG, and thus the bands can be expected to be similar and probably overlapping. But still, it illustrates the possibility to measure the Higgs jet veto efficiency, to an uncertainty of probably 5-10%, in Z events.

12.3 Jet Veto Efficiency in Data

A comparison of the jet veto efficiency in data and MC as a function of the leading jet p_T , in $Z \rightarrow ee$ events is shown in Figure 12.3(b). The full 2011 data is used. The MC was

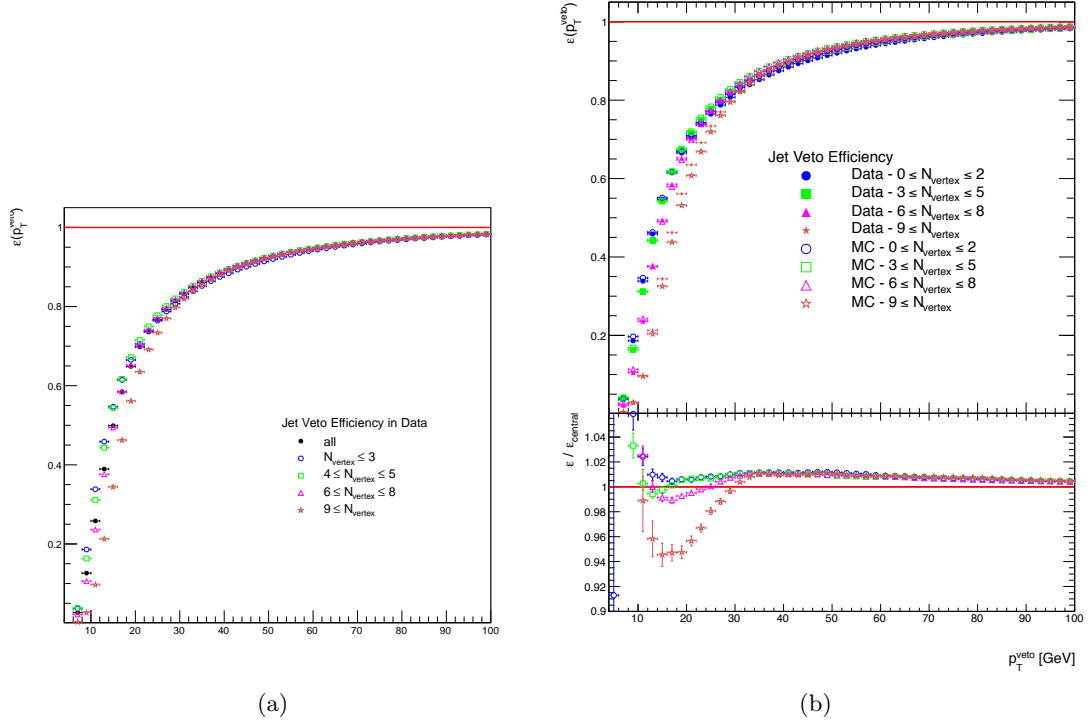


Figure 12.4: (a) Jet veto efficiency on data for different ranges of reconstructed vertices. (b) Difference in the jet veto efficiency between data and MC as a function of different number of reconstructed vertices.

generated using POWHEG+PYTHIA with the Z2 tune for the underlying event modeling. A full detector simulation was applied.

Besides the di-lepton triggers, as described in Section 9.3.1, the two electrons have to pass a minimum transverse momentum cut of 20 GeV and the invariant mass of the two electrons has to fulfill $75 < m_{ee} < 105$ GeV. Events with a third lepton are vetoed.

The jet veto efficiency is, for leading jets above 25-30 GeV, approximately 0.5-1% higher in MC than in data, which is an excellent agreement. For low p_T jets the difference is increasing which is a consequence of the low p_T jet reconstruction which has a large energy scale uncertainty. At $p_T^{\text{veto}} = 30$ GeV the difference between data and MC is around 1%.

Pile-up can be a possible origin of the difference between data and MC. In data one can clearly see a pile-up dependence. Figure 12.4(a) shows the jet veto efficiencies for different ranges of number of vertices in data. With increasing number of vertices, the jet veto efficiency gets reduced. This is due to the increased pile-up contributing to the jet energy.

The difference between data and MC is increasing with the number of vertices, as can be seen in Figure 12.4(b), especially for low p_T^{veto} . Above ~ 35 GeV the difference between data and MC is not pile-up dependent anymore.

Part IV

Summary and Appendices

Chapter 13

Summary and Discussion

13.1 Summary and Discussion of Part II

This Section summarizes the analysis of diffractive weak boson production at the LHC presented in Part II of this thesis and gives an outlook of possible improvements and future analyses.

13.1.1 Observation of Diffractive Weak Boson Production

The forward energy flow and the central charged particles multiplicity in W and Z boson events is studied in data and compared to different predictions from MC simulations. None of the MC tunes studied describes the forward energy deposit, the central charged particle multiplicity and the correlations between them simultaneously. This is mainly a consequence of the different tuning and of the event selection on which the tuning is based on.

A detailed study of W boson events with a LRG indicates the necessity of a diffractive component in both, the W production itself, as well as in the UE structure, which is currently not implemented in any MC simulation.

Due to the SD component in the total pp cross section, a significant fraction of pile-up events can not be vetoed by the single vertex requirement. This leads to an increased energy in the forward region and reduces the relative fraction of weak bosons having a LRG signature. A data driven correction of this reduction, based on measurements using zero bias collision data, yielded a fraction of about 1.5% out of the full single vertex W sample to have a LRG.

Exploiting the differences of the fractional momenta from standard parton PDFs and diffractive PDFs led to the observation of a SD component in W production. Using a binned maximum likelihood template fit, the relative fraction of SD W production in the full W sample having a LRG, was found to be around 50%. The templates were taken from SD and ND MC.

This gives a final fraction of diffractively produced W bosons of $(0.73 \pm 0.34)\%$ at the LHC, which is compatible with the observed fraction of $(1.0 \pm 0.11)\%$ at the Tevatron.

13.1.2 Future Analysis of Diffractive Weak Boson Production with CMS

During the 2010 data taking, where the average number of pile-up interactions was about 2-3 events, the relative fraction of weak vector boson events with a LRG signature was decreasing significantly with the increasing instantaneous luminosity. During 2011 and especially 2012, the average number of pile-up events was increasing to approximately 10 and 20 events respectively. Even with a large integrated luminosity, the number of single vertex weak vector boson events is still very small. Considering in addition the soft pile-up component, this makes the selection of a diffractive component using LRGs impossible.

An alternative way to select a diffractive component is to tag the intact proton using dedicated detectors very close to the beam pipe several hundred meters from the interaction point (often called roman pots) as it was done by the HERA and Tevatron experiments. As can be seen in Figure 4.4(b), this means a detector acceptance of up to $|\eta| \approx 10 - 12$ in pseudorapidity. In CMS, such a setup is available in form of the TOTEM detectors placed at approximately ± 150 m and ± 220 m from the interaction point, covering a fractional momentum loss $\xi = \frac{\Delta p}{p}$ of the proton of the order of few percent.

When using roman pots, pile-up effects are still present which via its SD component can “fake” the tagged proton. A diffractive component can be discriminated using the fractional momentum loss ξ of the intact proton. Figure 13.1 shows the $-\log(\xi)$ distribution for W events measured by CDF [91]. Due to the escaping neutrino in $W \rightarrow \ell\nu$, the momentum loss measured using the calorimeters ξ^{cal} has to be smaller than the momentum loss measured in the roman pots ξ^{RP} . This allows to distinguish between intact protons from actual SD W s and protons from SD pile-up. Also a cut on the transverse W mass can enhance a diffractive component. The diffractive W s gather thus at $-\log(\xi) \approx 1.5$ and can be discriminated from ND W production overlaid with SD pile-up.

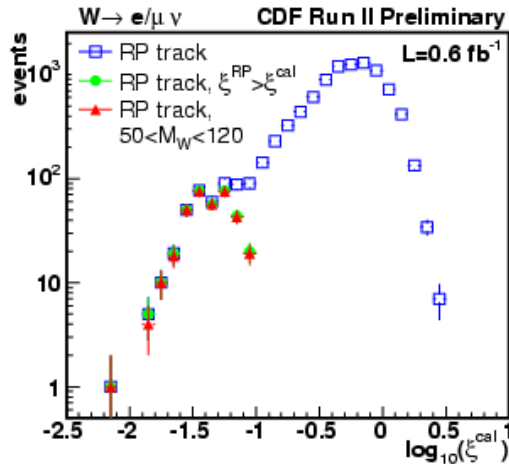


Figure 13.1: Fractional momentum loss ξ of the scattered proton in W events with a tagged proton in the roman pots.

To study the mechanisms of hard diffraction, diffractive PDFs or the the UE structure, one might consider running the LHC with special conditions. A dedicated running period with low average instantaneous luminosity would allow the selection of a large and almost pile-up free sample. This scenario might not be feasible in light of the searches for rare

processes as the SM Higgs boson or SUSY.

In order to avoid pile-up, an average instantaneous luminosity per bunch crossing of less than approximately $0.1 \mu\text{b}^{-1}\text{s}^{-1}$ is required. With 1500 bunches, one would need approximately 8-10 days of running, depending on the machine performance, in order to collect $\sim 100 \text{ pb}^{-1}$ of data with practically no additional pile-up, and thus intact LRGs. This dataset would probably already allow rather precise studies of diffractive W production, especially in combination with the larger acceptance from TOTEM.

13.2 Summary and Discussion of Part III

This Section summarizes the search for the SM Higgs boson in the fully leptonic final state of the $H \rightarrow WW$ channel which is presented in Part III of this thesis.

It also includes a short summary of the CMS results presented beginning of July 2012, which include the Higgs boson searches in other decay modes and updated analyses performed with 2012 pp collision data at $\sqrt{s} = 8 \text{ TeV}$. During the first half of 2012, the integrated luminosity has approximately doubled with respect to the 2011 data which leads to first observations of a new boson with a mass close to 125 GeV.

13.2.1 Search for the SM Higgs Boson in the $H \rightarrow WW$ Channel

First, the properties of the Higgs production and decay as well as the signature of the detectable final states are discussed. Gluon fusion is the dominant production mechanism at the LHC and the Higgs decay channel into a pair of W bosons is the most sensitive decay channel for an intermediate Higgs mass of approximately twice the W boson mass. In this mass range, the Higgs branching ratio is close to unity, and the clean leptonic final state of the subsequent W boson decays consists of two isolated high transverse momentum, oppositely charged leptons, accompanied by large missing transverse momentum from the escaping neutrinos. The absence of a mass peak, as one has in the di-photon channel, due to the escaping neutrinos is compensated by the large cross section times branching ratio $\sigma \times \text{BR}(H \rightarrow WW)$.

The main background is the irreducible WW continuum which has the same final state. An important discriminating variable, in order to separate signal and background, is the azimuthal opening angle between the two charged leptons. Due to spin correlations of the decay products of the scalar Higgs boson, the angle is expected to be smaller for the signal compared to the one in WW events. Other discriminating variables are the dilepton invariant and transverse masses and its transverse momentum as well as the lepton transverse momenta.

The distributions of all kinematic variables are fixed by the Higgs transverse momentum p_T , rapidity y and azimuthal angle ϕ . Thus, the correct simulation of these variables is important. The most up-to-date cross section calculation is performed at NNLO+NNLL which is expected to give the most precise description of the Higgs p_T . The NLO Higgs p_T simulations, which are used in the analysis, are re-weighted in order to match the NNLO+NNLL Higgs transverse momentum.

The generator studies performed in Chapter 8 lead to the following conclusions: The difference between the two studied generators (POWHEG and MC@NLO) are mainly due to the different parton shower models (i.e. PYTHIA and HERWIG); A factor 2 scale variation, which can be used to estimate the theoretical uncertainty due to missing higher order QCD corrections, leads to a 16% uncertainty on the Higgs cross section from MC@NLO; The jet bin fraction uncertainty from scale variation is 3% (4%) in the zero- (one-) jet bin; The underlying event structure has a negligible effect on the Higgs transverse momentum, while different PDF sets give a $\sim 2\%$ uncertainty. Finally, the tuning of input parameters in POWHEG can improve the agreement between the NNLO+NNLL predictions and POWHEG and render the differential re-weighting unnecessary.

In order to extract a possible signal from a SM Higgs boson, an event selection is applied in order to maximize the ratio of expected number of signal events compared to the expected number of background events passing the same selection (S/\sqrt{B}). This selection is followed by a hypothesis testing method in order to estimate the significance of a possible excess observed in data.

The analysis presented in this thesis performs a shape analysis, taking advantage of the information stored in the actual shapes of the distributions of the kinematic variables. A boosted decision tree (BDT) is used to combine different kinematic input variables into a single discriminator which is used as input to the shape analysis. The BDT discriminator is evaluated after a pre-selection enhancing the WW signature plus a mass dependent final selection based on the transverse and invariant di-lepton masses.

The MC simulation models the data well, especially for the input variables, as well for the BDT output. The BDT discriminating outputs are then used to compute upper limits on the $H \rightarrow WW$ production cross section and to evaluate the signal significance. Many systematic effects such as energy scales and resolutions and different theoretical uncertainties are determined (see Chapter 10) and included in the statistical tests.

The expected significance of this analysis, with statistics corresponding to the full 2011 dataset, is able to exclude a SM Higgs boson in a mass range from 125-230 GeV. The observed data excludes the SM Higgs boson at 95% confidence level in a mass range from 134-200 GeV. In the low Higgs mass region a $1-2\sigma$ excess of events over the expected background is observed.

A study of the jet veto in Higgs production is presented in Chapter 12, which can be used to determine the uncertainty of the jet veto efficiency for the Higgs signal for future precision measurements.

13.2.2 Observation of a New Boson With a Mass of Approximately 125 GeV

The Higgs search in the $H \rightarrow WW$ channel presented in this thesis is performed with 2011 pp collision data corresponding to 4.92 fb^{-1} . Many additional Higgs decay channels are studied by the CMS collaboration, with the main channels being $H \rightarrow \gamma\gamma$, $H \rightarrow ZZ$, $H \rightarrow WW$, $H \rightarrow b\bar{b}$ and $H \rightarrow \tau\tau$. The 2011 combination of these channels are published in Ref. [24]; the expected exclusion range is 117-573 GeV and the observed exclusion range is 127-600 GeV at 95% C.L.

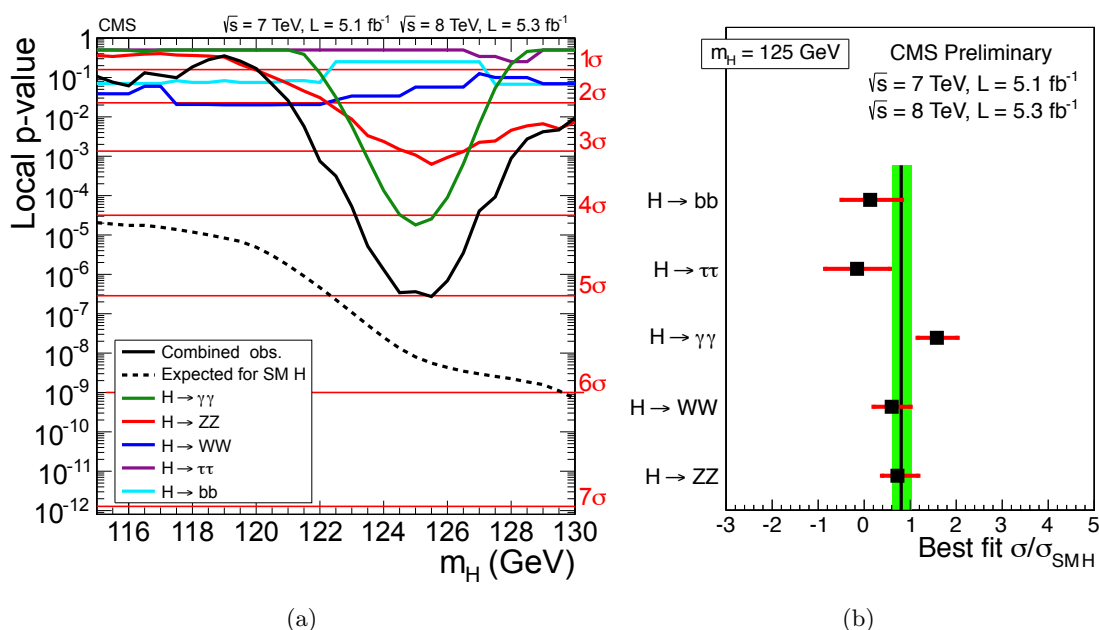


Figure 13.2: (a) The observed p-value for the different Higgs decay channels in the combination of the 2011 and 2012 data. The red lines indicate the significance in terms of σ . The dashed lines shows the expected p-value as a function of the mass of the SM Higgs boson. (b) The best fit $\hat{\mu} = \sigma/\sigma_{SM}$ for the combination of different search channels of the 2011 and 2012 data. Plots taken from Ref. [156].

The same decay channels are also analyzed with 2012 pp collision data at $\sqrt{s} = 8$ TeV. An update of these analyses combining up to 5.1 fb^{-1} of 2011 and 5.3 fb^{-1} of 2012 data for the individual channels are reported in Refs. [148–155] and the combination of these channels including the $\sqrt{s} = 7$ and 8 TeV data is presented in Ref. [156], which reports the observation of an excess over the expected background around 125 GeV.¹ This excess is consistent with the production of the SM Higgs boson of a mass of approximately 125 GeV. The combined significance of all channels of this observation is about 5σ (see Figure 13.2(a)). The expected significance of a 125 GeV Higgs boson is around 5.8σ . The $H \rightarrow \gamma\gamma$ and $H \rightarrow ZZ$ channels which both have a much better mass resolution than the other channels, contribute most to this excess. A fit to the $\gamma\gamma$ and ZZ final states yields a mass of 125 ± 0.4 (stat.) ± 0.5 (syst.) GeV. The combination excludes a SM Higgs boson in the mass range of 110–122.5 GeV and 127–600 GeV at the 95% confidence level.

The $H \rightarrow WW$ analysis of the $\sqrt{s} = 8$ TeV data excludes a Higgs boson in the mass range 135–198 GeV at 95% C.L. with an expected range of 128–250 GeV at 95% C.L. In combination with the $\sqrt{s} = 7$ TeV data, the observed exclusion range is 129–520 GeV, with an expected range of 122–450 GeV, both at 95% C.L. The excess observed at low masses is still persistent with an observed (expected) upper limit of about 2.2 (1.2) times the SM expectation, corresponding to a significance of about 1.5σ . [150]

Analogous results are also obtained from the ATLAS collaboration [157–161].

¹A historic media event took place at CERN on July 4th 2012, where the ATLAS and CMS collaborations presented their Higgs search results.

13.2.3 Next Steps Towards a Conclusive SM Higgs Boson Discovery

The observation of a new boson presented in Ref. [156] is compatible with a SM Higgs boson with a mass around 125 GeV, but one cannot conclusively say that it really is the SM Higgs. The determination of the spin of the new particle is crucial to conclude if it is the SM Higgs or not, as it is predicted to be a scalar particle.

The fact that it is observed in the di-photon final state confirms it to have spin-0 or 2, as a spin-1 particle cannot decay into two identical vector bosons. An observation of a significant excess in the $\tau\tau$ or $b\bar{b}$ final states would favor the spin-0 hypothesis, but both channels do not show any excess at 125 GeV with the current dataset [151,152].² Ref. [162] and many references therein discuss possible ways to measure the spin of the Higgs boson using angular distributions of the final states based on spin correlations. It seems that a much larger integrated luminosity is needed in order to draw a final conclusion.

The SM Higgs boson cross section and branching ratios are predicted by the theory. In order to confirm that the new boson is the SM Higgs boson, these properties have to be measured with increased statistics. The best fit signal strength $\hat{\mu}$ is shown in Figure 13.2(b). While the overall $\hat{\mu}$ value is 0.80 ± 0.22 , the individual channels are more spread. The $H \rightarrow b\bar{b}$ and $H \rightarrow \tau\tau$ channels are compatible with the presence of no signal. The $H \rightarrow WW$ and $H \rightarrow ZZ$ channels have a signal strength between 0.8 and 1 and for the $H \rightarrow \gamma\gamma$, $\hat{\mu}$ is around 1.6. The individual channels are compatible to within their errors (including statistical and systematic uncertainties) and only more data will allow to draw final conclusions.

²This is also true for ATLAS, even though there is no update including 2012 data yet.

Appendix A

Lepton Definitions

This Appendix contains the details for the cut based lepton reconstructions used in this thesis. For details on the multivariate electron identification used in the 2011 Higgs search, see Ref. [129].

A.1 2010 Electron Reconstruction

The 80% electron reconstruction working point used in the 2010 diffractive analysis had the following requirements:

- $|\Delta\eta|$ between extrapolated track and calorimeter supercluster has to be smaller than 0.004 (0.007) in the barrel (endcap)
- $|\Delta\phi|$ between extrapolated track and ECAL supercluster has to be smaller than 0.06 (0.03) in the barrel (endcap)
- $H/E < 0.04$ (0.025), where H is the hadronic energy and E the electromagnetic energy measured in the calorimeters
- $\sigma_{in\eta} < 0.01$ (0.03) (this is a shower shape variable) in the barrel (endcap)
- combined isolation variable $E_{\text{iso}}^{\text{comb.}}/E_{\text{electron}} < 0.07$ (0.06) to select isolated electrons only; combined because both the tracker and the calorimeter are used to measure energies
- electrons from conversions are removed

A.2 2010 Muon Reconstruction

Summary of the 2010 muon reconstruction used in the diffractive analysis:

- global muon
- transverse momentum $p_T > 20$ GeV

- pseudorapidity $|\eta| < 1.48$ (barrel only)
- number of hits in tracker system ≥ 10
- global fit normalized $\chi^2 < 10$
- impact parameter $|d_0| < 0.5$
- combined isolation < 10 GeV, using a cone size of $R = 0.5$

A.3 2011 Muon Reconstruction

Muons used in this analysis have to be reconstructed as global muons (see Section 3.7.3) and with a $\chi^2/\text{ndof} < 10$ on the global fit. In addition it must have at least one good muon hit and at least two matches to muon segments in different muon stations. Alternatively tracker muons are selected when satisfying the “TrackerMuonLastStationTight” selection, i.e. at least two muon segments matched at 3σ in local x - and y -coordinates, with one being in the outermost muon station.

For the so far selected muons, the following additional cuts are applied:

- ≥ 10 tracker hits
- transverse impact parameter (with respect to the primary vertex, see 9.3.2) $|d_0| < 0.02$ (0.01) cm for muons with $p_T > 20$ GeV ($p_T < 20$ GeV).
- longitudinal impact parameter (with respect to the primary vertex) $|d_z| < 0.1$ cm
- pseudorapidity $|\eta| < 2.4$
- relative p_T -resolution better than 10%

In order to reduce punch-through from hadrons and to suppress background, both muons have to be isolated. The isolation variable Iso_{PF} is calculated for each muon by summing scalarly the p_T of particle flow (PF) candidates satisfying the following requirements:

- PF candidate inside a cone of $\Delta R < 0.3$ around the muon
- $|d_z^{\text{PF candidate}} - d_z^{\text{muon}}| < 0.1$ cm, for charged PF candidates
- $p_T > 1$ GeV if the PF candidate is a neutral hadron or a photon

In order to be isolated, the barrel muons with $p_T > 20$ GeV ($p_T < 20$ GeV) are required to have $\frac{\text{Iso}_{\text{PF}}}{p_T} < 0.13(0.06)$. For endcap muons with $p_T > 20$ GeV ($p_T < 20$ GeV) $\frac{\text{Iso}_{\text{PF}}}{p_T} < 0.09(0.05)$ is required.

Table A.1 summarizes the muon efficiency scale factors.

			p_T [GeV]			
			0 – 15	15 – 20	20 – 50	> 50
η	Run2011A	> 1.47	0.991	0.959	0.994	0.993
		< 1.47	0.988	0.985	0.995	0.991
	Run2011B	< 1.47	0.961	0.959	0.985	0.984
		> 1.47	0.964	0.972	0.963	0.965

Table A.1: Muon identification efficiency scale factors as a function of electron p_T and η . The upper part of the table is for the Run2011A and the lower one for the Run2011B running period.

Appendix B

2010 and 2011 Datasets

This Appendix summarizes the data and Monte Carlo (MC) datasets used for the two analyses presented in this thesis.

B.1 2010 Datasets

The 2010 datasets used for the diffractive vector boson production analysis presented in this thesis are summarized in Table B.1 for the data and in table B.2 for the Monte Carlo.

Dataset Description	CMS Dataset Name
Single Electron	/EG/Run2010A-Nov4ReReco_v1 /Electron/Run2010B-Nov4ReReco_v1
Single Muon	/Mu/Run2010A-Nov4ReReco_v1 /Mu/Run2010B-Nov4ReReco_v1
Minimum Bias	/MinimumBias/Run2010A-Nov4ReReco_v1 /MinimumBias/Run2010B-Nov4ReReco_v1

Table B.1: Summary of the datasets used in the diffractive $W(Z)$ analysis.

B.2 2011 Datasets

The 2011 datasets used for the Higgs search presented in this thesis are summarized in table B.3 for the data and in table B.4 for the Monte Carlo.

Dataset Description	CMS Dataset Name
W	/WtoMuNu_TuneP0_7TeV-pythia6
	/WtoENu_TuneP0_7TeV-pythia6
	/WtoMuNu_TuneProQ20_7TeV-pythia6
	/WtoENu_TuneProQ20_7TeV-pythia6
	/WtoMuNu_TuneProPT0_7TeV-pythia6
	/WtoENu_TuneProPT0_7TeV-pythia6
	/WtoMuNu_TuneDW_7TeV-pythia6
	/WtoENu_TuneDW_7TeV-pythia6
	/WtoMuNu_Tune3_7TeV_pythia8
	/WtoENu_Tune3_7TeV_pythia8
	/WtoMuNu_TuneD6T_7TeV-pythia6
	/WtoENu_TuneD6T_7TeV-pythia6
	/WtoMuNu_TuneZ2_7TeV-pythia6
/WtoENu_TuneZ2_7TeV-pythia6	
Drell-Yan	/DYtoMuMu_M_20_TuneD6T_7TeV-pythia6
	/DYtoEE_M_20_TuneD6T_7TeV-pythia6
	/DYtoMuMu_M-20_TuneZ2_7TeV-pythia6
	/DYtoEE_M-20_TuneZ2_7TeV-pythia6
Minimum Bias	/MinBias_TuneD6T_7TeV-pythia6

Table B.2: Summary of the main Monte Carlo datasets used in the diffractive analysis.

Dataset Description	CMS Dataset Name
Single Electron	/SingleElectron/Run2011A-PromptReco-v4 /SingleElectron/Run2011A-PromptReco-v6 /SingleElectron/Run2011A-May10ReReco-v1 /SingleElectron/Run2011A-05Aug2011-v1 /SingleElectron/Run2011B-PromptReco-v1
Single Muon	/SingleMu/Run2011A-PromptReco-v4 /SingleMu/Run2011A-PromptReco-v6 /SingleMu/Run2011A-May10ReReco-v1 /SingleMu/Run2011A-05Aug2011-v1 /SingleMu/Run2011B-PromptReco-v1
Double Electron	/DoubleElectron/Run2011A-PromptReco-v4 /DoubleElectron/Run2011A-PromptReco-v6 /DoubleElectron/Run2011A-May10ReReco-v1 /DoubleElectron/Run2011A-05Aug2011-v1 /DoubleElectron/Run2011B-PromptReco-v1
Double Muon	/DoubleMu/Run2011A-PromptReco-v4 /DoubleMu/Run2011A-PromptReco-v6 /DoubleMu/Run2011A-May10ReReco-v1 /DoubleMu/Run2011A-05Aug2011-v1 /DoubleMu/Run2011B-PromptReco-v1
Electron-Muon	/MuEG/Run2011A-PromptReco-v4 /MuEG/Run2011A-PromptReco-v6 /MuEG/Run2011A-May10ReReco-v1 /MuEG/Run2011A-05Aug2011-v1 /MuEG/Run2011B-PromptReco-v1

Table B.3: Summary of the datasets used in the analysis.

Dataset Description	CMS Dataset Name
WW	/WWJetsTo2L2Nu_TuneZ2_7TeV-madgraph-tauola /GluGluToWWTo4L_TuneZ2_7TeV-gg2ww-pythia6
Top	/T_TuneZ2_tW-channel-DR_7TeV-powheg-tauola /Tbar_TuneZ2_tW-channel-DR_7TeV-powheg-tauola /T_TuneZ2_t-channel_7TeV-powheg-tauola /Tbar_TuneZ2_t-channel_7TeV-powheg-tauola /T_TuneZ2_s-channel_7TeV-powheg-tauola /Tbar_TuneZ2_s-channel_7TeV-powheg-tauola
$t\bar{t}$	/TTTo2L2Nu2B_7TeV-powheg-pythia6
Drell-Yan	/DYToEE_M-20_CT10_TuneZ2_7TeV-powheg-pythia /DYToMuMu_M-20_CT10_TuneZ2_7TeV-powheg-pythia /DYToTauTau_M-20_CT10_TuneZ2_7TeV-powheg-pythia-tauola /DYToEE_M-10To20_CT10_TuneZ2_7TeV-powheg-pythia /DYToMuMu_M-10To20_CT10_TuneZ2_7TeV-powheg-pythia /DYToTauTau_M-10To20_TuneZ2_7TeV-pythia6-tauola
Di-Boson	/ZZ_TuneZ2_7TeV_pythia6_tauola /WZJetsTo3LNU_TuneZ2_7TeV-madgraph-tauola
W +Jets	/WJetsToLNU_TuneZ2_7TeV-madgraph-tauola /WGToENUG_TuneZ2_7TeV-madgraph /WGToMuNuG_TuneZ2_7TeV-madgraph /WGToTauNuG_TuneZ2_7TeV-madgraph-tauola /WGstarToLNU2Mu_TuneZ2_7TeV-madgraph-tauola /WGstarToLNU2E_TuneZ2_7TeV-madgraph-tauola
Signal	/GluGluToHToWWTo2L2Nu_M-*_7TeV-powheg-pythia6 /GluGluToHToWWToLNU_TauNu_M-*_7TeV-powheg-pythia6 /GluGluToHToWWTo2Tau2Nu_M-*_7TeV-powheg-pythia6 /VBF_HToWWTo2L2Nu_M-*_7TeV-powheg-pythia6 /VBF_HToWWToLNU_TauNu_M-*_7TeV-powheg-pythia6 /VBF_HToWWTo2Tau2Nu_M-*_7TeV-powheg-pythia6 /WH_ZH_TTH_HToWW_M-*_7TeV-pythia6 /VBF_HToWWTo2LAndTau2Nu_M-*_7TeV-powheg-pythia6 /GluGluToHToWWTo2LAndTau2Nu_M-*_7TeV-powheg-pythia6

Table B.4: Summary of the main Monte Carlo datasets used in the analysis. For the signal samples, the asterisk has to be replaced with the actual Higgs mass.

Appendix C

2010 and 2011 Lepton Triggers

This Appendix summarizes the lepton triggers which are used in the two analyses presented in this thesis.

C.1 2010 Lepton Triggers

Table C.1 summarizes the lepton triggers used for the diffractive weak boson production analysis. The data has been split into run ranges of constant trigger requirements, i.e. periods in which certain trigger paths have not been pre-scaled. The logical OR of these triggers is required to pass the event selection.

Object	Trigger Name
Photon	HLT_Photon15_L1R
	HLT_Photon15_Cleaned_L1R
	HLT_Photon20_Cleaned_L1R
Single Electron	HLT_Ele10_LW_L1R
	HLT_Ele10_SW_L1R
	HLT_Ele15_SW_L1R
	HLT_Ele15_SW_CaloEleId_L1R
	HLT_Ele15_SW_TightEleId_L1R
	HLT_Ele17_SW_CaloEleId_L1R
	HLT_Ele17_SW_EleId_L1R
	HLT_Ele17_SW_TightEleId_L1R
	HLT_Ele17_SW_TighterEleIdIsol_L1R.v2
	HLT_Ele17_SW_TighterEleIdIsol_L1R.v3
Single Muon	HLT_Mu9
	HLT_Mu15

Table C.1: Summary of the trigger paths used for the 2010 data. In the very early data taking, photon triggers were used instead of electron triggers, which were not yet available at that time.

C.2 2011 Lepton Triggers

Tables C.2 and C.2 summarize the lepton triggers used for the Higgs search in 2011. The data has been split into run ranges of constant trigger requirements, i.e. periods in which certain trigger paths have not been pre-scaled.

Run Range	Trigger Name	Int. Lumi. [pb^{-1}]
160329-163261	HLT_Ele27_CaloIdVT_CaloIsoT_TrkIdT_TrkIsoT HLT_Mu15 HLT_Ele17_CaloIdL_CaloIsoVL_Ele8_CaloIdL_CaloIsoVL HLT_DoubleMu7 HLT_Mu17_Ele8_CaloIdL HLT Mu8 Ele17 CaloId	33.60
163262-164237	HLT_Ele27_CaloIdVT_CaloIsoT_TrkIdT_TrkIsoT HLT_Mu24 HLT_Ele17_CaloIdL_CaloIsoVL_Ele8_CaloIdL_CaloIsoVL HLT_DoubleMu7 HLT_Mu17_Ele8_CaloIdL HLT Mu8 Ele17 CaloId	168.60
165085-165099	HLT_Ele32_CaloIdVT_CaloIsoT_TrkIdT_TrkIsoT HLT_Mu24 HLT_Ele17_CaloIdL_CaloIsoVL_Ele8_CaloIdL_CaloIsoVL HLT_DoubleMu7 HLT_Mu17_Ele8_CaloIdL HLT Mu8 Ele17 CaloId	0.04
165102-165208	HLT_Ele32_CaloIdVT_CaloIsoT_TrkIdT_TrkIsoT HLT_Mu30 HLT_Ele17_CaloIdL_CaloIsoVL_Ele8_CaloIdL_CaloIsoVL HLT_DoubleMu7 HLT_Mu17_Ele8_CaloIdL HLT Mu8 Ele17 CaloId	4.84
165364-166967	HLT_Ele32_CaloIdVT_CaloIsoT_TrkIdT_TrkIsoT HLT_Mu30 HLT_Ele17_CaloIdL_CaloIsoVL_Ele8_CaloIdL_CaloIsoVL HLT_Mu13_Mu8 HLT_Mu17_Ele8_CaloIdL HLT Mu8 Ele17 CaloId	659.05
166968-167913	HLT_Ele52_CaloIdVT_TrkIdT HLT_Mu30 HLT_Ele17_CaloIdL_CaloIsoVL_Ele8_CaloIdL_CaloIsoVL HLT_Mu13_Mu8 HLT_Mu17_Ele8_CaloIdL HLT Mu8 Ele17 CaloId	265.75
167914-170901	HLT_Ele52_CaloIdVT_TrkIdT HLT_Mu30 HLT_Ele17_CaloIdL_CaloIsoVL_Ele8_CaloIdL_CaloIsoVL HLT_Mu13_Mu8 HLT_Mu17_Ele8_CaloIdL HLT Mu8 Ele17 CaloId	42.26

Table C.2: Summary of the trigger paths used for the Run2011A data. The blocks correspond to different run ranges of stable trigger paths, for which the integrated luminosity per run range is indicated. The listed triggers used have not been pre-scaled during the given run period.

Run Range	Trigger Name	Int. Lumi. [pb^{-1}]
171050-173235	HLT_Ele65_CaloIdVT_TrkIdT HLT_Mu30 HLT_Ele17_*_Ele8_* HLT_Mu13_Mu8 HLT_Mu17_Ele8_CaloIdL HLT_Mu8_Ele17_CaloId	706.67
173236-175910	HLT_Ele65_CaloIdVT_TrkIdT HLT_Mu40 HLT_Ele17_*_Ele8_* HLT_Mu13_Mu8 HLT_Mu17_Ele8_CaloIdL HLT_Mu8_Ele17_CaloId	302.08
175911-175921	HLT_Ele65_CaloIdVT_TrkIdT HLT_Mu40 HLT_IsoMu24 HLT_Ele17_*_Ele8_* HLT_Mu13_Mu8 HLT_Mu17_Ele8_CaloIdL HLT_Mu8_Ele17_CaloId	19.78
175973-178419	HLT_Ele65_CaloIdVT_TrkIdT HLT_Mu40_eta2p1 HLT_IsoMu24_eta2p1 HLT_Ele17_*_Ele8_* HLT_Mu13_Mu8 HLT_Mu17_Ele8_CaloIdT_CaloIsoVL HLT_Mu8_Ele17_CaloIdT_CaloIsoVL	1623.05
178420-999999	HLT_Ele80_CaloIdVT_TrkIdT HLT_Mu40_eta2p1 HLT_IsoMu24_eta2p1 HLT_Ele17_*_Ele8_* HLT_Mu17_Mu8 HLT_Mu17_TkMu8 HLT_Mu17_Ele8_CaloIdT_CaloIsoVL HLT_Mu8_Ele17_CaloIdT_CaloIsoVL	773.94

Table C.3: Summary of the trigger paths used for the Run2011B data. The blocks correspond to different run ranges of stable trigger paths, for which the integrated luminosity per run range is indicated. The listed triggers used have not been pre-scaled during the given run period. The asterisk (*) stands for CaloIdT_CaloIsoVL_TrkIdVL_TrkIsoVL.

Appendix D

Higgs Analysis — Detailed Results

This Appendix gives detailed event yields for the Higgs search presented in Part III which were omitted in the text for simplicity.

D.1 Detailed Event Yields at BDT-Level

m_H	$Z/\gamma^* \rightarrow \ell\ell$	Top	W+jets	VV	$gg \rightarrow WW$	$qq \rightarrow WW$	Σ Bkg.	Signal	Data
110	0.3 ± 0.4	8.2 ± 1.5	20.1 ± 7.3	6.5 ± 1.2	4.1 ± 0.4	98.8 ± 10.1	138.1 ± 12.6	3.1 ± 0.4	140
115	0.3 ± 0.4	9.9 ± 1.8	22.1 ± 8.0	7.4 ± 1.2	5.2 ± 0.5	122.0 ± 12.4	166.8 ± 15.0	7.6 ± 0.7	176
118	0.3 ± 0.4	11.4 ± 2.1	24.1 ± 8.7	7.8 ± 1.3	6.1 ± 0.6	134.6 ± 13.7	184.1 ± 16.4	11.7 ± 2.6	191
120	0.3 ± 0.4	11.7 ± 2.2	24.7 ± 9.0	8.0 ± 1.3	6.6 ± 0.7	143.3 ± 14.7	194.6 ± 17.4	14.5 ± 1.8	202
122	0.3 ± 0.4	12.6 ± 2.3	26.2 ± 9.5	8.1 ± 1.3	7.2 ± 0.7	152.9 ± 15.6	207.3 ± 18.4	17.7 ± 3.4	211
124	0.3 ± 0.4	13.4 ± 2.4	26.5 ± 9.6	8.2 ± 1.3	7.6 ± 0.8	160.2 ± 16.4	216.3 ± 19.3	22.1 ± 4.1	218
126	0.3 ± 0.4	16.9 ± 3.1	31.1 ± 11.2	9.3 ± 1.4	9.2 ± 0.9	193.6 ± 19.7	260.3 ± 23.0	28.4 ± 5.7	264
128	0.3 ± 0.4	17.6 ± 3.2	31.8 ± 11.5	9.4 ± 1.4	9.8 ± 1.0	202.3 ± 20.6	271.1 ± 23.9	32.9 ± 5.8	273
130	0.3 ± 0.4	18.2 ± 3.3	32.2 ± 11.7	9.5 ± 1.4	10.4 ± 1.1	210.5 ± 21.4	281.2 ± 24.7	42.3 ± 4.3	285
135	0.3 ± 0.5	24.5 ± 4.4	37.0 ± 13.4	11.0 ± 1.6	13.3 ± 1.4	257.5 ± 26.4	343.6 ± 30.0	60.0 ± 9.9	339
140	0.3 ± 0.5	26.5 ± 4.7	37.9 ± 13.7	11.2 ± 1.6	14.8 ± 1.5	275.4 ± 28.0	366.1 ± 31.6	81.3 ± 8.1	361
150	0.3 ± 0.5	35.9 ± 6.4	40.7 ± 14.7	12.9 ± 1.7	19.1 ± 1.9	333.0 ± 33.9	441.9 ± 37.6	121.7 ± 10.8	438
160	0.3 ± 0.5	40.2 ± 7.1	42.9 ± 15.5	13.2 ± 1.8	21.4 ± 2.2	354.8 ± 36.1	472.7 ± 40.0	172.4 ± 14.9	467
170	0.3 ± 0.5	45.3 ± 8.0	43.3 ± 15.6	13.5 ± 1.8	23.2 ± 2.4	366.4 ± 37.3	492.0 ± 41.3	170.8 ± 13.9	495
180	0.3 ± 0.5	52.8 ± 9.3	46.5 ± 16.8	15.4 ± 1.9	25.5 ± 2.6	402.2 ± 41.3	542.7 ± 45.6	143.9 ± 12.0	541
190	0.3 ± 0.5	60.4 ± 10.6	49.7 ± 18.0	16.9 ± 2.0	27.4 ± 2.8	433.2 ± 44.1	587.9 ± 48.9	108.7 ± 8.8	582
200	0.3 ± 0.5	66.0 ± 11.6	51.7 ± 18.7	17.7 ± 2.0	26.1 ± 0.4	397.6 ± 2.8	559.3 ± 22.2	83.5 ± 6.4	612
250	0.3 ± 0.5	96.0 ± 16.8	59.8 ± 21.6	20.7 ± 2.2	30.7 ± 0.5	492.6 ± 3.0	700.1 ± 27.6	47.1 ± 3.5	762
300	0.3 ± 0.5	101.3 ± 17.7	61.4 ± 22.1	20.9 ± 2.3	31.2 ± 0.5	503.5 ± 3.0	718.6 ± 28.6	31.7 ± 2.4	776
350	0.3 ± 0.5	104.0 ± 18.1	62.1 ± 22.4	21.0 ± 2.3	31.5 ± 0.5	508.9 ± 3.1	727.8 ± 29.1	28.8 ± 0.8	782
400	0.3 ± 0.5	104.8 ± 18.3	62.1 ± 22.4	21.3 ± 2.3	31.6 ± 0.5	511.7 ± 3.1	731.8 ± 29.2	22.1 ± 0.6	785
450	0.3 ± 0.5	105.4 ± 18.4	62.1 ± 22.4	21.6 ± 2.3	31.6 ± 0.5	512.7 ± 3.1	733.8 ± 29.3	13.6 ± 0.4	785
500	0.3 ± 0.5	105.5 ± 18.4	62.1 ± 22.4	21.6 ± 2.3	31.7 ± 0.5	513.4 ± 3.1	734.6 ± 29.3	8.3 ± 0.2	789
550	0.3 ± 0.5	105.5 ± 18.4	62.3 ± 22.5	21.6 ± 2.3	31.7 ± 0.5	513.9 ± 3.1	735.4 ± 29.3	5.3 ± 0.1	789
600	0.3 ± 0.5	105.7 ± 18.4	62.3 ± 22.5	21.6 ± 2.3	31.8 ± 0.5	514.2 ± 3.1	735.8 ± 29.3	3.4 ± 0.1	789

Table D.1: Background contributions and data yields for 4.92 fb^{-1} of integrated luminosity after the BDT selection in the zero jet bin for the mixed flavor final states. The data-driven corrections are applied.

D.2 Pre- and Post-Fit Normalization

Summary of the pre- and post-fit normalization ratios as described in Section 11.2.3.

m_H	$Z/\gamma^* \rightarrow \ell\ell$	Top	W+jets	VV	gg \rightarrow WW	qq \rightarrow WW	Σ Bkg.	Signal	Data
110	6.5 ± 10.8	4.0 ± 0.8	4.5 ± 1.7	2.1 ± 0.7	2.4 ± 0.2	59.8 ± 6.1	79.4 ± 12.6	0.9 ± 0.2	81
115	7.7 ± 10.7	5.1 ± 1.0	6.1 ± 2.3	2.9 ± 0.9	3.3 ± 0.3	76.5 ± 7.9	101.6 ± 13.5	2.9 ± 0.5	108
118	7.8 ± 10.8	6.0 ± 1.2	6.6 ± 2.4	3.3 ± 1.1	3.8 ± 0.4	88.0 ± 9.0	115.6 ± 14.3	4.6 ± 1.5	123
120	8.0 ± 10.8	6.8 ± 1.3	7.4 ± 2.7	3.6 ± 1.1	4.2 ± 0.4	94.8 ± 9.7	124.9 ± 14.9	6.4 ± 1.2	128
122	8.4 ± 10.6	7.2 ± 1.4	7.5 ± 2.8	4.0 ± 1.2	4.6 ± 0.5	102.1 ± 10.5	133.9 ± 15.3	8.8 ± 2.0	138
124	8.1 ± 10.9	8.0 ± 1.5	7.8 ± 2.8	4.1 ± 1.2	5.0 ± 0.5	108.4 ± 11.1	141.4 ± 15.9	10.7 ± 3.1	146
126	8.9 ± 12.6	9.8 ± 1.8	10.0 ± 3.7	5.2 ± 1.5	6.0 ± 0.6	127.5 ± 13.1	167.4 ± 18.7	14.6 ± 4.0	184
128	8.9 ± 12.6	10.7 ± 2.0	10.7 ± 3.9	5.4 ± 1.6	6.5 ± 0.7	134.7 ± 13.8	176.9 ± 19.3	19.1 ± 5.1	194
130	9.5 ± 12.3	11.1 ± 2.0	10.7 ± 3.9	5.6 ± 1.6	7.0 ± 0.7	141.8 ± 14.4	185.7 ± 19.5	23.7 ± 3.7	199
135	10.8 ± 11.6	13.4 ± 2.4	11.9 ± 4.3	6.1 ± 1.8	8.1 ± 0.8	156.8 ± 16.0	207.1 ± 20.4	35.8 ± 7.3	220
140	10.7 ± 11.8	15.8 ± 2.8	12.7 ± 4.6	6.7 ± 1.9	9.3 ± 1.0	170.4 ± 17.3	225.6 ± 21.7	50.2 ± 6.4	238
150	10.5 ± 12.0	20.0 ± 3.6	13.4 ± 4.9	7.4 ± 2.1	11.4 ± 1.2	192.2 ± 19.5	254.9 ± 23.8	85.6 ± 10.2	265
160	11.2 ± 11.7	22.7 ± 4.0	14.3 ± 5.2	8.1 ± 2.2	13.0 ± 1.3	205.7 ± 21.1	274.9 ± 25.1	132.2 ± 13.7	279
170	11.4 ± 11.6	24.9 ± 4.4	14.1 ± 5.1	8.6 ± 2.4	14.1 ± 1.4	213.4 ± 21.9	286.6 ± 25.8	133.3 ± 12.5	291
180	11.9 ± 12.2	27.4 ± 4.9	14.8 ± 5.4	9.9 ± 2.7	15.2 ± 1.6	225.5 ± 22.9	304.8 ± 27.2	107.8 ± 10.6	313
190	12.7 ± 13.5	32.4 ± 5.7	15.6 ± 5.7	11.7 ± 2.8	16.6 ± 1.7	247.8 ± 25.4	336.8 ± 30.1	71.7 ± 7.4	345
200	13.4 ± 14.1	35.8 ± 6.3	16.1 ± 5.8	13.0 ± 3.1	16.6 ± 0.3	239.9 ± 2.2	334.9 ± 16.9	54.2 ± 5.7	376
250	13.5 ± 16.0	56.3 ± 9.8	18.2 ± 6.6	17.0 ± 3.8	19.6 ± 0.4	312.7 ± 2.5	437.3 ± 20.4	26.5 ± 2.9	508
300	14.1 ± 15.8	58.7 ± 10.2	18.7 ± 6.8	19.5 ± 3.4	20.1 ± 0.4	319.4 ± 2.6	450.6 ± 20.5	19.6 ± 2.0	519
350	13.8 ± 16.0	60.0 ± 10.5	19.1 ± 6.9	24.1 ± 3.1	20.4 ± 0.4	322.4 ± 2.6	459.9 ± 20.7	18.2 ± 0.7	522
400	14.4 ± 15.7	60.5 ± 10.6	19.5 ± 7.1	24.5 ± 3.1	20.4 ± 0.4	324.0 ± 2.6	463.2 ± 20.6	14.5 ± 0.5	522
450	14.2 ± 15.8	60.7 ± 10.6	19.4 ± 7.0	24.7 ± 3.2	20.4 ± 0.4	324.6 ± 2.6	464.0 ± 20.7	9.0 ± 0.3	526
500	14.3 ± 15.8	60.9 ± 10.6	19.5 ± 7.0	24.8 ± 3.2	20.4 ± 0.4	325.2 ± 2.6	465.0 ± 20.7	5.6 ± 0.2	527
550	14.2 ± 15.8	60.9 ± 10.6	19.5 ± 7.1	24.8 ± 3.2	20.5 ± 0.4	325.4 ± 2.6	465.4 ± 20.7	3.4 ± 0.1	528
600	14.3 ± 15.8	60.9 ± 10.6	19.5 ± 7.1	24.9 ± 3.2	20.5 ± 0.4	325.7 ± 2.6	465.9 ± 20.7	2.3 ± 0.1	528

Table D.2: Background contributions and data yields for 4.92 fb^{-1} of integrated luminosity after the BDT selection in the zero jet bin for the same flavor final states. The data-driven corrections are applied.

m_H	$Z/\gamma^* \rightarrow \ell\ell$	Top	W+jets	VV	gg \rightarrow WW	qq \rightarrow WW	Σ Bkg.	Signal	Data
110	0.6 ± 1.0	21.1 ± 1.4	11.0 ± 4.0	4.0 ± 1.2	1.9 ± 0.5	31.9 ± 7.8	70.4 ± 9.0	1.5 ± 0.1	81
115	0.6 ± 1.0	25.4 ± 1.7	12.9 ± 4.7	4.5 ± 1.3	2.2 ± 0.5	38.8 ± 9.5	84.5 ± 10.9	3.3 ± 0.2	92
118	0.6 ± 1.0	28.1 ± 1.8	13.1 ± 4.8	4.7 ± 1.3	2.5 ± 0.6	42.0 ± 10.3	91.0 ± 11.6	5.2 ± 0.8	102
120	0.6 ± 1.0	29.7 ± 1.9	13.4 ± 4.9	4.8 ± 1.4	2.7 ± 0.7	44.7 ± 10.9	95.9 ± 12.3	6.5 ± 0.6	105
122	0.6 ± 1.0	31.5 ± 2.0	14.0 ± 5.1	4.8 ± 1.4	2.8 ± 0.7	47.0 ± 11.5	100.8 ± 12.9	7.0 ± 0.8	110
124	0.6 ± 1.0	33.4 ± 2.2	14.3 ± 5.2	4.9 ± 1.4	3.0 ± 0.7	49.6 ± 12.1	105.8 ± 13.5	9.9 ± 1.3	116
126	0.6 ± 1.0	43.4 ± 2.7	17.8 ± 6.5	5.6 ± 1.6	3.5 ± 0.9	61.6 ± 15.1	132.5 ± 16.7	12.1 ± 1.6	139
128	0.6 ± 1.0	45.8 ± 2.9	17.9 ± 6.5	5.8 ± 1.6	3.7 ± 0.9	64.2 ± 15.7	138.0 ± 17.4	13.9 ± 1.8	145
130	0.6 ± 1.0	48.2 ± 3.0	18.7 ± 6.8	5.9 ± 1.6	3.9 ± 0.9	67.2 ± 16.5	144.6 ± 18.2	17.5 ± 1.4	148
135	0.9 ± 1.5	63.2 ± 3.9	22.4 ± 8.1	6.7 ± 1.7	4.8 ± 1.2	82.8 ± 20.3	180.9 ± 22.3	26.3 ± 2.9	171
140	0.9 ± 1.5	70.2 ± 4.3	22.5 ± 8.1	7.0 ± 1.8	5.4 ± 1.3	89.3 ± 21.9	195.2 ± 23.9	34.0 ± 2.2	192
150	0.9 ± 1.5	92.0 ± 5.6	25.4 ± 9.2	8.0 ± 2.0	6.9 ± 1.7	111.2 ± 27.2	244.5 ± 29.4	51.6 ± 3.1	232
160	0.9 ± 1.5	104.4 ± 6.3	25.4 ± 9.2	8.1 ± 2.0	7.9 ± 1.9	121.0 ± 29.6	267.8 ± 31.8	79.0 ± 4.3	250
170	0.9 ± 1.5	114.1 ± 6.9	25.4 ± 9.2	8.3 ± 2.1	8.6 ± 2.1	128.2 ± 31.4	285.6 ± 33.6	82.5 ± 4.3	267
180	0.9 ± 1.5	131.1 ± 7.8	27.1 ± 9.8	8.9 ± 2.2	9.6 ± 2.3	143.6 ± 35.2	321.3 ± 37.5	73.6 ± 3.9	302
190	2.2 ± 2.2	145.8 ± 8.7	29.7 ± 10.7	9.4 ± 2.3	10.4 ± 2.6	157.7 ± 38.6	355.2 ± 41.2	58.1 ± 2.9	332
200	2.2 ± 2.2	157.8 ± 9.4	32.1 ± 11.6	9.8 ± 2.4	10.0 ± 0.3	145.5 ± 1.6	357.3 ± 15.4	44.7 ± 2.3	350
250	3.9 ± 3.2	211.9 ± 12.6	39.3 ± 14.2	12.5 ± 2.7	12.1 ± 0.3	189.0 ± 1.9	468.7 ± 19.6	27.9 ± 1.3	455
300	4.2 ± 3.7	219.3 ± 12.9	40.4 ± 14.6	12.8 ± 2.8	12.6 ± 0.3	195.8 ± 2.0	485.1 ± 20.1	21.2 ± 1.0	470
350	4.2 ± 3.7	222.5 ± 13.1	40.6 ± 14.7	13.0 ± 2.8	12.7 ± 0.3	199.0 ± 2.0	492.0 ± 20.3	20.3 ± 0.3	478
400	4.2 ± 3.7	223.8 ± 13.2	41.4 ± 14.9	13.0 ± 2.8	12.8 ± 0.3	200.5 ± 2.0	495.8 ± 20.6	16.2 ± 0.3	479
450	4.2 ± 3.7	224.4 ± 13.2	41.5 ± 15.0	13.1 ± 2.9	12.9 ± 0.3	201.8 ± 2.0	497.8 ± 20.6	10.7 ± 0.2	482
500	4.2 ± 3.7	224.6 ± 13.2	41.6 ± 15.0	13.1 ± 2.9	12.9 ± 0.3	202.6 ± 2.0	499.0 ± 20.7	7.1 ± 0.1	482
550	4.2 ± 3.7	224.9 ± 13.2	41.6 ± 15.0	13.1 ± 2.9	12.9 ± 0.3	202.8 ± 2.0	499.6 ± 20.7	4.8 ± 0.1	483
600	4.2 ± 3.7	225.0 ± 13.3	41.8 ± 15.1	13.1 ± 2.9	12.9 ± 0.3	203.1 ± 2.0	500.2 ± 20.7	3.3 ± 0.1	483

Table D.3: Background contributions and data yields for 4.92 fb^{-1} of integrated luminosity after the BDT selection in the one jet bin for the mixed flavor final states. The data-driven corrections are applied.

D.3 Channel Compatibility for Signal Injection

Same plot as in Figure 11.3 but for the case with a signal with $m_H = 126 \text{ GeV}$ injected. As expected the signal strength of each individual channel as well as for the combined fit is very close to one.

m_H	$Z/\gamma^* \rightarrow \ell\ell$	Top	W+jets	VV	gg \rightarrow WW	qq \rightarrow WW	Σ Bkg.	Signal	Data
110	8.6 ± 1.9	9.4 ± 0.7	2.3 ± 0.9	1.6 ± 0.9	0.7 ± 0.2	13.8 ± 3.4	36.4 ± 4.2	0.3 ± 0.0	36
115	11.2 ± 2.4	12.2 ± 0.9	3.5 ± 1.3	2.1 ± 1.1	1.0 ± 0.2	17.1 ± 4.2	47.1 ± 5.2	1.0 ± 0.1	47
118	12.3 ± 2.7	14.2 ± 1.0	3.8 ± 1.4	2.3 ± 1.1	1.2 ± 0.3	19.8 ± 4.8	53.5 ± 5.9	1.5 ± 0.4	54
120	13.1 ± 2.8	15.9 ± 1.1	3.9 ± 1.4	2.4 ± 1.2	1.2 ± 0.3	21.5 ± 5.3	58.0 ± 6.3	2.3 ± 0.4	58
122	14.3 ± 3.0	17.0 ± 1.2	3.7 ± 1.4	2.5 ± 1.2	1.5 ± 0.4	23.4 ± 5.7	62.4 ± 6.8	2.9 ± 0.6	65
124	15.5 ± 3.3	18.7 ± 1.3	4.1 ± 1.5	2.6 ± 1.3	1.6 ± 0.4	25.5 ± 6.3	67.9 ± 7.5	3.8 ± 0.8	68
126	20.3 ± 4.4	22.6 ± 1.5	4.0 ± 1.5	3.0 ± 1.5	1.9 ± 0.5	29.9 ± 7.3	81.7 ± 8.9	4.7 ± 0.9	87
128	20.9 ± 4.5	24.2 ± 1.6	3.9 ± 1.4	3.1 ± 1.5	2.0 ± 0.5	32.1 ± 7.9	86.3 ± 9.5	6.3 ± 1.2	96
130	21.5 ± 4.6	26.1 ± 1.7	4.3 ± 1.6	3.4 ± 1.5	2.2 ± 0.5	34.7 ± 8.5	92.1 ± 10.1	7.8 ± 1.0	101
135	23.9 ± 5.1	31.1 ± 2.0	4.8 ± 1.8	3.6 ± 1.6	2.6 ± 0.6	39.4 ± 9.6	105.4 ± 11.4	12.3 ± 1.8	115
140	26.8 ± 5.7	35.9 ± 2.3	6.3 ± 2.3	3.8 ± 1.7	3.1 ± 0.8	43.8 ± 10.7	119.8 ± 12.7	17.6 ± 1.6	120
150	25.6 ± 4.0	44.3 ± 2.7	6.4 ± 2.3	4.2 ± 1.9	3.9 ± 1.0	52.0 ± 12.7	136.4 ± 14.0	31.8 ± 2.6	139
160	26.9 ± 4.1	51.7 ± 3.2	6.9 ± 2.5	4.5 ± 2.0	4.6 ± 1.1	58.6 ± 14.4	153.3 ± 15.6	54.1 ± 3.9	152
170	27.6 ± 4.2	56.7 ± 3.5	7.0 ± 2.6	4.8 ± 2.1	5.0 ± 1.2	62.8 ± 15.4	163.8 ± 16.7	56.0 ± 3.8	164
180	28.5 ± 5.3	62.5 ± 3.8	7.7 ± 2.8	5.5 ± 2.2	5.4 ± 1.3	68.3 ± 16.6	177.9 ± 18.3	47.2 ± 3.3	181
190	31.2 ± 5.7	71.4 ± 4.3	8.1 ± 3.0	6.1 ± 2.5	5.8 ± 1.4	76.5 ± 18.7	199.3 ± 20.5	32.4 ± 2.3	199
200	37.9 ± 8.2	78.4 ± 4.7	9.1 ± 3.3	6.8 ± 2.8	5.9 ± 0.2	74.9 ± 1.2	213.0 ± 10.5	25.7 ± 1.8	220
250	41.7 ± 9.6	111.3 ± 6.6	11.3 ± 4.1	8.7 ± 3.5	7.2 ± 0.2	102.3 ± 1.4	282.5 ± 12.9	13.7 ± 1.0	295
300	42.4 ± 9.6	114.8 ± 6.8	11.6 ± 4.2	9.6 ± 3.0	7.4 ± 0.2	106.4 ± 1.5	292.3 ± 12.9	11.1 ± 0.8	312
350	35.5 ± 7.2	115.9 ± 6.8	11.9 ± 4.3	10.6 ± 2.5	7.5 ± 0.2	107.8 ± 1.4	289.3 ± 11.2	11.0 ± 0.3	317
400	42.3 ± 9.4	116.6 ± 6.9	12.2 ± 4.4	10.8 ± 2.5	7.6 ± 0.2	108.6 ± 1.4	298.1 ± 12.8	9.2 ± 0.2	320
450	42.2 ± 9.4	116.9 ± 6.9	12.3 ± 4.5	10.9 ± 2.6	7.6 ± 0.2	109.1 ± 1.4	298.9 ± 12.8	6.4 ± 0.1	321
500	42.5 ± 9.4	117.0 ± 6.9	12.3 ± 4.5	10.9 ± 2.6	7.6 ± 0.2	109.3 ± 1.4	299.7 ± 12.9	4.2 ± 0.1	321
550	42.4 ± 9.4	117.1 ± 6.9	12.4 ± 4.5	11.0 ± 2.6	7.6 ± 0.2	109.5 ± 1.4	300.1 ± 12.9	2.9 ± 0.1	322
600	43.3 ± 10.1	117.2 ± 6.9	12.4 ± 4.5	11.0 ± 2.6	7.6 ± 0.2	109.7 ± 1.4	301.2 ± 13.4	2.0 ± 0.0	323

Table D.4: Background contributions and data yields for 4.92 fb^{-1} of integrated luminosity after the BDT selection in the one jet bin for the same flavor final states. The data-driven corrections are applied.

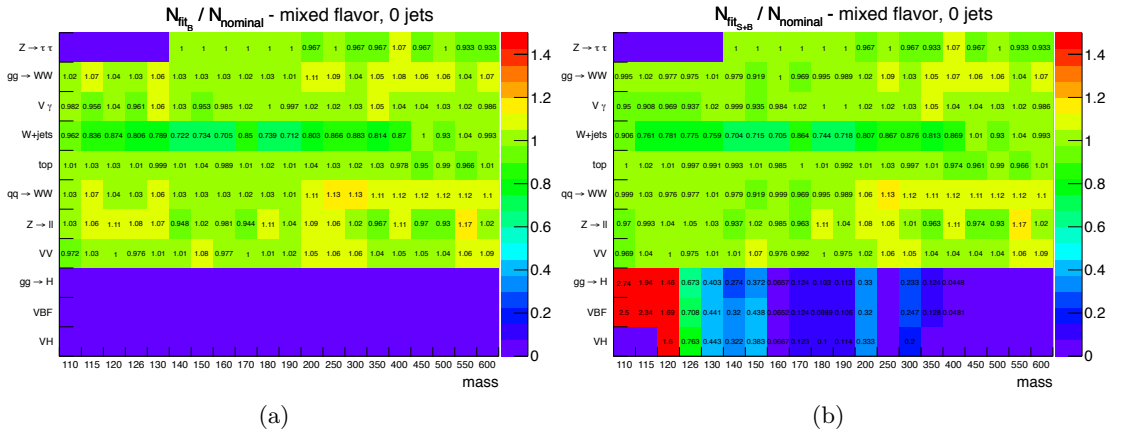


Figure D.1: Pre- and post-fit normalization ratio for the different background and signal processes and as a function of the Higgs mass for the mixed flavor, 0 jet channel. (a) For the background hypothesis only fit, and (b) for the signal plus background fit.

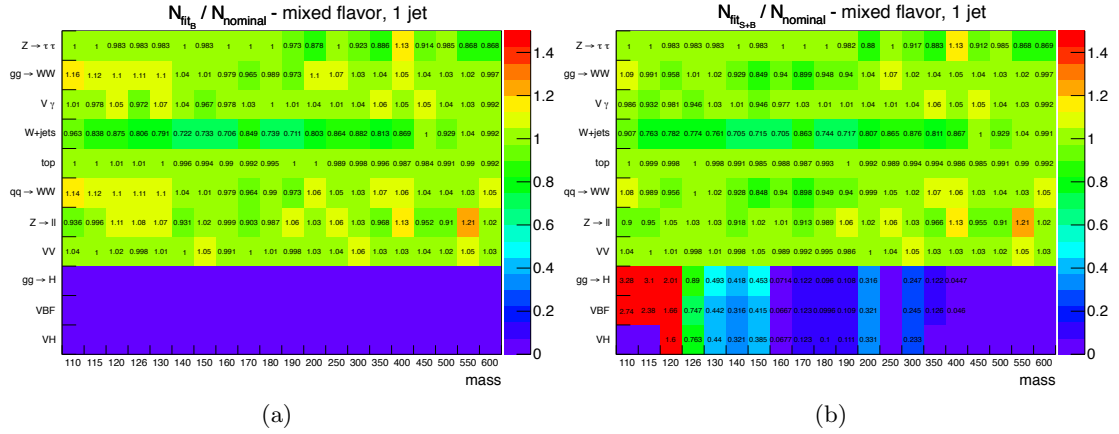


Figure D.2: Pre- and post-fit normalization ratio for the different background and signal processes and as a function of the Higgs mass for the mixed flavor, 1 jet channel. (a) For the background hypothesis only fit, and (b) for the signal plus background fit.

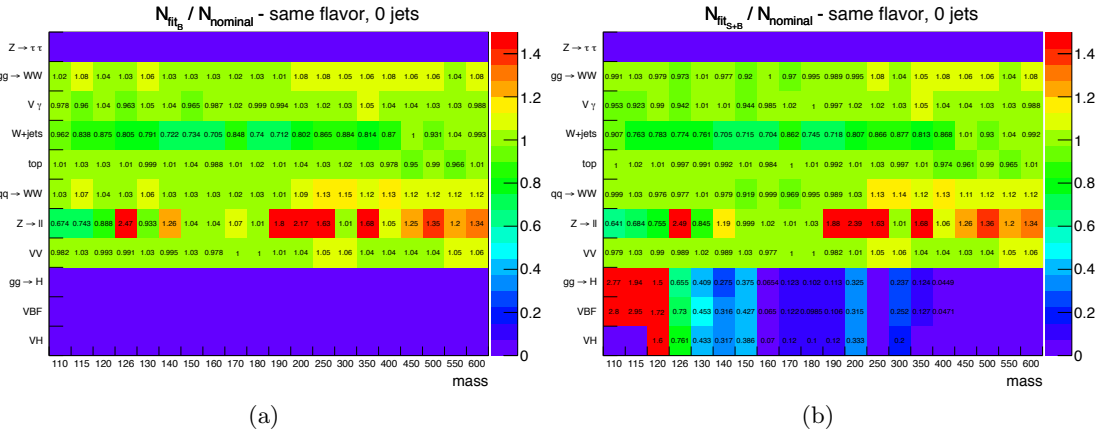


Figure D.3: Pre- and post-fit normalization ratio for the different background and signal processes and as a function of the Higgs mass for the same flavor, 0 jet channel. (a) For the background hypothesis only fit, and (b) for the signal plus background fit.

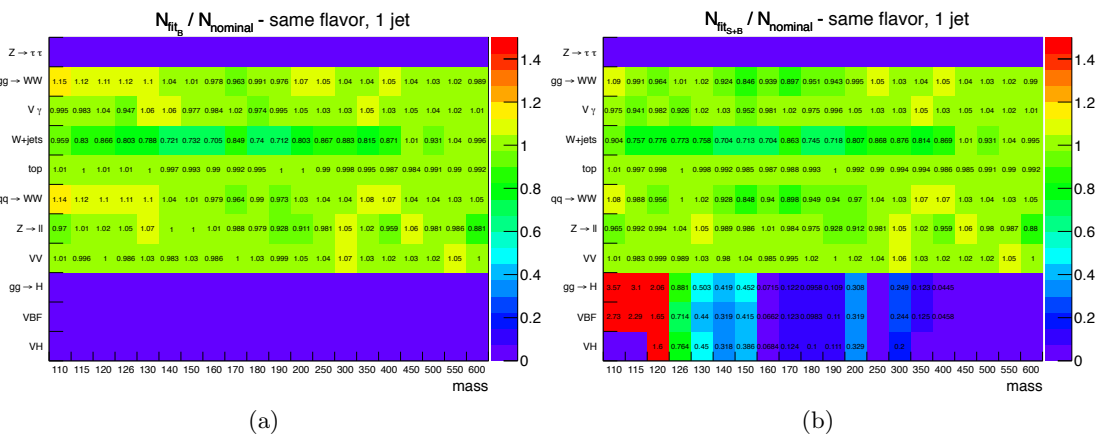


Figure D.4: Pre- and post-fit normalization ratio for the different background and signal processes and as a function of the Higgs mass for the same flavor, 1 jet channel. (a) For the background hypothesis only fit, and (b) for the signal plus background fit.

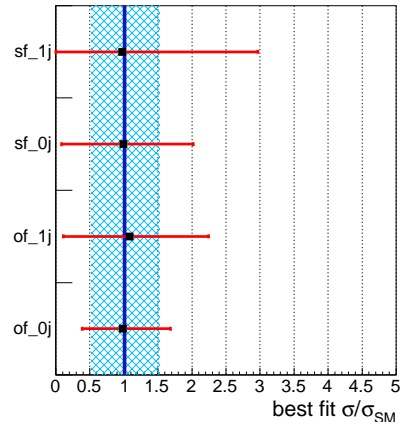


Figure D.5: Channel compatibility for $m_H = 126$ GeV for the signal injected (Higgs mass $m_H = 126$ GeV) expectation.

Appendix E

Event Display of a Diffractive W Event

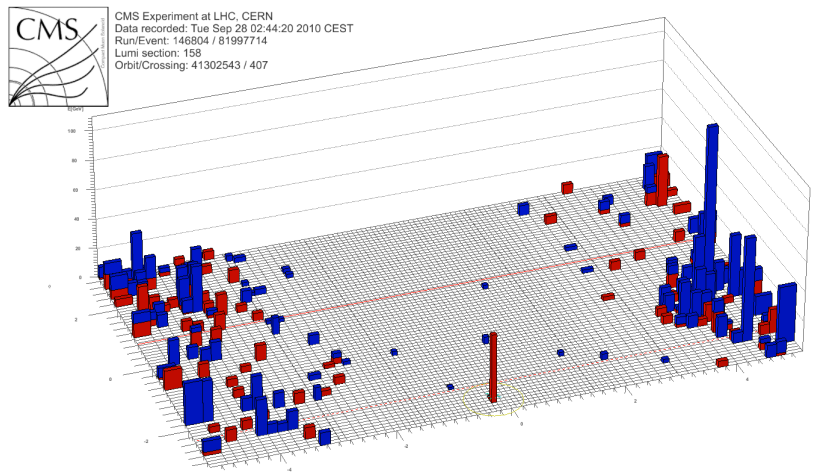
This Appendix shows event Displays of a non-diffractive and of a single diffractive W event.

E.1 Non-Diffractive W Event

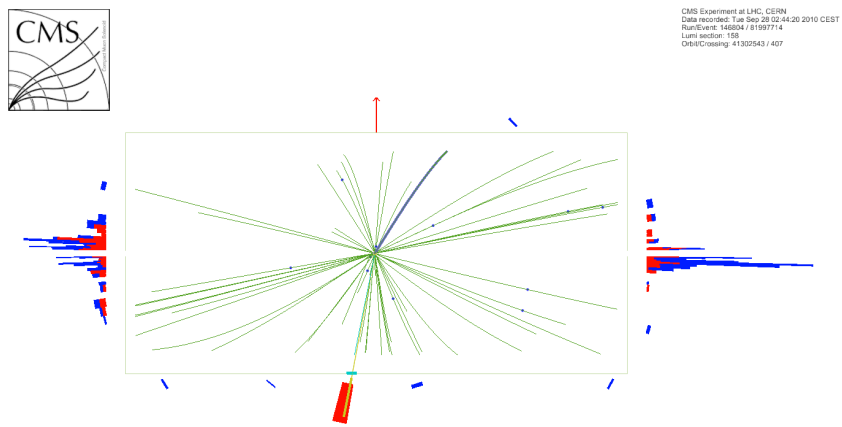
Figure E.1 shows a non-diffractive event display of a $W \rightarrow e\nu$ event. The central energy deposit in ECAL from the electron is clearly visible in Figure E.1(a). One can see relatively high energy deposits on both sides of CMS.

E.2 Diffractive W Event

Similar event displays for a diffractive W event. One can again see the electron. The large rapidity gap is nicely visible in Figure E.2.

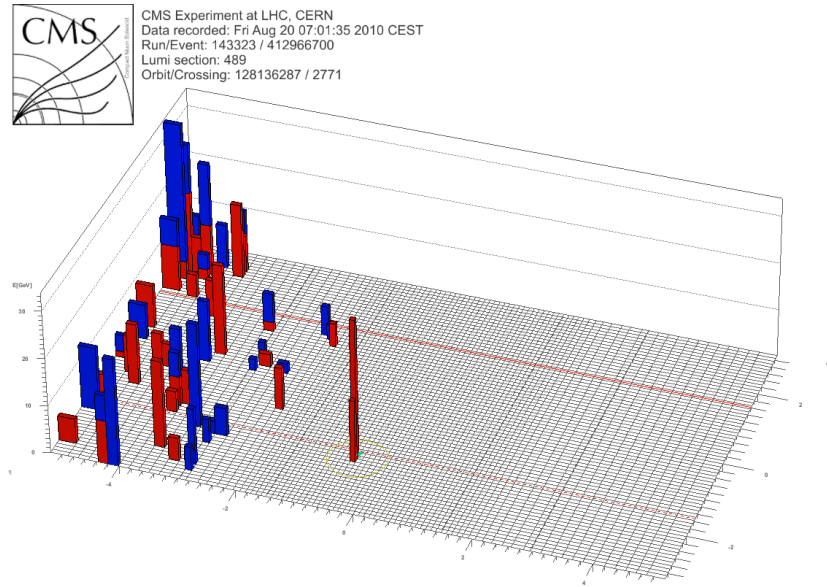


(a)

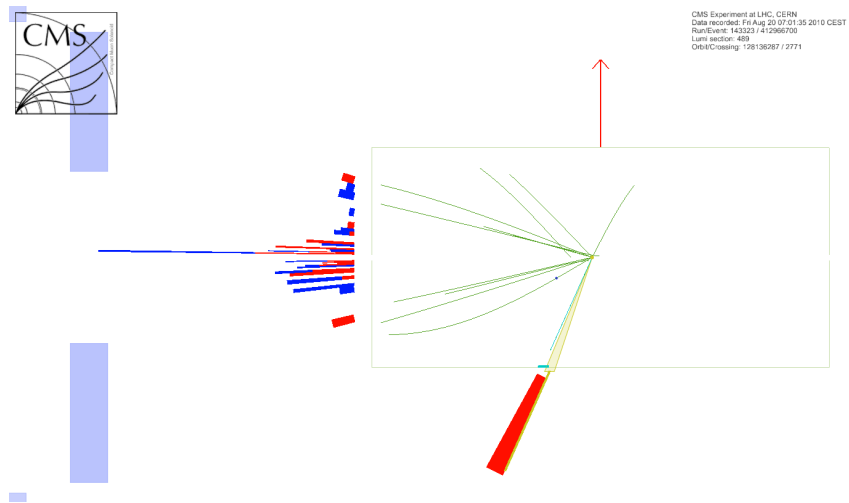


(b)

Figure E.1: Event displays of a non-diffractive W event in (a) “lego” representation of the calorimeter energy and (b) the rz -view.



(a)



(b)

Figure E.2: Event displays of a non-diffractive W event in (a) “lego” representation of the calorimeter energy and (b) the rz -view.

Bibliography

- [1] Peter Gillman and Leni Gillman. *The Wildest Dream: Mallory, His Life and Conflicting Passions*. The Mountaineers Book, 2000.
- [2] K. Nakamura et al. Review of Particle Physics. *Journal of Physics G*, 37:1, 2010.
- [3] Michael E. Peskin and Dan V. Schroeder. *An Introduction To Quantum Field Theory (Frontiers in Physics)*. Westview Press, 1995.
- [4] Francis. Halzen and Alan D. Martin. *Quarks and Leptons*. Wiley, 1985.
- [5] D. Perkins. *Introduction to High Energy Physics*. Addison-Wesley, 1982.
- [6] Bogdan Povh, Klaus Rith, Christoph Scholz, and Frank Zetsche. *Teilchen und Kerne. Eine Einfhruung in die physikalischen Konzepte*. Springer-Verlag GmbH, 2004.
- [7] F. Englert and R. Brout. Broken Symmetry and the Mass of Gauge Vector Mesons. *Physical Review Letters*, 13:321–323, August 1964.
- [8] P. W. Higgs. Broken Symmetries and the Masses of Gauge Bosons. *Physical Review Letters*, 13:508–509, October 1964.
- [9] G. S. Guralnik, C. R. Hagen, and T. W. Kibble. Global Conservation Laws and Massless Particles. *Physical Review Letters*, 13:585–587, November 1964.
- [10] S.L. Glashow. Partial Symmetries of Weak Interactions. *Nucl.Phys.*, 22:579–588, 1961.
- [11] Steven Weinberg. A Model of Leptons. *Phys.Rev.Lett.*, 19:1264–1266, 1967.
- [12] Abdus Salam. Weak and electromagnetic interactions. In Nils Svartholm, editor, *Elementary particle theory*, pages 367–377. Almquist & Wiksell.
- [13] F.J. Hasert et al. Observation of Neutrino Like Interactions Without Muon Or Electron in the Gargamelle Neutrino Experiment. *Phys.Lett.*, B46:138–140, 1973.
- [14] G. Arnison et al. Experimental Observation of Lepton Pairs of Invariant Mass Around $95 \text{ GeV}/c^2$ at the CERN SPS Collider. *Phys.Lett.*, B126:398–410, 1983.
- [15] G. Arnison et al. Experimental Observation of Isolated Large Transverse Energy Electrons with Associated Missing Energy at $s^{1/2} = 540 \text{ GeV}$. *Phys.Lett.*, B122:103–116, 1983.
- [16] P. Bagnaia et al. Evidence for $Z_0 \rightarrow e^+e^-$ at the CERN anti-p p Collider. *Phys.Lett.*, B129:130–140, 1983.
- [17] M. Banner et al. Observation of Single Isolated Electrons of High Transverse Momentum in Events with Missing Transverse Energy at the CERN anti-p p Collider. *Phys.Lett.*, B122:476–485, 1983.

- [18] M. Gomez-Bock, M. Mondragon, M. Muhlleitner, R. Noriega-Papaqui, I. Pedraza, et al. Rompimiento de la simetria electrodebil y la fisica del Higgs: Conceptos basicos. *J.Phys.Conf.Ser.*, 18:74–135, 2005.
- [19] Marc Sher. Electroweak Higgs Potentials and Vacuum Stability. *Phys.Rept.*, 179:273–418, 1989.
- [20] M. Baak, M. Goebel, J. Haller, A. Hoecker, D. Ludwig, et al. Updated Status of the Global Electroweak Fit and Constraints on New Physics. 2011.
- [21] R. Barate et al. Search for the Standard Model Higgs boson at LEP. *Phys.Lett.*, B565:61–75, 2003.
- [22] Combined CDF and D0 Search for Standard Model Higgs Boson Production with up to 10.0 fb^{-1} of Data. 2012.
- [23] ATLAS Collaboration. An update to the combined search for the Standard Model Higgs boson with the ATLAS detector at the LHC using up to 4.9 fb1 of pp collision data at $s = 7$ TeV. Technical Report ATLAS-CONF-2012-019, CERN, Geneva, Mar 2012.
- [24] CMS Collaboration. Combined results of searches for the standard model Higgs boson in pp collisions at $\sqrt{s} = 7$ TeV. *Phys.Lett.*, B710:26–48, 2012.
- [25] CMS Collaboration. Search for a Higgs boson in the decay channel H to $ZZ(*)$ to $q\bar{q}$ $l-l+$ in pp collisions at $\sqrt{s} = 7$ TeV. *JHEP*, 1204:036, 2012.
- [26] CMS Collaboration. Search for the standard model Higgs boson decaying into two photons in pp collisions at $\sqrt{s}=7$ TeV. *Phys.Lett.*, B710:403–425, 2012.
- [27] CMS Collaboration. Search for the standard model Higgs boson decaying to a W pair in the fully leptonic final state in pp collisions at $\sqrt{s} = 7$ TeV. *Phys.Lett.*, B710:91–113, 2012.
- [28] CMS Collaboration. Search for the standard model Higgs boson in the decay channel H to ZZ to 4 leptons in pp collisions at $\sqrt{s} = 7$ TeV. 2012.
- [29] CMS Collaboration. Search for the standard model Higgs boson in the H to ZZ to ll tau tau decay channel in pp collisions at $\sqrt{s}=7$ TeV. *JHEP*, 1203:081, 2012.
- [30] CMS Collaboration. Search for the standard model Higgs boson in the H to ZZ to $2l$ 2ν channel in pp collisions at $\sqrt{s} = 7$ TeV. *JHEP*, 1203:040, 2012.
- [31] CMS Collaboration. Search for neutral Higgs bosons decaying to tau pairs in pp collisions at $\sqrt{s}=7$ TeV. *Phys.Lett.*, B713:68–90, 2012.
- [32] CMS Collaboration. Search for the standard model Higgs boson decaying to bottom quarks in pp collisions at $\sqrt{s}=7$ TeV. *Phys.Lett.*, B710:284–306, 2012.
- [33] G. Dissertori, I. Knowles, and M. Schmelling. *Quantum Chromodynamics, High Energy Experiments and Theory*. International Series of Monographs on Physics Nr. 115. Oxford University Press, 2003.
- [34] J. Beringer et al. (Particle Data Group) Review of Particle Physics. *Phys. Rev.*, D 86, 2012.
- [35] F. D. Aaron et al. Combined Measurement and QCD Analysis of the Inclusive ep Scattering Cross Sections at HERA. *JHEP*, 01:109, 2010.
- [36] James Stirling. Personal website: <http://www.hep.phy.cam.ac.uk/~wjs/>, 2010.
- [37] (Ed.) Bruning, Oliver S., (Ed.) Collier, P., (Ed.) Lebrun, P., (Ed.) Myers, S., (Ed.) Ostojic, R., et al. LHC Design Report. 1. The LHC Main Ring. 2004.

- [38] (Ed.) Buning, O., (Ed.) Collier, P., (Ed.) Lebrun, P., (Ed.) Myers, S., (Ed.) Ostojic, R., et al. LHC Design Report. 2. The LHC infrastructure and general services. 2004.
- [39] (Ed.) Benedikt, M., (Ed.) Collier, P., (Ed.) Mertens, V., (Ed.) Poole, J., and (Ed.) Schindl, K. LHC Design Report. 3. The LHC injector chain. 2004.
- [40] SLAC News Center. Website: <https://news.slac.stanford.edu/sites/default/files/images/image/ce/lhc-aerial.jpg>, May 2011.
- [41] M. Lamont. LHC Beam Operations: Past, Present and Future. 2011.
- [42] M. Ferro-Luzzi. LHC 2011 Operation - As viewed from the Experiments. 2012.
- [43] Jan Kretzschmar. Electroweak Measurements at ATLAS & CMS. Presented at the 47th Rencontres de Moriond, La Thuile, Italy, 2012.
- [44] CMS Collaboration. CMS physics: Technical design report. 2006.
- [45] CMS Collaboration. The CMS experiment at the CERN LHC. *JINST*, 3:S08004, 2008.
- [46] CMS Collaboration. Tracker technical design report. 1998.
- [47] CMS Collaboration. Addendum to the CMS tracker TDR. 2000.
- [48] CMS Collaboration. The electromagnetic calorimeter. Technical design report. 1997.
- [49] CMS Collaboration. Search for a Standard Model Higgs boson decaying into two photons. *CMS Note*, AN-2012-160, 2012.
- [50] David Wardrope Claire Timlin and Alexandre Zabi. Personal website: Comparison between data and simulation of the detector response using test beam data http://www.hep.ph.ic.ac.uk/cms/physics/ECAL/alex_claire_david_ecal.html.
- [51] CMS Collaboration. Addendum to the CMS ECAL technical design report: Changes to the CMS ECAL electronics. 2002.
- [52] CMS Collaboration. CMS: The hadron calorimeter technical design report. 1997.
- [53] R.L. Gluckstern. Uncertainties in track momentum and direction, due to multiple scattering and measurement errors. *Nuclear Instruments and Methods*, 24(0):381 – 389, 1963.
- [54] CMS Collaboration. Precise mapping of the magnetic field in the CMS barrel yoke using cosmic rays. *Journal of Instrumentation*, 5:3021, March 2010.
- [55] CMS Collaboration. CMS, the magnet project: Technical design report. 1997.
- [56] CMS Collaboration. CMS, the Compact Muon Solenoid. Muon technical design report. 1997.
- [57] CMS Collaboration. Performance of CMS muon reconstruction in pp collision events at $\sqrt{s} = 7$ TeV. *ArXiv e-prints*, June 2012.
- [58] W. Adam et al. The CMS high level trigger. *Eur.Phys.J.*, C46:605–667, 2006.
- [59] W. Erdmann. Offline Primary Vertex Reconstruction with Deterministic Annealing Clustering. *CMS Note*, IN-2011-014, 2011.
- [60] CMS Collaboration. Electron reconstruction and identification at $\sqrt{s} = 7$ TeV. *CMS PAS*, EGM-2010-004, 2010.
- [61] Wolfgang Adam, R Fruehwirth, Are Strandlie, and T Todor. Reconstruction of Electrons with the Gaussian-Sum Filter in the CMS Tracker at the LHC. Technical Report CMS-NOTE-2005-001, CERN, Geneva, Jan 2005.

- [62] CMS Collaboration. Performance of CMS muon reconstruction in pp collisions at $\sqrt{s} = 7$ TeV. *CMS Paper*, MUO-10-004, 2010.
- [63] CMS Collaboration. Jet Performance in pp Collisions at $\sqrt{s} = 7$ TeV. *CMS PAS*, JME-2010-003, 2010.
- [64] CMS Collaboration. ParticleFlow Event Reconstruction in CMS and Performance for Jets, Taus, and E_T^{miss} . *CMS PAS*, PFT-2009-001, 2009.
- [65] M. Cacciari, G. P. Salam, and G. Soyez. The anti-kt jet clustering algorithm. *JHEP*, 0804:063, 2008.
- [66] CMS Collaboration. Jet energy calibration with photon+jet events. *CMS PAS*, JME-2009-004, 2009.
- [67] CMS Collaboration. Jet Energy Corrections. *CMS Internal Twiki*, <https://twiki.cern.ch/twiki/bin/view/CMSPublic/WorkBookJetEnergyCorrections>, 2012.
- [68] Matteo Cacciari and Gavin P. Salam. Pileup subtraction using jet areas. *Phys.Lett.*, B659:119–126, 2008.
- [69] S. Agostinelli et al. GEANT4: A Simulation toolkit. *Nucl.Instrum.Meth.*, A506:250–303, 2003.
- [70] CMS Collaboration. CMS Luminosity Based on Pixel Cluster Counting - Summer 2012 Update. *CMS PAS*, CMS PAS LUM-2012-001, 2012.
- [71] S. van der Meer. Calibration of the effective beam height in the ISR. [oai:cds.cern.ch:296752](http://oai.cds.cern.ch:296752). Technical Report CERN-ISR-PO-68-31. ISR-PO-68-31, CERN, Geneva, 1968.
- [72] CMS Collaboration. Measurement of CMS Luminosity. *CMS PAS*, EWK-2010-004, 2010.
- [73] CMS Collaboration. Measurement of the inclusive $W \rightarrow \mu\nu$ and $Z \rightarrow \mu^+\mu^-$ cross sections in pp collisions at $\sqrt{s} = 14$ TeV. *CMS Analysis Note*, CMS AN-2007-031, 2007.
- [74] CMS Collaboration. Measurement of the inclusive $W \rightarrow \mu\nu$ and $Z \rightarrow \mu^+\mu^-$ cross sections in pp collisions at $\sqrt{s} = 14$ TeV. *CMS Analysis Note*, CMS AN-2007-026, 2007.
- [75] CMS Collaboration. The CMS Luminosity System. *CMS Internal Note*, CMS IN-2007-030, 2007.
- [76] R. Bonino et al. Evidence for Transverse Jets in High Mass Diffraction. *Phys.Lett.*, B211:239, 1988.
- [77] CMS Collaboration. Forward Energy Flow, Central Charged-Particle Multiplicities, and Pseudorapidity Gaps in W and Z Boson Events from pp Collisions at 7 TeV. *Eur.Phys.J.*, C72:1839, 2012.
- [78] T.: G. Antchev et al. Elastic Scattering and Total Cross-Section in $p + p$ reactions measured by the LHC Experiment TOTEM at $\sqrt{s} = 7$ TeV. 2012.
- [79] Torbjorn Sjostrand, Stephen Mrenna, and Peter Z. Skands. PYTHIA 6.4 Physics and Manual. *JHEP*, 0605:026, 2006.
- [80] G. Latino, G. Antchev, P. Aspell, I. Atanassov, V. Avati, et al. First Results from the TOTEM Experiment. 2011.
- [81] P. D. B. Collins. *An Introduction to Regge Theory and High-Energy Physics*. Cambridge University Press, 1977.

- [82] Michele Arneodo and Markus Diehl. Diffraction for non-believers. 2005.
- [83] Niklaus E. Berger. Measurement of diffractive Phi meson photoproduction at HERA with the H1 fast track trigger. 2006.
- [84] U. Amaldi, M. Jacob, and G. Matthiae. Diffraction of Hadronic Waves. *Ann.Rev.Nucl.Part.Sci.*, 26:385–456, 1976.
- [85] A. Brandt. Jets in single diffraction and pomeron structure. *Nucl.Phys.Proc.Suppl.*, 25B:26–29, 1992.
- [86] A. Brandt et al. Evidence for a superhard pomeron structure. *Phys.Lett.*, B297:417–424, 1992.
- [87] Sparsh Navin. Diffraction in Pythia. 2010.
- [88] S. Chekanov et al. A QCD analysis of ZEUS diffractive data. *Nucl.Phys.*, B831:1–25, 2010.
- [89] A. Aktas et al. Dijet Cross Sections and Parton Densities in Diffractive DIS at HERA. *JHEP*, 0710:042, 2007.
- [90] A. Aktas et al. Measurement and QCD analysis of the diffractive deep-inelastic scattering cross-section at HERA. *Eur.Phys.J.*, C48:715–748, 2006.
- [91] Michele Gallinaro. Forward physics at the LHC. 2010.
- [92] F. Abe et al. Observation of diffractive W boson production at the Tevatron. *Phys.Rev.Lett.*, 78:2698–2703, 1997.
- [93] V.M. Abazov et al. Observation of diffractively produced W and Z bosons in $\bar{p}p$ collisions at $\sqrt{s} = 1800$ GeV. *Phys.Lett.*, B574:169–179, 2003.
- [94] T. Aaltonen et al. Diffractive W and Z Production at the Fermilab Tevatron. *Phys.Rev.*, D82:112004, 2010.
- [95] M. Arneodo A.Vilela Pereira. Study of single-diffractive production of W bosons at the LHC. *CMS Note*, AN-2007-033, 2008.
- [96] A. Sanchez. *Studies of W and Z Bosons with the CMS Experiment at the LHC*. PhD thesis, ETH Zurich, July 2012.
- [97] CMS Collaboration. CMS tracking performance results from early LHC operation. *European Physical Journal C*, 70:1165–1192, December 2010.
- [98] CMS Collaboration. Commissioning of the Particle-Flow Reconstruction in Minimum-Bias and Jet Events from pp Collisions at 7 TeV. *CMS PAS*, CMS PAS PFT-2010-002, 2010.
- [99] Torbjorn Sjostrand, Stephen Mrenna, and Peter Z. Skands. A Brief Introduction to PYTHIA 8.1. *Comput.Phys.Commun.*, 178:852–867, 2008.
- [100] CMS Collaboration. Observation of diffraction in proton-proton collisions at 900 and 2360 GeV centre-of-mass energies at the LHC. *CMS PAS*, FWD-2010-001, 2010.
- [101] LHC Higgs Cross Section Working Group, S. Dittmaier, C. Mariotti, G. Passarino, and R. Tanaka (Eds.). Handbook of LHC Higgs Cross Sections: 1. Inclusive Observables. *CERN-2011-002*, CERN, Geneva, 2011.
- [102] G. Davatz, M. Dittmar, and F. Pauss. Simulation of a Cross Section and Mass Measurement of a SM Higgs Boson in the $gg \rightarrow H \rightarrow WW \rightarrow \ell\nu\ell\nu$ Channel at the CERN LHC. *Phys.Rev.*, D76:032001, 2007.

- [103] LHC Higgs Cross Section Working Group. Internal Twiki: <https://twiki.cern.ch/twiki/bin/view/LHCPhysics/CrossSections>, 2010.
- [104] M. Dittmar and H. Dreiner. $h^0 \rightarrow W^+W^- \rightarrow \ell^+\ell'^-\nu_{\ell}\bar{\nu}_{\ell'}$ as the Dominant SM Higgs Search Mode at the LHC for $M_{h^0} = 155\text{--}180$ GeV. *Phys. Rev.*, D 55:167, 1996.
- [105] Paolo Nason. A New method for combining NLO QCD with shower Monte Carlo algorithms. *JHEP*, 0411:040, 2004.
- [106] Stefano Frixione, Paolo Nason, and Carlo Oleari. Matching NLO QCD computations with Parton Shower simulations: the POWHEG method. *JHEP*, 0711:070, 2007.
- [107] Simone Alioli, Paolo Nason, Carlo Oleari, and Emanuele Re. A general framework for implementing NLO calculations in shower Monte Carlo programs: the POWHEG BOX. *JHEP*, 1006:043, 2010.
- [108] Stefano Frixione and Bryan R. Webber. Matching NLO QCD computations and parton shower simulations. *JHEP*, 0206:029, 2002.
- [109] G. Corcella, I.G. Knowles, G. Marchesini, S. Moretti, K. Odagiri, et al. HERWIG 6: An Event generator for hadron emission reactions with interfering gluons (including supersymmetric processes). *JHEP*, 0101:010, 2001.
- [110] G. Corcella, I.G. Knowles, G. Marchesini, S. Moretti, K. Odagiri, et al. HERWIG 6.5 release note. 2002.
- [111] G. Bozzi, S. Catani, D. de Florian, and M. Grazzini. The q(T) spectrum of the Higgs boson at the LHC in QCD perturbation theory. *Phys. Lett.*, B564:65–72, 2003.
- [112] Giuseppe Bozzi, Stefano Catani, Daniel de Florian, and Massimiliano Grazzini. Transverse-momentum resummation and the spectrum of the Higgs boson at the LHC. *Nucl. Phys.*, B737:73–120, 2006.
- [113] Daniel de Florian, Giancarlo Ferrera, Massimiliano Grazzini, and Damiano Tommasini. Transverse-momentum resummation: Higgs boson production at the Tevatron and the LHC. *JHEP*, 1111:064, 2011.
- [114] G. Davatz, G. Dissertori, M. Dittmar, M. Grazzini, and F. Pauss. Effective K-factors for $gg \rightarrow H \rightarrow WW \rightarrow l\nu l\nu$ at the LHC. *JHEP*, 0405:009, 2004.
- [115] LHC Higgs Cross Section Working Group, S. Dittmaier, C. Mariotti, G. Passarino, and R. Tanaka (Eds.). Handbook of LHC Higgs Cross Sections: 2. Differential Distributions. *CERN-2012-002*, CERN, Geneva, 2012.
- [116] D. de Florian, G. Ferrera, M. Grazzini, and D. Tommasini. Higgs boson production at the LHC: transverse momentum resummation effects in the $H \rightarrow 2\gamma$, $H \rightarrow WW \rightarrow l\nu l\nu$ and $H \rightarrow ZZ \rightarrow 4l$ decay modes. *JHEP*, 1206:132, 2012.
- [117] CMS Collaboration. Measurement of $W+W^-$ Production and Search for the Higgs Boson in pp Collisions at $\sqrt{s} = 7$ TeV. *Phys.Lett.*, B699:25–47, 2011.
- [118] CMS Collaboration. Search for the Higgs boson in the $WW^{(*)}$ decay channel with the CMS experiment. *CMS PAS*, CMS PAS HIG-2007-001, 2007.
- [119] CMS Collaboration. Search Strategy for a Standard Model Higgs Boson Decaying to two W Bosons in the Fully Leptonic Final State. *CMS PAS*, CMS PAS HIG-2008-006, 2008.
- [120] CMS Collaboration. Search for Higgs Boson Decays to Two W Bosons in the Fully Leptonic Final State at $\sqrt{s} = 7$ TeV. *CMS PAS*, CMS PAS HIG-2010-003, 2010.
- [121] CMS Collaboration. Search for Higgs Boson Decays to Two W Bosons in the Fully Leptonic Final State at $\sqrt{s} = 7$ TeV. *CMS Analysis Note*, CMS AN-2010-411, 2010.

- [122] CMS Collaboration. First Measurement of WW Production and Search for Higgs Boson in pp Collisions at $\sqrt{s} = 7$ TeV. *CMS PAS*, CMS PAS EWK-2010-009, 2010.
- [123] CMS Collaboration. Search for the Higgs Boson Decaying to W^+W^- in the Fully Leptonic Final State. *CMS PAS*, CMS PAS HIG-2011-003, 2010.
- [124] W. Andrews et al. Search for Higgs Boson Decays to Two W Bosons in the Fully Leptonic Final State with Full 2011 pp Dataset at $\sqrt{s} = 7$ TeV. *CMS Note*, AN-2011-432, 2011.
- [125] W. Andrews et al. Search for Higgs Boson Decays to Two W Bosons in the Fully Leptonic Final State $\sqrt{s} = 7$ TeV with 2011 data of CMS detector. *CMS Note*, AN-2011-148, 2011.
- [126] CMS Collaboration. Search for the Higgs Boson Decaying to W^+W^- in the Fully Leptonic Final State. *CMS PAS*, CMS PAS HIG-2011-014, 2011.
- [127] J. Varela. Triggers for physics at instantaneous luminosity $1E33$ in the CMS experiment. *CMS Note*, CMS CR-2011/158, 2011.
- [128] CMS Collaboration. Physics Validation: Pileup Studies. *CMS Internal Twiki*, <https://twiki.cern.ch/twiki/bin/viewauth/CMS/PileupInformation>, 2012.
- [129] A. Apyan et al. Electron Identification Using Multivariate Methods. *CMS Note*, AN-2011-413, 2011.
- [130] W. Andrews et al. Uncertainties on the Lepton Selection Efficiency for $t\bar{t}$ Cross Section Analysis. *CMS Note*, AN-2010-274, 2010.
- [131] G. Bauer et al. Lepton efficiencies for the inclusive W cross section measurement with 36.1 pb^{-1} . *CMS Note*, AN-2011-097, 2011.
- [132] CMS Collaboration. Commissioning of b-jet identification with pp collisions at $\sqrt{s} = 7$ TeV. *CMS PAS*, CMS PAS BTV-2010-001, 2010.
- [133] S. Xie et al. Study of Data-Driven Methods for Estimation of Fake Lepton Backgrounds. *CMS Note*, AN-2009-120, 2009.
- [134] W. Andrews et al. Fake Rates for dilepton Analyses. *CMS Note*, AN-2010-257, 2010.
- [135] W. Andrews et al. A Method to Measure the Contribution of $DY \rightarrow l^+l^-$ to a di-lepton + MET Selection. *CMS Note*, AN-2009-023, 2009.
- [136] A. Hoecker et al. TMVA - Toolkit for Multivariate Data Analysis. *ArXiv Physics e-prints*, March 2007.
- [137] G. Dissertori, P. Lecomte, D. Luckey, F. Nessi-Tedaldi, F. Pauss, T. Otto, S. Roesler, and C. Urscheler. A study of high-energy proton induced damage in cerium fluoride in comparison with measurements in lead tungstate calorimeter crystals. *Nuclear Instruments and Methods in Physics Research A*, 622:41–48, October 2010.
- [138] CMS Collaboration. ECAL response variations due to LHC irradiation. *CMS Performance Note*, CMS DP-2012-027, 2012.
- [139] CMS Collaboration. Jet Energy Corrections. *CMS Internal Twiki*, <https://twiki.cern.ch/twiki/bin/view/CMSPublic/WorkBookJetEnergyCorrections#JetCorUncer>, 2011.
- [140] CMS Collaboration. Absolute Calibration of the Luminosity Measurement at CMS: Winter 2012 Update. *CMS PAS*, SMP-2012-008, 2012.

- [141] Thomas Junk. Confidence level computation for combining searches with small statistics. *Nucl.Instrum.Meth.*, A434:435–443, 1999.
- [142] Alexander L. Read. Presentation of search results: The CL(s) technique. *J.Phys.G*, G28:2693–2704, 2002.
- [143] CERN. *oai:cds.cern.ch:411537. 1st Workshop on Confidence Limits*, Geneva, 2000. CERN.
- [144] M. Chen A. Korytov, G. Petrucciani et al. Procedure for the LHC Higgs boson search combination in summer 2011. *CMS Note*, AN-2011-298, 2011.
- [145] CMS Collaboration. Measurement of WW production rate in pp collisions at $\sqrt{s} = 7$ TeV. *CMS PAS*, CMS PAS SMP-2012-005, 2012.
- [146] CMS Collaboration. Measurement of the WW production cross section in pp collisions at $\sqrt{s} = 8$ TeV. *CMS PAS*, CMS PAS SMP-2012-013, 2012.
- [147] Charalampos Anastasiou, Kirill Melnikov, and Frank Petriello. Fully differential Higgs boson production and the di-photon signal through next-to-next-to-leading order. *Nucl.Phys.*, B724:197–246, 2005.
- [148] CMS Collaboration. Evidence for a new state decaying into two photons in the search for the standard model Higgs boson in pp collisions. *CMS PAS*, CMS PAS HIG-2012-015, 2012.
- [149] CMS Collaboration. Evidence for a new state in the search for the standard model Higgs boson in the H to ZZ to 4 leptons channel in pp collisions at $\sqrt{s} = 7$ and 8 TeV. *CMS PAS*, CMS PAS HIG-2012-016, 2012.
- [150] CMS Collaboration. Search for the standard model Higgs boson decaying to W^+W^- in the fully leptonic nal state in pp collisions at $\sqrt{s} = 8$ TeV. *CMS PAS*, CMS PAS HIG-2012-017, 2012.
- [151] CMS Collaboration. Search for the standard model Higgs boson decaying to tau pairs in pp collisions. *CMS PAS*, CMS PAS HIG-2012-018, 2012.
- [152] CMS Collaboration. Search for the standard model Higgs boson produced in association with W or Z bosons, and decaying to bottom quarks (ICHEP 2012). *CMS PAS*, CMS PAS HIG-2012-019, 2012.
- [153] CMS Collaboration. Search for the standard model Higgs boson in the $H \rightarrow ZZ \rightarrow 2\ell 2\nu$ channel in pp collisions at $\sqrt{s} = 7$ and 8 TeV. *CMS PAS*, CMS PAS HIG-2012-023, 2012.
- [154] CMS Collaboration. Search for the Standard Model Higgs boson in the $H \rightarrow WW \rightarrow \ell\nu jj$ decay channel in pp collisions at $\sqrt{s} = 8$ TeV. *CMS PAS*, CMS PAS HIG-2012-021, 2012.
- [155] CMS Collaboration. Search for Higgs boson production in association with a top quark pair in pp collisions. *CMS PAS*, CMS PAS HIG-2012-025, 2012.
- [156] CMS Collaboration. Observation of a new boson with a mass near 125 GeV. *CMS PAS*, CMS PAS HIG-2012-020, 2012.
- [157] ATLAS Collaboration. Observation of a new particle in the search for the Standard Model Higgs boson with the ATLAS detector at the LHC. 2012.
- [158] ATLAS Collaboration. Observation of an excess of events in the search for the Standard Model Higgs boson in the gamma-gamma channel with the ATLAS detector. *ATLAS CONF*, ATLAS-CONF-2012-091, 2012.

- [159] ATLAS Collaboration. Observation of an excess of events in the search for the Standard Model Higgs boson in the $H \rightarrow ZZ^{(*)} \rightarrow 4l$ channel with the ATLAS detector. *ATLAS CONF*, ATLAS-CONF-2012-092, 2012.
- [160] ATLAS Collaboration. Observation of an Excess of Events in the Search for the Standard Model Higgs Boson in the $H \rightarrow WW \rightarrow l\nu l\nu$ Channel with the ATLAS Detector. *ATLAS CONF*, ATLAS-CONF-2012-098, 2012.
- [161] ATLAS Collaboration. Search for the Higgs boson in the associated mode $WH \rightarrow WWW^{(*)} \rightarrow l\nu l\nu$ with the ATLAS detector at $\sqrt{s}=7\text{TeV}$. *ATLAS CONF*, ATLAS-CONF-2012-078, 2012.
- [162] John Ellis and Dae Sung Hwang. Does the ‘Higgs’ have Spin Zero? 2012.

Acknowledgment

The first years of data taking at the LHC at CERN have been very exciting and it is huge privilege that I had the opportunity to take part in this extraordinary journey which culminated in the discovery of long sought Higgs boson.

I would like especially to thank Günther Dissertori for giving me the possibility to write my Ph. D. thesis in the high energy physics group of the Institute for Particle Physics of ETH Zürich and I am very grateful for his support during the last years.

I would like to express my gratitude to Maiko and Alessandro, my collaborators and office mates during the Higgs analysis as well as during the writing of this thesis, for their extraordinary support. I learned a lot from you.

Further I would like to thank Ann-Karin for the teamwork during the diffractive analysis and Paolo for his supervision. A big thank goes to Hannes for his help and the many interesting discussions. I also thank Michael, for the countless discussions, explanations and constructive comments to this thesis.

A special thank goes to Babis who accepted to be the co-examiner for my defense and to Fabian who always gave some of his precious time to help me.

Further I would like to thank all the members and past members of the ETH group, as well as my friends, especially Pascal and Yves.

I am very grateful to my family for their endless support and last but not least to Christina for everything!

Curriculum Vitae: Jürg Eugster

Born: 21. October 1981

Nationality: Swiss

Education

2008 - 2012 **Ph.D. in high energy physics**, *ETH Zürich, Switzerland*
Thesis: “*Observation of Diffractive W and Z Boson Production and Search for a Standard Model Higgs Boson in the $H \rightarrow WW \rightarrow \ell\nu\ell\nu$ Channel at CMS with $\sqrt{s} = 7$ TeV pp-Collision Data*”
Supervisor: Prof. Günther Dissertori

2008 **Diploma in experimental physics**, *ETH Zürich, Switzerland*
Thesis: “*Fast Simulation Studies of Calorimeter and Particle Flow Jet Reconstruction in CMS*”
Supervisor: Prof. Günther Dissertori

2002 - 2008 **Studies of physics**, *ETH Zürich, Switzerland*
Experimental Particle Physics

2002 **Matura Type C**, *Lyceum Alpinum Zuoz, Switzerland*
Mathematics and Physics

Publications (Selection of publications with major contributions.)

2011 The CMS Collaboration
“*Forward Energy Flow, Central Charged-Particle Multiplicities, and Pseudorapidity Gaps in W and Z Boson Events from pp Collisions at 7 TeV.*”
Eur.Phys.J. C72 (2012) 1839, arXiv:1110.0181 [hep-ex]

2012 The CMS Collaboration
“*Search for the standard model Higgs boson decaying to a W pair in the fully leptonic final state in pp collisions at $\sqrt{s} = 7$ TeV*”
Phys.Lett. B710 (2012) 91-113, arXiv:1202.1489 [hep-ex]